Measurement of the top-quark pair production cross-section in pp collisions at $\sqrt{s} = 7$ TeV using final states with an electron or a muon and a hadronically decaying τ-lepton

Yuta TAKAHASHI

High Energy Physics Laboratory
Department of Physics, Nagoya university

October, 2012

Abstract

The t-quark is the heaviest elementary particle observed so far (172.9±1.5 GeV [1]). Owing to its largest mass, the t-quark is believed to have a strong connection with physics beyond the Standard Model (SM). It is thus essential to understand the production and the decay process of the t-quark in the context of the SM through a measurement of the t-quark pair ($t\bar{t}$) production cross-section ($\sigma_{t\bar{t}}$) at the collider experiment. By using a large number of proton-proton (pp) collision data at $\sqrt{s} = 7$ TeV produced by the Large Hadron Collider (LHC), ATLAS experiment has been measured $\sigma_{t\bar{t}}$ in the single-lepton ($t\bar{t} \to \ell^+\nu_\ell q q^{'} b\bar{b}$) [2] , di-lepton ($t\bar{t} \to \ell^+\nu_\ell \ell^-\bar{\nu}_\ell b\bar{b}$) [3] and all-hadronic ($t\bar{t} \to q q^{'} q^{''} q^{'''} b\bar{b}$) [4] channel ($\ell = e, \mu$). The combined result (177±11 pb) is in good agreement with the SM prediction (164^{+11}_{-16} pb).

This thesis reports on the first ATLAS measurement of the $\sigma_{t\bar{t}}$ using final states characterized by a lepton (a muon or an electron) and a hadronically decaying τ-lepton ($t\bar{t} \to \tau^+\nu_\tau \ell^-\bar{\nu}_\ell b\bar{b}$). This measurement is of importance toward the search for charged Higgs boson ($H^\pm$) that in some scenarios predominantly decays into $\tau\nu_\tau$ and contribute to this decay process.

Candidate events are extracted from the 2.05 fb^{-1} pp collision data by requiring a lepton, a hadronically decaying τ candidate, more than two jets where at least one of them is identified as originating from a b-quark and a large missing transverse momentum. The τ-lepton either decays into leptonic (35%, $\tau \to \ell\nu_\ell\nu_\tau$) or hadronic (65%, $\tau \to h{+}n\pi^0$, where $h = \pi^\pm, K^\pm$), where the former case is not used for the identification as it is not distinguishable to that of primary leptons. The hadronically decaying τ-lepton is reconstructed as a narrow and collimated jet compared to the quark, gluon originated jet. However, as there is no distinct variable that can separate between them, a majority of the candidate events come from $t\bar{t}$ single-lepton events by one of the jets misidentified as a hadronically decaying τ-lepton.

In order to isolate signal events among candidate events, the analysis exploits a multivariate analysis based on more than 8 parameters related to the observed τ candidate to calculate the similarity to the real τ-lepton, which leads to the discrimination of the signal events from background processes. This is then followed by the background estimation in a data-driven way to minimize the systematic uncertainty. As the result, $\sigma_{t\bar{t}}$ is measured to be :

$$\sigma_{t\bar{t}} = 186 \pm 13 \text{ (stat.)} \pm 20 \text{ (syst.)} \pm 7 \text{ (lumi.) pb},$$

where each uncertainty represents the statistical uncertainty, the systematic uncertainty, and the uncertainty related to the luminosity determination, respectively.

The observed cross-section is the first $\sigma_{t\bar{t}}$ measurement with τ-lepton final state at $\sqrt{s} =$ 7 TeV, with unprecedented accuracy of dσ/σ =13%. The observed cross-section is consistent with the theoretical calculation based on the Standard Model. Using the measurement obtained in this thesis, the upper limit on the branching ratio that the t-quark decays into $t \to H^\pm b$ has been calculated to be 4 - 8% with 95% confidence level, depending on the assumed charged Higgs boson mass. The ratio of the observed cross-section with that of measured in di-lepton channel gives 1.00 ± 0.09. With above results, this thesis demonstrated the validity of the SM, especially about the t-quark decay into a hadronically decaying τ-lepton ($t \to \tau^+\nu b$).

Contents

Chapter 1

Introduction

Practically, all the experimental data in particle physics experiments can be accounted for by the Standard Model (SM) formulated in 1970 s, which is based on the quantum field theory. In the SM, all matter is built from fundamental spin 1/2 particles (fermions), six quarks and six leptons, with its interaction mediated by the gauge field carried by bosons. The Higgs boson is predicted as a consequence of the spontaneous symmetry breaking of the Higgs field to endow the gauge boson masses.

The SM has successfully explained most of the experimental observations derived so far. Up to now, any significant disagreements have not been reported yet. However, it is insufficient as there are several deficiencies to be explained, such as a fine tuning problem of the Higgs boson mass, where the cancellation of $\mathcal{O}(10^{19})$ GeV is necessary to obtain the Higgs boson mass, $\mathcal{O}(100)$ GeV. This is considered to be unnatural unless otherwise a well-motivated physical mechanism that can naturally explain the cancellation. One of such solution is a supersymmetry (SUSY) model, where SM counterparts differing by spin 1/2 are postulated as well as five Higgs bosons (three neutral, two charged) in its minimal extension.

The t-quark is the up-type fermion that belongs to the 3^{rd}-generation of the quark family. It was firstly discovered at the Tevatron in 1995, which is the former energy frontier experiment at the center-of-mass energy, $\sqrt{s} = 1.96$ TeV. Since then, the t-quark mass has been measured precisely to be 172.9 $\pm$ 1.5 GeV [1], which is the heaviest fundamental particle observed so far. Owing to its largest mass, there are several theoretical predictions that new physics could appear in both the production and the decay process of the t-quark such as the production via a 4^{th}-generation quark, or decay through a charged Higgs boson. These new effect can be probed upon our understanding of the t-quark related to the production and the decay process, that can be established by measuring the t-quark pair ($t\bar{t}$) production cross-section at the collider experiment. The proton-proton (pp) collision data at the world highest center-of-mass energy of $\sqrt{s} = 7$ TeV produced by the Large Hadron Collider (LHC), and accumulated by the ATLAS detector provides a unique opportunity for this measurement.

Based on the 0.7 - 4.7 fb^{-1} pp collision data, ATLAS experiment has been measured $\sigma_{t\bar{t}}$ using the single-lepton ($t\bar{t} \to \ell^+\nu_\ell q q^{'} b\bar{b}$, $\ell = e, \mu$) [2], the di-lepton ($t\bar{t} \to \ell^+\nu_\ell \ell^-\bar{\nu}_\ell b\bar{b}$) [3] and the all-hadronic channel ($t\bar{t} \to q q^{'} q^{''} q^{'''} b\bar{b}$) [4], with its combined cross-section measured to be:

$$\sigma_{t\bar{t}} = 177 \pm 3(\text{stat.})^{+8}_{-7}(\text{syst.}) \pm 7(\text{lumi.}), \tag{1.1}$$

where each uncertainty represents the statistical uncertainty, the systematic uncertainty and the uncertainty related to the luminosity determination. The result is consistent with the SM prediction (164^{+11}_{-16} pb) with the uncertainty of 6%, already smaller than the theoretical accuracy of 10%. With this result, the ATLAS Collaboration has been demonstrated the validity of the SM about the t-quark production and the decay process.

This thesis reports on the first ATLAS measurement on the $t\bar{t}$ production cross-section using final states characterized by a lepton and a hadronically decaying τ-lepton ($t\bar{t} \to \tau^+\nu_\tau\ell^-\bar{\nu}_\ell b\bar{b}$). This measurement is challenging as the identification of the τ-lepton is difficult among such a busy environment at the LHC. However, it is worth measuring toward a search for new physics beyond the SM such as the charged Higgs boson ($H^\pm$), predicted by supersymmetry of nature. If the charged Higgs boson exists with its mass lower than the t-quark mass minus the b-quark mass, the t-quark can have a substantial branching ratio to $H^\pm b$. Since the charged Higgs boson predominantly decays into $\tau\nu_\tau$ in large $\tan\beta$ (the ratio of the vacuum expectation value for two Higgs doublets in the supersymmetry model), this may increase the branching ratio with τ-lepton final state. It is therefore necessary to understand the t-quark decay in the context of the SM through the $\sigma_{t\bar{t}}$ measurement.

As the analysis makes use of single lepton triggers relying on its large reduction rate, the commissioning and the daily operation of the ATLAS endcap muon trigger detector has been performed. This thesis also describes the main achievement during the commissioning period.

The remaining part of the thesis proceeds as followings. In Chapter 2, a framework of the Standard Model and the theoretical aspect of the $t\bar{t}$ production and the decay process are described. The experimental results on the $t\bar{t}$ production cross-section are also reviewed to show how well they currently match SM predictions. In Chapter 3, the LHC accelerator and the ATLAS detector are explained. In Chapter 4, the commissioning of the muon trigger detector is described. In Chapter 5, the measurement of the $t\bar{t}$ production cross-section using final states with a lepton and a hadronically decaying τ-lepton is described. Chapter 6 includes the conclusion.

Chapter 2

Physics Backgrounds

2.1 The Standard Model and the $t\bar{t}$ production cross-section measurement

2.1.1 The Standard Model

The Standard Model (SM) of particle physics is the currently accepted as a theoretical framework by which the phenomena of the elementary particles are explained. The SM is based on the quantum field theory, which is a combination of the quantum mechanism and the special relativity. The guiding principle is a local gauge symmetry, where the Lagrangian is kept to be invariant under the local gauge transformation.

$$\psi(x) \rightarrow \psi^{'}(x) = e^{i\alpha(x)}\psi(x), \tag{2.1}$$

where $\psi(x)$ and $\psi^{'}(x)$ are the wave functions of the field before and after the transformation and $\alpha(x)$ represents a phase at each space point x. This requirement leads to a conservation laws according to the Noether theorem and naturally introduces an interaction between particles in terms of the exchange of mediated gauge bosons.

Table 2.1 summarizes all the elementary particles that compose matter, three pairs of quarks and three of leptons, all of them have a spin 1/2 (fermion). The interactions between fermions are mediated by the gauge field carried by bosons, the γ for the electromagnetic, the $W^{\pm}/Z$ for the weak, the gluon (g) for the strong and the Graviton (G) for the gravitational interactions. The list of the gauge bosons are shown in Table 2.2.

In addition, the Higgs boson with the neutral charge and the spin zero is predicted to endow the gauge boson masses ($M_W = 80$ GeV, $M_Z = 91$ GeV) which is originally required to be zero by the local gauge symmetry [A.1]. On July 2012, both the ATLAS and CMS experiment announced the discovery ($> 5\sigma$) of a new boson in the mass region around $125 - 126$ GeV. Although the observed excess of the event is consistent with the predicted Higgs boson, further experimental verifications are needed to decide its spin, parity and its coupling constant to the SM particles.

In spite of the successful description of the experimental observations derived so far, the SM is considered to be insufficient as there are several deficiencies to be explained. One of

Quarks			Q	I_3^W	Y^W	B	L	C
$\begin{pmatrix} u \\ d' \end{pmatrix}_L$	$\begin{pmatrix} c \\ s' \end{pmatrix}_L$	$\begin{pmatrix} t \\ b' \end{pmatrix}_L$	$\begin{pmatrix} +\frac{2}{3} \\ -\frac{1}{3} \end{pmatrix}$	$\begin{pmatrix} +\frac{1}{2} \\ -\frac{1}{2} \end{pmatrix}$	$+\frac{1}{3}$	$+\frac{1}{3}$	0	(R,G,B)
u_R	c_R	t_R	$+\frac{2}{3}$	0	$+\frac{4}{3}$	$+\frac{1}{3}$	0	(R,G,B)
d_R	s_R	b_R	$-\frac{1}{3}$	0	$-\frac{2}{3}$	$+\frac{1}{3}$	0	(R,G,B)
Leptons								
$\begin{pmatrix} \nu_e \\ e \end{pmatrix}_L$	$\begin{pmatrix} \nu_\mu \\ \mu \end{pmatrix}_L$	$\begin{pmatrix} \nu_\tau \\ \tau \end{pmatrix}_L$	$\begin{pmatrix} 0 \\ -1 \end{pmatrix}$	$\begin{pmatrix} +\frac{1}{2} \\ -\frac{1}{2} \end{pmatrix}$	-1	0	1	0
e_R	μ_R	τ_R	-1	0	-2	0	1	0

Table 2.1: Fermions in the Standard Model. Three generations of quarks and leptons categorized by its mass. Q denotes the electric charge in the unit of e, I_3^W is a third component of the weak isospin, $Y^W = 2(Q - I_3^W)$ is a weak hyper charge, B denotes the baryon number, L denotes the lepton number and C denotes the color. The subscription L (R) denotes the left (right) handed, where only left-handed fermion composes $SU(2)$ doublet.

Boson	Composition	Q	I_3^W	Y^W	B	L	Spin
g	G_μ	0	0	0	0	0	1
$W^\pm$	$\begin{pmatrix} W^+ \\ W^- \end{pmatrix} = \begin{pmatrix} \frac{W_\mu^1 + W_\mu^2}{\sqrt{2}} \\ \frac{W_\mu^1 - W_\mu^2}{\sqrt{2}} \end{pmatrix}$	$\begin{pmatrix} +1 \\ -1 \end{pmatrix}$	$\begin{pmatrix} +1 \\ -1 \end{pmatrix}$	0	0	0	1
Z^0	$Z_\mu = \cos\theta_W W_\mu^3 - \sin\theta_W B_\mu$	0	0	0	0	0	1
γ	$A_\mu = \sin\theta_W W_\mu^3 + \cos\theta_W B_\mu$	0	0	0	0	0	1
H	$\begin{pmatrix} \phi^+ \\ \phi^0 \end{pmatrix} = \begin{pmatrix} 0 \\ v/\sqrt{2} \end{pmatrix}$	$\begin{pmatrix} +1 \\ 0 \end{pmatrix}$	$\begin{pmatrix} +\frac{1}{2} \\ -\frac{1}{2} \end{pmatrix}$	1	0	0	0

Table 2.2: Gauge bosons in the Standard Model: three types of gauge bosons with spin one, each accounts for the strong (g), the weak ($W^\pm, Z^0$) and the electromagnetic (γ) interaction. The gravity is not listed here. Higgs boson with spin zero is predicted to endow the gauge boson masses. W_μ ($\mu = 1, 2, 3$) and B_μ are the gauge fields corresponding to the $SU(2)$ and $U(1)$ gauge group, respectively.

such example is a hierarchy problem, where there is 10^{40} difference between the strength of the electroweak force and the gravity. The energy scale at which the gravity approaches to the electroweak energy scale is given by the plank mass scale, $\mathcal{M}_{\text{plank}} = \sqrt{\hbar c / G_N} = 10^{19}$ GeV. This brings up a fine tuning problem of the Higgs boson mass, where the correction term of the Higgs boson mass squared (δm_H^2) is given by

$$m_H^2 = (m_H)_0^2 + \delta m_H^2 \tag{2.2}$$

$$\delta m_H^2 = \frac{3\Lambda^2}{16\pi^2 v^2}(-4m_t^2 + 2m_W^2 + m_Z^2 + m_H^2 + \cdots). \tag{2.3}$$

Λ is a energy scale to which the SM is applicable (cut-off energy) and $(m_H)_0$ is a bare Higgs

boson mass and v is the vacuum expectation value. The correction term comes from the t-quark loop, the $W^{\pm}, Z$ boson loop and the H boson loop as is shown in Figure 2.1.

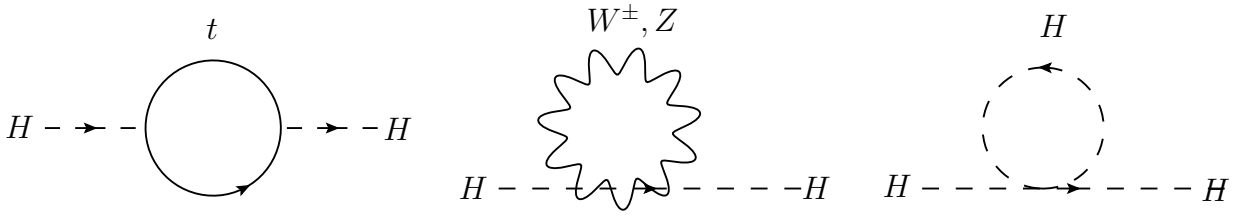

Figure 2.1: Feynman diagrams of the correction term to the Higgs boson mass squared.

Suppose the cut-off energy is close to the plank mass scale ($\Lambda \sim \mathcal{M}_{\rm plank}$), the bare Higgs boson mass and the correction term need to be finely tuned to be the electroweak energy scale, $\mathcal{O}(100)$ GeV after canceling out $\mathcal{O}(10^{19})$ GeV. This level of cancellation is considered to be unnatural without a well motivated physical mechanism[1]. This is so-called the hierarchy problem.

The SM extension, called supersymmetry (SUSY), is one of the theoretical candidate that can naturally explain the hierarchy problem [A.2]. The hypothesis of the supersymmetry postulates a fermion-boson symmetry, where the new fermion (boson) partners are predicted for all known fundamental bosons (fermions). Since the radiative corrections from virtual boson and fermion loops are of opposite sign and can cancel out the divergent amplitudes as is shown in Figure 2.2. Since there are no experimental proof of the SUSY particles with its mass exactly same with the SM partners, the supersymmetry is somehow a broken symmetry. However, from the view point of naturalness, it can exist up to the TeV energy scale.

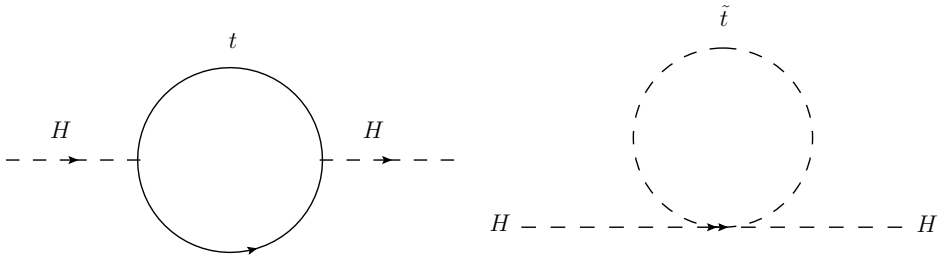

Figure 2.2: If the $\tilde{t}$-quark (the bosonic parter of the t-quark in the SUSY model) exist, the hierarchy problem will be naturally solved through the contribution from the right diagram.

One of the widely quoted scheme of the SUSY is the Minimal Supersymmetric Standard Model (MSSM), where two complex Higgs doublets are required, yielding five physical Higgs particles (three neutral: h, H, A, and two charged: $H^{\pm}$). Suppose the newly discovered boson at 126 GeV is a Higgs boson, it is a crucial aspect to find another Higgs boson to verify if the

[1]In the case of the fermion and the gauge boson, the cancellation becomes proportional to $\ln \Lambda$. Therefore, the fine tuning is the unique problem for the scalar particle.

nature adopts the supersymmetry. The discovery of more than two Higgs bosons or the charged Higgs boson will directly connects to new physics.

2.1.2 $t\bar{t}$ production cross-section

The t-quark was discovered in 1995 by CDF [5] and DØ [6] experiment at the proton-antiproton ($p\bar{p}$) collider at the Tevatron, which is the former energy frontier collider at $\sqrt{s} = 1.96$ TeV. The t-quark is currently known as the third generation of the up-type quark with its mass measured to be m_t =172.9±1.5 GeV [1], which is the heaviest elementary particle so far. Owing its largest mass, the t-quark is considered to have a strong connection with new physics such as the production via a 4^{th}-generation quark or decay through a charged Higgs boson. These effect can be probed upon our understanding of the t-quark production and the decay, which can be tested by measuring the t-quark pair ($t\bar{t}$) production cross-section ($\sigma_{t\bar{t}}$). By comparing the measured cross-section to that of the SM prediction, one can assess the validity of our knowledge concerning to the production and the decay of the t-quark. Furthermore, rather fortunately, the t-quark possesses following unique characteristics enough to predict $\sigma_{t\bar{t}}$ with relatively small accuracy.

- In order to produce $t\bar{t}$, a momentum transfer $q^2 \sim 2m_t = 345$ GeV is needed. In this q^2, the strong coupling constant (α_s), which runs as a function of q^2, becomes small ($\alpha_s \approx 0.1$) enough to calculate the cross-section precisely ($\approx 10\%$) as a perturbative series in α_s.

- The t-quark has a large partial decay width ($\propto m_t^3$) of 1.5 GeV. This means a typical decay time of 10^{-25} s, which is shorter than the hadronization timescale (10^{-23} s). Therefore, the $t\bar{t}$ system is so short-lived that no discrete bound state is formed. The decay process is thus purely through the well-known weak interaction with small ambiguity ($\approx 1\%$)

At the pp collider with $\sqrt{s} = 7$ TeV, the t-quark pair production cross-section is calculated to be $\sigma_{t\bar{t}} = 164^{+11}_{-16}$ pb, with only 10% accuracy.

Using 0.7 fb^{-1} pp collision data accumulated by the ATLAS detector, $\sigma_{t\bar{t}}$ has been measured precisely using the single-lepton ($t\bar{t} \to \ell^+\nu_\ell q q' b\bar{b}$, $\ell = e, \mu$) [2], the di-lepton ($t\bar{t} \to \ell^+\nu_\ell \ell^-\bar{\nu}_\ell b\bar{b}$) [3] and the all-hadronic ($t\bar{t} \to q q' q'' q''' b\bar{b}$) [4] channel. Figure 2.3 shows the observed cross-section and the combined result (177±11 pb), all of them found to be consistent with the SM prediction. The uncertainty of the combined cross-section reaches 6%, which is smaller than the theoretical accuracy of 10%. The uncertainty is already limited by the systematic uncertainty except for the all-hadronic channel.

Now that the $t\bar{t}$ production cross-section is verified using major decay processes, the next step is to measure $\sigma_{t\bar{t}}$ in a segmented manner to look ahead for new physics. At this point, $\sigma_{t\bar{t}}$ measurement in τ-lepton final state is of importance as this process is sensitive to the existence of the charged Higgs boson. If the charged Higgs boson exists, and its mass lower than the t-quark mass minus the b-quark mass, the t-quark predominantly decays into a charged Higgs boson and a b-quark. In MSSM, one of the two Higgs doublet couples to the up-type fermion and the other doublet couples to the down-type fermion with different vacuum expectation

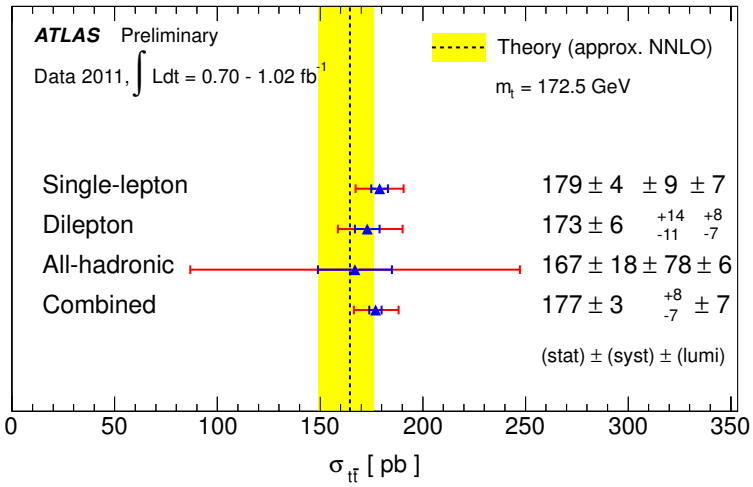

Figure 2.3: The measured $t\bar{t}$ production cross-section in ATLAS experiment. The combined cross-section is shown in the bottom.

values of v_u and v_d, respectively[2]. The event topology depends on the ratio of the vacuum expectation values, defined as $\tan\beta = v_u/v_d$, and the mass of the charged Higgs boson ($m_H^{\pm}$). The coupling of the charged Higgs boson to the up-type fermion to the down-type fermion ($g_{Hf_uf_d}$) is calculated to be

$$g_{Hf_uf_d} = \frac{g}{\sqrt{2}M_W}\left\{m_u\left(\frac{1+\gamma_5}{2}\right)\cot\beta + m_d\left(\frac{1-\gamma_5}{2}\right)\tan\beta\right\}. \tag{2.4}$$

Therefore, the charged Higgs boson predominantly decays into $\tau\nu_\tau$ when $\tan\beta$ is large. This will enhance the $t\bar{t}$ production cross-section in τ-lepton final state compared to the SM prediction. Figure 2.4 shows the diagram of the charged Higgs boson decay.

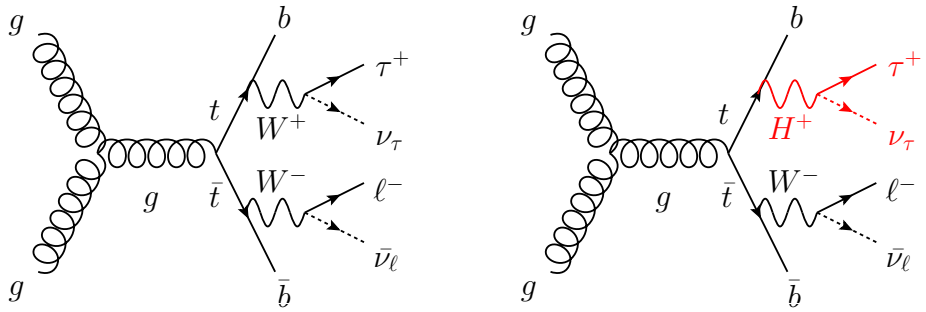

Figure 2.4: $t\bar{t}$ events with τ-lepton final states via the W boson decay (left) and the charged Higgs boson decay.

[2] $\sqrt{v_u^2 + v_d^2}$ is normalized to be the vacuum expectation value in the SM, $v = 246$ GeV

The measurements of the $t\bar{t}$ production cross-section in τ-lepton final state and its comparison between different decay channels were performed in the former experiments. Under the assumption that the charged Higgs boson decays into $\tau\nu_\tau$ with 100% of the time, the LEP experiment set the lower limit for the charged Higgs boson mass to be $m_H^\pm > 90$ GeV. At the Tevatron, no evidence were found for the charged Higgs boson production, and the upper limit was placed on the branching ratio that the t-quark decays into a charged Higgs boson and a b-quark to be 15 - 20%.

2.2 Theoretical aspect of the $t\bar{t}$ production cross-section

2.2.1 Overview

Figure 2.5 shows a schematic diagram of the $t\bar{t}$ production and its decay. The production process is the result of an interaction between quarks and gluons which are the constituents of the incoming protons, called partons. The partons possess varying fractions (x_1 and x_2) of the four-momenta of their parent protons (p_1 and p_2). The production cross-section is given by,

$$\sigma_{p\bar{p}\to t\bar{t}} = \sum_{i,j=g,q,\bar{q}} \int_0^1 f_i(x_1)\ \mathrm{d}x_1 \int_0^1 f_j(x_2)\ \mathrm{d}x_2\ \times \hat{\sigma}_{ij\to t\bar{t}}\ (\alpha_s), \tag{2.5}$$

where $\hat{\sigma}_{ij\to t\bar{t}}$ is the short-distance cross-section between parton i and j (called partonic cross-section), the α_s is the strong coupling constant and $f_i(x_1)$ is the parton distribution function (PDF) for the parton type i ($i = g, q, \bar{q}$, where $q = u, d, c, s, b$). The strong coupling constant is known to be varied as a function of the momentum transfer in the event (Q). In case of the $t\bar{t}$ production, α_s becomes the order of ≈ 0.1, which is small enough to calculate the partonic cross-section as a perturbation series in the strong coupling constant.

2.2.2 The strong coupling constant and the partonic cross-section

The strong coupling constant (α_s) decreases with increasing momentum transfer of the event (Q) due to the antiscreening effect of the strong interaction. The dependence of α_s to the momentum transfer can be written as followings:

$$\alpha_s(Q^2) = \frac{\alpha_s(\mu_R^2)}{1 + b_0\alpha_s(\mu_R^2)\ln(-Q^2/\mu_R^2)} \tag{2.6}$$

$$b_0 = \frac{11N_C - 2n_f}{12\pi}, \tag{2.7}$$

where N_C is the number of quark colors ($N_C = 3$), n_f is the number of quark flavors with its mass lower than Q ($n_f = 6$ in case of the $t\bar{t}$ production), and μ_R denotes the (unphysical) renormalization scale, at which the strong coupling constant is renormalized to keep the consistent dimension of the observable. Typically, μ_R is chosen so that it is close to the momentum transfer in a given process to be an effective strength of the strong interaction. In case of the $t\bar{t}$ production process, $\mu_R = m_t$ is selected.

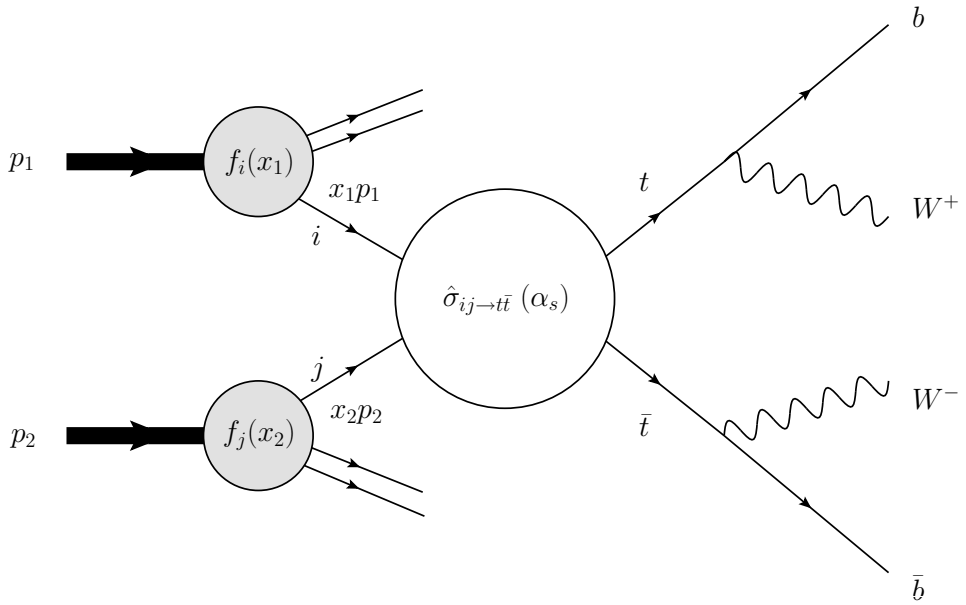

Figure 2.5: The diagram of the $t\bar{t}$ production and decay.

The strong coupling constant has been measured in various experiments as shown in Figure 2.6. The red point is an experimental input [7] from the LEP experiment measured at $Q = M_Z$ [A.3] by which the prediction line is calculated based on the equation (2.6). The prediction and the data show a decent agreement.

Since the strong coupling constant at $Q^2 \approx 2m_t = 350$ GeV is around 0.1, the partonic cross-section can be calculated in a perturbative way. Up to the leading-order (LO) and the next-to-leading-order (NLO) approximation, the partonic cross-section is calculated as a perturbation series in α_s as followings,

$$\hat{\sigma}_{ij\to t\bar{t}}(\alpha_s) = \sigma_1(x_1p_1, x_2p_2)\alpha_s + \sigma_2(x_1p_1, x_2p_2)\alpha_s^2, \tag{2.8}$$

where σ_1 (σ_2) denotes the calculated cross-section based on the LO (NLO) diagram, as is shown in Figure 2.7. As the number of possible diagrams rapidly increase for the higher-order calculation, it is more time-consuming to calculate quantitatively based on the diagrams. Given the fact that the effect from NNLO is about $\mathcal{O}(1\%)$ compared to the LO effect, the partonic cross-section is calculated up to the NLO effect.

2.2.3 Parton Distribution Function

A proton is composed of several quarks and gluons, which is collectively referred to as partons. The partons can be categorized into valence quarks, sea quarks and the gluons. The valence quark denotes the quark or anti-quark which gives rise to the quantum numbers (uud for the proton, udd for the neutron). The sea quark denotes the quark-antiquark pair ($q\bar{q}$) arising from a gluon splitting. The sea quarks are much less stable than the valence quarks, and they typically annihilate each other within hadrons. Although it is not always possible to maintain

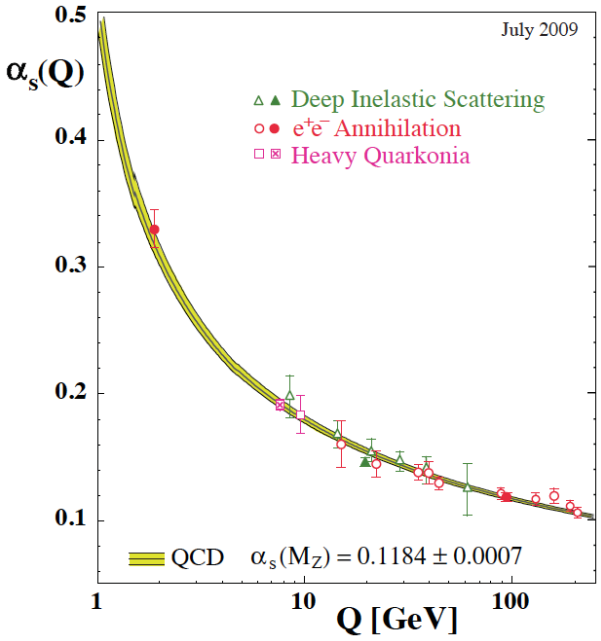

Figure 2.6: Summary of the measurements of α_s as a function of Q. The curves are QCD predictions for the combined world average value of $\alpha_s(M_Z)$.

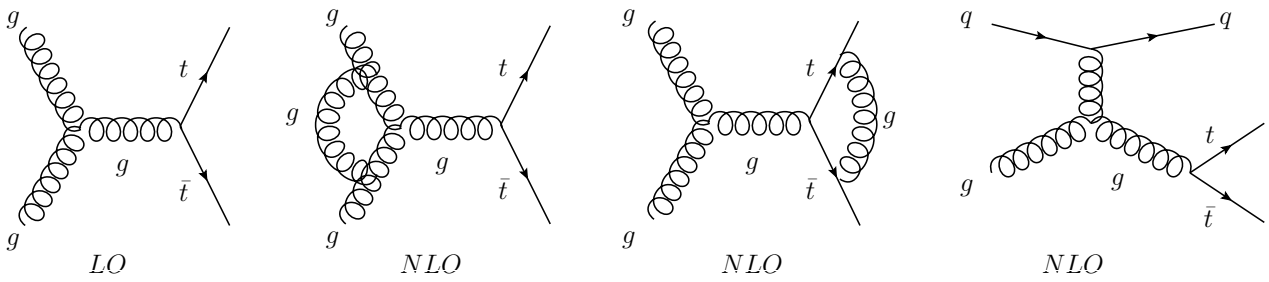

Figure 2.7: An example of the $t\bar{t}$ production diagrams in the LO and NLO approximation.

the distinction between the valence quark and the sea quark, their kinematic properties are sufficiently different that the distinction is useful.

The parton is considered to carry a momentum fraction among the total momentum of the parent proton. The probability density for finding a parton i ($i = g, q, \bar{q}$, where $q = u, d, c, s, b$) with a momentum fraction x at certain Q^2 is known as the parton distribution function (PDF) and have been measured experimentally using a deep inelastic scattering process with a lepton and a nucleon[3]. Figure 2.8 shows the PDF at $Q^2 = 10$ GeV^2 and $Q^2 = 10^4$ GeV^2, respectively. The gluon grows rapidly in small x, which is roughly scaled by x^{-2}. The contribution from the

[3]For example, $f_d(x)$ is measured by $\nu_\mu p \to \mu^- X$ scattering, as W^- only interacts with u quark inside a proton via $u + W^- \to d$ process. Similarly, $\bar{\nu_\mu} p \to \mu^+ X$ process is used to derive $f_u(x)$ and $q + g \to q + \gamma$ and $gg \to gg$ process is used to derive $f_g(x)$.

sea quark becomes much more visible in high-Q^2 as the process probes more deeply inside a proton. Given the same process that requires certain Q^2, LHC can make use of more gluons compared to the former energy frontier experiment, Tevatron. It is expected that the gluon fusion process ($gg \to t\bar{t}$) and the quark-antiquark annihilation process ($q\bar{q} \to t\bar{t}$) occurs with 70% and 30% probability of the time at the LHC ($\sqrt{s} = 7$ TeV), while it is 10% and 90% probability at the Tevatron ($\sqrt{s} = 1.96$ TeV), respectively.

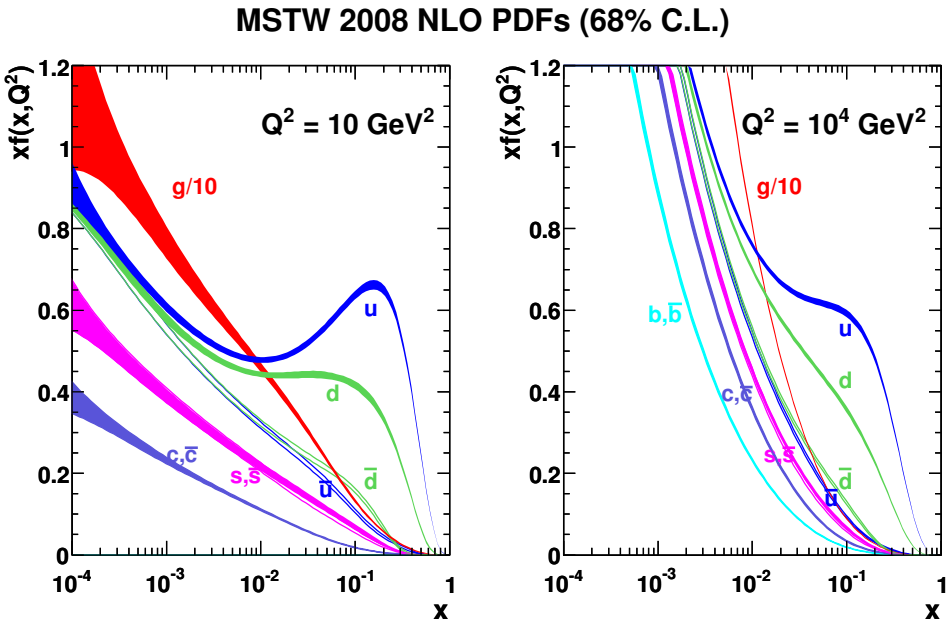

Figure 2.8: The PDF for $Q^2 = 10$ GeV^2 (left) and $Q^2 = 10^4$ GeV^2 (right).

There are soft parton emissions in the initial state associated to the $t\bar{t}$ production process, as is depicted by the red line in Figure 2.9. These are basically the interactions which occur long before the hard scattering process and are called as the initial state radiation (ISR). Since the majority of these processes have low-Q^2, perturbative calculation becomes divergent due to its large α_s (called collinear limit). Therefore, those processes with the transverse momentum, $p_T < \mu_F$ are factored out and absorbed into the PDF. The μ_F is called as the factorization scale and can be thought of as the scale which separates the long and short distance physics. The choice of μ_F is arbitrary, and typically chosen to be of the order of the momentum transfer, Q in a given process. In case of the $t\bar{t}$ events, $\mu_F = m_t$ is chosen. Since the majority of the soft parton emissions always satisfy $p_T < \mu_F$, almost all the initial state radiations are included to the PDF. The evolution of the PDF as a function of the momentum transfer [A.4] is evaluated by the DGLAP (Dokshitzer-Gribov-Lipatov-Altarelli-Parisi) evolution equation [8][9][10] and the theoretical prediction has been checked to be consistent with the measurements [11].

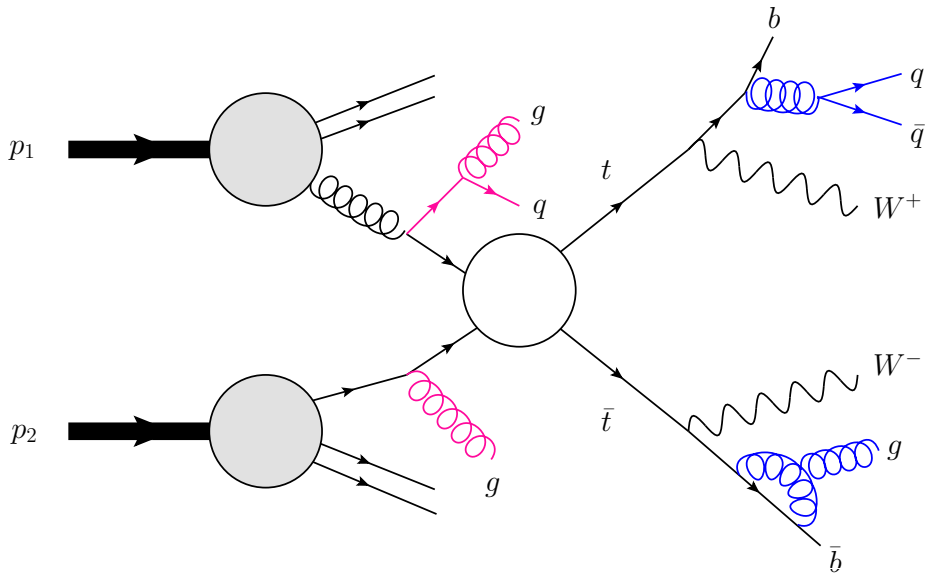

Figure 2.9: The diagram of the Initial (red) and the Final State Radiation (blue).

2.2.4 Total $t\bar{t}$ production cross-section

Finally, based on the equation (2.5), the $t\bar{t}$ production cross-section ($\sigma_{t\bar{t}}$) at $\sqrt{s} = 7$ TeV pp collision is calculated, assuming the t-quark mass to be 172.5 GeV. Using the CTEQ parton distribution function [12], $\sigma_{t\bar{t}}$ becomes:

$$\sigma_{t\bar{t}} = 164.57^{+4.3}_{-9.3}\ (\text{scales})\ ^{+7.2}_{-6.5}\ (\text{PDF})\ \ \text{pb}, \tag{2.9}$$

where, the first uncertainty (4.1%) comes from the choice of the renormalization and the factorization scale, and the second uncertainty (4.2%) comes from the PDF [13][14][15][16]. The renormalization and the factorization scale is taken to be $\mu_R = \mu_F = m_t$, and these uncertainties are estimated by varying them in a range of $[\frac{m_t}{2}, 2m_t]$. The PDF uncertainty is evaluated by varying them within a possible range. The total uncertainty of the theoretical prediction is an order of 10%.

2.3 Theoretical aspect of the $t\bar{t}$ final state

2.3.1 Decay of the t-quark

In the leading-order approximation, the partial decay width of the t-quark via the weak interaction can be calculated as,

$$\Gamma(t^{\pm} \to W^{\pm}b) = \frac{G_F m_t^3 |V_{tb}^2|}{8\pi\sqrt{2}} \approx 1.5\ \text{GeV}, \tag{2.10}$$

where $G_F = 1.16639 \times 10^{-5}$ GeV^{-2} is the Fermi coupling constant and the V_{tb} is the coupling strength of the left-handed Wtb coupling in the CKM matrix. The partial decay width of 1.5 GeV corresponds to the lifetime of $\tau = 1/\Gamma \approx 10^{-25}$ s.

On the other hand, equation (2.6) suggests that the α_s becomes large when the denominator becomes close to zero. Suppose the momentum transfer $\Lambda_{\rm QCD}$, at which the denominator in equation (2.6) becomes zero, $\Lambda_{\rm QCD}$ is calculated to be:

$$\Lambda_{\rm QCD} = \mu_R \exp\left\{-\frac{6\pi}{(33-2n_f)\alpha_s(\mu_R^2)}\right\}. \tag{2.11}$$

$\Lambda_{\rm QCD}$ is called as the hadronization scale, representing the typical energy scale when the strong interaction becomes strong enough to confine quarks and gluons into hadrons. Assuming $\mu_R^2 = 100$ GeV^2, $\alpha_s(\mu_R^2) = 0.2$ and $n_f = 5$ (the number of quark flavors below the energy scale μ_R) one obtains $\Lambda_{\rm QCD} = O(200)$ MeV, which corresponds to the time scale of $\tau \approx 10^{-23}$ s. Therefore, the t-quark is the only quark that decays into a on-shell W boson and a bottom-type quark (d, s, b) before the hadronization.

Since the W boson couples $u \leftrightarrow d^{'}$, $c \leftrightarrow s^{'}$, and $t \leftrightarrow b^{'}$ where $d^{'}, s^{'}$, and $b^{'}$ denotes the left-handed weak eigenstates of quarks, the probability for each type of the down-type quark to be observed (mass eigenstate, denoted as d, s, and b) is derived by the following relations:

$$\begin{pmatrix} d_L^{'} \\ s_L^{'} \\ b_L^{'} \end{pmatrix} = V_{\rm CKM} \begin{pmatrix} d_L \\ s_L \\ b_L \end{pmatrix}, \tag{2.12}$$

where,

$$V_{\rm CKM} = \begin{pmatrix} V_{ud} & V_{us} & V_{ub} \\ V_{cd} & V_{cs} & V_{cb} \\ V_{td} & V_{ts} & V_{tb} \end{pmatrix} = \begin{pmatrix} 0.9743 & 0.2253 & 0.0035 \\ 0.2252 & 0.9735 & 0.0410 \\ 0.0086 & 0.0403 & 0.9992 \end{pmatrix}. \tag{2.13}$$

The above CKM parameters have been derived by the global fit based on the experimental results obtained so far and the theory under the condition assuming the unitarity of the three quark generations. In the framework of the SM, it can be said that the t-quark decays into a W boson and a b-quark ($t \to W^+ b$ or $\bar{t} \to W^- \bar{b}$) with almost 100% of the time.

2.3.2 Decay of the W boson

The W boson decays into either leptonic ($W \to \ell\nu$, where $\ell = e, \mu, \tau$) or hadronic ($W \to u d^{'}, c s^{'}$, where $W \to t b^{'}$ is not allowed kinematically), where the latter case includes three color combinations, $R\bar{R}, G\bar{G}, B\bar{B}$. Since the coupling of the W boson is proportional to the weak isospin charge, each of the above decay occurs at the same rate as they all have an isospin charge of 1/2. Therefore, 3/9 of the W boson decays into leptonic, while 6/9 of the W boson decays into hadronic. The uncertainty of the branching ratio is less than 1%. Taking into account that the detector signatures are completely different, and that there is a specific motivation for the individual decay mode, $t\bar{t}$ events are categorized based on the decay products of two W bosons, as summarized in Table 2.3.

Decay mode		Branching fraction
di-lepton channel	$t\bar{t} \to W(\to e\nu_e)b + W(\to e\nu_e)b$	1.2%
	$t\bar{t} \to W(\to \mu\nu_\mu)b + W(\to \mu\nu_\mu)b$	1.2%
	$t\bar{t} \to W(\to e\nu_e)b + W(\to \mu\nu_\mu)b$	2.5%
	$t\bar{t} \to W(\to \tau\nu_\tau)b + W(\to e\nu_e)b$	2.5%
	$t\bar{t} \to W(\to \tau\nu_\tau)b + W(\to \mu\nu_\mu)b$	2.5%
	$t\bar{t} \to W(\to \tau\nu_\tau)b + W(\to \tau\nu_\tau)b$	1.2%
single-lepton channel	$t\bar{t} \to W(\to e\nu_e)b + W(\to q\bar{q})b$	14.8%
	$t\bar{t} \to W(\to \mu\nu_\mu)b + W(\to q\bar{q})b$	14.8%
	$t\bar{t} \to W(\to \tau\nu_\tau)b + W(\to q\bar{q})b$	14.8%
all-hadronic channel	$t\bar{t} \to W(\to q\bar{q})b + W(\to q\bar{q})b$	44.4%

Table 2.3: The categorization of the $t\bar{t}$ decays with its branching fraction. ℓ denotes an electron or a muon. The latter three decay channels include τ-lepton in its final states.

2.3.3 Soft parton emissions

In order to describe the final states of the $t\bar{t}$ events, it is necessary to deal with soft parton (quark or gluon) emissions in the final state, collectively referred to as the final state radiation (FSR), which is shown in the Figure 2.9 by blue lines. As any partons have a color charge, these partons themselves emit further gluons or produce quark-antiquark pairs, leading to the formation of parton showers. As the parton shower requires higher-order corrections, a theoretical approximation called parton shower method is used for the calculation.

The parton showers are commonly formulated as the branchings of one particle into two. Suppose the parton with type i splits into $j + k$ (e.g, $q \to q + g$), the splitting probability (dP) is given by

$$dP = \frac{\alpha_s}{2\pi}\frac{d\theta^2}{\theta^2}dzd\phi P_{ji}(z) = \frac{\alpha_s}{2\pi}\frac{dE^2}{E^2}dzd\phi P_{ji}(z), \tag{2.14}$$

where θ and ϕ is the opening angle and the azimuthal angle of the splitting, and P_{ji} denotes the $i \to j$ splitting function, which describes the distribution of the energy fraction z of the parton i carried by the parton j, as shown in Figure 2.10. The splitting function can be calculated as followings:

$$P_{qq} = \frac{3}{4}\left(\frac{1+z^2}{1-z}\right), \tag{2.15}$$

$$P_{qg} = \frac{1}{2}\left\{z^2 + (1-z)^2\right\}, \tag{2.16}$$

$$P_{gg} = 6\left\{\frac{z}{1-z} + \frac{1-z}{z} + z(1-z)\right\}, \tag{2.17}$$

$$P_{gq} = \frac{3}{4}\left(\frac{1+z^2}{(1-z)^2}\right). \tag{2.18}$$

The sequential applications of the above probability will provide a parton shower developed from each colored parton.

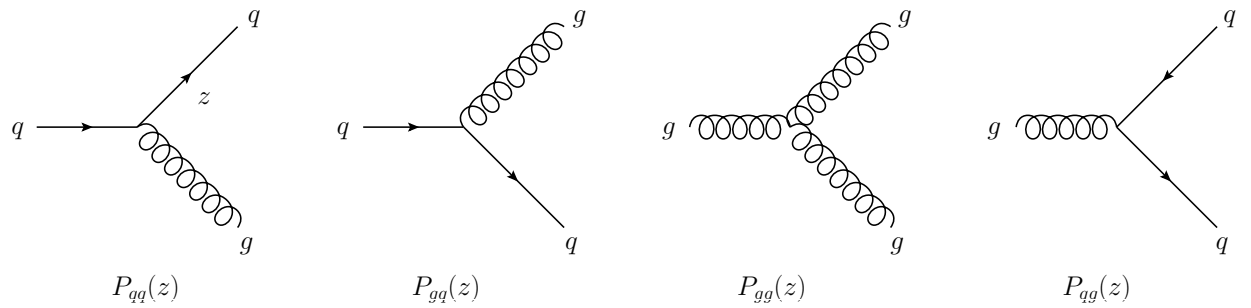

Figure 2.10: The lowest order QCD splitting functions. $P_{p'p}$ gives the probability that a parton type p converts into a parton type $p^{'}$. z denotes the momentum fraction of the initial parton.

In order to handle the infrared divergence, where the probability diverges as the emitted parton becomes collinear ($\theta \to 0$) or carries small energy ($z \to 0$), the sudakov form factor Δ_s is applied to the equation (2.14) which is given by

$$\Delta_s(q_1^2, q_2^2) = \exp\left\{-\frac{\alpha_s}{2\pi}\int_{q_2^2}^{q_1^2}\frac{dq^2}{q^2}\int_{z_{\min}}^{z_{\max}}dz\int_0^{2\pi}d\phi P_{ji}(z)\right\}, \tag{2.19}$$

giving the probability for a parton to evolve from q_1^2 to q_2^2 without emitting a further parton. The q_1^2 and q_2^2 are called the virtuality, which is defined as the squared of the four-momentum (invariant mass) before and after the splitting. The parton shower is terminated when the virtuality falls into the hadronization scale ($q^2 \sim \Lambda_{\mathrm{QCD}}$).

2.3.4 Hadonization

As the parton shower glows, the interaction scale falls (lower-Q^2) and the strong interaction coupling rises, and eventually triggers the process of the hadronization. In the hadronization process, partons are bound into colorless hadrons. It is therefore detected as a group of hadrons, called hadronic jet, in the detector. All the partons such as the b-quark from the t-quark decays, the $q\bar{q}$ from the W boson decays and the other soft parton emissions experience the hadronization process.

Since the hadronization process is non-perturbative, there are several models that relies on the general features of the QCD with its tuning based on the experimental observation. A widely used model is called the string-model, where the final state partons are connected by the color strings with its thickness of the order of 1 fm and breaking them up into hadrons. The breaking condition is that the string has a potential energy of the order of the hadron masses, where it becomes energetically favored to create a new quark-antiquark pair. The two string segments then begin to stretch and break again until all the energy has been converted into quark-antiquark pairs connected by short string segments, which can be identified as hadrons.

Chapter 3

LHC−ATLAS experiment

The $t\bar{t}$ production cross-section measurement exploits the proton-proton (pp) collision data at $\sqrt{s} = 7$ TeV produced by the Large Hadron Collider (LHC), and recorded by the ATLAS (A Toroidal LHC Apparatus) detector. This section gives the brief review about the LHC and the ATLAS detector, as well as the particle reconstruction scheme.

3.1 LHC and the $t\bar{t}$ production

The LHC lies in the underground tunnel which was excavated at depth varying between 45 and 170 m with its circumference of 26.7 km. It is located at the borderline between Switzerland and France. The accelerator consists of 1232 dipole superconducting magnets and 392 quadrupole magnets. The former magnets are used to bend the protons to keep the beam trajectory to follow the circular path with its magnetic field strength of 8.3 T. The latter magnets are used to focus the proton beam to raise the collision probability. Two set of protons are accelerated up to 7 TeV in opposite directions, and designed to make a collision at $\sqrt{s} = 14$ TeV. During 2011, LHC was operated at $\sqrt{s} = 7$ TeV due to the safety concerns.

Figure 3.1 shows a schematic view of the LHC. Protons are firstly generated using a hydrogen nuclei by separating the electron and injected to the LINear ACcelerator (LINAC), where it is accelerated up to 50 MeV. Then, one after the other, protons are injected to the Proton Synchrotron Booster (PSB, 1.4 GeV), the Proton Synchrotron (PS, 26 GeV), the Super Proton Synchrotron (SPS, 450 GeV) before injected to the LHC. Table 3.1 summarizes LHC main parameters. In 2011, protons are bundled into 1380 bunches, each consists of 1.4×10^{11} protons. The collision interval is 50 ns (20 MHz) and the maximum instantaneous luminosity reaches up to 3.5×10^{33} ($1/\mathrm{cm}^2\mathrm{s}$).

Figure 3.2 shows the theoretical cross-sections for various physics processes as a function of $\sqrt{s}$ in pp ($p\bar{p}$) collisions at the luminosity of $\mathcal{L} = 10^{33}/\mathrm{cm}^2\mathrm{s}$. The total production cross-section is an order of $\mathcal{O}(100)$ mb, which is dominated by the inelastic scattering processes via the strong interactions. The σ_t denotes the inclusive t-quark production cross-section, including both the $t\bar{t}$ production and the single t-quark production as is shown in Figure 3.3. At $\sqrt{s} = 7$ TeV, the $t\bar{t}$ production cross-section is predicted to be 164.6 pb, while that of the single t-quark is 84.9 pb. This requires 10^{-9} reduction to extract the meaningful $t\bar{t}$ events. In this thesis, this reduction is achieved by using a lepton trigger (10^{-5}) and the event selection (10^{-4}).

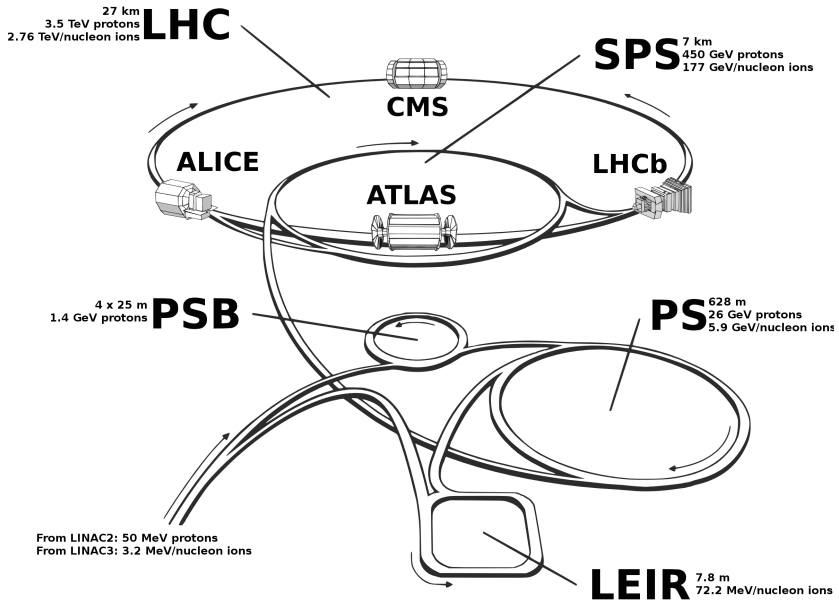

Figure 3.1: The schematic view of the LHC accelerator, where protons are accelerated up to 7 TeV. The ATLAS detector is placed at one of the four interaction points.

	unit	designed	parameter (2011)
Proton beam energy	[TeV]	7	3.5
Relativistic γ	–	7461	3730
Magnetic field strength of the dipole magnet	[T]	8.3	4.2
Number of protons per bunch	–	1.15×10^{11}	1.4×10^{11}
Number of bunches	–	2808	1380
Circulated beam current	[kA]	11.85	5.93
RMS bunch length (σ_z)	[cm]	7.55	6
RMS beam size (σ_x, σ_y)	[μm]	16.7	22
Instantaneous peak luminosity	[1/cm^{2}s]	1.0×10^{34}	3.5×10^{33}
Interval of the beam collision	[ns]	25	50

Table 3.1: The LHC main parameters. The upper half shows the beam related parameters, while the latter half shows the luminosity related parameters.

3.2 ATLAS detector and the $t\bar{t}$ identification

There are four interaction points at the LHC, where oppositely running protons collide each other. The collision events are closely observed by the dedicated detector, called ATLAS (A Toroidal LHC ApparatuS), CMS (Compact Muon Solenoid), LHCb (LHC-beuty) and ALICE (A Large Ion Collider Experiment). The ATLAS and the CMS detector [18] are the general-purpose detector designed to cover a wide range of physics at the LHC.

Figure 3.4 shows the schematic view of the ATLAS detector. From inner to outer, it consists

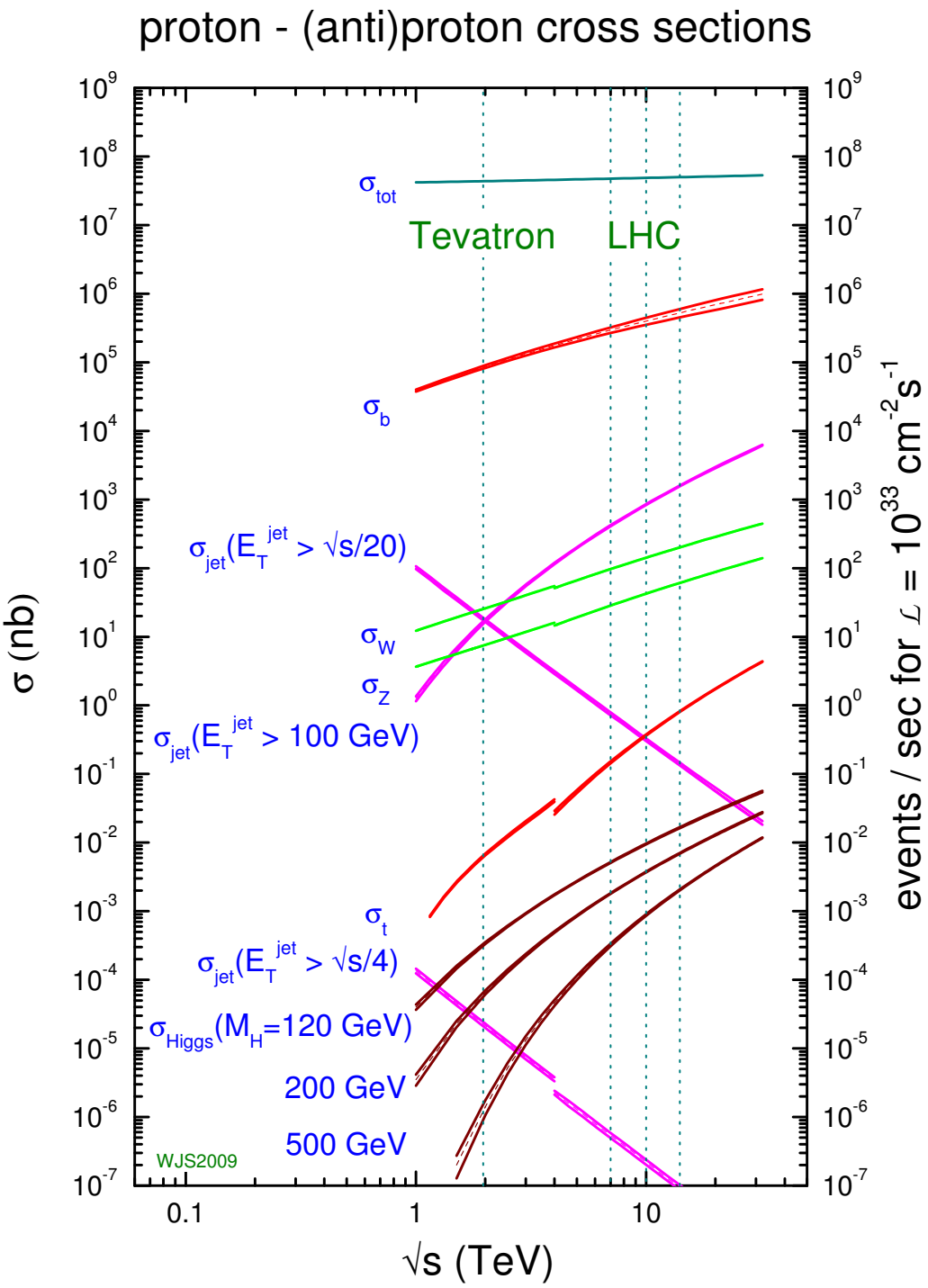

Figure 3.2: The cross-sections for various physics processes at the luminosity of $\mathcal{L} = 10^{33}/\text{cm}^2\text{s}$. Left side of the plot is for $p\bar{p}$ collision, while right side for pp collision [17].

of the inner tracker, the solenoid magnet, the liquid-argon (LAr) electromagnetic calorimeter (ECAL), the hadronic calorimeter (HCAL), the toroid magnet, and the muon spectrometer.

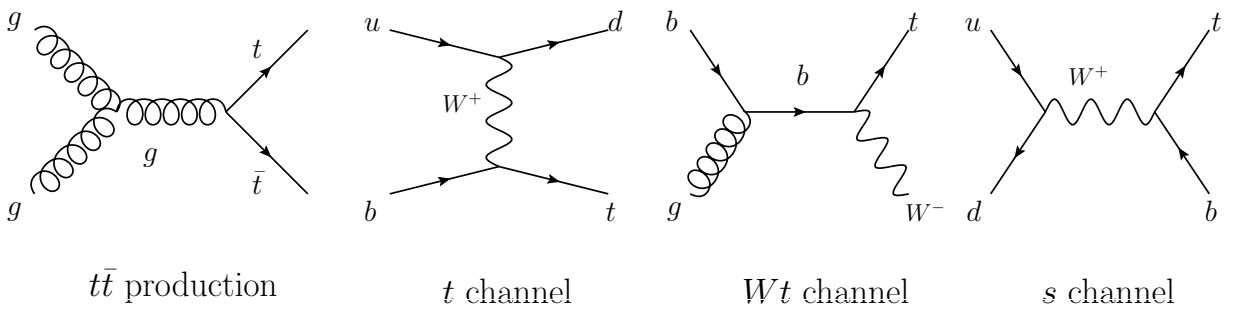

Figure 3.3: Diagrams including a t-quark in the final state. From left to right, the $t\bar{t}$ production and the single-top production via the t-channel, the Wt-channel and the s-channel.

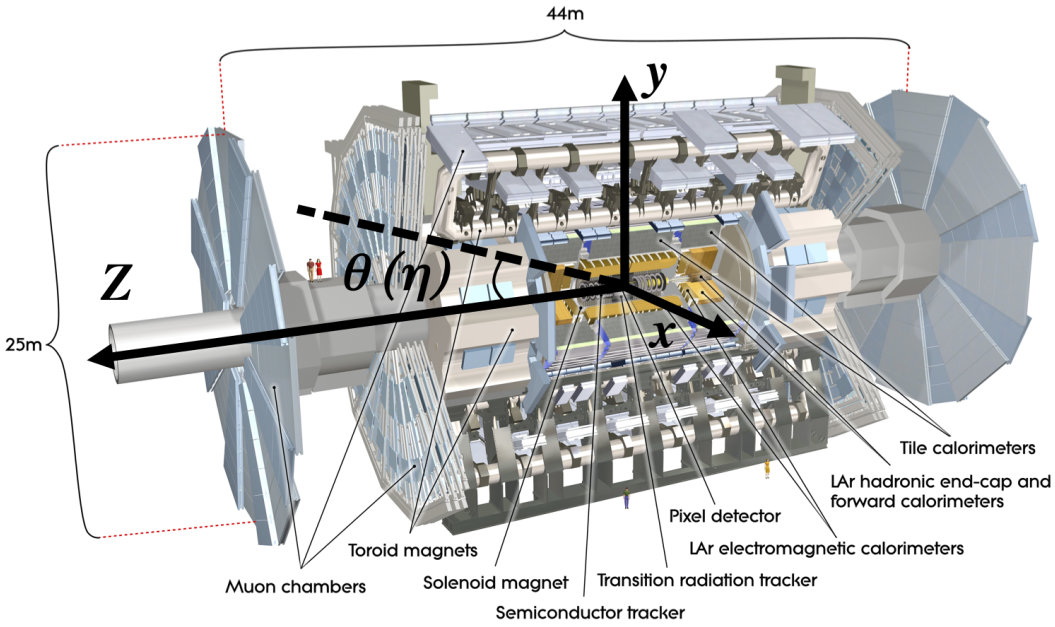

Figure 3.4: The schematic view of the ATLAS detector. The detector has a cylindrical shape with its size of 25 m×25 m×44 m. The overall weight is 7000 tonnes.

The origin of the coordinate system is defined to be the interaction point. The positive $x-$axis is defined in a direction from the origin towards the center of the LHC ring. The positive $y-$axis is taken to be upward. The positive $z-$axis is defined according to the right-handed system and is in parallel with the beam direction. The azimuthal angle ϕ is measured from the positive $x-$axis and the polar angle θ is measured from the positive $z-$axis. In most cases, pseudo-rapidity (η) is used instead of θ which is defined as

$$\eta = -\ln\left\{\tan\left(\frac{\theta}{2}\right)\right\}. \tag{3.1}$$

The pseudo-rapidity is an approximation of the rapidity [B.1], assuming that the particle mass to be zero. The rapidity is additive under the Lorentz transformations along the z-axis, which means that the rapidity difference is boost-invariant. The particle production rate is constant as a function of the rapidity.

Figure 3.5 shows the expected event topology of the signal events ($t\bar{t} \to \tau^+\ell^-\nu_\tau\bar{\nu}_\ell b\bar{b}$). The signal event includes one high-p_T lepton (a muon or an electron), one hadronically decaying τ-lepton, two b-quarks directly coming from the t-quark, and two neutrinos.

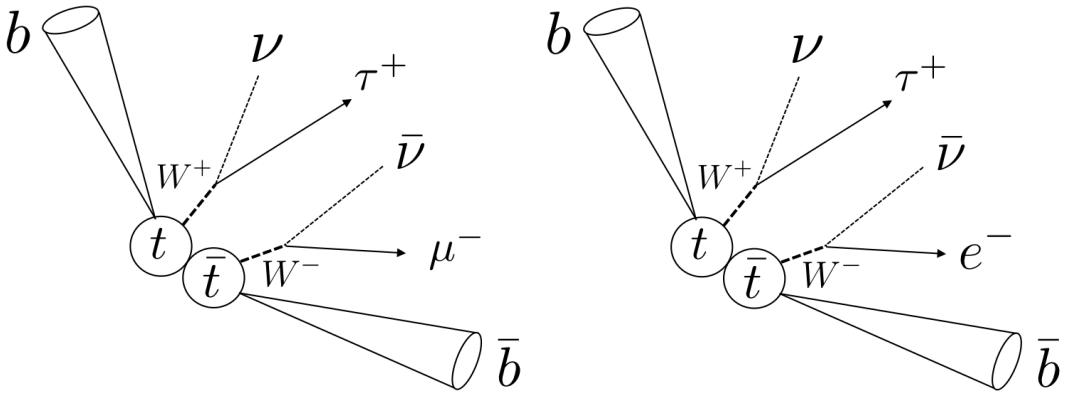

Figure 3.5: The expected final state of the signal events for the muon channel (left) and the electron channel (right). The charge of the τ-lepton and the lepton can be opposite.

The electrons are stopped by the LAr calorimeter by forming the electromagnetic shower, while quarks (u, d, c, s, b) and gluons are fragmented into group of hadrons, so-called hadronic jets, and stopped by the hadronic calorimeter. The radiation length[1] of the electromagnetic calorimeter ($\approx 22X_0$) and the interaction length[2] of the hadronic calorimeter ($\approx 10\lambda$) were optimized enough to contain target particles, while limiting punch-through to the muon spectrometer. Figure 3.6 shows the radiation length for the inner tracker, electromagnetic calorimeter, and the interaction length for the hadronic calorimeter as a function of $|\eta|$. Among the hadronic jets, one can identify the jet originated from the b-quark by observing a large secondary vertex inside the jet with respect to the primary vertex, as it composes b-hadron state having a large lifetime of $c\tau = 420$ μm. The identification of the b-jet is called b-tagging. The τ-lepton has a short lifetime of 2.9×10^{-13} s ($c\tau = 87$ μm) enough to decay before reaching the detector. It is identified using hadronic decay (e.g, $\tau \to \pi^\pm\pi^0\nu_\tau$, 65%), as the leptonic decay ($\tau \to \ell\nu_\ell\nu_\tau$, 35%) is not distinguishable between primary leptons coming from the interaction point. The hadronically decaying τ-lepton composes narrow jet compared to the other hadronic jet, and leaves odd number of charged tracks inside the inner tracker. Since the decay products of the hadronically decaying τ-lepton normally includes π^0 and $\pi^\pm$, both the electromagnetic and the hadronic calorimeter detect the energy deposits. The muons are identified by observing a charged track at the outermost muon spectrometer with matching tracks in the inner tracker.

[1]The path length by which an electron loses its energy up to $1/e \approx 37\%$ due to the bremsstrahlung.
[2]A mean free path to reduce the number of relativistic charged particle to $1/e$.

The missing transverse momentum is constructed based on the momentum imbalance calculated by the vector sum of p_T from all visible particles, projected onto the transverse plane, which is used as a signature of the neutrino.

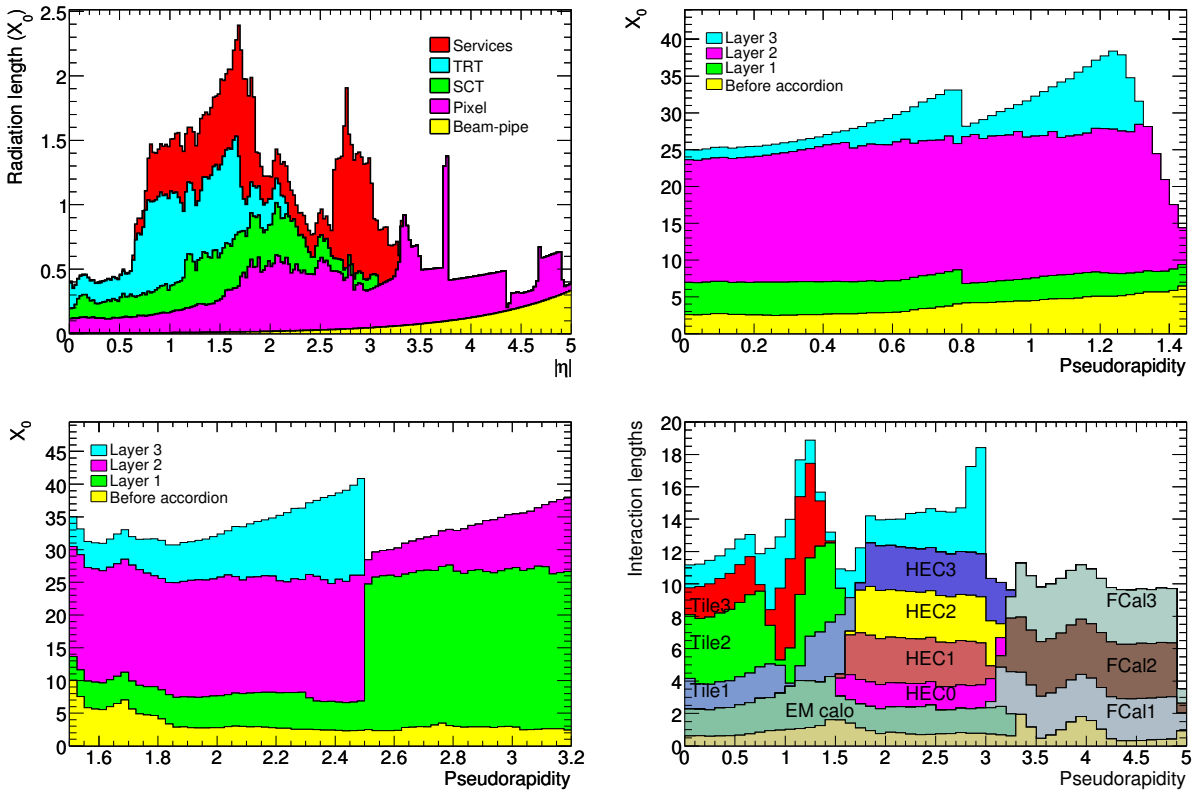

Figure 3.6: (From left top to right bottom) Radiation length for the inner tracker, electromagnetic calorimeter in the barrel and the endcap, and the interaction length for the hadronic calorimeter as a function of $|\eta|$.

3.3 ATLAS sub-detector

3.3.1 Inner Tracker and the Solenoid Magnet

The main role of the inner tracker is to detect charged particles and to reconstruct its trajectory for the p_T measurement. The designed p_T resolution is,

$$\frac{\sigma_{p_T}}{p_T} = 0.05 \times p_T \text{ (GeV)} \oplus 1\%. \quad (|\eta| < 2.5) \tag{3.2}$$

The another role is to reconstruct primary vertices with its resolution of 10 μm in xy plane and 50 μm in z direction for the identification of the collision vertex and the b-tagging.

The inner tracker includes, from inner to outer, the Pixel detector (Pixel), the SemiConductor Tracker (SCT), and the Transition Radiation Tracker (TRT). These are immersed in 2 T magnetic field produced by the superconducting solenoid magnet with its size of 5.3 m (length) $\times$2.5 m (ϕ). Figure 3.7 shows the cross-sectional view of the inner tracker and Table 3.2 summarizes its coverage with its intrinsic accuracy.

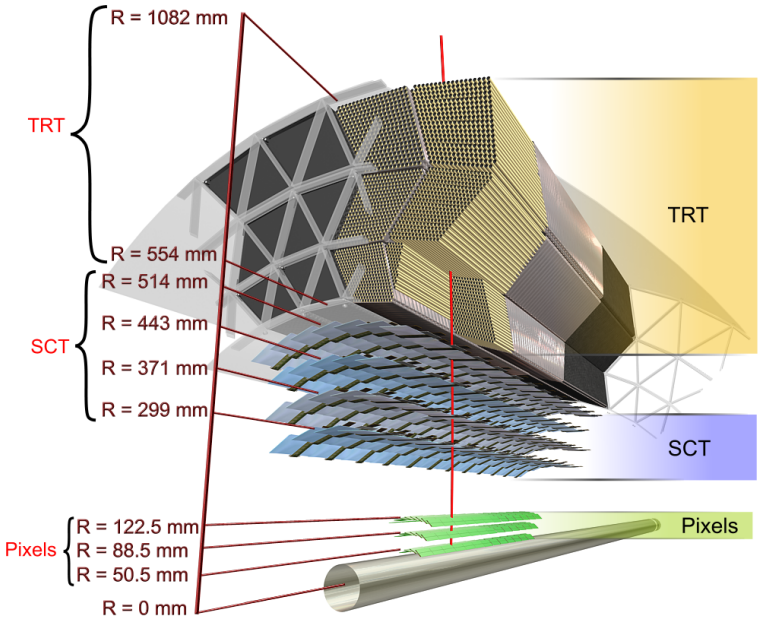

Figure 3.7: The cross-sectional view of the inner tracker in the barrel.

	R coverage (mm)	z coverage (mm)	accuracy (μm)
Beam pipe	$29 < R < 36$		
Pixel			
3 cylindrical layers (barrel)	$51 < R < 123$	$0 < \|z\| < 401$	10 (R-ϕ) 115(z)
2×3 disks (endcap)	$89 < R < 150$	$495 < \|z\| < 650$	10 (R-ϕ) 115(R)
SCT			
4 cylindrical layers (barrel)	$299 < R < 514$	$0 < \|z\| < 749$	17 (R-ϕ) 580(z)
2×9 disks (endcap)	$275 < R < 560$	$839 < \|z\| < 2735$	10 (R-ϕ) 580(R)
TRT			
73 straw planes (barrel)	$563 < R < 1066$	$0 < \|z\| < 712$	130
160 straw planes (endcap)	$644 < R < 1004$	$848 < \|z\| < 2710$	130

Table 3.2: Coverage of the inner tracker and its intrinsic accuracy.

Pixel Detector (Pixel)

The pixel detector is placed at the innermost part of the detector and consists of three cylindrical layers placed from $R = 50.5$ mm to 122.5 mm in the barrel. In case of the endcap, three disk-

shaped pixel detectors are placed vertical to the beam axis from $z = 495$ mm to $z = 650$ mm. The coverage of the pixel detector is $|\eta| < 2.5$.

The outstanding feature of the pixel detector is its fine granularity. It consists of two-dimensional semi-conducting silicon sensors with a pixel size of 50×400 μm^2. The intrinsic accuracy of the space-point measurement is 10 μm in ϕ and 115 μm in z (R) direction at the barrel (endcap) region. The detection efficiency of the pixel detector is more than 99% at a bias voltage of 150 V.

Semiconductor Tracker (SCT)

The second part of the inner tracker is the semiconductor tracker (SCT), covering $|\eta| < 2.5$. The SCT consists of strip type semiconductor sensor with four layers in the barrel ($r = 299$ mm, 371 mm, 443 mm, 514 mm, respectively) and nine disk-shape layers in the endcap, starting from $z = 839$ mm to $z = 2735$ mm. Each layer has two sided readout. It is aligned so that the charged particle can cross more than 8 layers in total.

The SCT consists of 6.4 cm long silicon sensors in z direction with a mean strip pitch of 80 μm in ϕ at the barrel. In case of the endcap, it is aligned radially with 80 μm pitch in ϕ direction. One side of the SCT strip sensor has a small stereo angle of 40 mrad with respect to the another side in order to achieve space point measurement. The intrinsic position resolution is 17 μm in ϕ, and 580 μm in z (R) direction in the barrel (endcap). The SCT is operated with a bias voltage of 150 V and its hit efficiency reaches up to 99%.

Transition Radiation Tracker (TRT)

The outermost part of the inner tracker is surrounded by the Transition Radiation Tracker (TRT). It covers up to $|\eta| < 2.0$, starting from $R = 563$ mm to $R =$1066 mm in the barrel, while from $z =$848 mm to $z = 2710$ mm in the endcap region. The TRT is composed of 73 layers of straws interleaved with fibers (barrel) and 160 straw planes interleaved with foils (endcap), which provides transition radiation for the electron identification. All charged tracks with $p_T > 0.5$ GeV and $|\eta| < 2.0$ will traverse at least 36 straws except fo the barrel-endcap transition region ($0.8 < |\eta| < 1.0$). Each straw tube has an anode sense-wire with its radius of 31 μm with gold plated tungsten and polypropylene-fiber with 70 mg/cm^3 used as a radiator. The diameter of the tube is 4 mm and its length is 144 cm in the barrel and 37 cm radially placed in the endcap. These tubes are superimposed so that the charged track with $p_T > 0.5$ GeV can cross at least 36 layers. The tube is filled with mixed gas of Xe : CO_2 : O_2 = 70 : 27 : 3. The intrinsic position resolution is 130 μm at the operating voltage of 1530 V.

Owing to the interleaved radiators, the charged track experiences transition radiation with its power (W) proportional to $W \propto \hbar\omega_p\gamma$ where ω_p is the plasma frequency and typically $\hbar\omega_p \approx 20$ eV [19]. Given the same momentum, the light particle such as an electron tend to deposit large energy (typically 6 GeV) and emits ultraviolet rays ($3 - 30$ keV), while this is not the case for the heavy particles such as the proton and the charged pion. This feature is used to discriminate electrons among other charged particles.

Solenoid Magnet

In order to measure the transverse momentum (p_T) of the charged particle, ATLAS detector has a 2 T superconducting solenoid magnet between the inner tracker and the calorimeter (2.46 m $< R <$2.56 m) with its length of 5.3 m. The solenoid magnet is operated under the current of 7.73 kA and at the temperature of 4.5 K. To reduce materials as low as possible while keeping the required magnetic field strength, the radiation length of the solenoid magnet is designed to be $\approx 0.66 X_0$.

3.3.2 Calorimeter

The main role of the calorimeter is to stop the electromagnetic (originated from electrons or photons) jet and the hadronic (originated from quarks or gluons) jet and to measure its energy. The liquid-argon (LAr) calorimeter is used as the electromagnetic calorimeter (denote as ECAL) for both the barrel ($|\eta| < 1.475$) and the endcap ($1.375 < |\eta| < 3.2$) region. The hadronic calorimeter (denote as HCAL) consists of three different types of calorimeters: scintillator tile-calorimeter ($|\eta| < 1.7$), LAr hadronic endcap calorimeter ($1.5 < |\eta| < 3.2$) and LAr forward calorimeter ($3.1 < |\eta| < 4.9$). The designed energy resolution is:

$$\frac{\sigma_E}{E} = \frac{10}{\sqrt{E(\mathrm{GeV})}} \oplus 0.7\% \quad (|\eta| < 3.2, \mathrm{EM\ calorimeter}), \tag{3.3}$$

$$\frac{\sigma_E}{E} = \frac{50}{\sqrt{E(\mathrm{GeV})}} \oplus 3\% \quad (|\eta| < 3.2, \mathrm{hadronic\ calorimeter}), \tag{3.4}$$

$$\frac{\sigma_E}{E} = \frac{100}{\sqrt{E(\mathrm{GeV})}} \oplus 10\% \quad (3.2 < |\eta| < 4.9, \mathrm{hadronic\ calorimeter}). \tag{3.5}$$

Figure 3.8 shows the cutaway view of the calorimeter system and Figure 3.9 shows its structure. The eta coverage and the channel granularity is one of the key aspect of the detector design in order to reconstruct several benchmark physics processes with desired resolution, which is arranged as shown in Table 3.3.

EM calorimeter

The electromagnetic calorimeter is placed outside the solenoid magnet and covers $|\eta| < 3.2$. It consists of the accordion shaped lead absorber plates with the thickness of 1.1 mm$\sim$2.2 mm with liquid-argon filled between them. Three layers of Kapton electrodes are placed in the middle of the lead plate, where the ionized electron is detected. Owing to its accordion geometry, not only complete ϕ symmetry without azimuthal crack but also the uniformity of the signal detection is achieved. The LAr calorimeter has a fine granularity with its typical size of $\Delta\eta \times \Delta\phi = 0.025 \times 0.025$ enough to achieve the desired mass resolution of $\mathcal{O}(1\ \%)$ needed for the benchmark physics process such as $H \to \gamma\gamma$.

Since the drift time of the ionized electron is 5 mm/μs, the maximum drift time results in 400 ns. In order to achieve better time response, only first arrival electrons within 50 ns is used. In $|\eta| < 1.8$, active LAr layer with a thickness of 1.1 cm ($|\eta| < 1.52$) and 0.5 cm ($1.5 < |\eta| < 1.8$) is used to correct the energy loss by electrons and photons upstream of the calorimeter (called presampler).

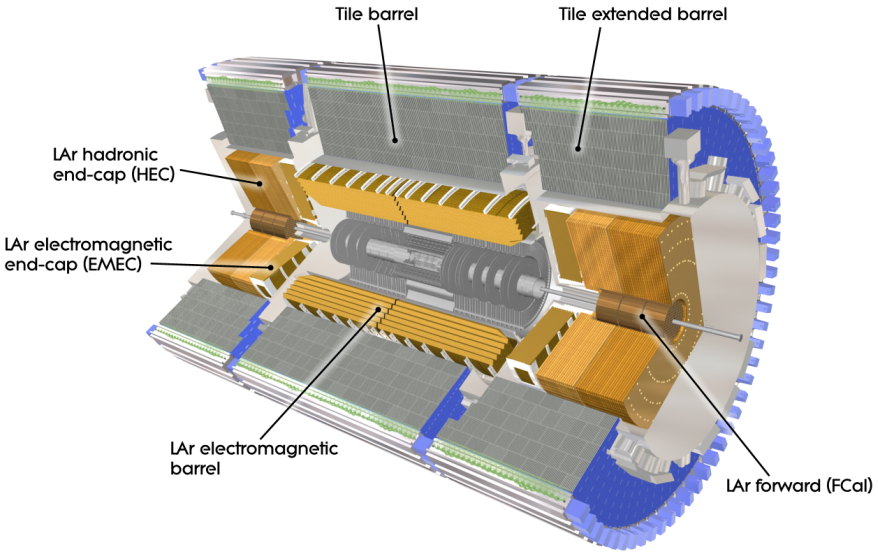

Figure 3.8: The cutaway view of the ATLAS calorimeter.

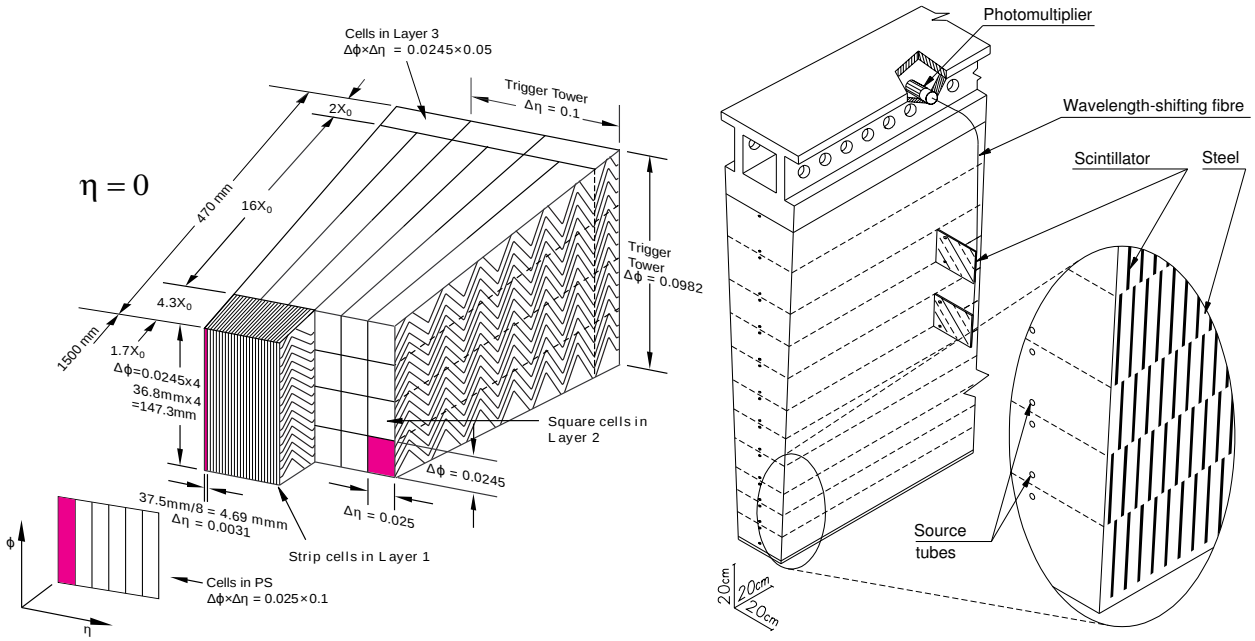

Figure 3.9: The basic structure of the LAr electromagnetic calorimeter (left) and the hadronic calorimeter (right). The granularity of the LAr calorimeter is $\Delta\eta \times \Delta\phi = 0.025 \times 0.025$, while it is $\Delta\eta \times \Delta\phi = 0.1 \times 0.1$ for the hadronic calorimeter.

Hadronic calorimeter

The tile-calorimeter, covering $|\eta| < 1.7$ and 2.28 m$< R <$4.25 m, is a sampling calorimeter using a series of steel (as the absorber) and scintillator (as the active layer). The tile-calorimeter is

	barrel		endcap	
EM calorimeter	#layers	$\lvert\eta\rvert$ coverage	#layers	$\lvert\eta\rvert$ coverage
	3	$\lvert\eta\rvert < 1.35$	2	$1.375 < \lvert\eta\rvert < 1.5$
	2	$1.35 < \lvert\eta\rvert < 1.475$	3	$1.5 < \lvert\eta\rvert < 2.5$
			2	$2.5 < \lvert\eta\rvert < 3.2$
	$\Delta\lvert\eta\rvert \times \Delta\phi$		$\Delta\lvert\eta\rvert \times \Delta\phi$	
1^{st} layer	$0.025/8 \times 0.1$	$\lvert\eta\rvert < 1.40$	0.050×0.1	$1.375 < \lvert\eta\rvert < 1.425$
	0.025×0.025	$1.40 < \lvert\eta\rvert < 1.475$	0.025×0.1	$1.425 < \lvert\eta\rvert < 1.5$
			$0.025/8 \times 0.1$	$1.5 < \lvert\eta\rvert < 1.8$
			$0.025/6 \times 0.1$	$1.8 < \lvert\eta\rvert < 2.0$
			$0.025/4 \times 0.1$	$2.0 < \lvert\eta\rvert < 2.4$
			0.025×0.1	$2.4 < \lvert\eta\rvert < 2.5$
			0.1×0.1	$2.5 < \lvert\eta\rvert < 3.2$
2^{nd} layer	0.025×0.025	$\lvert\eta\rvert < 1.40$	0.050×0.025	$1.375 < \lvert\eta\rvert < 1.425$
	0.075×0.025	$1.40 < \lvert\eta\rvert < 1.475$	0.025×0.025	$1.425 < \lvert\eta\rvert < 2.5$
			0.1×0.1	$2.5 < \lvert\eta\rvert < 3.2$
3^{rd} layer	0.050×0.025	$\lvert\eta\rvert < 1.35$	0.050×0.025	$1.5 < \lvert\eta\rvert < 2.5$
LAr hadronic endcap			#layers	
			4	$1.5 < \lvert\eta\rvert < 3.2$
			$\Delta\lvert\eta\rvert \times \Delta\phi$	
			0.1×0.1	$1.5 < \lvert\eta\rvert < 2.5$
			0.2×0.2	$2.5 < \lvert\eta\rvert < 3.2$
LAr forward calorimeter			#layers	
			3	$3.1 < \lvert\eta\rvert < 4.9$
			$\Delta x \times \Delta y$ (cm)	
		1^{st} layer	0.75×0.65	$3.10 < \lvert\eta\rvert < 3.15$
			3.0×2.6	$3.15 < \lvert\eta\rvert < 4.30$
			0.75×0.65	$4.30 < \lvert\eta\rvert < 4.83$
		2^{nd} layer	0.83×1.05	$3.20 < \lvert\eta\rvert < 3.24$
			3.3×4.2	$3.24 < \lvert\eta\rvert < 4.50$
			0.83×1.05	$4.50 < \lvert\eta\rvert < 4.81$
		3^{rd} layer	1.35×1.18	$3.29 < \lvert\eta\rvert < 3.32$
			5.4×4.7	$3.32 < \lvert\eta\rvert < 4.60$
			1.35×1.18	$4.60 < \lvert\eta\rvert < 4.75$
Scintillator tile calorimeter	#layers		#layers	
	3	$\lvert\eta\rvert < 1.0$	3	$0.8 < \lvert\eta\rvert < 1.7$
	$\Delta\lvert\eta\rvert \times \Delta\phi$		$\Delta\lvert\eta\rvert \times \Delta\phi$	
1^{st}, 2^{nd} layer	0.1×0.1	$\lvert\eta\rvert < 1.0$	0.1×0.1	$0.8 < \lvert\eta\rvert < 1.7$
3^{rd} layer	0.2×0.1	$\lvert\eta\rvert < 1.0$	0.2×0.1	$0.8 < \lvert\eta\rvert < 1.7$

Table 3.3: $|\eta|$ coverage, granularity, and the segmentation in depth of the ATLAS calorimeter.

segmented in depth in three layers, approximately 1.5, 4.1 and 1.8 interaction lengths (λ) for $|\eta| < 1$ and 1.5, 2.6 and 3.3 λ for $0.8 < |\eta| < 1.7$, as shown in Figure 3.10. The typical detection granularity is $\Delta\eta \times \Delta\phi = 0.1 \times 0.1$.

The endcap region ($1.5 < |\eta| < 3.2$) is covered by the LAr hadronic calorimeter. which consists of two independent wheels per each endcap. Each wheel is divided into two segments in depth with a typical granularity of $\Delta\eta \times \Delta\phi = 0.1 \times 0.1$ ($1.5 < |\eta| < 2.5$) and $\Delta\eta \times \Delta\phi = 0.2 \times 0.2$ ($2.5 < |\eta| < 3.2$).

Finally, extremely forward region ($3.1 < |\eta| < 4.9$) is covered by the LAr calorimeter with copper tube electrode to accommodate with high ionization rate. This benefits the uniformity of the calorimeter coverage and the reduction of the background levels to the muon spectrometer. The interaction length of the forward calorimeter is 10λ.

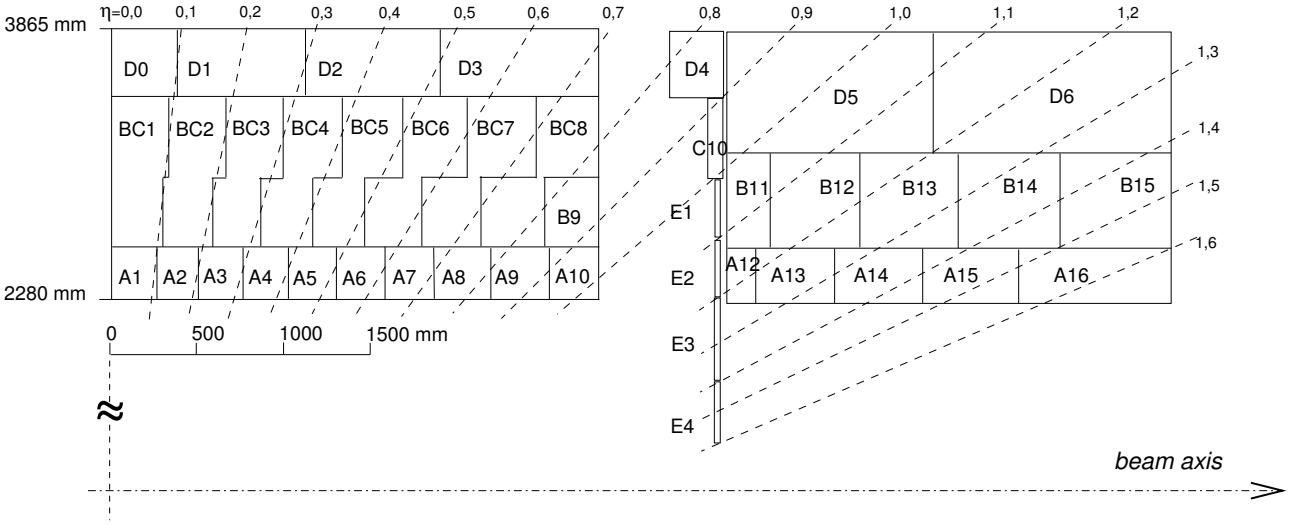

Figure 3.10: Segmentation in depth and η of the tile-calorimeter for $|\eta| < 1$ (left) and for $0.8 < |\eta| < 1.7$ (right). The vertical axis is R.

3.3.3 Muon Spectrometer and the Toroid Magnet

Figure 3.11 shows the schematic view of the ATLAS muon spectrometer. The muon spectrometer has two kinds of trigger chambers and two kinds of precision tracking chambers. RPC (Resistive Plate Chamber, $|\eta| < 1.1$) and TGC (Thin Gap Chamber, $1.1 < |\eta| < 2.4$) are dedicated to the fast muon trigger by which the trigger decision is made to the muons with $p_T > 6$ GeV from 40 MHz pp collisions. On the other hand, MDT (Monitored Drift Tube, $|\eta| < 2.7$) and CSC (Cathode Strip Chamber, $2.0 < |\eta| < 2.7$) are dedicated to the precise p_T measurement by means of the magnetic deflection produced by the toroidal magnetic field of 2 to 6 T·m. The designed p_T resolution is:

$$\frac{\sigma_{p_T}}{p_T} = 3\% \quad (p_T < 100 \text{ GeV}), \tag{3.6}$$

$$< 10\% \quad (p_T < 1 \text{ TeV}). \tag{3.7}$$

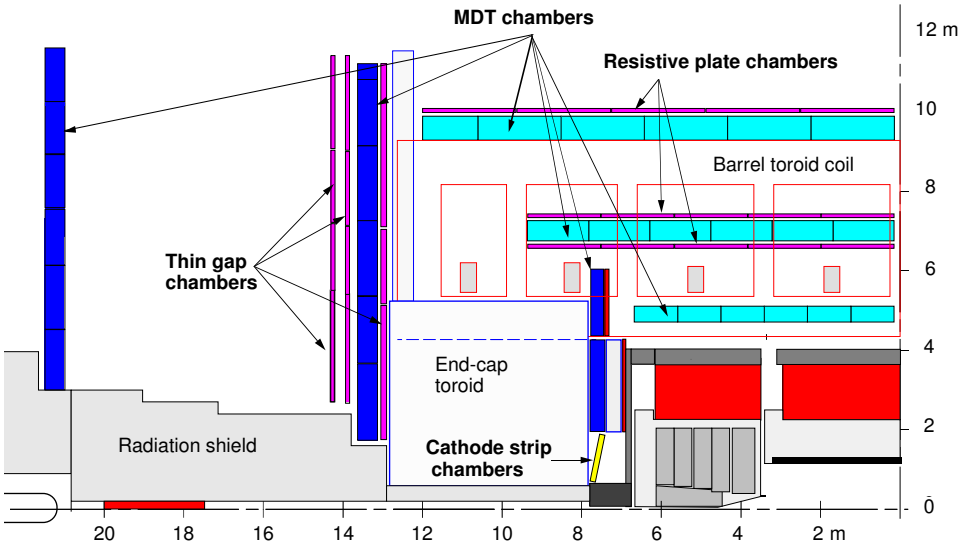

Figure 3.11: Schematic view of the ATLAS muon spectrometer (Quarter cut). There are two trigger detector (RPC and TGC) and two precision tracking chamber (MDT and CSC).

Thin Gap Chamber (TGC)

TGC is a multi-wire gas chamber filled with mixed gas of CO_2 : nC_5H_{12} = 55 : 45. In order to accommodate with 25 ns bunch crossing, the distance between the anode sense-wire to the cathode strip is determined to be 1.4 mm. The interval of the sense-wire is 1.8 mm. TGC is operated under the limited proportional region [C.1] and its gain is 10^6. The hit efficiency is more than 98% in an active region.

Resistive Plate Chamber (RPC)

RPC consists of the high-resistance Bakelite plate (10^{10} Ωm) faced each other, filled with mixed gas of $C_2H_2F_4$ (tetrafluoroethane) : C_4H_{10} (isobutane) : SF_6 (sulphur hexafluoride) = 94.7% : 5% : 0.3%. By applying 9 kV to the electrode, induced pulse by the charged particle is read out with the position resolution of 1 cm and the time resolution of 2 ns.

Monitored Drift Tube (MDT)

MDT is composed of a set of proportional counter with the conductor tube (radius of 30 mm) and the anode sense-wire with its radius of 25 μm. It is filled with mixed gas of Ar : CO_2 = 93% : 7% at 3 bar. High voltage of 3400 V is applied to the anode-wire. By measuring the drift time (typically a few 100 ns) and its corresponding drift circle, one can perform the tracking making use of three widely separated stations. The position resolution is 50 μm for the individual tube.

Cathode Strip Chamber (CSC)

CSC is a multi wire gas chamber, which is similar to TGC. The interval of the anode-wire is 2.5 mm and the cathode-strip is orthogonally aligned to the anode-wire with 5 mm pitch. By actively letting the charged particle to have a cross talk between the strip channels (typically 3 $\sim$ 5 channel), the position resolution of 60 μm is achieved by making use of barycenter of the readout charge.

Toroid Magnet

The large air core superconducting toroid magnet is placed to perform the p_T measurement of the traveling muon. It consists of the eight-fold superconducting coils and placed in the barrel and both endcap region, as shown in Figure 3.12 (Left). The coverage of the magnetic field is 25.3 m in length and 9.4 m $< r <$ 20.1 m for the barrel, while 1.65 m $< r <$ 10.7 m with axial length of 5.0 m for the endcap region. Figure 3.12 (Right) shows the computed magnetic field integrals as a function of $|\eta|$. The prediction line has been partially confirmed in the barrel region with a precision of 0.2%. The magnetic field is not uniform, especially around barrel-endcap transition region ($1.35 < |\eta| < 1.65$) due to the superposition of the magnetic field produced by both magnet system.

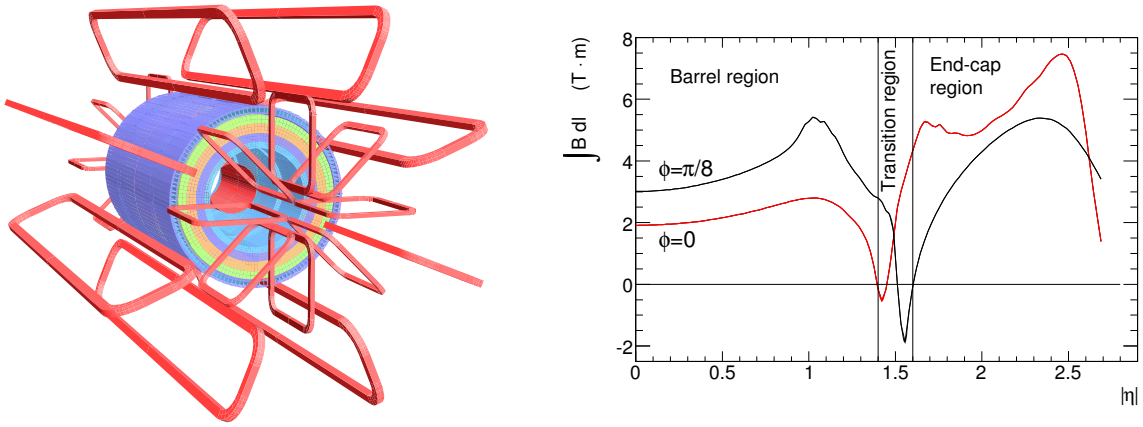

Figure 3.12: (Left) The schematic view of the ATLAS magnet system and (Right) magnetic filed integrals as a function of $|\eta|$.

3.4 Particle Reconstruction and the Trigger

All the detector signals are collected and converted into the particles, so-called particle reconstruction. This section summarizes the particle reconstruction scheme for the tracks, vertices, as well as the physics objects such as the electrons, hadronic jets, muons and the τ-leptons.

3.4.1 Track and Vertex Reconstruction

In order to reconstruct tracks and corresponding vertices, five parameters (so-called track parameters) are calculated at the perigee, the closest approach of a track to the beam line. The typical parametrization is the inverse transverse momentum (q/p_T), where q denotes the charge of the track, azimuthal angle (ϕ), polar angle ($\cot\theta$), transverse impact parameter (d_0), and longitudinal impact parameter ($z_0 \times \sin\theta$) with respect to the interaction point. The track parameters are derived in five steps:

1. The hit information from the Pixel and the SCT is converted into the cluster, while TRT hit timing is converted into the drift circle.

2. Track seeds are formed from a combination of the space points from three layers in the Pixel and the first layer in the SCT. The track seed is then extended to the remaining part of the SCT and becomes a track candidate after performing the fitting. Any clusters that are not associated to the track candidates are removed.

3. Selected tracks are extrapolated to the TRT and takes association with its drift circle. The left-right ambiguity of the TRT drift circle is resolved at this stage.

4. Track is refitted again with the full information from all three detectors.

5. After reconstructing tracks, vertex finder algorithm [B.2] is used to reconstruct the primary vertex.

Figure 3.13 shows the typical vertex resolution in xy and xz plane during 2011. The RMS of the vertex is 10$\sim$ 20 μm in xy plane and 60 mm in z direction, which is already close to the designed value. The p_T resolution is evaluated using $Z \to \mu\mu$ process in data, and estimated to be:

$$\frac{\sigma_{p_T}}{p_T} = 0.038 \times p_T \text{ (GeV)} \oplus 1.5\%, \tag{3.8}$$

which is also equivalent to the designed performance. The slightly larger offset term is attributed to the multiple scatterings.

3.4.2 Electron reconstruction

Electron reconstruction starts from a seed electromagnetic cluster with transverse energy above 2.5 GeV. Then, all the tracks found in the inner tracker that is not coming from γ conversion ($\gamma \to e^+e^-$) pair are extrapolated to the electromagnetic calorimeter. The matching is taken within a broad $\Delta\eta \times \Delta\phi = 0.075 \times 0.125$ window. If there is no matching tracks, those jets are discarded. To ensure the considering electromagnetic jet coming from the electron, the ratio E/p, the energy of the cluster to the momentum of the track is required to be less than 10. According to the MC simulation, 93% of the true isolated electrons with $E_T > 20$ GeV and $|\eta| < 2.5$ is kept as an electron candidate.

The energy resolution of the electron has been evaluated using $Z \to ee$ process in data, by fitting the invariant mass distribution using a Breit-Wigner convolved function. The obtained mass resolution is 2 - 4 GeV, which corresponds to the electron energy resolution of 1 - 3 GeV.

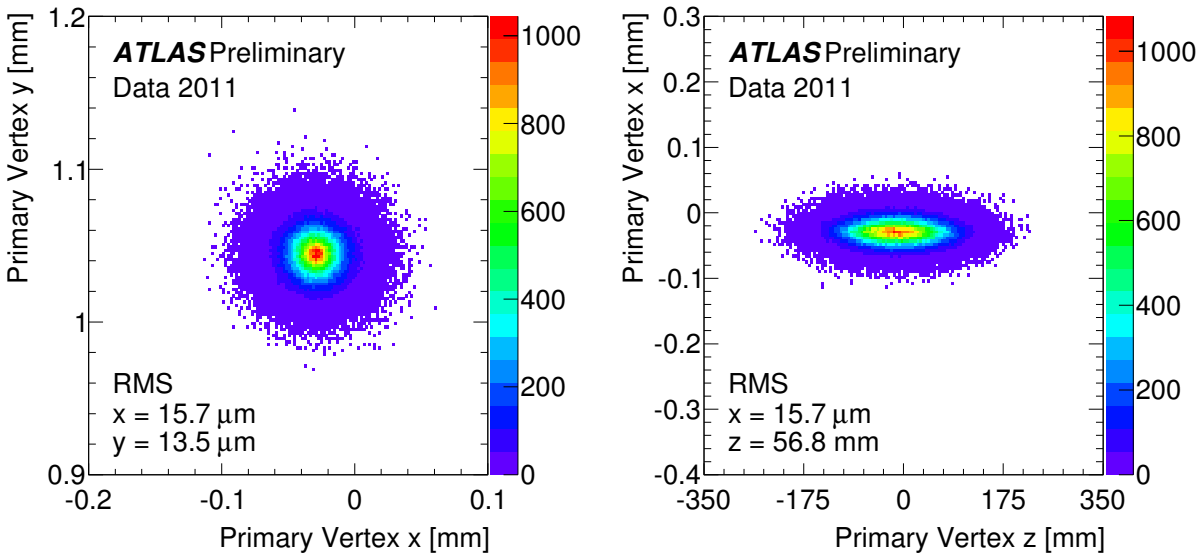

Figure 3.13: Typical vertex resolution in (left) xy plane and (right) xz plane.

Although this is slightly worse compared to the one expected from the equation (3.3), this is almost within our expectation.

3.4.3 Muon reconstruction

Muon is reconstructed in following four steps:

1. Build the track segment in each of the three MDT layers and link them to form the muon track. Hough transformation [B.3] is used to find straight tracks.

2. Extrapolate the track segments into the inner tracker taking into account the multiple scattering and the energy loss (typically 3 GeV) in the calorimeter.

3. Matching is taken between the extrapolated track segment and the track found in the inner tracker. If the matching is taken, it is called as the combined muon. The fake muons such as the punch through muons from π/K decay in the calorimeter and the muons from the beam background is drastically suppressed.

4. Finally, matching χ^2 (denote as $\chi^2_{\mathrm{matching}}$) is defined for the combined muon as

$$\chi^2_{\mathrm{matching}} = (\mathbf{T_{MS}} - \mathbf{T_{ID}})^{\mathbf{T}}(\mathbf{C_{MS}} + \mathbf{C_{ID}})^{-\mathbf{1}}(\mathbf{T_{MS}} - \mathbf{T_{ID}})^{\mathbf{T}}, \tag{3.9}$$

   where $\mathbf{T}$ denotes a vector of the track parameters and C represents its covariance matrix. The subscript of ID and MS represents the inner tracker and the muon spectrometer. The combined track is selected so that it gives the minimum $\chi^2_{\mathrm{matching}}$.

The muon p_T is calculated by means of the sagitta in the barrel [B.4], and the point-angle measurement in the endcap region. As is described in [B.4], the muon p_T resolution ($\Delta p_T/p_T$) is determined by the energy loss fluctuation traversing the material in front of the muon spectrometer ($\propto 1/p_T$), multiple coulomb scattering ($\propto$ const.) and the single hit resolution, such as the miss-alignment effect and the calibration ($\propto p_T$).

During 2009, the muon p_T resolution has been measured using cosmic ray muons by means of the width of the fitted distribution of the relative p_T difference ($\Delta p_T/p_T$) between the top and the bottom halves of the track. The observed p_T resolution is fitted as a function of p_T with following formula:

$$\frac{\Delta p_T}{p_T} = \frac{p_0}{p_T} \oplus p_1 \oplus p_2 p_T, \tag{3.10}$$

where p_0, p_1, and p_2 represents energy loss fluctuation term, multiple scattering term, and intrinsic resolution term, respectively. The result shows 4% in $p_T < 100$ GeV and 12% up to $p_T = 1$ TeV, while it is designed to be a few % in $p_T < 100$ GeV and 10% up to $p_T = 1$ TeV. This is almost consistent with our initial expectation.

3.4.4 Jet reconstruction

Jets are reconstructed in three steps: (1) the clustering, (2) jet finding and (3) the energy calibration.

1. **Clustering**
   The clustering is performed starting from each calorimeter clusters reconstructed by the topological cluster algorithm. The seed cell is defined by requiring high energy deposit with S/N > 4, where all the neighboring cells are collected into the cluster. The next-to-next neighboring cells are added if S/N > 2. In this way, four-vector (E, p_x, p_y, p_z) is reconstructed assuming the cluster mass to be zero.

2. **Jet finding**
   Jet finding is performed using the anti-k_T algorithm [20] to translate each cluster information into jets. In the anti-k_T algorithm, the distance between the cluster i and the cluster j is defined in the $p_T - R$ plane (d_{ij}) defined as

   $$d_{ij} = \min(p_{T,i}^{-2}, p_{T,j}^{-2}) \frac{\Delta R(i,j)^2}{R^2}, \tag{3.11}$$

   where $\Delta R(i,j) = \sqrt{(\Delta\eta_{ij}^2 + \Delta\phi_{ij}^2)}$. $R = 0.4$ is used as the distant parameter within which jet finding is performed.

   The anti-k_T algorithm proceeds by identifying the smallest d_{ij}, denote as $d_{\min}$. If $d_{\min} = d_{ij} \neq d_{ii}$, anti-$k_T$ combines i^{th} and j^{th} jet into k^{th} jet by adding the four-vector by $p_k = p_i + p_j$. On the other hand, if $d_{\min} = d_{ii}$ is satisfied, meaning there is no clusters to be added within $\Delta R < 0.4$, it is recognized as a jet and removed from the list of considering jets. This procedure is repeated until all the clusters will be removed from the list of considering clusters. In this way, all the original clusters belong either one of the jets.

3. **Energy calibration**
   The observed energy at the calorimeter does not represent the energy of the original parton (a quark or a gluon) due to the undetected neutron and the initial and the final state radiation. Therefore, the energy calibration is performed to get back the energy of the original parton.

   - Energy loss due to the undetected neutron. This requires the biggest energy calibration of about 25%. The other effect such as the detector hole, noise, track bending in or out the jet cone due to the solenoid magnet are also considered.
   - Energy loss or increase due to the underlying events such as the initial and the final state radiation, the fragmentation, and the pile-up.

   The energy calibration is performed based on the MC where the generated energy and the reconstructed energy is compared to make a response function as a function of p_T, η and the energy density. This level of jet is called particle-level jet. Second, calibration parameters are derived from data by using p_T-balanced events such as di-jet or $\gamma+$ jet. By using γ as a tag, one can check the detector response for the known-p_T jet. This provides a series of calibration parameters as a function of p_T and η. This level of jet is called parton-level jet, which is the one used in the analysis.

In 2011, the jet energy resolution is evaluated using di-jet events, featuring its p_T balance. The data is used by requiring two back-to-back leading jets, satisfying at least $\Delta\phi \geq 2.8$ rad between them, and that both jets to be in the same rapidity region. The jet energy resolution is evaluated as the asymmetry between the transverse momenta of two leading jets and the fitted gaussian σ is used to characterize the jet energy resolution. The obtained resolution is 10-14% worse compared to the expectation.

3.4.5 b-tagging

The identification of the b-jet (b-tagging) makes use of their specific properties: the long lifetime of the b-hadron ($c\tau = 420$ μm), where measurable secondary vertices that are well separated from the primary vertex is observed, the large b-hadron mass, and the large branching ratio into leptons. In this analysis, the output score from two b-taggers, JetFitter and IP3D, are combined using a neural network and used as a discriminant variable.

The JetFitter exploits the topology of b and c hadron decays inside the jet to find a common line on which the primary vertex, the b and c hadron decay vertices lie, as well as their position on this line, giving an approximated flight path for the b-hadron. The discrimination between b-jet and other jets is based on a likelihood using masses, momenta, flight-length significances, and track multiplicities of the reconstructed vertices. The IP3D b-tagger uses transverse and longitudinal impact parameter significances of each track within the jet to determine a likelihood that the jet originates from a b-quark.

3.4.6 Reconstruction of the hadronically decaying τ-lepton

As is mentioned in section 3.2, the reconstruction of the τ-lepton only focuses on the hadronically decaying τ-lepton. Since the τ-lepton originally has an electric charge, the hadronically

decaying τ-lepton can be classified into 1 prong (denote as τ_1), where the number of charged track (N_{track}) inside the jet is one, or the multi prong (denote as τ_3) where $N_{\text{track}} \geq 2$, taking into account the inefficiency of the track reconstruction. Table 3.4 summarizes the basic decay mode of the hadronically decaying τ-lepton and Figure 3.14 shows its typical signatures.

	Decay mode	Branching fraction
τ_1	$\tau^- \to \pi^- \nu_\tau$, $\tau^+ \to \pi^+ \bar{\nu_\tau}$	18%
	$\tau^- \to \pi^- \pi^0 \nu_\tau$, $\tau^+ \to \pi^+ \pi^0 \bar{\nu_\tau}$	40%
	$\tau^- \to \pi^- \pi^0 \pi^0 \nu_\tau$, $\tau^+ \to \pi^+ \pi^0 \pi^0 \bar{\nu_\tau}$	15%
	$\tau^- \to \pi^- \pi^0 \pi^0 \pi^0 \nu_\tau$, $\tau^+ \to \pi^+ \pi^0 \pi^0 \pi^0 \bar{\nu_\tau}$	2%
	others including $K^\pm$	2%
τ_3	$\tau^- \to \pi^- \pi^+ \pi^- \nu_\tau$, $\tau^+ \to \pi^+ \pi^- \pi^+ \bar{\nu_\tau}$	15%
	$\tau^- \to \pi^- \pi^+ \pi^- \pi^0 \nu_\tau$, $\tau^+ \to \pi^+ \pi^- \pi^+ \pi^0 \bar{\nu_\tau}$	7%
	others including $K^\pm$	1%

Table 3.4: The dominant decay mode of the hadronically decaying τ-lepton. 60% of the decay mode includes additional π^0 which immediately decays into 2γ.

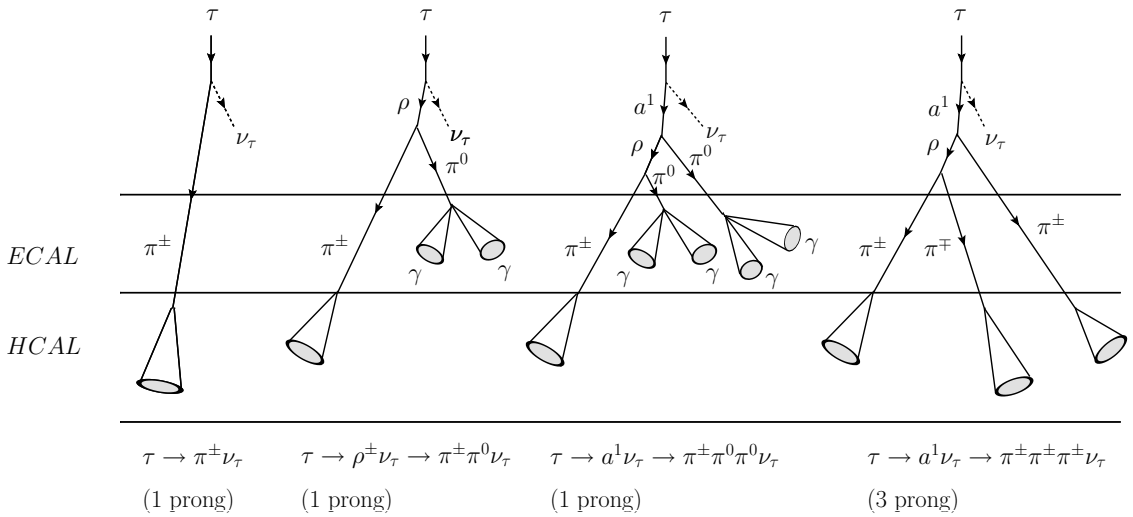

Figure 3.14: Basic signatures of the hadronically decaying τ-lepton. The weak current that couples to the τ-lepton is either pseudo-scalar ($\pi^\pm$), vector (ρ) and axial vector (a^1). If the τ-lepton decays via ρ or a^1, additional π^0 is emitted, which immediately decays into 2γ.

The reconstruction of the hadronically decaying τ-lepton starts from the calorimeter jets with $p_T > 10$ GeV and $|\eta| < 2.5$ reconstructed by the anti-k_T algorithm. The four-vector is calculated based on the topological clusters associated to them, assuming the mass to be zero. Then, all the tracks satisfying $p_T > 1$ GeV, number of pixel hits ≥ 2, number of pixel hits plus number of SCT hits ≥ 7, $|d_0| < 1.0$ mm and $|z_0 \sin\theta| < 1.5$ mm are associated to the jet

if these are within $\Delta R < 0.2$. d_0 is the distance of the closest approach of the track to the reconstructed primary vertex in the transverse plane. The jet satisfying this requirement is called τ candidate.

3.4.7 Trigger

At the LHC's designed luminosity of $\mathcal{L} = 10^{34}/\text{cm}^2\text{s}$, the total cross-section of the inelastic scattering is an order of $\mathcal{O}(100)$ mb. This results in pp collision rate about 1 GHz. However, data recording rate is limited to 300 MB/s from the view point of current resources. Assuming 1.5 MB/event is needed, trigger rate must be suppressed up to $\mathcal{O}(200)$ Hz. This requires 10^5 reduction against the huge inelastic scattering background, while keeping maximum efficiency for the standard model processes and possible new physics processes.

In order to achieve 10^5 reduction, there are three stages of the trigger decision scheme: leve-1 (40 MHz $\rightarrow$ 75 kHz), leve-2 (75 kHz $\rightarrow$ 3.5 kHz), and the Event-filter (3.5 kHz $\rightarrow$ 200 Hz). The leve-1 trigger is a hardware-based trigger, built on the detector electronics. Based on the information from the muon trigger detector (TGC and RPC) and the calorimeter (ECAL and HCAL), trigger is generated if there is a distinctive signals such as high$-p_T$ leptons or energetic jets in the event. The higher level trigger (leve-2, Event-Filter) is a software-based, where offline reconstruction is performed and further suppression is performed up to 200 Hz. The reduction rate is $\mathcal{O}(20)$ in both cases.

Table 3.5 shows the main trigger menu adopted at the end of 2011 at $\mathcal{L} = 3.3\times10^{33}$ $(1/\text{cm}^2\text{s})$ [21] as well as its trigger rate. The level-1 and the Event-filter successfully reduces the total trigger rate up to 75 kHz and 200 Hz, respectively.

Trigger	L1 selection	EF selection	L1 rate (kHz)	EF rate (Hz)	Target physics
Single muon	11 GeV	18 GeV	8	100	$W, Z, t\bar{t}$
Single electron	16 GeV	22 GeV	9	55	$W, Z, t\bar{t}$
Two muon	2×11 GeV	15, 11 GeV	8	4	$J/\psi, \Upsilon, Z, B$
Two electron	2×10 GeV	2×12 GeV	2	1	$J/\psi, \Upsilon, Z$
Two τ-lepton like jet	15, 11 GeV	29, 20 GeV	7.5	15	$Z \rightarrow \tau\tau, H \rightarrow \tau\tau$
Two photon	2×12 GeV	2×20 GeV	3.5	5	$H \rightarrow \gamma\gamma$
singel jet plus E_T^{miss}	50, 35 GeV	75, 55 GeV	0.8	18	$W, t\bar{t}$
E_T^{miss}	50 GeV	70 GeV	0.6	5	$W, t\bar{t}$, SUSY
multi jet	5×10 GeV	5×30 GeV	0.2	9	QCD
Total			< 75	212	

Table 3.5: Main trigger menu and its trigger rate at the end of 2011 at $\mathcal{L} = 3.3 \times 10^{33}$ $(1/\text{cm}^2\text{s})$. L1 represents leve-1 and EF represents Event-filter. Sensitive physics processes are also shown.

Chapter 4

Commissioning of the ATLAS endcap muon trigger detector

4.1 Introduction

In this thesis, single lepton (a muon or an electron) triggers are used, relying on its large reduction rate. Given the fact that the lepton trigger efficiency directly affects to the acceptance of the signal events, I've conducted the commissioning and the daily operation of the endcap muon trigger detector, Thin Gap Chamber (TGC), which is dedicated to trigger muons with $p_T > 6$ GeV from 40 MHz pp collision in $1.0 < |\eta| < 2.4$. In order to maximize the trigger efficiency, which is the most essential parameter of the detector, following steps are taken:

1. Measure the hit efficiency using cosmic ray muons. Based on the result, operation parameters (e.g, applied high-voltage and the threshold voltage for the signal digitization) are optimized chamber by chamber basis to maximize the hit efficiency.

2. Timing adjustment between the TGC hit and the data acquisition timing (distributed radio-frequency clock) in ATLAS to maximize the matching efficiency.

This chapter describes above accomplishment after a brief review of the detector.

4.2 Thin Gap Chamber

4.2.1 Detection principle

TGC consists of 3408 multi-wire gas chambers with a typical size of 2×2 m^2. It is aligned along the concentric circle with its radius of 12.5 m, called big-wheel, as shown in Figure 4.1. There are three big-wheels: TGC1, TGC2 and TGC3 at both endcap, each consists of three, two and two gas-gap layers located at $|z| = 13$ m, 14 m and 14.5 m, respectively.

The structure of the chamber is depicted in Figure 4.2. TGC adopts two-dimensional readout by the anode sense-wire (denote as wire) for r measurement and the cathode-strip (denote as strip) for ϕ measurement. The wire is made from tungsten with its radius of 50 μm aligned with 1.8 mm pitch, where 7 - 20 wires (depending on η) are bundled together as one

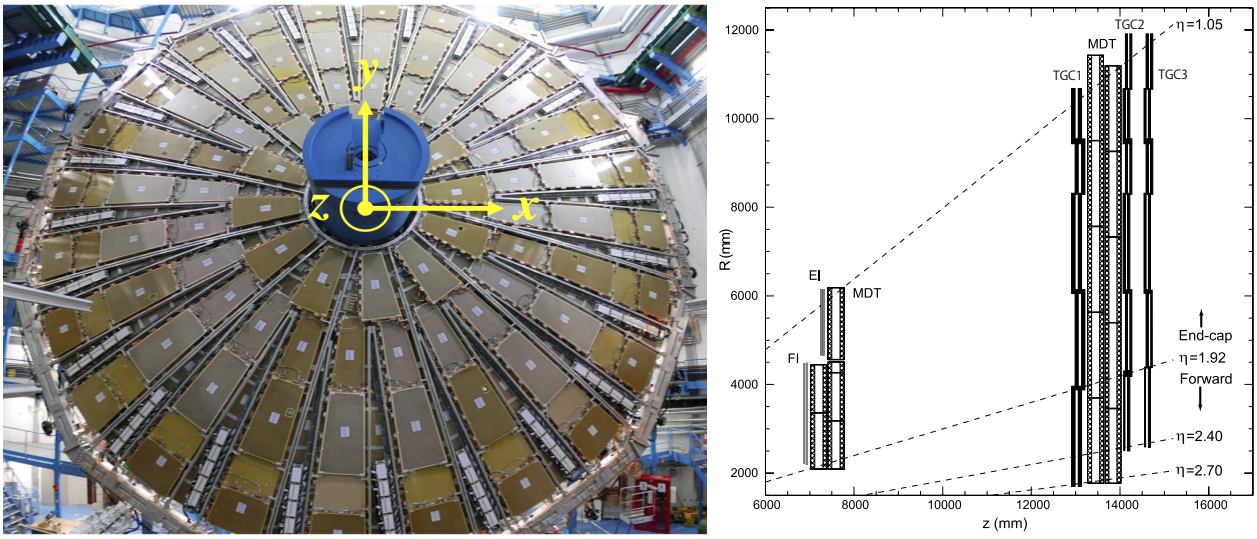

Figure 4.1: (Left) TGC big-wheel viewed from the interaction point. (Right) TGC layout in the longitudinal plane. Horizontal axis represents z (mm) and vertical axis represents r (mm).

readout channel. The strip is made from glass epoxy plate with pasted carbon on the surface to see mirror charges induced by the wire. The strip is aligned perpendicularly to the wire apart from 1.4 mm, which is optimized to accommodate with short bunch-crossing intervals (25 ns). There are 264,472 readout channels for the wire and 53,760 readout channels for the strip.

The chambers are operated under the limited proportional mode [C.1] with mixed gas of $CO_2 : nC_5H_{12} = 55\% : 45\%$ at 1 atm. The high-voltage of 2800 V is applied to the wire for the readout. When the muon passes through the gas-gap, it ionizes gas molecules and produce 10 - 20 primary electrons through its trajectory. These electrons drift to the wire and experiences townsend-type avalanche [C.2]. This results in $\mathcal{O}(10^6)$ electrons (≈1pC), which leads to the expected hit efficiency in an active region with more than 98%. The hit efficiency depends on the applied high-voltage and the threshold voltage for the digitization.

Figure 4.3 shows an intrinsic time jitter distribution depending on the incident angle. The typical time jitter is 25 ns, which is comparable to that of the bunch-crossing intervals. Therefore, the timing adjustment between the rising edge of the time jitter distribution and the data acquisition timing is inevitable to maximize the trigger efficiency (Section 4.4).

4.2.2 Trigger decision scheme

TGC is designed to trigger muons with $p_T > 6$ GeV, by roughly calculating the transverse momentum of the traveling muon within a latency of 2-3 μs. The p_T calculation makes use of the magnetic deflection induced by the endcap toroid magnet located before TGC. Since the muon trajectory is bent with its curvature proportional to p_T^{-1}, comparison between the actual hit position and the one assumed by the infinity momentum muon ($p_T = \infty$, no magnetic effect) gives an index of the muon p_T. The calculation is performed based on the detector electronics:

1. Require three out of four (denote as 3/4) coincidence in TGC2+TGC3 and two out of

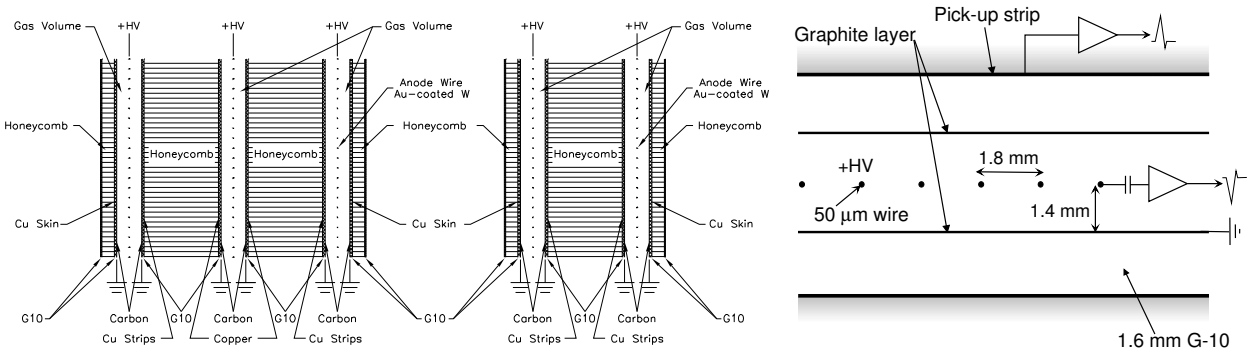

Figure 4.2: Cross-sectional view of (left) the triplet chamber and (right) the doublet chamber. The triplet has strips on the two outer layers only. (Right) Typical structure of the gas-gap.

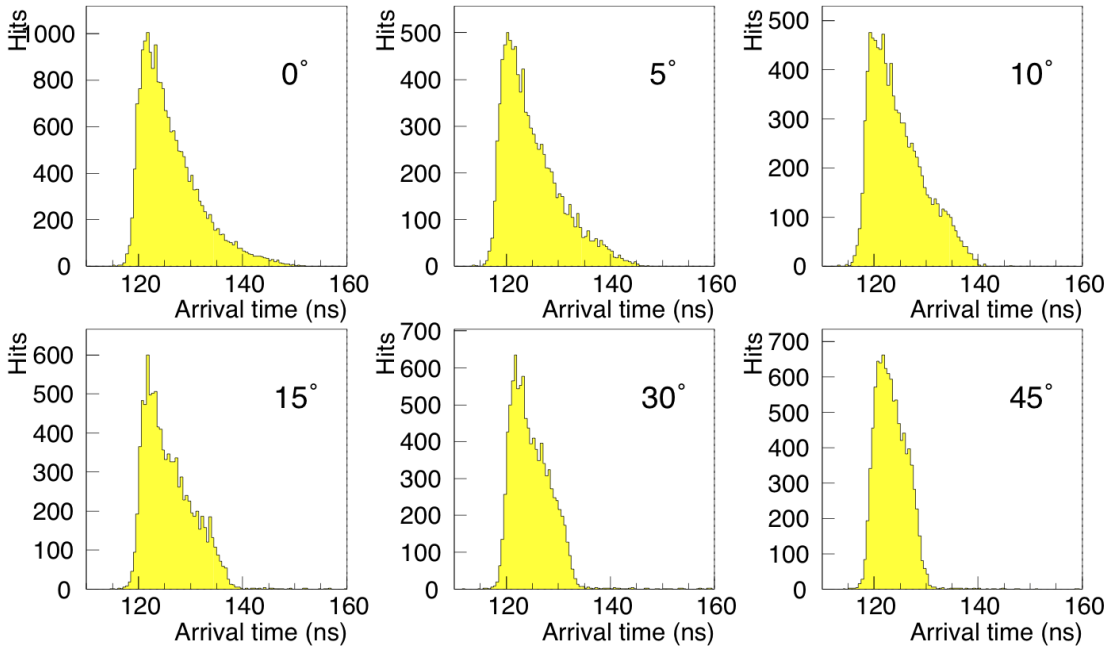

Figure 4.3: Intrinsic time jitter distribution depending on the incident angle. The incident angle is measured from vertical with respect to the TGC plane. This measurement is performed using 3 GeV π^- beam with small chamber (1.8 mm $\times$1.4 mm) operated at 3.1 kV.

three (denote as 2/3) coincidence in TGC1 to avoid an accidental coincidence.

2. Make the infinity momentum line by connecting the interaction point and the actual hit position at TGC3.

3. Evaluate the cross-point of the infinity momentum line at TGC1 and compare it to the actual hit position at TGC1. The difference $(\delta r, \delta\phi)$ becomes an index of p_T and

compared to the predefined coincidence window as shown in Figure 4.4. Each colored region corresponds to the p_T in a range of [6,10,15,20,40] GeV. If the observed $(\delta r, \delta\phi)$ is inside this range, trigger is generated together with its p_T label.

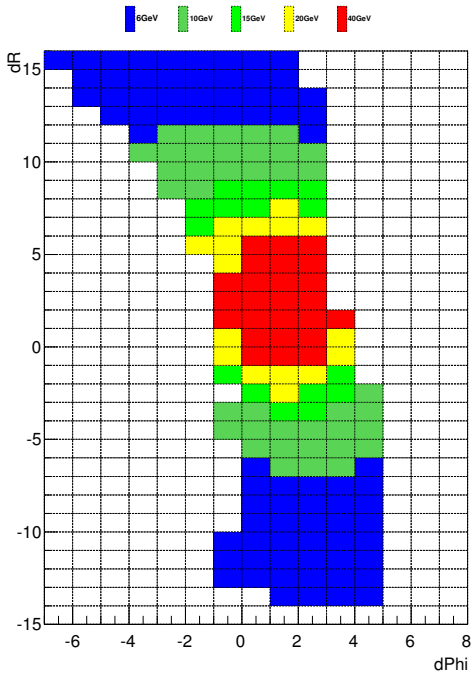

Figure 4.4: Example of the coincidence window

Figure 4.5 shows the TGC electronics system with which all the above calculations are performed. First of all, all the signals from each chamber are amplified, discriminated and shaped by the chamber-mounted electronics called ASD (Amplifier-Shaper-Discriminator). The threshold voltage of the digitization is one of the operation parameter that decides the hit efficiency. These signals are sent to the Patch-Panel (PP) ASIC, where the collision bunch-crossing is identified (BCID). Then, 2/3 coincidence (TGC1) and 3/4 coincidence (TGC2+TGC3) are performed by the Slave Board ASIC (SLB). SLB also has a readout buffer (L1 Buffer), where all the hit information is held while waiting the level-1 trigger signal. The maximum latency is 3.2 μs.

As a second step, all the coincidence signals from SLB are sent to the high-p_T module (HPT) located at the outer rim of the TGC1 big-wheel. HPT module takes a coincidence between TGC1 and TGC2+TGC3, independently in r (wire) and ϕ (strip) direction. These coincidence signals are sent to the electronics-hut outside the ATLAS cavern via 50 - 90 m optical fibers and received by the Sector Logic (SL) module. The SL takes r-ϕ coincidence and passes it to the Muon Interface to the Central Trigger Processor (MUCTPI). Together with calorimeter information, Central Trigger Processor (CTP) performs the final trigger decision.

Finally, once the trigger decision is made, trigger signal is sent back to the SLB and all the hit information at the specified bunch-crossing is sent to the Read Out Driver (ROD) via the Star Switch module (SSW).

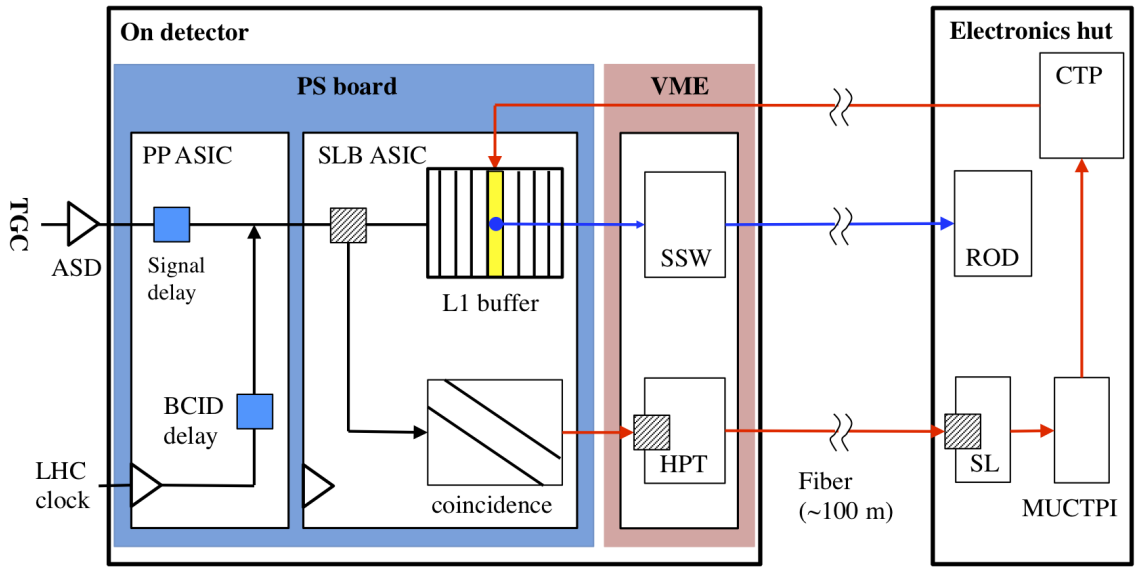

Figure 4.5: Overview of the TGC electronics system. The blue box represents a variable delay. The trigger line is shown in the red line and the readout line is shown in the blue line.

In order to adjust the trigger timing and to achieve flexible data-taking, more than 122,832 registers are implemented on the electronics such as the signal delay functionality, masking functionality to mask the noisy channels and the monitoring functionality to detect any error states. These registers are implemented on ASICs and FPGAs (Field Programmable Gate Array) and controlled/monitored by the Single Board Computer. Table 4.1 summarizes number of main electronics board and registers implemented in the trigger system.

Item	# of electronics	# of registers
ASD (Amplifier Shaper Discriminator)	20704	0
PS (PP and SLB) board	672	118800
SSW (Star Switch) module	224	1536
HPT (high-p_T) module	192	1536
SL (Sector Logic) module	72	960

Table 4.1: Number of main electronics board and registers used in the trigger system.

In order to make a trigger decision, all the hit information from the same bunch-crossing need to be adjusted at the input of the coincidence logic located at the SLB. The time of flight difference depending on the incident position (44.9 ns - 63.9 ns) and the different cable length from ASD to PP (65 ns - 116 ns) were absorbed by the signal delay and the BCID delay circuit implemented on the PP ASIC. The arrival timing at the SLB was adjusted within 0.9 ns [22].

4.3 Measurement of the hit efficiency

In order to measure the TGC hit efficiency, the analysis exploits cosmic ray muons that could penetrate to the underground experiment area. Since the angle dependence of the cosmic ray muon is proportional to $\cos^2\theta$, where θ is the measured angle from the top, most of the muon comes from the vertical direction. Since the coincidence window only accepts particles coming from the interaction point ($40^\circ < \theta < 70^\circ$), trigger condition is loosened to have 3/4 coincidence in TGC2 + TGC3 instead of additionally requiring 2/3 coincidence at TGC1. With this condition a trigger rate of 10 Hz was obtained per each side of the detector, resulting in more than 500 M cosmic ray muons collected during the commissioning period.

Following method was developed for the hit efficiency measurement (following discussion focuses on TGC2+TGC3 case, as an example):

- To evaluate the hit efficiency in i^{th} layer, it is required to have one and only one wire and strip hit in each of the other three layers. In this way, 3/4 trigger condition is satisfied independently of the presence of a hit in the layer under evaluation. The number of events satisfying this requirement becomes a denominator.

- Check if the i^{th} layer has at least one hit within the acceptable region. The number of events satisfying this requirement becomes a numerator

Figure 4.6 shows the hit efficiency of the wire as a function of the applied high-voltage. The hit efficiency is separately measured for each side (A or C) and TGC1 or TGC2+TGC3. The horizontal axis represents the applied high-voltage, where the data points are taken at 2650 V, 2750 V, 2800 V and 2850 V, respectively. The hit efficiency increases as a function of the applied high-voltage and reaches its plateau at 2800 V with 93%. In order to see more detail, Figure 4.7 shows the efficiency map in r-ϕ (wire-strip) plane and its η projection, meaning the strip efficiency. The efficiency drop is observed due to the support materials inside the chamber. The direction of the support material is in parallel to the strip channel and its fraction accounts for 3-6%, depending on the chamber type. The observed efficiency drop is consistent with the wire support location, which is shown in the blue band. The chamber has an ideal hit efficiency of 98% in an active region, which is limited by the inefficiency caused by the insufficient number of primary electrons or short distance of the muon passage. The observed efficiency of 98% is almost consistent with the calculation based on the simulation. In this way, 93% hit efficiency can be attributed to the intrinsic efficiency decreased by the fraction of the support materials.

In order to maximize the hit efficiency, optimization has been performed for the applied high-voltage and the threshold voltage used in the discriminator at ASD. The threshold has been firstly optimized based on the occupancy level derived by the random trigger data, where -60 mV is found to be optimal for the wire and $+70$ mV for the strip. For those channels with its occupancy higher than 10^{-4}, threshold is raised individually to suppress fake triggers.

Then, the optimization of the applied high-voltage is performed based on the efficiency at 2800 V (denote as ε_{2800}) and the efficiency difference between 2800 V and 2850 V (denote as $\Delta\varepsilon = \varepsilon_{2800} - \varepsilon_{2850}$). For those chambers with $\varepsilon_{2800} < 90\%$ or $\Delta\varepsilon < -5\%$, applied high-voltage was raised from 2800 V to 2850 V or 2900 V. For other chambers, high-voltage of 2800 V is

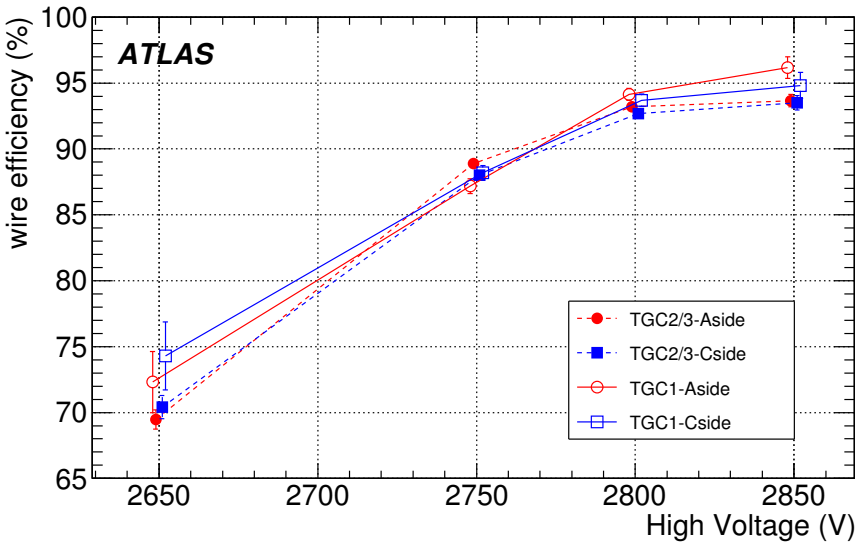

Figure 4.6: Measured wire hit efficiency as a function of the applied high-voltage (turn-on curve). The hit efficiency reaches its plateau at 2800 V with 93%.

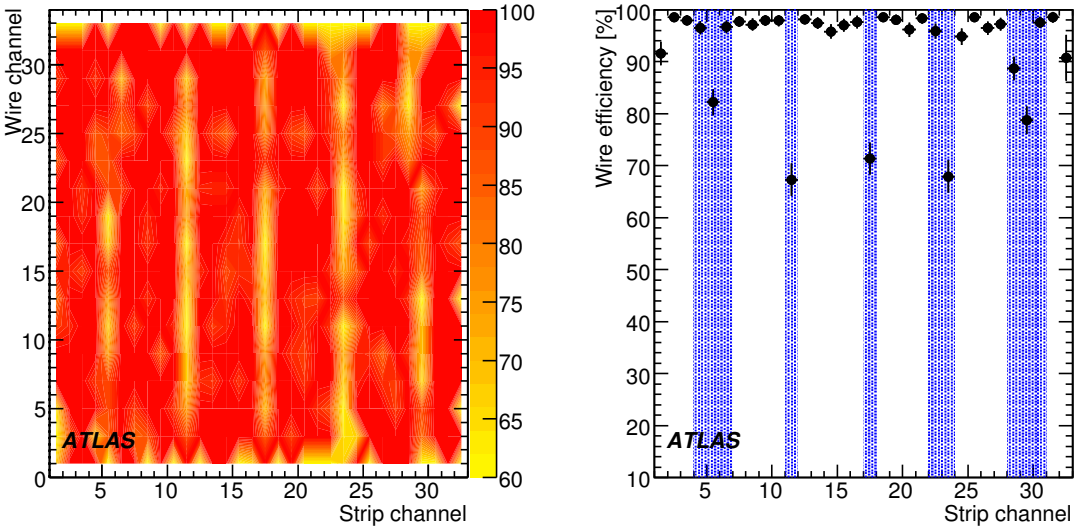

Figure 4.7: (Left) efficiency map in the wire-strip (r-ϕ) plane. Same type of the chamber is combined. The vertical axis is the wire channel and the horizontal axis is the strip channel. (Right) Projection to the strip channels, meaning the strip efficiency. The blue band shows the location of the support materials.

chosen. As the result, 178 chambers (5.2%) are raised to 2850 V and 151 chambers (4.4%) are raised to 2900 V. By this optimization, almost all the chamber successfully reaches its plateau efficiency, and the uniformity of the hit efficiency has been improved. As a consequence, the systematic uncertainty related to the hit efficiency was reduced from 2.6% to 0.7%. At the same time, one could minimize the load to the detector, while keeping the ideal hit efficiencies, which helps to keep the ideal trigger performance for the long-term use in the future.

4.4 Adjustment of the trigger timing

Once the hit efficiency is ensured, the trigger timing was adjusted to the rising edge of the data acquisition timing, i.e, the rising edge of the distributed radio-frequency clock to maximize the matching efficiency. The concept of the timing adjustment is depicted in Figure 4.8. The left figure shows the best clock phase, where all the hits from the TGC are recognized as one bunch-crossing wherever the actual hit (shown in the blue arrow) is inside the time jitter distribution. However, it is not the case for the right figure.

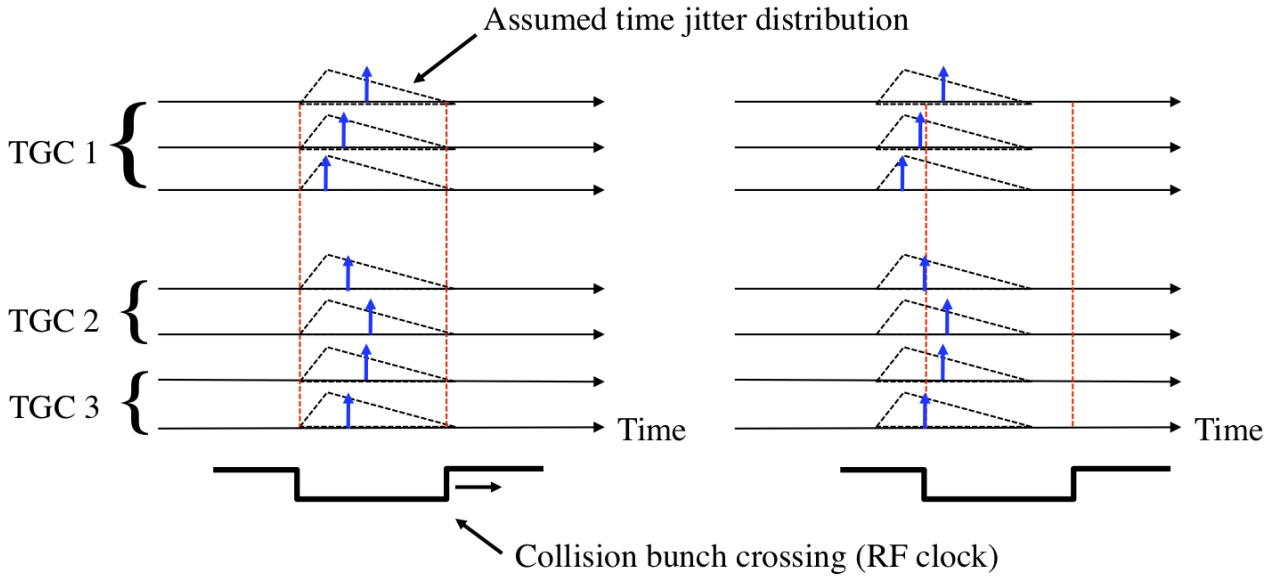

Figure 4.8: The sketch of the timing adjustment. Note that the rising edge of each time jitter distribution has been already adjusted within 0.9 ns, using the signal delay and the BCID delay circuit, as is described in see Section 4.2.2.

In order to find out the best clock phase, following scheme has been established:

1. Shift the clock phase of the distributed radio-frequency clock. The shift is performed by using the additional delay module and fed into the LHC clock line in Figure 4.5.

2. Evaluate the fraction of events at the expected collision bunch-crossing. If the clock phase is the best position, all the events are detected at one bunch-crossing. The best clock

phase is determined when the fraction of the events become maximum at the expected collision bunch-crossing.

The method has been applied to the beam collision data when there are 25 bunches filled by protons out of 2808. This enables us to specify the exact collision bunch-crossing. If the trigger is generated, data at the collision bunch-crossing is recorded together with neighboring bunch-crossings. Figure 4.9 shows the observed fraction of events at the expected collision bunch-crossing as a function of the shifted clock phase. According to this measurement, -2 ns is found to be optimal. However, -4 ns is taken as the final value taking into account the fluctuation of the clock phase caused by the possible temperature fluctuation. The success of this timing adjustment leads to the maximization of the trigger efficiency.

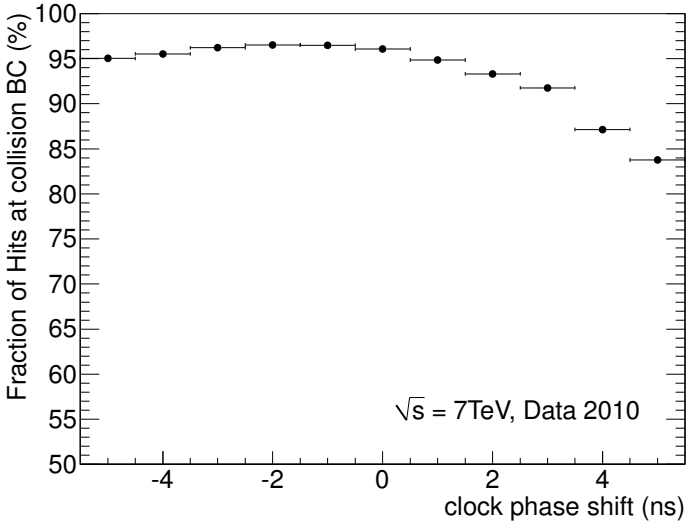

Figure 4.9: The observed fraction of events at the expected collision bunch-crossing as a function of the shifted clock phase. The origin is the clock phase when the data-taking started.

Finally, after the trigger timing was adjusted, muon trigger efficiency was measured. In order to avoid the trigger bias, the data acquired by the jet trigger is used. Figure 4.10 shows the trigger efficiency for the p_T threshold of 6 GeV as a function of p_T. The horizontal axis is the offline muon p_T, while the vertical axis is the trigger efficiency. The efficiency reaches its plateau at $p_T = 10$ GeV with its efficiency of 93.6%. The data points are fitted using the Fermi function which is defined as

$$f = \frac{A}{1 + \exp\left(-\frac{p_T - B}{C}\right)}, \tag{4.1}$$

where A is the plateau efficiency, B is the threshold and C is the resolution.

The result is slightly better than the original expectation of 93%, which is estimated based on the detector performance and the fraction of the dead region. This demonstrate that the success of the commissioning, especially the optimization of the threshold voltage and the applied high-voltage as well as the timing adjustment developed in this thesis. This achievement ensures

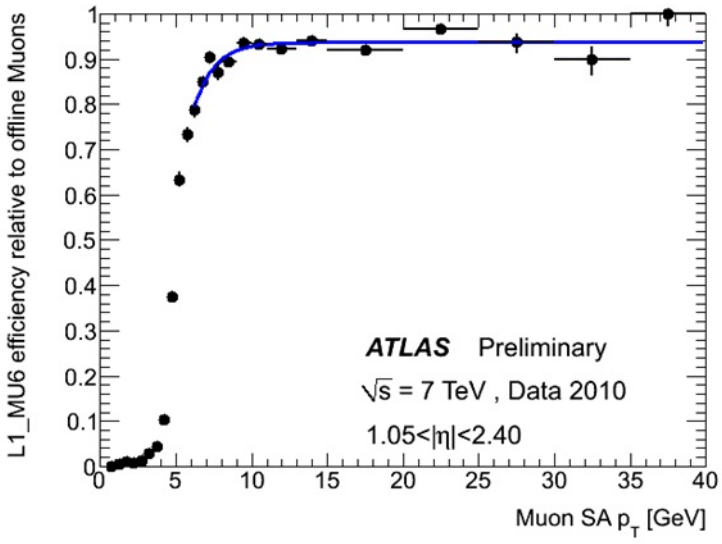

Figure 4.10: The turn-on curve of the muon trigger efficiency with p_T threshold of $p_T > 6$ GeV. 1

the application of the muon trigger for collecting the $t\bar{t}$ events including a lepton, and measure the production cross-section with high signal acceptance.

4.5 Development of the TGC monitoring system

Figure 4.11 shows the TGC monitoring tool, which has been developed to periodically monitor the detector condition and to spot any TGC-related issues (e.g, wrong electronics configuration, temporal power-glitch and the rapid trigger spike) as soon as possible. More than 1000 status registers from PP, SLB, SSW, HPT and SL modules are monitored every 30 seconds and, in case of the problems, alert the shifter about the problem as well as its prescription. There are mainly four categories that the monitoring tool pays attention:

Status of the TGC electronics All the status registers are checked every 30 seconds. The check result is displayed at the left-top window. If there are any problems to be noticed, alert the shifter and display the instructions at the bottom message window.

Trigger rate The trend of the TGC trigger rate is shown every 10 seconds. The shifter is notified if there is any suspicious trigger drops and spikes that could be caused by the beam condition and the power-glitch.

Luminosity Instantaneous luminosity is continuously monitored every 1 second and the correlations between the luminosity and the total trigger rate is shown, where one can expect the linear correlation. If it is not, it could be the signature of the problems such as the noisy channels disturbing the meaningful trigger or the temporal power-glitch.

Detector performance The relevant histograms can be checked to see the detector performance (Figure 4.11, right). For example, hit profiling, trigger timing, hit efficiency and the occupancy level can be monitored to find out any problematic signatures. This tool is used for the daily calibration to investigate noisy channels, dead channels, and trigger functionality during the beam injection. The operation parameters are tuned based on the result every day.

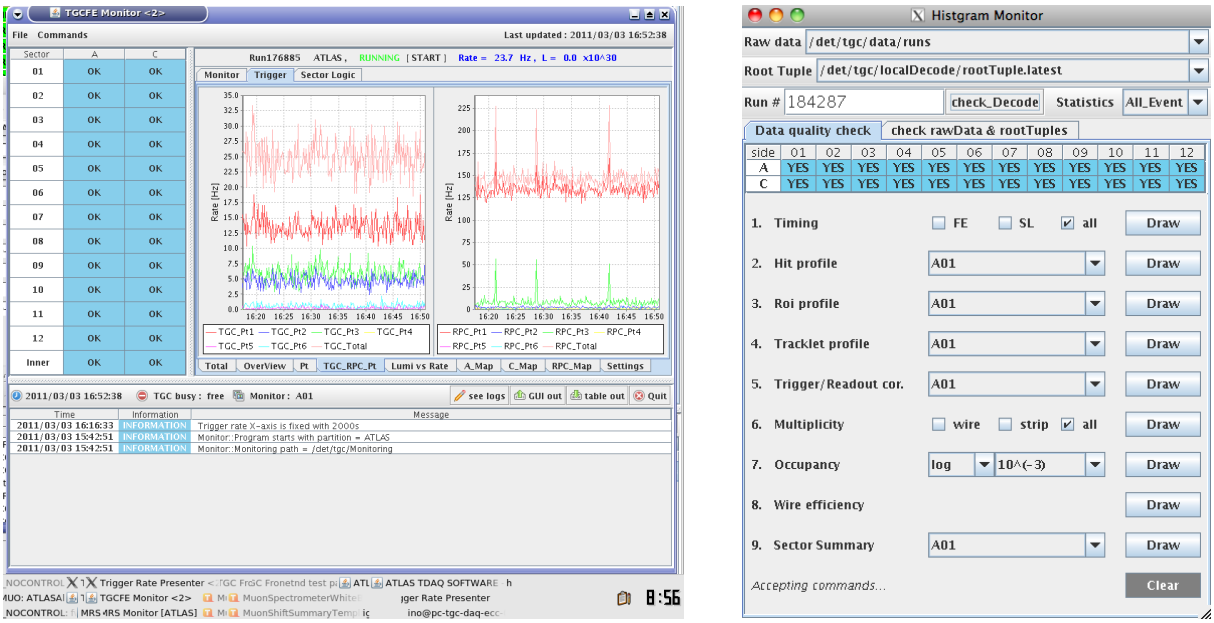

Figure 4.11: (Left) Example of the TGC monitoring panel, and (right) data quality monitor by which one can check the various histograms to see the detector performance.

The usage of the monitoring system has helped to minimize the loss time due to the TGC-related issues. The TGC operating efficiency during the physics data-taking in 2011 has been kept to be more than 98%, while overall data-taking efficiency of the ATLAS detector reaches more than 94% [23]. This helps to increase the available *pp* collision data and results in better statistics for all physics analysis that relies on the muon trigger.

Chapter 5

Measurement of the $t\bar{t}$ production cross-section using final states with a lepton and a hadronically decaying τ-lepton

5.1 Analysis overview

The $t\bar{t}$ production cross-section is measured using 2.05 fb^{-1} pp collision data accumulated by the ATLAS detector, from April to August in 2011. The analysis exploits the final states with a lepton and a hadronically decaying τ-lepton as is shown in Figure 5.1, which includes,

- $t\bar{t} \to W(\to \tau_{\rm had}\nu_\tau)W(\to \ell\nu_\ell)b\bar{b}$
- $t\bar{t} \to W(\to \tau_{\rm had}\nu_\tau)W(\to \tau(\to \ell\nu_\ell\nu_\tau)\nu_\tau)b\bar{b}$

where ℓ denotes an electron or a muon[1], and $\tau_{\rm had}$ denotes the hadronically decaying τ-lepton.

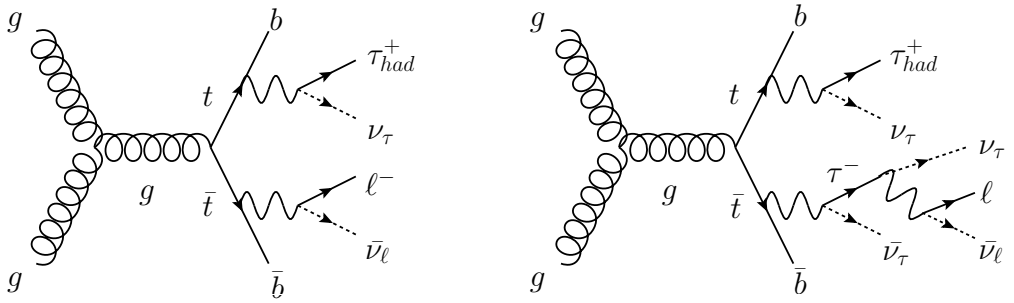

Figure 5.1: The diagrams of the $t\bar{t}$ events including a lepton and a hadronically decaying τ-lepton. These processes are treated as the signal events in the analysis.

[1]In the following thesis, the word lepton denotes an electron or a muon, unless otherwise mentioned.

Starting from single lepton triggers, a series of event selections are applied to extract candidate events based on the expected final topology: a lepton, a hadronically decaying τ candidate, more than two jets where at least one of them is identified as originating from the b-quark, and a large missing transverse energy (E_T^{miss}). For the remaining candidate events, the cross-section is calculated as

$$\sigma_{t\bar{t}} = \frac{N_{\text{data}} - N_{\text{background}}}{\mathcal{A}\mathcal{L}} \tag{5.1}$$

where,

- N_{data} : Number of events which pass the event selection
- $N_{\text{background}}$: Number of estimated backgrounds in N_{data}
- $\mathcal{A}$: Acceptance of the signal events including a branching ratio that the t-quark pair decays into τ and lepton pairs, and the detector efficiency (estimated by the simulation).
- $\mathcal{L}$: Integrated luminosity

The most essential aspects of the analysis is (1) to determine and optimize the event selection, by which statistically sufficient signals are expected against backgrounds and (2) to estimate the number of backgrounds ($N_{\text{background}}$) with lowest possible uncertainty. The background processes to be considered are shown in Figure 5.2. The appearance of the hadronically decaying τ-lepton is similar to that of the electromagnetic jet or the hadronic jet. Therefore, most of the background processes mimic the signal event either by jet faking τ candidate or by electron faking τ candidate. The former case is the majority. Table 5.1 categorizes background processes and its estimation method used in the analysis. The background processes coming from jet faking τ candidate is estimated in a data-driven way, while other backgrounds are estimated using corresponding MC simulation.

	background processes	estimation method
real lepton + jet faking τ	(a), (b)	data-driven
real lepton + electron faking τ	(d) (e)	MC
real lepton + real τ (irreducible)	(f), (g), (h)	MC
fake lepton + jet faking τ	(c)	data-driven

Table 5.1: Categorization of the background processes and the estimation method.

After the event selection, dominant background comes from $t\bar{t}$ events that decay into lepton plus jet ($t\bar{t} \to \ell^- \bar{\nu}_\ell q \bar{q} b \bar{b}$), where one of the jets is misidentified as the τ candidate. In order to isolate signal events against backgrounds, multivariate technique based on the boosted decision tree (BDT) is used, relying on its large separation power between signal and background. The number of signal events are extracted by fitting the distributions of the BDT output score to background and signal templates. The signal template is derived from the simulation, while the background template is derived from data in order to suppress the systematic uncertainty.

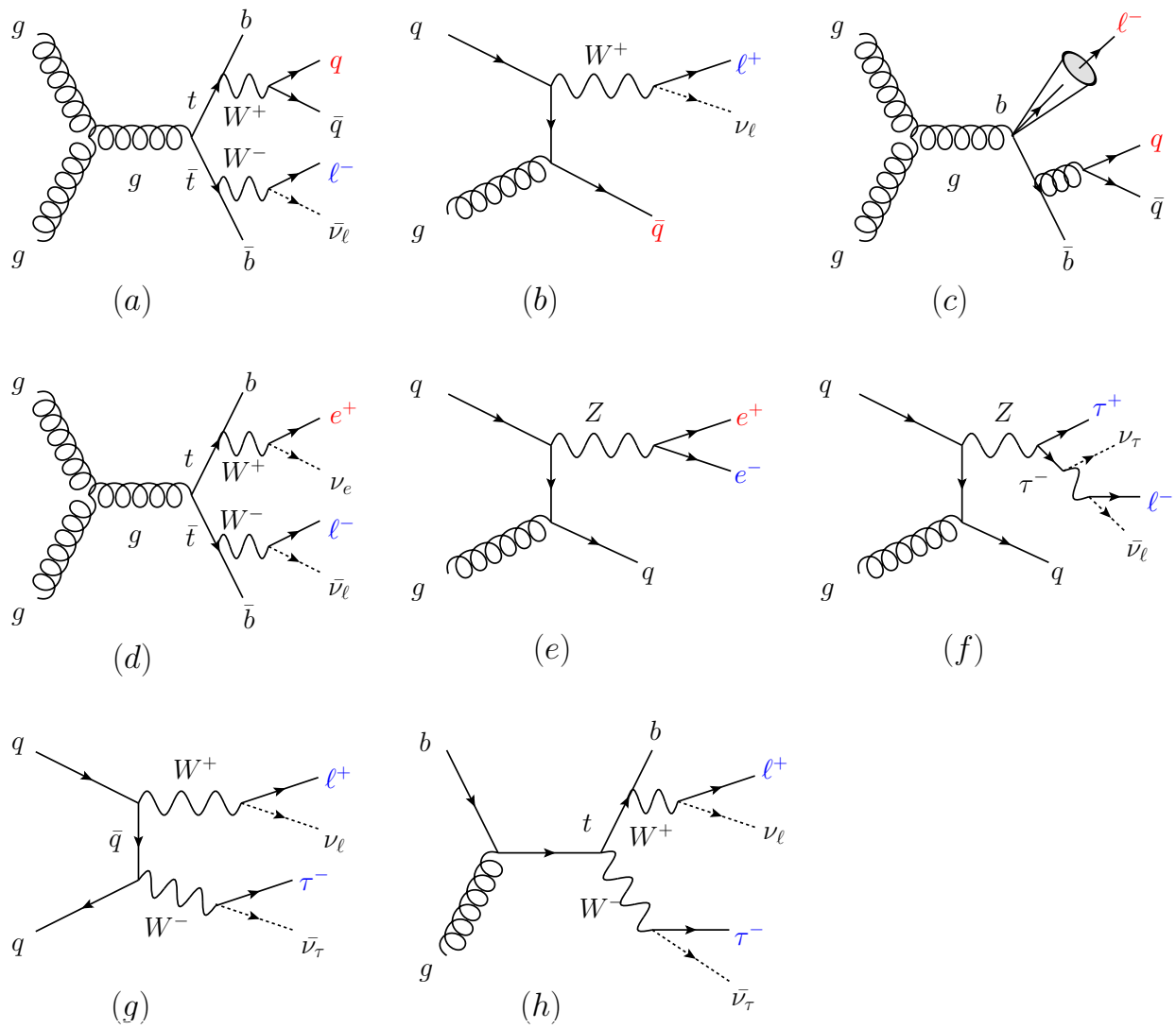

Figure 5.2: The dominant background processes to be considered in the analysis: (a) $t\bar{t}$ lepton plus jet ($t\bar{t} \to \ell^-\bar{\nu}_\ell q\bar{q}b\bar{b}$), ($b$) W+jet, (c) QCD multi-jet, (d) $t\bar{t}$ di-lepton ($t\bar{t} \to \ell^-\bar{\nu}_\ell\ell^+\bar{\nu}_\ell b\bar{b}$), ($e$) $Z(\to ee)$+jet, (f) $Z(\to \tau\tau)$+jet, (g) diboson (WW, WZ, ZZ), (h) single-top via the Wt production. Blue represents genuine objects, while red represents fake objects that possibly mimic the τ candidate.

In the remaining part of the thesis, three control regions are used to validate the analysis without the presence of signals. Table 5.2 summarizes its selection criteria, all of them are orthogonal to the event selection used for the signal extraction which is described in section 5.4.

In Table 5.2, N_{lepton} represents the number of lepton, $N_{\tau\text{ cand.}}$ is the number of τ candidate, N_{jet} denotes the number of jets, where all objects are defined in Section 5.3. M_T is the transverse

	Notation	N_{lepton}	$N_{\tau \text{ cand.}}$	N_{jet}	E_T^{miss}	M_T	$N_{b\text{-jet}}$
SR	≥ 1 b-tag	$= 1$	≥ 1	≥ 2	> 30 GeV		≥ 1
CR	0 b-tag	$= 1$	≥ 1	≥ 2	> 30 GeV		$= 0$
	$Z \to \tau_\ell \tau_{\text{had}}$	$= 1$	≥ 1	$= 0$		< 20 GeV	
	$W + 1$ fake τ	$= 1$	≥ 1	$= 0$		$40 - 100$ GeV	

Table 5.2: Definition of the signal region (SR) and the control region (CR).

mass between a lepton and E_T^{miss}, which is defined as,

$$M_T(\ell, E_T^{\text{miss}}) = \sqrt{(E_T^\ell + E_T^{\text{miss}})^2 - (p_x^\ell + E_x^{\text{miss}})^2 - (p_y^\ell + E_y^{\text{miss}})^2} \tag{5.2}$$

$$\cong \sqrt{2 p_T^\ell E_T^{\text{miss}} (1 - \cos \Delta\phi(\ell, E_T^{\text{miss}}))} \tag{5.3}$$

where E_T^ℓ and p_T^ℓ represent the energy and the momentum of the lepton. The second equation assumes the lepton mass ($m_\mu = 105$ MeV, $m_e = 0.5$ MeV) to be negligible compared to the p_T^ℓ and E_T^ℓ.

The 0 b-tag control region is used for the background modeling, as the events are kinematically close to the signal region. $Z \to \tau_\ell \tau_{\text{had}}$ control region (Figure 5.2, (f)) provides a plenty of genuine τ-leptons, and thus used to validate the signal modeling. On the other hand, $W + 1$ fake τ control region (Figure 5.2, (b)) provides a plenty of fake τ candidate that originated from the light-flavor (u, d, c, s) jet. This can be used to validate the background template used for the template fitting.

In the following sections, the data and the Monte Carlo simulation used in the analysis (Section 5.2), the object definition (Section 5.3), and the event selection (Section 5.4) are shown. The multivariate technique based on the Boosted Decision Tree is described in Section 5.5, followed by the background estimation method in Section 5.6. After describing the systematic uncertainty (Section 5.7), the measurement of the $t\bar{t}$ production cross-section is described in Section 5.8.

5.2 Datasets and the Monte Carlo simulation

5.2.1 Datasets and the luminosity calculation

The analysis exploits the pp collision data with a center-of-mass energy of $\sqrt{s} = 7$ TeV accumulated by the ATLAS detector from April to August in 2011. The data have been collected requiring single lepton triggers with p_T threshold of 20 GeV for the electron (22 GeV during periods of high instantaneous luminosity) and 18 GeV for the muon.

The segments of the data, known as the luminosity blocks, are used for the analysis if they were collected during periods in which the LHC was circulating stable colliding beams and all the detector components were producing data of sufficient quality. The latter ensures the reliability of the particle identification and the calculation of the missing transverse momentum, which is the signature of the undetected neutrino. Taking into account the luminosity block

selection, the total integrated luminosity was calculated to be 2.05 fb^{-1}. Figure 5.3 shows the integrated luminosity as a function of time.

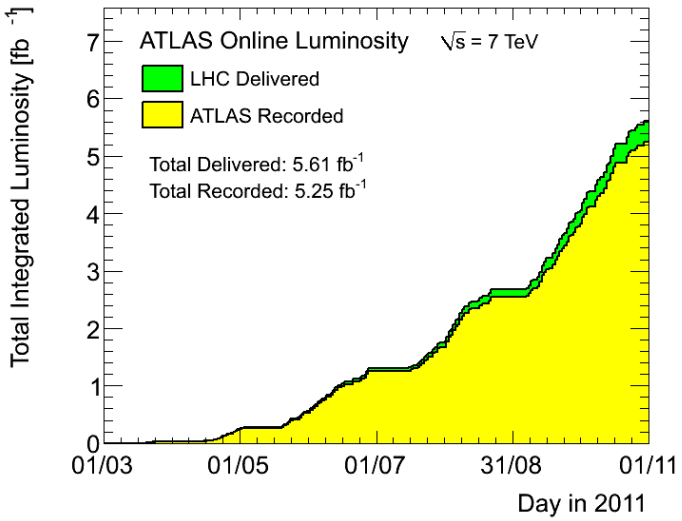

Figure 5.3: Total integrated luminosity as a function of time during 2011.

The integrated luminosity is calculated as the integral of the instantaneous luminosity over the given time. Suppose, ε is the detection efficiency including the geometrical acceptance, σ_{inel} is the cross-section of the inelastic scattering and μ is the average number of interactions per bunch crossing measured by the forward detector, the instantaneous luminosity ($\mathcal{L}$) satisfies,

$$\mu = \varepsilon \sigma_{\text{inel}} \mathcal{L}. \tag{5.4}$$

In principle, $\mathcal{L}$ can be calculated by evaluating ε and σ_{inel} from the simulation and μ from the detector in collision events. However, this requires to use the events in the extremely forward region and thus the understanding of ε and σ_{inel} leads to the large systematic uncertainty. Therefore, LHC adopts the van der Meer scan to measure the beam size in x, y plane (σ_x, σ_y) as well as the number of protons in each bunch (n_1, n_2) by using the current monitor. Given the equation,

$$\mathcal{L} = \frac{n_b f_r n_1 n_2}{2\pi \sigma_x \sigma_y}, \tag{5.5}$$

where n_b is the number of bunch and f_r is the beam circulating frequency (11.2 kHz), the luminosity is directly measured in this scan. By substituting the luminosity to equation (5.4), $\varepsilon\sigma_{\text{inel}}$ can be calculated beforehand in a data driven way. Since ε is mainly determined by the detector geometry and σ_{inel} is determined by the physics process, $\varepsilon\sigma_{\text{inel}}$ is almost constant with respect to the slight variations of the beam position. In this way, one can calculate the luminosity with an accuracy of 3.7%. The dominant uncertainty comes from the beam current measurement which accounts for 3.0% [24][25].

5.2.2 Monte Carlo simulation and the pile-up reweighting

In the following analysis, the Monte Carlo (MC) simulation are used for the following reasons:

- optimization of the event selection criteria
- estimation of the signal acceptance ($\mathcal{A}$)
- estimation of the number of backgrounds (see Table 5.1)

The $t\bar{t}$ events are simulated using MC@NLO event generator [26] with next-to-leading order (NLO) approximation, assuming the $t-$quark mass to be 172.5 GeV. The CTEQ6.6 [12] is used as the PDF[2], while the cross-section is normalized to the prediction of HATHOR (164.6^{+11}_{-16} pb), which employs the next-to-next-to-leading-order (NNLO) perturbative QCD calculation. The decay process of the τ-lepton is handled by the TAUOLA simulation [27].

The background processes such as W+jet, Z+jet and diboson (WW, WZ, ZZ) are modeled based on the ALPGEN generator [28] with leading order (LO) approximation. The cross-section of these processes are normalized to the NLO approximation. For the single-top events, MC@NLO event generator with NLO approximation is used [29] with its cross-section normalized to the NNLO approximation. The relevant parameters are summarized in Table 5.3.

process	event generator	approximation	PDF	σ (pb)
$t\bar{t}$	MC@NLO	NLO	CTEQ6.6	165
W+jet	ALPGEN	LO	CTEQ6L1	31452
Z+jet	ALPGEN	LO	CTEQ6L1	3218
diboson (WW, WZ, ZZ)	ALPGEN	LO	CTEQ6L1	70
single-top	MC@NLO	NLO	CTEQ6.6	85

Table 5.3: Summary of the MC simulation used in this analysis.

All the MC samples are processed by the standard ATLAS detector and trigger simulation, GEANT4 [30], and are subject to the reconstruction algorithms [31] as the data does. Due to the difficulty of the modeling for the QCD multi-jet background, it is estimated in a data-driven way, as is discussed in Section 5.4.3.

In addition to the simulated events described above, actual pp collision data also includes pile-up events, where additional pp collisions are observed due to the $\mathcal{O}(10^{11})$ protons per each bunch. At the instantaneous luminosity of $\mathcal{L} = 10^{33}$ (1/cm^{2}s), seven interactions are observed in average, which denote as $\langle\mu\rangle = 7$, while $\langle\mu\rangle = 25$ is expected at the designed luminosity of $\mathcal{L} = 10^{34}$ (1/cm^{2}s). The average number of interactions are calculated as,

$$\langle\mu\rangle = \frac{\mathcal{L}_{\text{inst}}\sigma_{\text{inel}}}{n_b f_r} \tag{5.6}$$

[2]The Coordinated Theoretical Experimental Project on QCD

where n_b is the number of proton bunches, f_r is the beam circulating frequency (11.2 kHz), $\mathcal{L}_{\text{inst}}$ is the instantaneous luminosity (equation (5.4)), and $\sigma_{\text{inel}} = 71.5$ mb is the total cross-section of the inelastic scatterings.

The effect of the pile-up events especially appear in the missing transverse momentum and the jet multiplicity. The missing transverse momentum is calculated based on the energy imbalance of all the detected particles. As the pile-up event increases, the number of detected particles will increase. Since the resolution of the E_T^{miss} is proportional to the squared root of the number of detected particles in the event, this leads to the smearing of the E_T^{miss} distribution. The effect is particularly strong for those processes with intrinsically no neutrino and small jet multiplicity, such as $Z \to \ell\ell$ and di-jet events. The pile-up effect need to be correctly taken into account by the MC simulation to have a reasonable agreement with data enough to rely on the MC simulation for the signal acceptance calculation and part of the background estimations.

In order to accommodate with possible range of the pile-up events, MC simulations were made with additional inelastic scatterings ($0 < \langle\mu\rangle < 18$) randomly overlaid to the simulated hard process. The MC simulation were then re-weighted to reproduce the $\langle\mu\rangle$ distribution in data and its weighting factor is applied event by event basis. This technique is called as the pile-up reweighting. Figure 5.4 shows the comparison of the $\langle\mu\rangle$ distribution between data and the MC simulation.

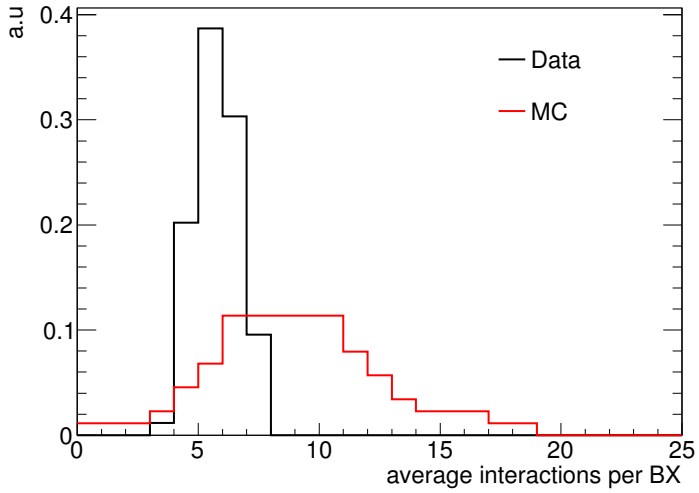

Figure 5.4: Average interactions per bunch crossing ($\langle\mu\rangle$) for the MC simulation (red) and the Data (black). The data distribution is derived at the instantaneous luminosity of $\mathcal{L} \sim 10^{33}$ $(1/\text{cm}^2\text{s})$.

Figure 5.5 shows the comparison of the missing transverse momentum and the jet multiplicity distribution before and after the pile-up reweighting, respectively. Both distributions are derived from data where two oppositely signed charge muons are required with its invariant mass within the mass window of the Z boson ($81 < m_{\mu\mu} < 101$ GeV). According to the MC simulation, one can obtain almost pure $Z \to \mu\mu$ sample, with its purity more than 99.8%. Since the MC simulation is overlaid with more pile-up effect, as shown in figure 5.4, the higher

jet multiplicity and more smeared E_T^{miss} distribution are observed without any reweighting. By applying the pile-up reweighting, both distributions are in decent agreement between data and MC simulation.

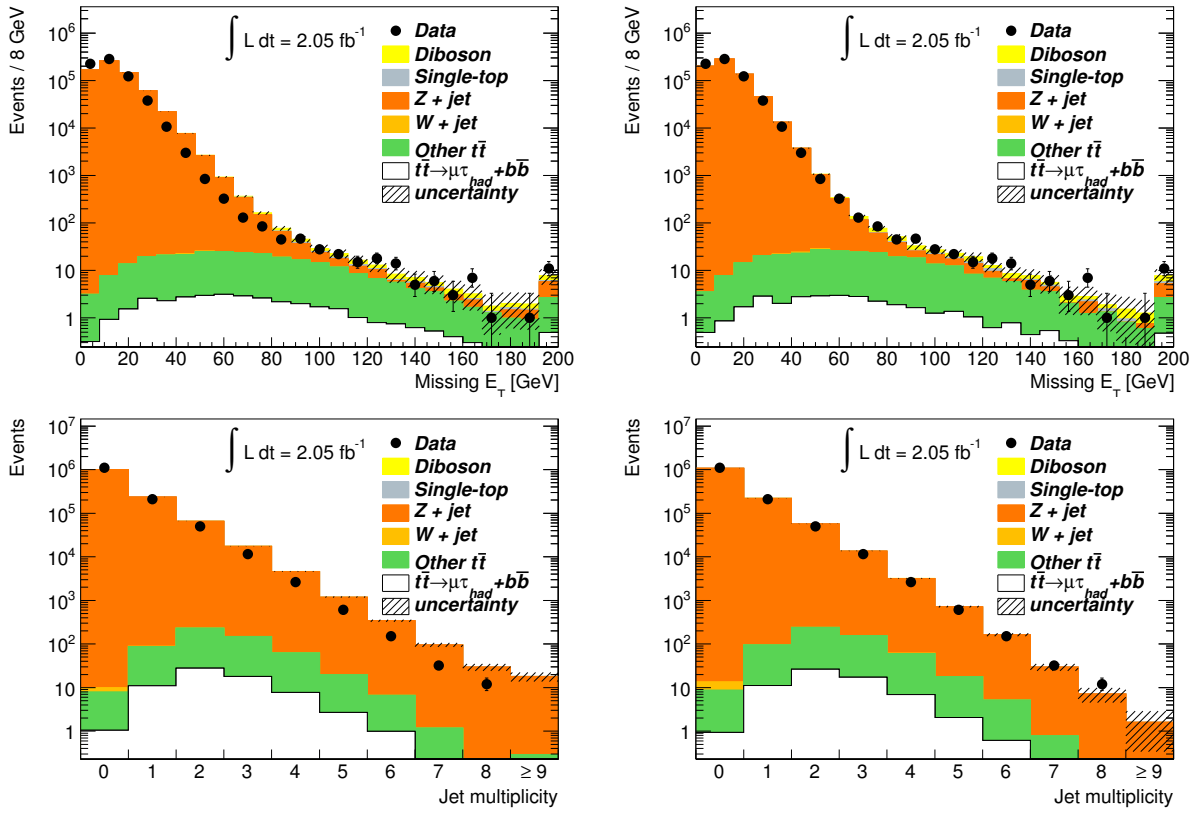

Figure 5.5: Missing transverse momentum (top) and jet multiplicity (bottom) distribution in $Z \to \mu\mu$ control region, (left) before and (right) after the pile-up reweighting.

5.3 Object Definition

Particles such as electron, muon, hadronically decaying τ-lepton, hadronic jets, b-tagged jets, and the missing transverse momentum are defined starting from the reconstructed object described in Section 3.3. Figure 5.6 shows an example of the appearance for the electron, muon, hadronically decaying τ-lepton and hadronic jet which passes the object definition described in this section.

5.3.1 Muon identification

Muon candidates are reconstructed based on the track information from the MDT. To ensure the track coming from collisions, they are combined with tracks found in the inner tracker taking into account the magnetic field and energy loss in the calorimeter which is typically 3 GeV.

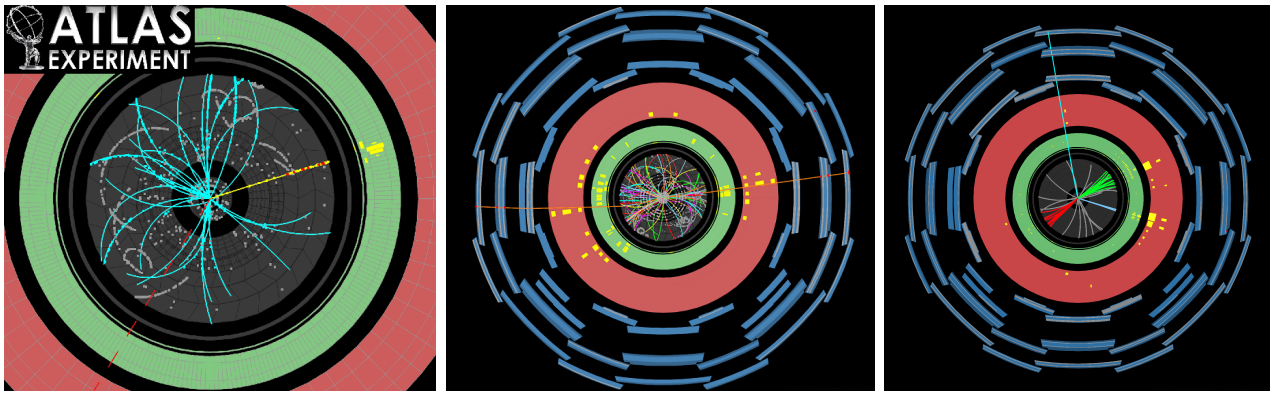

Figure 5.6: Typical appearance of the electron (left, yellow line), muon (middle, orange line), hadronic jet (right, green line) and the hadronically decaying τ-lepton (right, light blue line).

Those muon candidates are refitted using the complete track information from the MDT and the inner tracker. It is required to satisfy $p_T > 20$ GeV and $|\eta| < 2.5$, where the p_T threshold is determined so that the trigger efficiency reaches its plateau region.

In order to reject muons coming from heavy flavour decays (such as b baryon and meson decays through $b \to Wc \to \mu\nu c$ and π/K decays in flight), energy deposit in the calorimeter around the muon candidate in $\Delta R < 0.3$ is required to be less than 4 GeV. ΔR is the distance between two objects defined in η-ϕ plane,

$$\Delta R = \sqrt{\Delta\phi^2 + \Delta\eta^2} \tag{5.7}$$

The definition of R in terms of $\Delta\eta$ (not $\Delta\theta$) ensures the invariance under the longitudinal boosts. Similarly, the sum of the track transverse momenta with $p_T > 1$ GeV in $\Delta R < 0.3$ region is required to satisfy less than 4 GeV. The muon candidate is rejected if it overlaps with any jets with $p_T > 20$ GeV in $\Delta R < 0.4$.

5.3.2 Electron identification

Electron candidates are required to be $p_T > 25$ GeV and $|\eta_{\text{cluster}}| < 2.47$. In order to avoid the fake electrons, the barrel-endcap transition region of $1.37 < |\eta_{\text{cluster}}| < 1.52$ are excluded, where η_{cluster} is the pseudo-rapidity of the energy cluster associated with the candidate. In order to avoid electrons coming from jets, and semi-leptonic b decay, the transverse energy deposited in the calorimeter which is not associated to the electron candidate in $\Delta R < 0.2$ is required to be less than 3.5 GeV. The electron identification efficiency is about 75%, depending on the E_T and η of the reconstructed electron.

5.3.3 Jet identification

The hadronic jet is reconstructed with anti-k_t algorithm [20] (Section 3.3.2) with distance parameter of $R = 0.4$ starting from electromagnetic energy clusters. The jet candidates are calibrated as a function of p_T and η based on the MC simulation to restore full hadronic energy

scale. Jets are required to have $p_T > 25$ GeV, $|\eta| < 2.5$ and removed if they include electron candidate within $\Delta R < 0.4$. The p_T threshold has been optimized to be robust for the pile-up effect.

5.3.4 b-jet identification

The analysis cuts on the output score of the b-tagger described in section 3.4.5 to accept b-jets with approximately 70% efficiency in $t\bar{t}$ decays. The rejection, which is the reciprocal of the identification efficiency, for the light-flavor (u, d, c, s and gluon) jets [32] is estimated to be 99. Figure 5.7 shows the rejection against the light-flavor jet as a function of the b-tagging efficiency for several tagging algorithms for the simulated $t\bar{t}$ events.

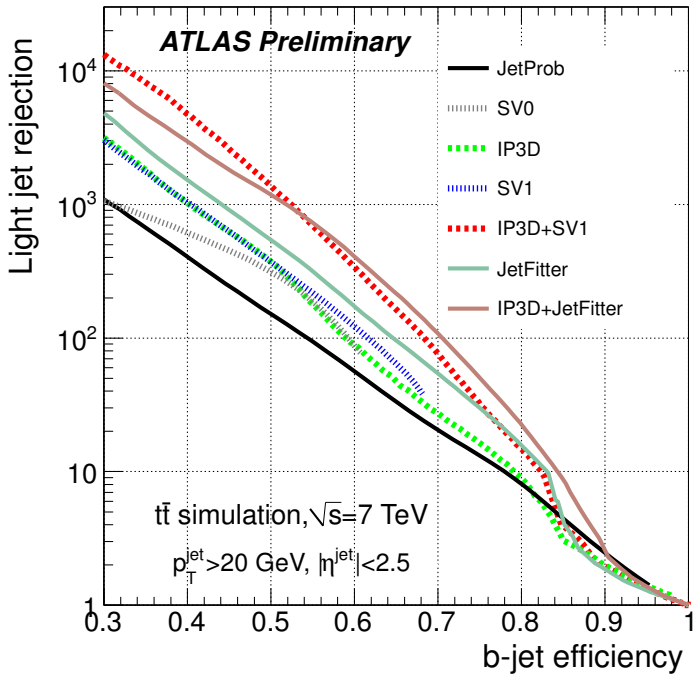

Figure 5.7: Light jet rejection as a function of the b-tagging efficiency. IP3D+JetFitter is used (Ocher line).

5.3.5 Missing transverse momentum

The missing transverse momentum is used as the signature of an undetected neutrino. The quantity is calculated based on the energy imbalance in a transverse plane, since $\sum p_T = 0$ is satisfied at the beginning of the collision. All the detected particles such as leptons (e, μ), jets (including low p_T jets, called soft-jet), and energy deposit not associated with any reconstructed objects (called cellout) in $|\eta| < 4.5$ are all considered for the calculation. Contributions from

muons passing selection requirements are included, while contributions of any calorimeter cells associated with the muon is removed. The definition is,

$$E_{T,x}^{\mathrm{miss}} = -\left(\sum_{\mathrm{electron}} p_{T,x} + \sum_{\mathrm{muon}} p_{T,x} + \sum_{\mathrm{jets}} p_{T,x} + \sum_{\mathrm{soft\ jets}} p_{T,x} + \sum_{\mathrm{cellout}} E_{T,x} \right) \tag{5.8}$$

$$E_{T,y}^{\mathrm{miss}} = -\left(\sum_{\mathrm{electron}} p_{T,y} + \sum_{\mathrm{muon}} p_{T,y} + \sum_{\mathrm{jets}} p_{T,y} + \sum_{\mathrm{soft\ jets}} p_{T,y} + \sum_{\mathrm{cellout}} E_{T,y} \right) \tag{5.9}$$

$$E_{T}^{\mathrm{miss}} = \sqrt{(E_{T,x}^{\mathrm{miss}})^2 + (E_{T,y}^{\mathrm{miss}})^2} \tag{5.10}$$

5.3.6 τ candidate

As is described in Section 3.4.6, the reconstruction of the τ-lepton only focuses on its hadronic decay. Since, the hadronically decaying τ-lepton has an intermediate characteristics between electromagnetic jets and hadronic (quark, gluon originated) jets, a large number of fake τ are expected from electrons or jets. At the object definition stage, following loose selections are applied on the reconstructed jets. The jet that satisfied these requirements are called as the τ candidate.

- $p_T > 20$ GeV, $|\eta| < 2.3$
- the number of charged tracks in $\Delta R < 0.4$ around the jet axis (N_{trk}) is required to be $0 < N_{\mathrm{trk}} < 4$
- leading track inside the jet is required to have $p_T > 4$ GeV.
- If there are muons with $p_T > 4$ GeV or electrons with $p_T > 15$ GeV within $\Delta R < 0.4$, the candidates are removed
- If there are b-jets within $\Delta R < 0.4$, the candidates are removed.

Figure 5.8 shows the track multiplicity and the leading track p_T distribution in the $t\bar{t}$ events, separately shown for the real τ-lepton (blue) and the jets faking τ candidate (red).

As is later described in Section 5.5, multivariate technique based on the Boosted Decision Tree (BDT) is introduced [33] to further discriminate τ candidate against electrons (BDT_e) and quark, gluon originated jets (BDT_j).

5.4 Event selection

The event selection aims to extract signal events, with its amount statistically sufficient against backgrounds.

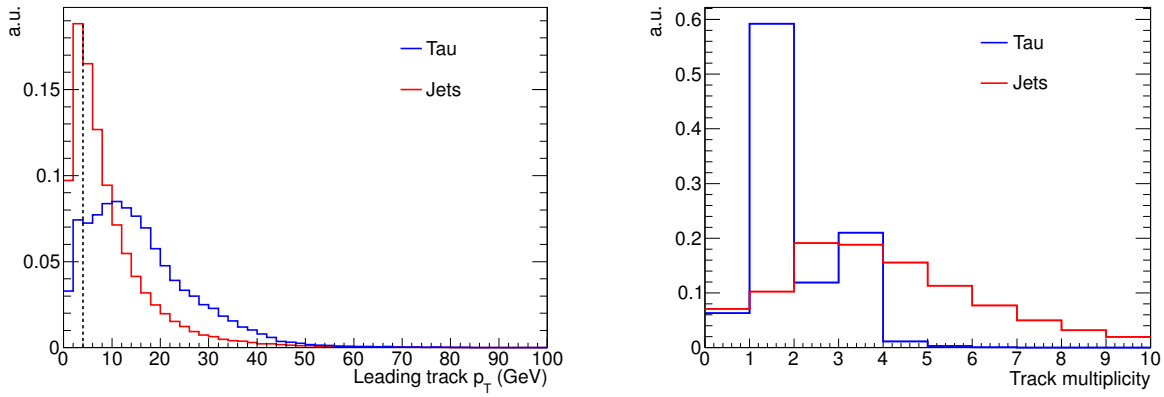

Figure 5.8: (Left) The leading track p_T distribution and (right) the track multiplicity distribution of the τ candidate.

5.4.1 Event cleaning cuts

Before the event selection, event cleaning cuts are applied to raise the reliability of the events. In particular, events with spurious E_T^{miss}, arising from the detector effects and the cosmic ray muons are rejected.

Non-collision background rejection In order to ensure the event coming from the collision, events are required to have a primary vertex with at least five tracks within $z < 150$ mm. The primary vertex is reconstructed from tracks in the inner tracker with $p_T > 150$ MeV, $|d_0| < 4$ mm, $\sigma(d_0) < 5$ mm, $\sigma(z_0) < 10$ mm, more than 4 hits in the SCT, and more than 6 hits in the pixel and the SCT.

Hadron Endcap Calorimeter noise Single cell at the hadron endcap calorimeter is known to generate continuous noise. This can be eliminated by requiring number of cells that account for 90% of the jet energy ($n90$) is more or equal to 6, and the energy fraction in the hadronic endcap calorimeter is less than 0.8.

LAr coherent noise LAr calorimeter sometimes issues the coherent noise which leads to the significantly large E_T^{miss}. If there are any jets with the fraction of jet energy from bad-quality calorimeter cells is larger than 0.8 or the energy fraction in the EM calorimeter is larger than 0.95, events are rejected.

Cosmic ray muons The cosmic ray muon causes bremsstrahlung at the calorimeter and deposits high$-p_T$ jets, which mimic like a mono-jet event. The event rate generating $p_T >$ 100 GeV jet is an order of 0.1 Hz. This is eliminated by requiring no associated tracks along the cluster and that the fraction of the energy deposit between HCAL and ECAL is small. In addition, a jet is required to have the calorimeter deposits within 50 ns after the collision

timing, in order to remove out-of-time energy depositions in the calorimeter such as the cosmic ray muons.

Beam halo The beam halo is an event caused by the secondary particle generated from the (in)elastic scattering between the proton beam and the residual gas in the beam pipe. This is eliminated by requiring no associated tracks along the cluster.

Figure 5.9 shows the examples of the above-mentioned events in ρ-z plane of the cylindrical coordinates.

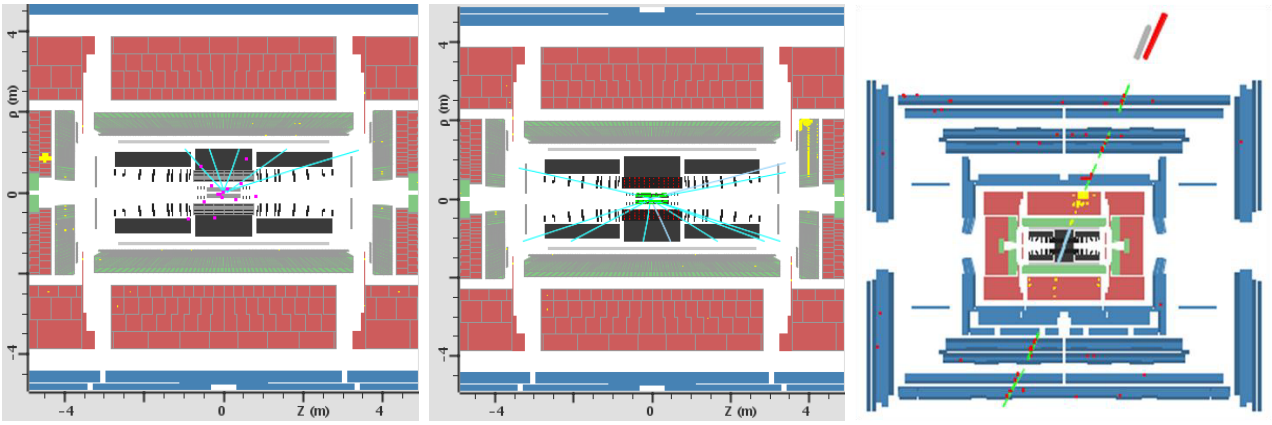

Figure 5.9: (Left) Example of the hadron endcap calorimeter noise. There is a single cell firing at the endcap region shown in the yellow color. (Middle) Example of an event containing a LAr coherent noise, where several clusters generating a noise in the endcap region at the right-hand side. (Right) A candidate event generated by a cosmic ray muon.

5.4.2 Event selection

Starting from single lepton triggers with p_T threshold of 18 GeV for the muon and 20 GeV (22 GeV during the data-taking period with high instantaneous luminosity) for the electron, event selection is applied based on the expected signal topology.

- Exactly one isolated muon (denote as muon channel) or electron (electron channel)
- ≥ 1 τ candidate
- ≥ 2 jets, not overlapping with any τ candidates
- $E_T^{\text{miss}} > 30$ GeV
- The scaler sum of p_T (H_T) for all the visible objects and the missing transverse momentum, defined as,

$$H_T + |\vec{E_T^{\text{miss}}}| = \sum_{\text{lepton}} |\vec{p}_T| + \sum_{\tau \text{ cand.}} |\vec{p}_T| + \sum_{\text{jets}} |\vec{p}_T| + |\vec{E_T^{\text{miss}}}|, \tag{5.11}$$

is required to be $H_T + |\vec{E}_T^{\rm miss}| > 200$ GeV

- At least one b-tagged jet

The cut thresholds for the jet p_T, $E_T^{\rm miss}$, H_T and b-tagging are optimized based on the MC simulation to maximize the signal significance $S/\sqrt{S+B}$, where S is the number of signals, and B is the number of backgrounds. The example of the optimization result can be found in [D.1].

Table 5.4 (muon channel) and Table 5.5 (electron channel) shows the event yield at each stage of the event selection after requiring one lepton and one τ candidate. The numbers are separately shown for the 1prong (τ_1) and the multi prong (τ_3). The numbers except for the data and the QCD multi-jet are derived from the MC simulation, while the QCD multi-jet event is estimated in a data-driven way as described in the next section. After the event selection, more than 70% of the events are expected to come from $t\bar{t}$ process, while 20% of them come from W+jet and 6% come from single-top process. The data and the MC prediction are in decent agreement.

Cut (τ_1)	$t\bar{t}(\mu,\tau)$	$t\bar{t}(\ell+\text{jets})$	$t\bar{t}(\ell\ell')$	W+jets	Z+jets	Wt	Diboson	QCD	Total	Data
$N_{\rm jet} \geq 2$	673 ± 6	3017 ± 12	139 ± 3	13179 ± 140	2265 ± 35	378 ± 8	287 ± 9	9061	28999 ± 146	28114
$E_T^{\rm miss}$	584 ± 5	2418 ± 11	126 ± 3	9428 ± 114	1003 ± 24	302 ± 7	203 ± 8	2175	16239 ± 118	15624
H_T	578 ± 5	2405 ± 11	125 ± 3	7896 ± 93	808 ± 21	289 ± 7	177 ± 7	1269	13547 ± 97	12954
≥ 1 b-jet	498 ± 5	1988 ± 10	100 ± 2	552 ± 20	55 ± 6	204 ± 6	16 ± 2	263	3677 ± 25	3804
Cut (τ_3)	$t\bar{t}(\mu,\tau)$	$t\bar{t}(\ell+\text{jets})$	$t\bar{t}(\ell\ell')$	W+jets	Z+jets	Wt	Diboson	QCD	Total	Data
$N_{\rm jet} \geq 2$	501 ± 5	7359 ± 19	425 ± 5	33893 ± 228	3916 ± 46	891 ± 13	568 ± 13	25915	73468 ± 234	70909
$E_T^{\rm miss}$	441 ± 5	5899 ± 17	383 ± 4	24443 ± 185	1597 ± 29	705 ± 11	397 ± 11	5512	39376 ± 189	38981
H_T	435 ± 5	5864 ± 17	380 ± 4	20838 ± 151	1348 ± 27	679 ± 11	347 ± 10	3017	32910 ± 155	32901
≥ 1 b-jet	364 ± 4	4878 ± 16	305 ± 4	1603 ± 35	107 ± 8	477 ± 9	42 ± 3	865	8641 ± 41	9386

Table 5.4: The event yield in the muon channel for τ_1 (top four column) and for τ_3 (bottom four column) candidate. $t\bar{t}(\ell\ell')$ is $t\bar{t} \to \ell + \ell$ channel with only one lepton reconstructed as a lepton and a lepton or jet reconstructed as a τ candidate. The errors are the statistical uncertainties.

Cut (τ_1)	$t\bar{t}(e,\tau)$	$t\bar{t}(\ell+\text{jets})$	$t\bar{t}(\ell\ell')$	W+jets	Z+jets	Wt	Diboson	QCD	Total	Data
$N_{\rm jet} \geq 2$	610 ± 6	2741 ± 12	123 ± 3	10358 ± 120	4010 ± 47	343 ± 8	270 ± 8	11295	29749 ± 131	29333
$E_T^{\rm miss}$	526 ± 5	2145 ± 10	111 ± 2	6997 ± 97	1405 ± 28	255 ± 7	166 ± 7	2685	14289 ± 102	14052
H_T	521 ± 5	2135 ± 10	110 ± 2	5907 ± 72	1240 ± 26	247 ± 6	148 ± 6	1761	12069 ± 78	11957
≥ 1 b-jet	447 ± 5	1761 ± 9	87 ± 2	423 ± 16	68 ± 6	172 ± 5	14 ± 2	300	3272 ± 21	3384
Cut (τ_3)	$t\bar{t}(e,\tau)$	$t\bar{t}(\ell+\text{jets})$	$t\bar{t}(\ell\ell')$	W+jets	Z+jets	Wt	Diboson	QCD	Total	Data
$N_{\rm jet} \geq 2$	459 ± 5	6697 ± 19	391 ± 5	27341 ± 212	8343 ± 69	840 ± 12	537 ± 12	35562	80170 ± 225	73547
$E_T^{\rm miss}$	401 ± 5	5244 ± 16	347 ± 4	18631 ± 170	2674 ± 38	638 ± 11	328 ± 10	8418	36682 ± 176	34498
H_T	397 ± 4	5220 ± 16	346 ± 4	16327 ± 148	2468 ± 37	622 ± 11	294 ± 9	5872	31544 ± 154	29962
≥ 1 b-jet	335 ± 4	4346 ± 15	274 ± 4	1346 ± 36	155 ± 9	438 ± 9	32 ± 3	1296	8220 ± 42	8225

Table 5.5: The event yield in the electron channel (detail in the caption in Table 5.4).

5.4.3 The modeling of the QCD multi-jet events

The QCD multi-jet events (denote as QCD events) arise from the inelastic scattering via the strong interaction. The total cross-section is an order of $\mathcal{O}(100)$ mb, which is nine order

of magnitudes larger than the $t\bar{t}$ production process. Owing to its large cross-section, the estimation of the QCD process is necessary, although it is largely rejected by the event selections described in the previous section. Given the fact that the most of the QCD events have a small Q^2, i.e, large strong coupling constant, quantitative prediction of its production rate based on the perturbative QCD is rather difficult. Therefore, QCD events are estimated in a data driven way as followings:

1. At each stage of the event selection, control samples are derived by inverting the lepton isolation requirement. In case of the muon channel, events are selected by requiring the energy deposit around the muon candidate is greater than 4 GeV or the sum of the track p_T is greater than 4 GeV in $\Delta R < 0.3$. In case of the electron channel, the transverse energy deposit in the calorimeter which is not associated to the electron candidate in $\Delta R < 0.2$ is required to be greater than 4 GeV. This sample is called as the non-isolated sample, and dominated by the QCD multi-jet events.

2. Small contributions from other SM processes (2-3%) are subtracted based on the MC simulation.

3. The number of QCD events are estimated by fitting the $M_T(\ell, E_T^{\rm miss})$ distribution in the signal region with the M_T distribution derived from the non-isolated sample and the other SM processes in the signal region, which is derived from the MC simulation.

The M_T distribution provides a good separation power between the QCD multi-jet events and the other SM processes. The QCD events tend to distribute at the lower values of M_T, while the other SM processes including a W boson tend to have a peak around W boson mass. Figure 5.10 (left) shows the M_T distribution derived from the non-isolated sample (muon channel, τ_1 candidate) and Figure 5.10 (right) shows the result of the fitting. Both distributions are derived after all the event selection were applied.

The estimated number of QCD events at each stage of the event selection are shown in Table 5.4 and Table 5.5, as well. The contributions from the QCD events are estimated to be 7% for the τ_1 candidate and 10% for the τ_3 candidate at the end of the event selection. However, as will be later described in section 5.6, the same-sign (SS) events, the charge correlation between the τ candidate and the lepton is negative ($Q_\tau Q_\ell < 0$), is subtracted from the opposite-sign (OS) events ($Q_\tau Q_\ell > 0$) to remove part of the backgrounds, and to estimate number of backgrounds in a data-driven way. Since the QCD events are not correlated with the lepton charge (charge symmetric), QCD events are largely rejected by this operation and are reduced to a negligible level, which is estimated to be less than 3%.

5.4.4 Data and MC comparison

In order to see the validity of the event selection and the reliability of the MC simulation, Figure 5.11 and Figure 5.12 shows the $E_T^{\rm miss}$ distribution before the $E_T^{\rm miss}$ cut, H_T distribution before the H_T cut, and M_T distribution after the b-tagging in τ_1 and τ_3 candidate, respectively. All the distributions except for the QCD multi-jet events only include statistical uncertainty.

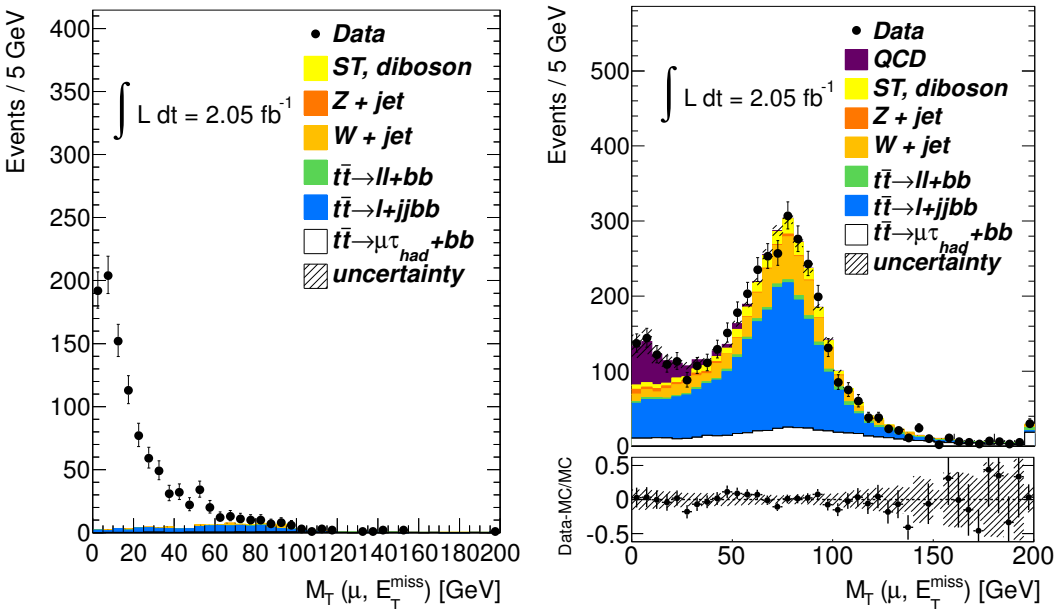

Figure 5.10: (Left) M_T distribution in the non-isolated sample after all the event selection is applied. (right) Fitting result based on the M_T distribution by means of the M_T distribution in the non-isolated sample and the other SM processes in the signal region, which is derived from the MC simulation.

Since there are no guarantees that the distribution derived from the non-isolated sample is identical to that of the isolated sample, 30% uncertainty is assigned, based on the study for the mis-identified lepton backgrounds in $t\bar{t}$ events [34]. Within the uncertainty, data and MC simulation shows a decent agreement.

The dominant background comes from the QCD multi-jet events (purple) before the $E_T^{\rm miss}$ requirement, and W+jet events (orange) before the b-tagging, and $t\bar{t}$ lepton plus jet events (blue) in the end of the event selection ($>$ 70% contributions). Most of the backgrounds come from jets miss-identified as τ candidate, while small fraction of events from electrons miss-identified as τ candidate. The S/N ratio is 0.15 for the τ_1 candidate and 0.05 for the τ_3 candidate.

5.5 Development of the Boosted Decision Tree

In order to separate signal events from backgrounds, the analysis exploits the multivariate technique based on the Boosted Decision Tree (BDT) as the tight discriminant. For the background processes coming from electrons faking τ candidate, BDT$_e$ discriminant is developed and the cut is applied. For the background processes coming from jets faking τ candidate, BDT$_j$ is developed, followed by the template fit to the BDT$_j$ distribution by the signal and the background template.

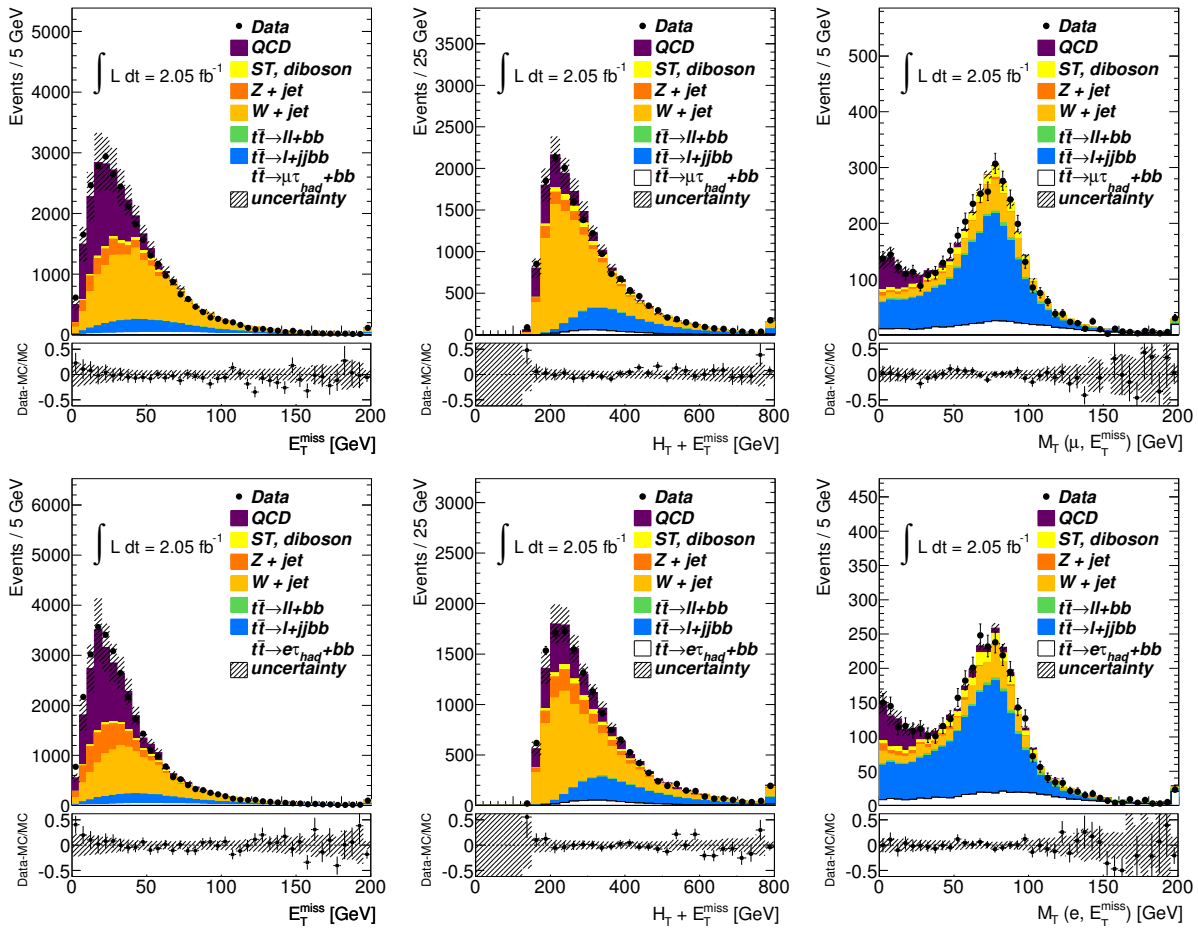

Figure 5.11: (From left to right) E_T^{miss}, H_T and M_T distribution in the muon (top) and the electron (bottom) channel in τ_1 candidates. Black points show data, and other colored histogram represents MC simulation. QCD events (purple) are estimated in a data-driven way. The bottom plot shows (Data − MC) / MC, demonstrating a good agreement between data and MC simulation.

5.5.1 Boosted Decision Tree

The decision tree [35][36][37] is one of the classification algorithm. By applying recursive cuts on a set of identification variables, events are classified with the output score from 0 (background-like) to 1 (signal-like). Unlikely to the simple cut, the decision tree does not discard the events, but continues by determining cuts on other variables to save the signal events which did not pass the selection.

The decision tree is firstly trained using a sample of known composition, so-called the training sample. Starting from the entire training samples at the root node, the optimal cut which separates signals from backgrounds is determined separately for each variable. The best cut among these optimal cuts is chosen and two child nodes are constructed as a consequence. The same thing is applied recursively on each child node, which results in a binary tree structure

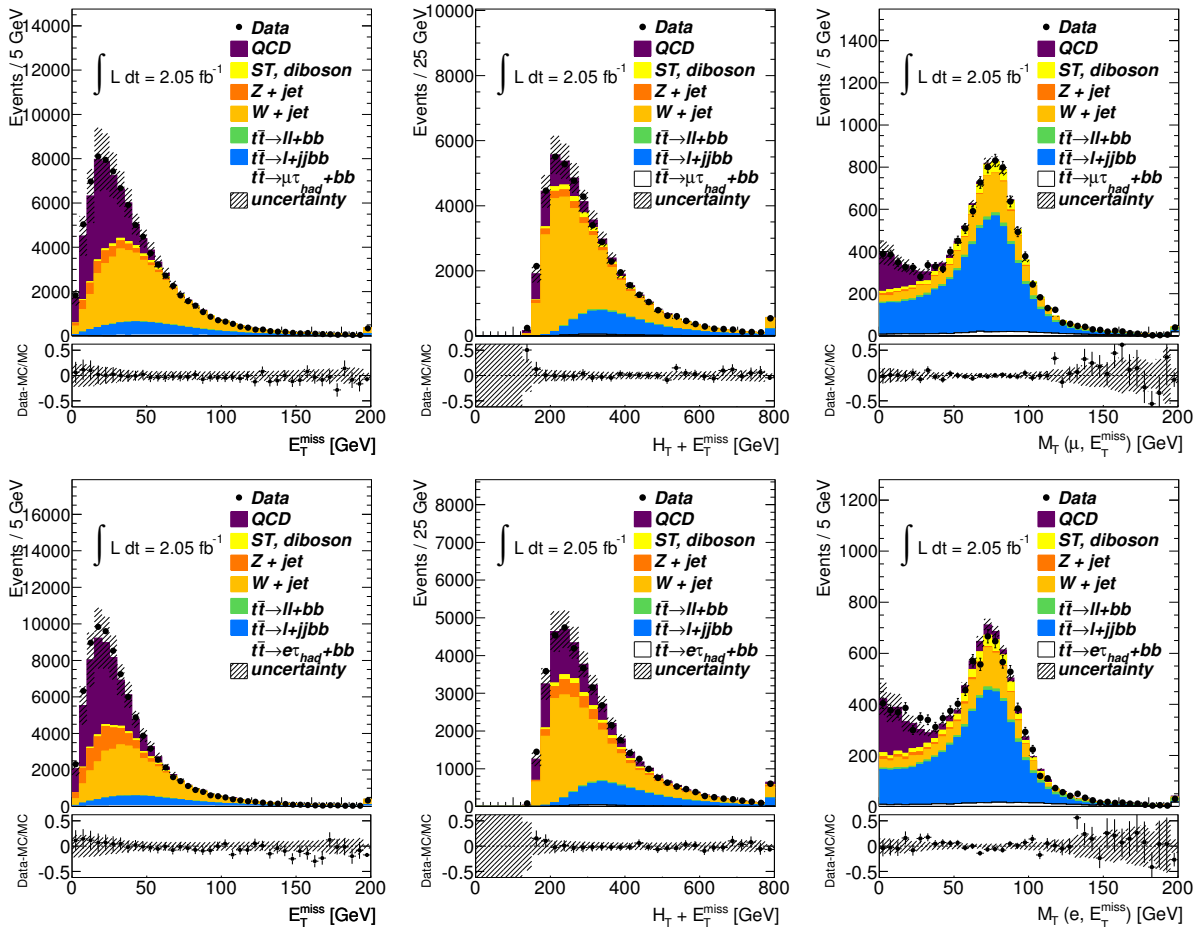

Figure 5.12: Same distribution in τ_3 candidates (detail in the caption in Figure 5.11).

as is shown in Figure 5.13.

The cut value is optimized at each node based on the Gini index. Suppose the signal purity p defined as $p = N_{\rm sig}/(N_{\rm sig} + N_{\rm bkg})$, where $N_{\rm sig}$ and $N_{\rm bkg}$ represents the number of signal and background at each node, Gini index $i^{\rm node}_{\rm Gini}$ is defined as

$$i^{\rm node}_{\rm Gini} = p(1-p) = \frac{N_{\rm sig}N_{\rm bkg}}{(N_{\rm sig}+N_{\rm bkg})^2} \tag{5.12}$$

The optimal cut is determined to minimize $i^{\rm node}_{\rm Gini}$. This will maximize the background purity $(1-p)$ on one side of the cut, while maximizing the signal purity p on the other side of the cut. This recursive splitting process continues until any split results in the child node containing less than certain events. The terminated node is called as a leaf node. The score assigned to the event by the decision tree is simply the purity p of the leaf node at which the event lands on. The more signal-like an object is, the closer its score to be one.

In order to improve the stability and the performance of the decision tree, Boosted Decision Tree (BDT) technique is used in this analysis. BDT increases the weight of the miss-classified

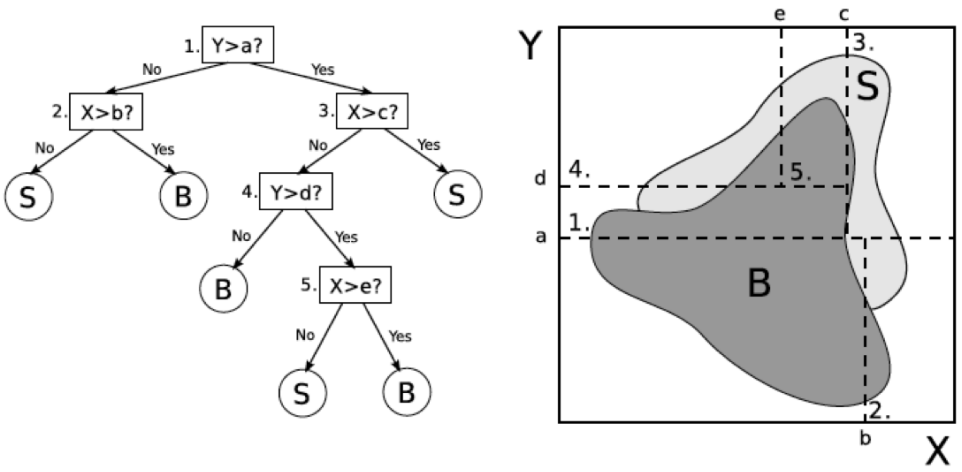

Figure 5.13: A simple example of the decision tree training process in case of two distributions labelled as signal (S) and background (B) over two variables X and Y. The process begins at **1** by determining the best cut value of the best variable to cut on, which in this case is $Y > a$. All objects with $Y > a$ are passed to the right and all objects with $Y < a$ are passed to the left. This process continues recursively until a stopping condition is satisfied.

events and suppresses the weight of the correctly classified events in the initial decision tree and a second decision tree is constructed using these new weights. The weight α_m at m^{th} decision tree is given by

$$\alpha_m = \beta \ln\left(\frac{1-\varepsilon_m}{\varepsilon_m}\right) \quad \text{where} \quad \varepsilon_m = \frac{N_{\text{miss-classified}}}{N_{\text{total}}}. \tag{5.13}$$

ε_m is the error fraction of the m^{th} decision tree, which is the sum of the miss-classified events ($N_{\text{miss-classified}}$) over the total number of events (N_{total}). A signal object is miss-classified if it lands on a leaf node with $p < 0.5$ and a background object is miss-classified if it lands on a leaf node with $p > 0.5$. β is a parameter which scales the amount by which the weights are boosted or suppressed in the next tree. β has been optimized to be 0.2. Depending on whether an event i is correctly classified by the current tree, the weight for that event in the next tree will be,

$$\left(\frac{1-\varepsilon_m}{\varepsilon_m}\right)^{\beta \times h(i)} \quad \text{where} \quad h(i) = \begin{cases} +1 & \text{(miss-classified)} \\ -1 & \text{(correctly-classified)} \end{cases} \tag{5.14}$$

This process continues until the output performance becomes saturated.

The output score is a weighted series of the decision tree output, where the score assigned to an object is the normalized weighted sum of the scores assigned by each decision tree,

$$H(\vec{x}) = \frac{\sum_m \alpha_m H_m(\vec{x})}{\sum_m \alpha_m} \tag{5.15}$$

where m loops over the decision trees. The $H_m(\vec{x})$ and α_m represents a purity and the boost-weight of the m^{th} decision tree. $H(\vec{x})$ has a value between 0 to 1, since $H_m(\vec{x}) \in [0, 1]$.

5.5.2 Training of the BDT$_j$

In order to separate the genuine τ-lepton in τ candidate from the one coming from hadronic (quark or gluon originated) jets, BDT$_j$ has been developed based on the 8 kinematic variables for τ_1 candidates and 11 variables for τ_3 candidates. The τ candidates from the MC simulated $Z \to \tau\tau$ and $W \to \tau\nu$ events are used as the signal after taking a truth matching to the hadronically decaying τ-lepton in $\Delta R < 0.2$. On the other hand, QCD multi-jet events collected by the jet trigger with p_T threshold of 10 GeV is used as the background[3]. Followings are the list of variables used for the BDT$_j$ training. The distributions for each variables are shown in figures in [D.2].

- p_T weighted track width ($R_{\rm track}$)

$$R_{\rm track} = \frac{\sum_i^{\Delta R_i<0.4} p_{T,i}\Delta R_i}{\sum_i^{\Delta R_i<0.4} p_{T,i}} \tag{5.16}$$

  where $p_{T,i}$ is the track transverse momentum for the $i^{\rm th}$ track. For τ_1 candidates, $R_{\rm track}$ corresponds to the ΔR between the track and the axis of the τ candidate.

- Leading track momentum fraction ($f_{\rm track}$)

$$f_{\rm track} = \frac{p_{T,1}^{\rm track}}{p_T^{\tau}} \tag{5.17}$$

  where $p_{T,1}^{\rm track}$ is the transverse momentum of the leading track within $\Delta R < 0.2$ from the axis of the τ candidate. p_T^{τ} is the transverse momentum of the τ candidate. For τ_1 candidates, $f_{\rm track}$ corresponds to the fraction of the candidate's momentum attributed to the track, compared to the total momentum of the candidate, which can have contributions from the calorimeter deposit from π^0 and other neutrals.

- Fraction of the transverse energy within $\Delta R < 0.1$ of the τ candidate ($f_{\rm core}$)

$$f_{\rm core} = \frac{\sum_i^{\Delta R_i<0.1} E_{T,i}}{\sum_j^{\Delta R_j<0.4} E_{T,j}} \tag{5.18}$$

  where $E_{T,i}$ represents cell transverse energy, and ΔR_i is defined between a calorimeter cell and the axis of the τ candidate.

- Number of charged track in $0.2 < \Delta R < 0.4$ ($N_{\rm track}^{\rm iso}$)

- the E_T weighted shower width ($R_{\rm cal}$)

$$R_{\rm cal} = \frac{\sum_i^{\Delta R_i<0.4} E_{T,i}\Delta R_i}{\sum_i^{\Delta R_i<0.4} E_{T,i}} \tag{5.19}$$

[3]The pp collision data of 130 pb is used. In order to avoid real τ contributions, leading τ candidate above 30 GeV is discarded. All the sub-leading τ candidates above 15 GeV is used for the training.

- The invariant mass calculated from the constituent clusters of the τ candidate ($m_{\text{eff. clusters}}$)

$$m_{\text{eff. clusters}} = \sqrt{\left(\sum_{\text{clusters}} E\right)^2 - \left(\sum_{\text{clusters}} \vec{p}\right)^2} \tag{5.20}$$

  To minimize the effect from the pile-up, first N leading E_T clusters, called effective clusters, are used in the calculation, which is defined as,

$$N = \frac{(\sum_i E_{T,i})^2}{\sum_i E_{T,i}^2} \tag{5.21}$$

  where i runs over all the clusters associated to the τ candidate, and N is rounded up to the nearest integer.

- Impact parameter significance of the leading track ($S_{\text{lead track}}$)

$$S_{\text{lead track}} = \frac{d_0}{\delta d_0} \tag{5.22}$$

  where d_0 is the distance of the closest approach of the track to the reconstructed primary vertex in the transverse plane, and δd_0 is the uncertainty related to the d_0 measurement.

- The ratio of the energy of the first three leading clusters over the total energy of all clusters associated to the τ candidate ($f_{3\text{ lead clusters}}$)

- The invariant mass of the track system in $\Delta R < 0.4$ (m_{tracks})

$$m_{\text{tracks}} = \sqrt{\left(\sum_{\text{tracks}} E\right)^2 - \left(\sum_{\text{tracks}} \vec{p}\right)^2} \tag{5.23}$$

  This variable is used for the τ_3 candidate only.

- The decay length significance of the secondary vertex of the τ_3 candidate in the transverse plane (S_T^{flight})

$$S_T^{\text{flight}} = \frac{L_T^{\text{flight}}}{\delta L_T^{\text{flight}}} \tag{5.24}$$

  where L_T^{flight} is the reconstructed signed decay length, and $\delta L_T^{\text{flight}}$ is the corresponding uncertainty.

- The maximal ΔR between a track in $\Delta R < 0.2$ and the axis of the τ candidate (ΔR_{max}). This variable is used for the τ_3 candidates only.

Figure 5.14 shows the BDT$_j$ distribution after the event selection, which is derived by applying the trained BDT$_j$. The signal events (white histogram) tend to distribute close to one, while it is not the case for other backgrounds in τ_1 candidate. This tendency is not

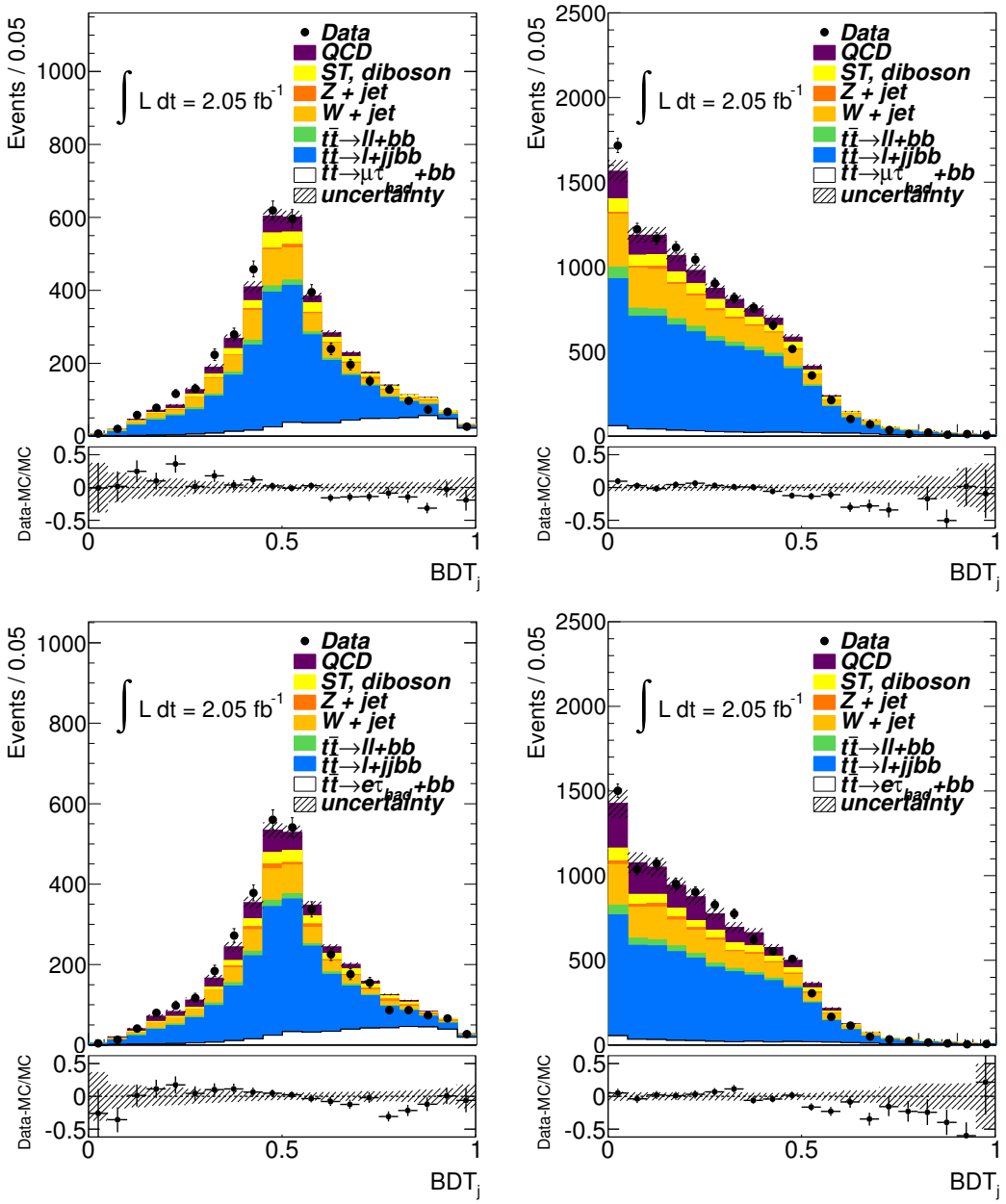

Figure 5.14: BDT_j distribution in the muon (top) and the electron (bottom) channel for (left) τ_1 and (right) τ_3 candidate.

visible in τ_3 candidate due to a large number of fake τ candidate coming from jets even in the signal events. The background distribution in τ_1 candidate has a peak around 0.5, which suggests the background process has an intermediate feature that one cannot obviously identify as hadronically decaying τ-lepton or hadronic jet.

It is also clear, from figure 5.14, that the data distribution is not well modeled by the MC simulation, especially in the higher BDT_j region. Figure 5.16 shows the example of distributions

for two input variables: R_{cal} and F_{core}, as well as the BDT$_j$ distribution in $Z \to \tau_\mu \tau_{\mathrm{had}}$ control region and $W + 1$ fake τ control region defined in section 5.1. The former control region is enriched by the genuine τ candidate, while the latter region dominated by the jet faking τ candidate. The data and MC shows a decent agreement in $Z \to \tau_\mu \tau_{\mathrm{had}}$ control region, while the background distribution is not well modeled by the MC simulation. This tendency can be also observed in the BDT$_j$ distribution itself, where the higher BDT$_j$ region shows a decent agreement, while it is not the case in the lower BDT$_j$ region. The disagreement of the BDT$_j$ distribution between data and MC simulation could be attributed to the miss-modeling of the fragmentation process of the jets faking τ candidate. To be robust for such a miss-modeling, the backgrounds are modeled in a data-driven way in this analysis.

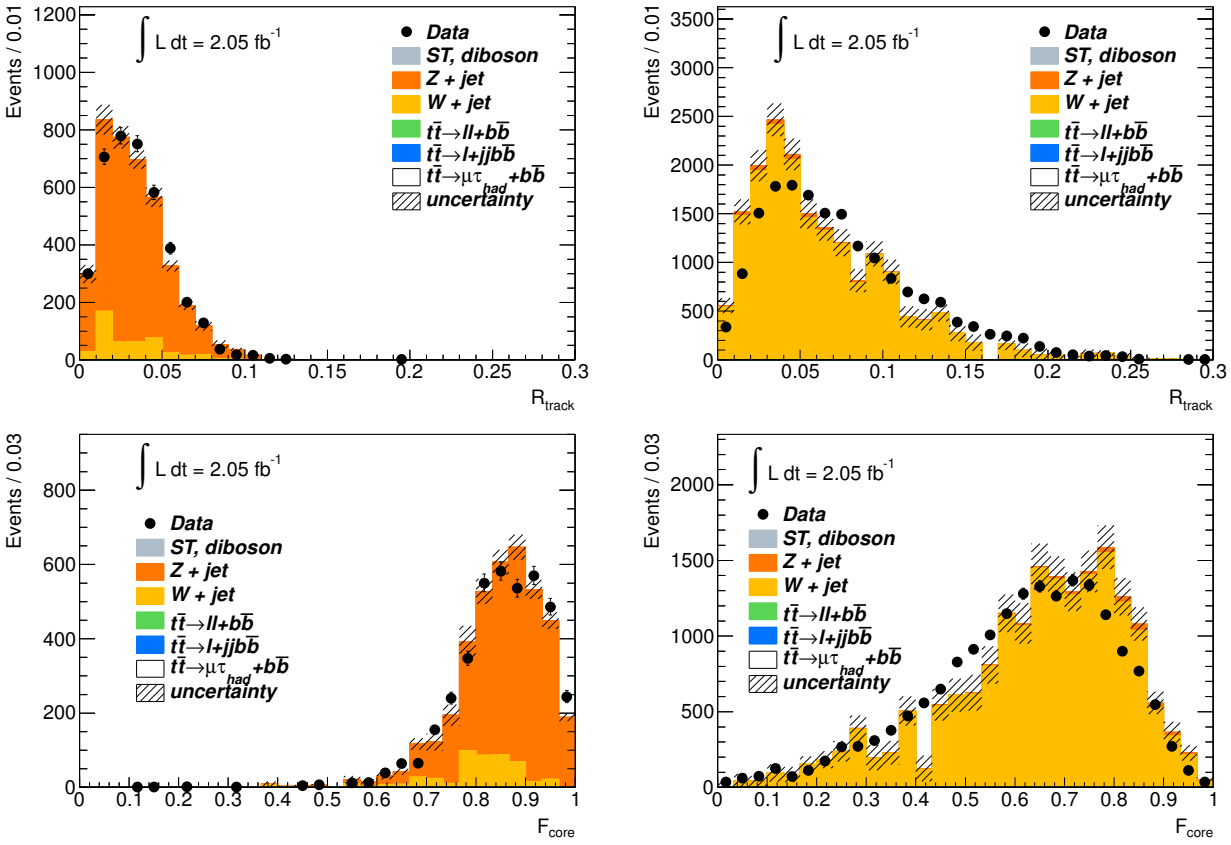

Figure 5.15: R_{cal} (top) and F_{core} (bottom) distributions in (left) $Z \to \tau_\mu \tau_{\mathrm{had}}$ control region and in (right) W+1 fake τ control region in τ_1 candidates. The uncertainty in the plot represents the statistical uncertainty and the uncertainty related to the modeling of the simulated Z+jet events.

5.5.3 Training of the BDT$_e$

In spite of the similarity between the τ candidate and the electromagnetic jet, there are several properties that can be used to distinguish them. BDT$_e$ has been trained using $Z \to \tau\tau$

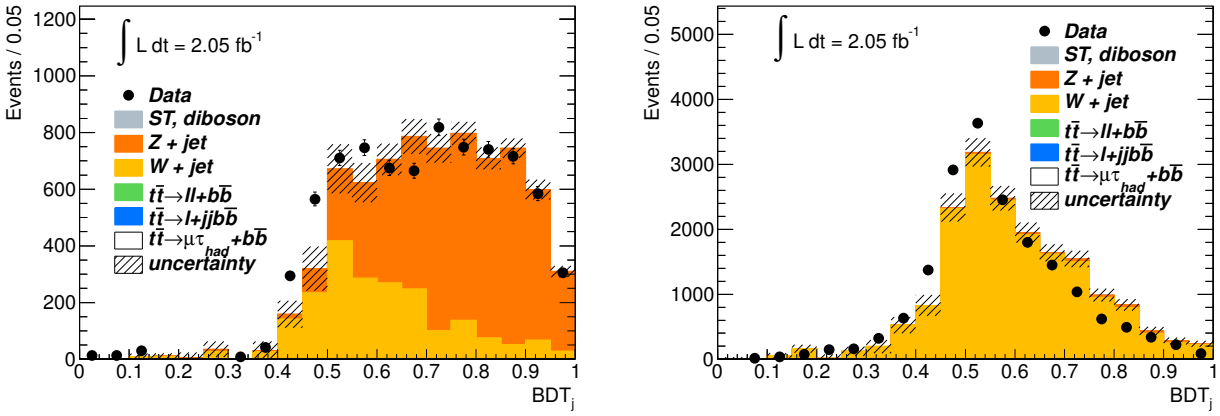

Figure 5.16: BDT_j distribution in (left) $Z \to \tau_\mu \tau_{\mathrm{had}}$ control region and in (right) W+1 fake τ control region in τ_1 candidates.

event as a signal and $Z \to ee$ event as a background, both of them are simulated by the MC simulation. The signal candidates are required to match the hadronically decaying τ-lepton and the background candidates are required to match a true electron within $\Delta R < 0.2$. The BDT_e has been trained based on the R_{track}, f_{track}, and f_{core} variables, which are also used for the BDT_j training, and following 6 variables:

- E_T weighted shower width in the hadronic calorimeter (R_{Had})

$$R_{\mathrm{Had}} = \frac{\sum_{i \in \mathrm{Had}}^{\Delta R_i < 0.4} E_{T,i} \Delta R_i}{\sum_{i \in \mathrm{Had}}^{\Delta R_i < 0.4} E_{T,i}} \tag{5.25}$$

- The fraction of the energy deposit in $0.1 < \Delta R < 0.2$ among $\Delta R < 0.4$ (f_{iso})

$$f_{\mathrm{iso}} = \frac{\sum_{i}^{0.1 < \Delta R_i < 0.2} E_{T,i}}{\sum_{j}^{\Delta R_j < 0.4} E_{T,j}} \tag{5.26}$$

- The fraction of the transverse energy of the τ candidate deposited in the electromagnetic calorimeter (f_{EM})

$$f_{\mathrm{EM}} = \frac{\sum_{i \in \mathrm{EM}}^{\Delta R_i < 0.4} E_{T,i}}{\sum_{j \in \mathrm{all}}^{\Delta R_j < 0.4} E_{T,j}} \tag{5.27}$$

  where $E_{T,i}$ ($E_{T,j}$) is the transverse energy deposited in cell i (j), and i runs over the cells in the first three layers of the EM calorimeter, while j runs over the cells in all layers of the calorimeter.

- The ratio of the high-threshold hits to low-threshold hits in the TRT for the leading p_T track in $\Delta R < 0.2$ (f_{HT})

$$f_{\mathrm{HT}} = \frac{\text{High-threshold TRT hits}}{\text{Low-threshold TRT hits}} \tag{5.28}$$

Since the electron is lighter than $\pi^{\pm}$, electron tends to have a higher Lorentz γ factors given the same momentum. Therefore, electron tends to produce more transition radiation that causes high-threshold hits in the TRT.

- The ratio of the transverse energy in the calorimeter over the transverse momentum of the leading track ($f_{\mathrm{Had}}^{\mathrm{track}}$)

$$f_{\mathrm{Had}}^{\mathrm{track}} = \frac{\sum_{i\in\mathrm{Had}}^{\Delta R_i<0.4} E_{T,i}}{p_{T,i}^{\mathrm{track}}} \tag{5.29}$$

  where i runs over all cells in the hadron calorimeter.

- The maximum transverse energy deposited in the pre-sampler layer of the ECAL, which is not associated with that of the leading track ($E_{\mathrm{T,\ max}}^{\mathrm{strip}}$)

The BDT_e has been optimized separately in four regions depending on the $|\eta|$, which is the barrel region ($|\eta| < 1.37$), crack region ($1.37 < |\eta| < 1.52$), endcap region ($1.52 < |\eta| < 2.0$) and forward endcap region ($2.0 < |\eta| < 2.3$). Seven of the best performing variables are used in each $|\eta|$ region, taking into account the different detector performance.

By applying the BDT_e discriminant on the reconstructed τ candidate, the τ candidate is required to satisfy $\mathrm{BDT}_e > 0.51$, which corresponds to 78% (92%) efficiency of the reconstructed τ_1 (τ_3) candidate in $t\bar{t}$ events, as shown in Figure 5.17. The additional rejection factor, which is the reciprocal of the efficiency, for the electron is estimated using $Z \to ee$ samples in data. Figure 5.18 shows the invariant mass distribution between the τ candidate and the electron (left) before and (right) after the $\mathrm{BDT}_e > 0.51$ cut. Before the BDT_e cut, there is a clear peak at Z boson mass, meaning that the most of the τ candidates are coming by electron faking τ candidate. On the other hand, most of the events are reduced after the BDT_e cut. The ratio of the observed events within the Z mass window (81 GeV - 101 GeV) before and after the BDT_e cut becomes the rejection factor and estimated to be 60. The distribution outside the Z mass window comes from the jet faking τ candidate in $Z(\to ee)$+jet process.

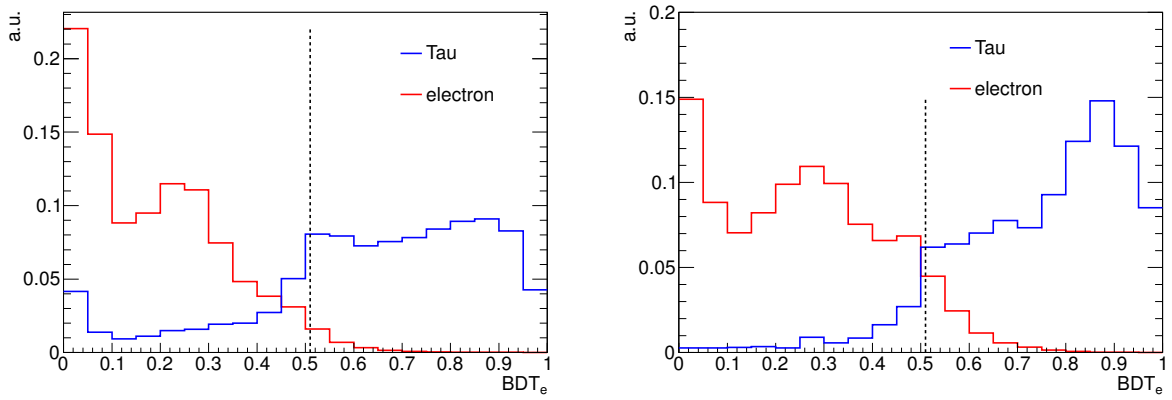

Figure 5.17: BDT_e distribution for the hadronically decaying τ-lepton (blue) and the electron (red) in the $t\bar{t}$ events, both of them are matched to the truth object in MC.

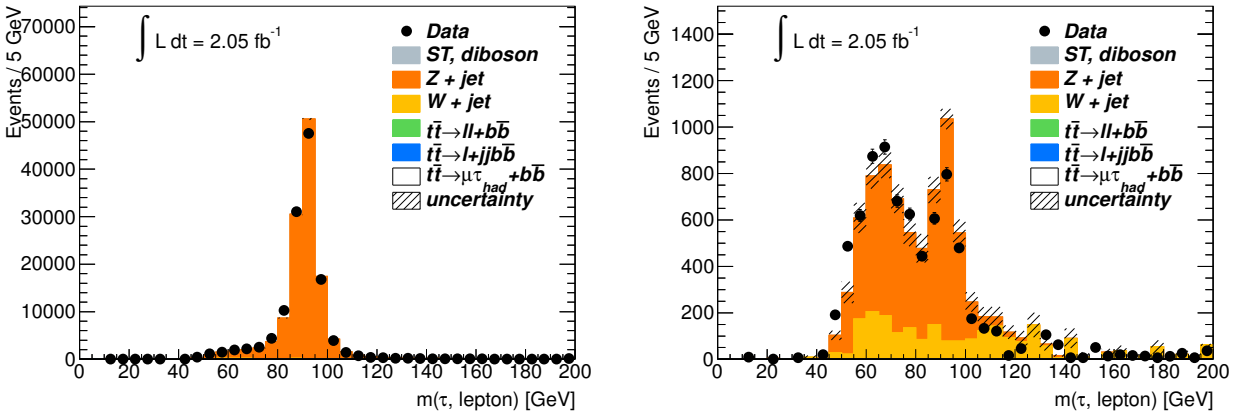

Figure 5.18: The invariant mass distribution between the hadronically decaying τ candidate and the electron in $Z \to ee$ control region, (left) before and (right) after the $\mathrm{BDT}_e > 0.51$ cut.

5.6 Background estimation using BDT_j distribution

5.6.1 Template fitting method and the OS − SS subtraction technique

The background estimation and the signal measurement are established through fitting templates to the BDT_j distribution in data, by means of the background and the signal template. The signal template is derived from the MC simulation, while the background template is derived from the 0 b-tag control region in data to minimize the systematic uncertainty and to avoid possible miss-modelings of the BDT_j distribution.

Concerning to the background template, there is a fact that the shape of the BDT_j distribution is different according to the jet types that mimic the τ candidate. Figure 5.19 shows the breakdown of the BDT_j distributions after the event selection, according to the jet type: light-flavor jet (u, d, c, s), b-jet, and the gluon. Due to their narrow shower width and the low multiplicity characteristics, the light-flavor jets tend to have a higher probability of faking a τ candidate (higher BDT_j), while the b-quark and the gluon tend to have a lower BDT_j value as they typically composes wider jet. This means that the jet composition can strongly influence the fake rate. According to the MC simulation, 16% of the fake τ candidates come from the gluon, 78% from the light-flavor jet and 6% from the b-jet for the τ_1 candidates, while 17% from the gluon, 67% from the light-flavor jet, and 8% from the b-jet for the τ_3 candidates. This requires three different background templates, which are neither easy to derive from data nor to determine the percentage of each without relying on the MC simulation that leads to a large systematic uncertainty.

In order to reduce the need to estimate the jet composition of the fake τ candidates in the signal region, the remaining events are split into the same-sign (SS) sample ($Q_\tau Q_\ell > 0$) and the opposite-sign (OS) sample ($Q_\tau Q_\ell < 0$) depending on the charge correlation between a lepton and a τ candidate. OS−SS subtraction is then used to eliminate the fake τ candidates

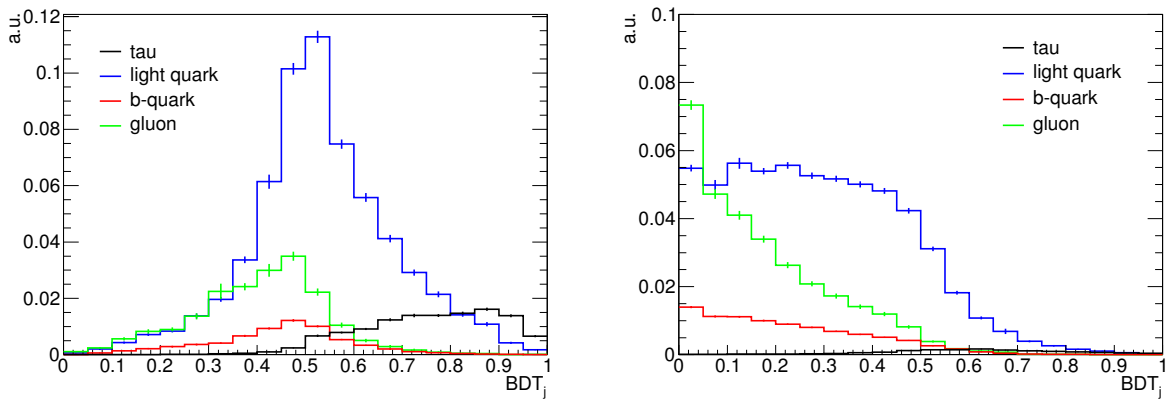

Figure 5.19: MC simulated BDT$_j$ distribution depending on the jet type that fakes to the τ_1 (left) and τ_3 (right) candidate.

from the gluon and the b-jets. Since the gluon does not to do with the lepton charge, and the b-jet is produced as a pair ($b\bar{b}$), they are expected to appear in equal quantities in the OS and the SS distributions. Given the fact that the signal events only exist in the OS sample, OS$-$SS subtraction can remove gluon and b-jet contributions without loosing any signal events[4] The τ candidate originated from the light-flavor jet is expected to be OS $>$ SS, as it predominantly emerges from the pairing W boson. Conceptually, the situation can be summarized as followings:

$$N_{\text{OS}} = N_{g\to\tau} + N_{b\text{-jet}\to\tau} + N_{\text{light-flavor}\to\tau,\text{OS}} + N_{\tau} \tag{5.30}$$

$$N_{\text{SS}} = N_{g\to\tau} + N_{b\text{-jet}\to\tau} + N_{\text{light-flavor}\to\tau,\text{SS}} \tag{5.31}$$

$$N_{\text{OS-SS}} = N_{\text{light-flavor}\to\tau,\text{OS}-\text{SS}} + N_{\tau} \tag{5.32}$$

where the subscription denotes the origin of the τ candidate. The template fit to the OS$-$SS subtracted BDT$_j$ distribution can then be performed on the signal region with the assumption that all the fake τ candidates are light-flavor jet in origin. The background template derived from the 0 b-tag control region is also applied OS$-$SS subtraction to extract the fake τ candidate originated from the light-flavor jet.

The OS$-$SS subtraction technique has been validated using the MC simulation as is shown in Figure 5.20. The left plot shows the BDT$_j$ distribution: OS events are in the positive area, SS events are in the negative area. The different color corresponds to a different jet type. The right plot shows the OS$-$SS distribution, where the τ candidates coming from gluons and b-jets are almost cancelled out. The remnant of the OS$-$SS subtraction is the light-flavor jet and the genuine τ candidate from signal events. Although Figure 5.20 does not include QCD events, the OS$-$SS subtraction also removes such events, as the fake τ candidate originated from the gluon or the light-flavor jet in the QCD multi-jet events does not to do with a lepton charge (charge symmetric). By separately estimating the QCD events for the OS and SS sample, with

[4]There is a small probability (¡1%) of the charge miss-reconstruction, which is almost negligible.

the same procedure described in Section 5.4.3, the contributions from the QCD multi-jet events after the OS−SS subtraction is estimated to be less than 3% among the total events, which is the negligible level within the measurement uncertainty.

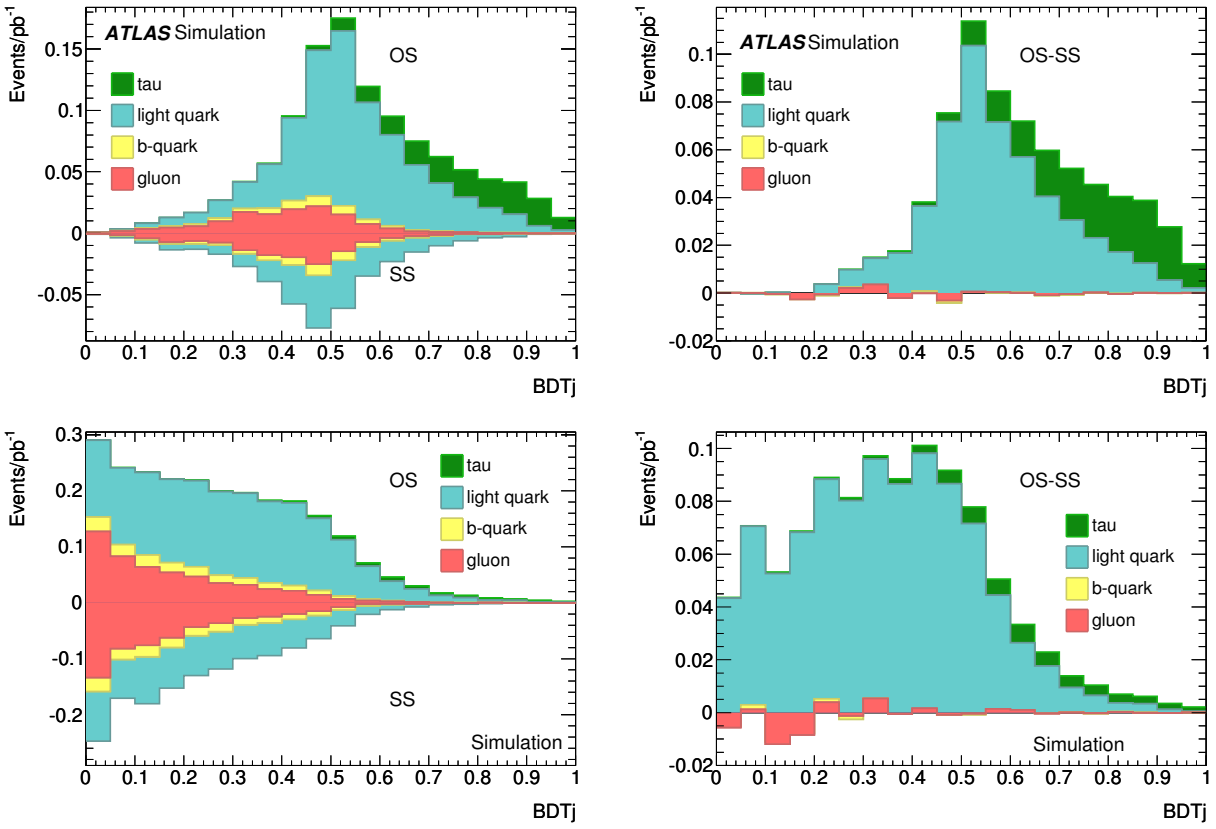

Figure 5.20: (Left) BDT$_j$ distribution for the OS in the positive area and the SS in the negative area. Color corresponds to the jet type, (right) BDT$_j$ distribution after the OS−SS subtraction. (Top) τ_1 and (bottom) τ_3 candidates. Note that the QCD events are not included in this plots.

Figures in [D.3] show the transverse mass distributions ($M_T(\ell, E_T^{\text{miss}})$) after the OS−SS subtraction. The low transverse mass region, where the QCD contributions are dominant, agrees well between data and MC simulation. An overestimation of the MC normalization is apparent in some plots, especially in τ_1 candidate in the muon channel. This is due to a larger number of events in the SS distributions than the MC prediction, leading to lower normalizations after the OS−SS subtraction. The OS and SS fractions are difficult to model exactly by the MC simulation, which is the another motivation to model the background in a data-driven way.

5.6.2 Construction of the signal template

The signal template is derived from the τ candidates in the MC simulation that are truth-matched to a real τ-lepton in the proportion expected from the simulated events passing the

event selection. The majority (90%) of them comes from the signal events (Figure 5.1), while small contributions (8%) from $Z \to \tau^+\tau^-$ (Figure 5.2 (f)), diboson (Figure 5.2 (g)) and the single-top process (Figure 5.2 (h)). There are also a tiny contributions (2%) from electron faking τ candidate, such as $t\bar{t}$ di-lepton (Figure 5.2 (d)) and $Z \to e^+e^-$ (Figure 5.2 (d)) process which are also included to the signal template, since the BDT$_j$ shape is similar to that of real τ-leptons. In this case, τ candidates that are truth-matched to the electrons are added to the signal template. Note that the contributions except for the signal process are subtracted relying on the MC after the template fit is performed.

Table 5.6 shows the breakdown of the events after the event selection, according to the origin of the τ candidate. The numbers in the 0 b-tag control region is also shown as it is relevant for the background template construction. Figure 5.21 shows the derived signal template used for the template fitting. The binning of the BDT$_j$ distribution has been adjusted to avoid the negative entry when performing the OS−SS subtraction in the background template[5].

$\tau + \mu$	τ_1				τ_3			
	0 b-tags		≥ 1 b-tags		0 b-tags		≥ 1 b-tags	
	OS	SS	OS	SS	OS	SS	OS	SS
μ+jets	5005 ± 72	3022 ± 56	496 ± 17	297 ± 13	12230 ± 120	8669 ± 89	1293 ± 28	928 ± 24
multi−jets	465 ± 140	537 ± 160	117 ± 35	146 ± 44	995 ± 300	1123 ± 340	464 ± 139	401 ± 120
$t\bar{t}(\mu$+jets)	308 ± 4	163 ± 3	1528 ± 9	660 ± 6	685 ± 6	443 ± 5	3484 ± 13	2000 ± 10
$t\bar{t}(\mu + e)$	3 ± 1	< 1	12 ± 1	1 ± 1	1 ± 1	< 1	2 ± 1	< 1
$Wt(\tau + \mu)$	7 ± 1	< 1	18 ± 1	1 ± 1	2 ± 1	< 1	5 ± 1	< 1
Z $\to \tau\tau$	301 ± 13	2 ± 1	16 ± 3	< 1	75 ± 7	1 ± 1	3 ± 2	< 1
$t\bar{t}(\tau + \mu)$	60 ± 2	< 1	390 ± 4	2 ± 1	17 ± 1	1 ± 1	118 ± 2	2 ± 1
Total	6149 ± 160	3724 ± 180	2577 ± 40	1106 ± 45	14010 ± 323	10240 ± 350	5371 ± 139	3322 ± 120
Data	5450 ± 74	3700 ± 61	2472 ± 50	1332 ± 36	13322 ± 115	10193 ± 101	5703 ± 76	3683 ± 61
$\tau + e$	τ_1				τ_3			
	0 b-tags		≥ 1 b-tags		0 b-tags		≥ 1 b-tags	
	OS	SS	OS	SS	OS	SS	OS	SS
e+jets	3949 ± 63	2590 ± 51	380 ± 20	256 ± 16	10140 ± 100	7530 ± 87	1120 ± 33	841 ± 29
multi−jets	602 ± 180	617 ± 185	165 ± 50	135 ± 41	2010 ± 600	2020 ±600	690 ± 207	606 ± 182
Z $\to ee$	92 ± 10	3 ± 2	9 ± 3	< 1	11 ± 3	2 ± 1	< 1	< 1
$t\bar{t}(e$+jets)	273 ± 17	146 ± 12	1335 ± 37	599 ± 24	633 ± 25	399 ± 20	3093 ± 56	1780 ± 42
$t\bar{t}(e + e)$	2 ± 1	< 1	11 ± 3	< 1	< 1	< 1	2 ± 1	< 1
$Wt(\tau + e)$	7 ± 3	< 1	17 ± 4	< 1	1 ± 1	< 1	6 ± 2	< 1
Z $\to \tau\tau$	217 ± 15	2 ± 2	15 ± 4	< 1	56 ± 8	1 ± 1	3 ± 2	< 1
$t\bar{t}(\tau + e)$	54 ± 7	1 ± 1	342 ± 18	4 ± 2	15 ± 4	< 1	103 ± 10	2 ± 1
Total	5200 ± 190	3360 ± 190	2274 ± 68	995 ± 50	12870 ± 610	9950 ± 610	5020 ± 217	3226 ± 192
Data	5111 ± 71	3462 ± 59	2277 ± 48	1107 ± 33	12102 ± 110	9635 ± 98	5033 ± 71	3192 ± 56

Table 5.6: The number of τ plus lepton candidates for the MC simulation and data. $t\bar{t}(\ell e)$ are $t\bar{t}$ events with one identified lepton and an electron reconstructed as a τ candidate. $t\bar{t}(\ell + \text{jets})$ denotes $t\bar{t}$ events with one identified lepton and a jet reconstructed as a τ candidate. ℓ+jets are events with one identified lepton and a jet reconstructed as a τ candidate from sources other than $t\bar{t}$ and QCD events.

The validity of the signal template has been checked by comparing the BDT$_j$ distribution in $Z \to \tau_\mu\tau_{\text{had}}$ control region, as shown in Figure 5.16), which shows a good agreement. As an another check, the template fit is performed using $Z \to \tau_\mu\tau_{\text{had}}$ control region in data, where the signal template is derived from the MC simulation and the background template is derived

[5]The obtained cross-section is almost independent to the binning.

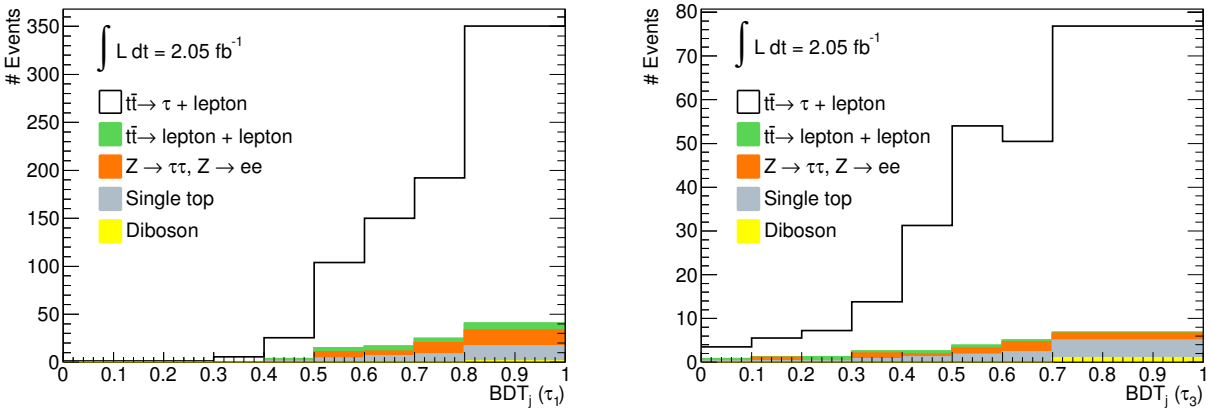

Figure 5.21: Signal template for (left) τ_1 and (right) τ_3.

from $W+1$ fake τ control region in data after OS−SS subtraction. Figure 5.22 shows the fitting result and Table 5.7 summarizes the number of extracted events with real τ-like signal, in this case coming from $Z \to \tau^+\tau^-$ process.

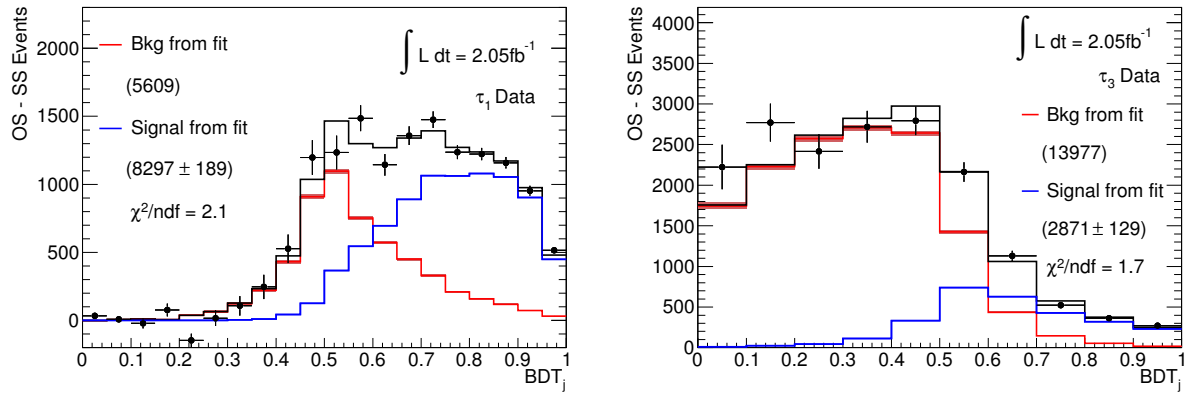

Figure 5.22: Template fitting result using $Z \to \tau_\mu \tau_{\text{had}}$ control region for (left) τ_1 and (right) τ_3.

	Extracted number of signal	χ^2/n.d.f	MC expectation
τ_1 candidate	8297 ± 189	2.1	8710
τ_3 candidate	2871 ± 129	1.7	2917

Table 5.7: Summary of the fitting results using $Z \to \tau_\mu \tau_{\text{had}}$ control region in data.

The uncertainty related to the τ identification efficiency comes from the statistical uncertainty of the data (3%), the uncertainty of the predicted Z+jet cross-section (4%) [38] and the jet energy scale uncertainty (3%). The total uncertainty is 5.0% for the τ_1 candidate and 7.0%

for the τ_3 candidate. The observed difference between the MC prediction and the number of extracted signal events by the template fit is covered by this uncertainty. Therefore, signal template is considered to be applicable for the signal extraction. The above uncertainties are propagated to the systematic uncertainty on the cross-section measurement.

5.6.3 Construction of the background template

The background template is derived in a data-driven way to minimize the systematic uncertainty and to avoid possible miss-modeling of the MC simulation. For this purpose, 0 b-tag control region is used, where explicitly no b-jet is required in the event. The other selections are identical with that of the signal region. As the true background shape in the signal region is unknown, it is desirable to choose the control region, which is kinematically as close as possible to the signal region. As is described in the previous section, OS−SS subtraction is performed to derive the background template which is enriched by the fake τ candidates originated from the light-flavor jet.

Figure 5.23 shows the comparison of the BDT_j distribution between the electron and the muon channel in 0 b-tag control region, after subtracting real τ and electron contributions (mainly $Z \to \tau^+\tau^-$ and $Z \to e^+e^-$ processes) relying on the MC simulation. Since both distributions show a good agreement within the statistical uncertainty, the electron and the muon channel are combined to reduce the statistical uncertainty.

Table 5.6 also shows the composition in the 0 b-tag control region, where the dominant process comes from the W+jet events. Since there are real τ or electron contributions from $Z \to \tau^+\tau^-$, $t\bar{t}$ events with τ and lepton channel (signal events) that failed the b-tag requirement, single-top process, and $Z \to e^+e^-$ process, these are subtracted based on the MC simulation. The fraction of the subtracted events are 15% (20%) for τ_1 candidate and 2% (3%) for τ_3 candidate in the muon (electron) channel. More than 80% of the subtraction comes from Z+jet events. Since the uncertainty of the MC production cross-section for the Z+jet process has been estimated to be 4% [38], the possible fluctuation related to the subtraction is estimated to be less than 1%, which can be neglected.

Finally, it is necessary to consider about the fact that the BDT_j distribution depends on the kinematics, especially on the p_T of the τ candidate and the jet multiplicity in the events, as shown in the Figure 5.24.

Since the hadronically decaying τ-lepton composes a narrow and isolated jet, higher p_T results in higher BDT_j score (more collimated), while the higher jet multiplicity results in the lower BDT_j score. Given the fact that the 0 b-tag control region is dominated by the W+jet process (lower p_T, lower jet multiplicity compared to the $t\bar{t}$ events), while actual signal region is dominated by the $t\bar{t}$ lepton plus jet events (higher p_T, higher jet multiplicity compared to the W+jet events), the kinematical difference need to be absorbed to correctly model the background in the signal region. For this purpose, correction factor based on the MC simulation is applied to the derived background template in 0 b-tag control region in data, as followings.

$$\langle \mathrm{BDT}_j \rangle_{\text{data, } \geq 1\ b\text{-tags}} = \frac{\langle \mathrm{BDT}_j \rangle_{\text{MC, } \geq 1\ b\text{-tags}}}{\langle \mathrm{BDT}_j \rangle_{\text{MC, 0 } b\text{-tags}}} \times \langle \mathrm{BDT}_j \rangle_{\text{data, 0 } b\text{-tags}}, \tag{5.33}$$

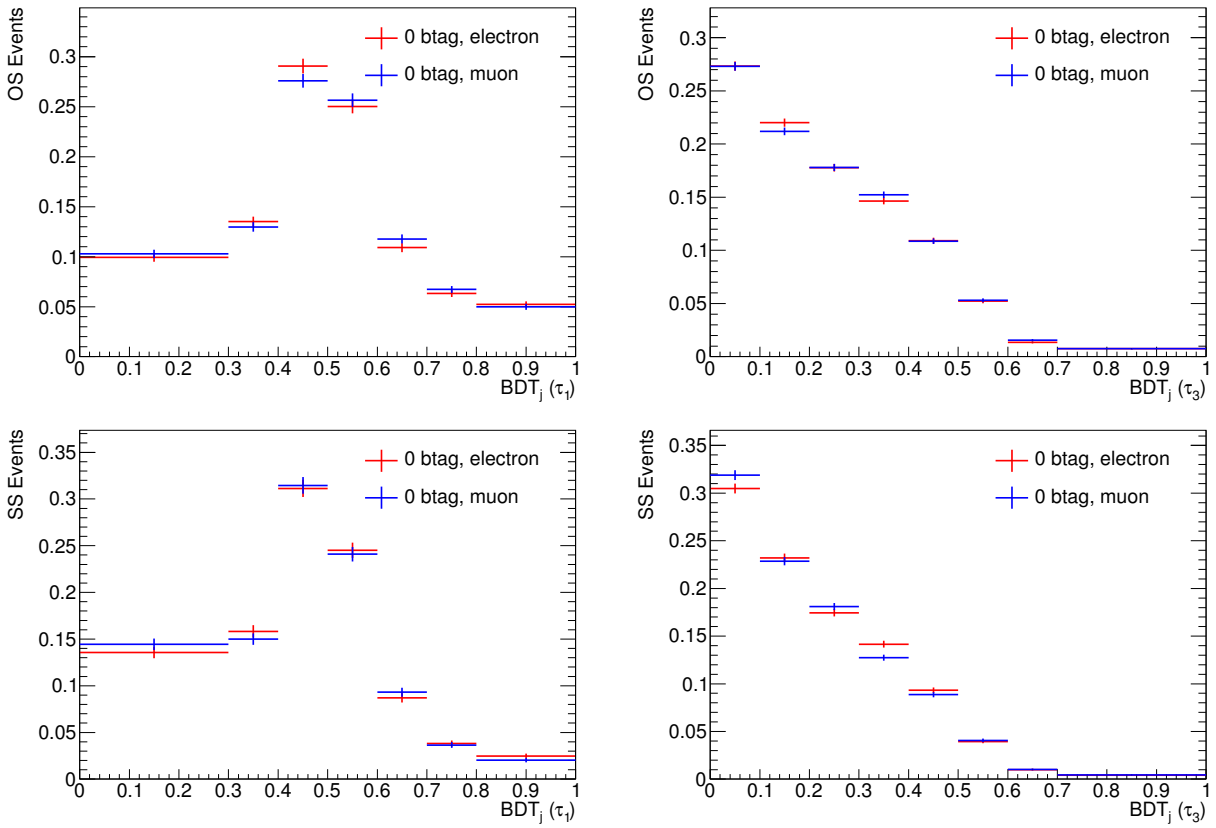

Figure 5.23: The comparison of the BDT$_j$ distribution (data) in 0 b-tag control region in data for (top) OS and (bottom) SS sample in (left) τ_1 and (right) τ_3 candidate.

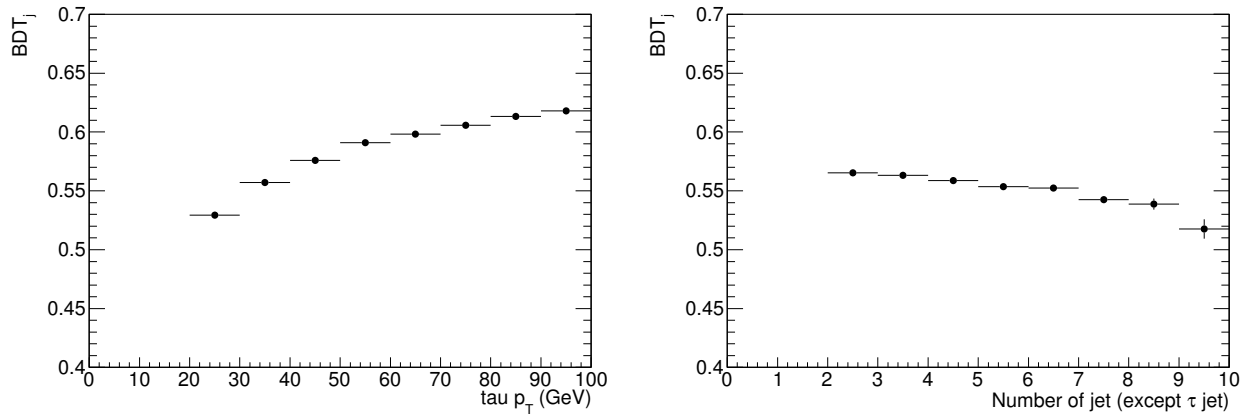

Figure 5.24: BDT$_j$ dependence as a function of p_T of the τ candidate (left) and the jet multiplicity of the events (right). The dependency is estimated based on the MC simulation for the light-flavor jet in $t\bar{t}$ events.

where $\langle \mathrm{BDT}_j \rangle$ denotes the background BDT_j distribution. Figure 5.25 shows the MC correction factor and the derived background template.

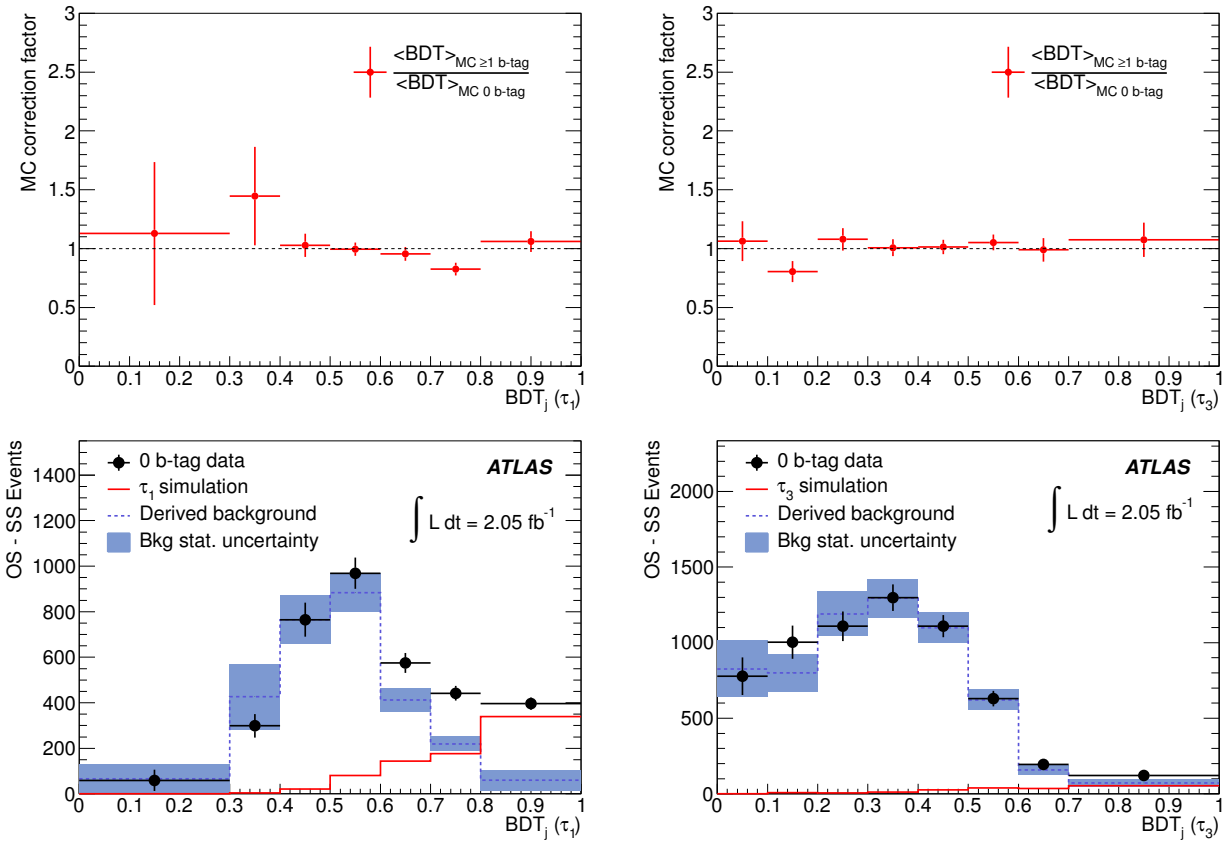

Figure 5.25: (Top) The MC correction factor for τ_1 (left) and τ_3 (right) candidates and (bottom) the corresponding background template used in the analysis. The template starts from 0 b-tag control region in data after OS $-$ SS subtraction (black) and subtracting genuine τ and electron components based on the MC simulation (red). In order to match the background shape to that of the b-tag signal region, MC correction factor is applied to derive the background template (hatched-blue).

In order to validate the background template, following tests have been performed.

- The background template derived from the $W + 1$ fake τ control region is used, followed by the MC correction to look like the background distribution in 0 $b-$tag control region. The derived template is compared to the background distribution in 0 b-tag control region after subtracting real τ and electron contributions based on the MC simulation. This can be written as,

$$\langle \mathrm{BDT}_j \rangle_{\text{data, 0 } b\text{-tags}} \leftrightarrow \frac{\langle \mathrm{BDT}_j \rangle_{\text{MC, 0 } b\text{-tags}}}{\langle \mathrm{BDT}_j \rangle_{\text{MC, } W+1 \text{ fake } \tau}} \times \langle \mathrm{BDT}_j \rangle_{\text{data, } W+1 \text{ fake } \tau}. \tag{5.34}$$

Figure 5.26 shows the result, where both distributions are in decent agreement within the uncertainty, demonstrating the validity of the correction method.

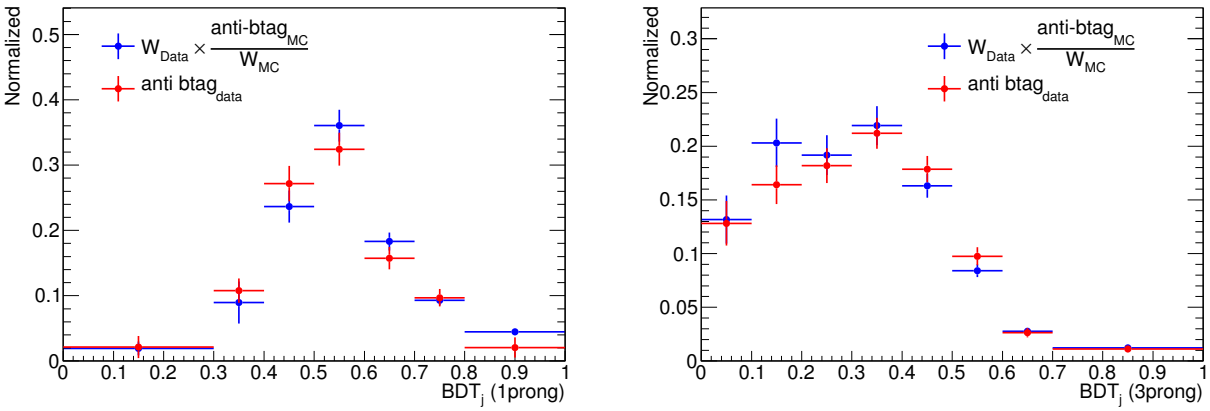

Figure 5.26: Comparison of the background BDT_j distribution between the 0 b-tag control region (red) and the one derived from W+1 fake τ control region (blue) in (left) τ_1 and (right) τ_3 candidates.

- The background template derived from the 0 b-tag control region is compared to the background distribution in the signal region after subtracting real τ and electron contributions based on the MC simulation. In order to keep blind for the signal events, comparison is performed using $\mathrm{BDT}_j < 0.6$ region only, where the signal contribution is less than 10%. This can be written as,

$$\langle \mathrm{BDT}_j \rangle_{\text{data, } \geq 1\ b\text{-tags, BDT}_j > 0.6} \leftrightarrow \frac{\langle \mathrm{BDT}_j \rangle_{\text{MC, } \geq 1\ b\text{-tags}}}{\langle \mathrm{BDT}_j \rangle_{\text{MC, 0 } b\text{-tags}}} \times \langle \mathrm{BDT}_j \rangle_{\text{data, 0 } b\text{-tags}}. \tag{5.35}$$

  Figure 5.27 shows the result of the comparison, also showing a decent agreement within the uncertainty.

Based on the result obtained in this validation test, the background template was considered to be applicable to the signal region without adding any additional uncertainties except for the statistical one.

5.6.4 Validation test of the fitting method

Before applying the template fit to the signal region, the analysis performed the validation test of the fitting method by using the pseudo data-samples (ensemble test). The purpose of the validation test is,

- to check if there is any bias for the cross-section measurement
- to check the uncertainty for the cross-section measurement

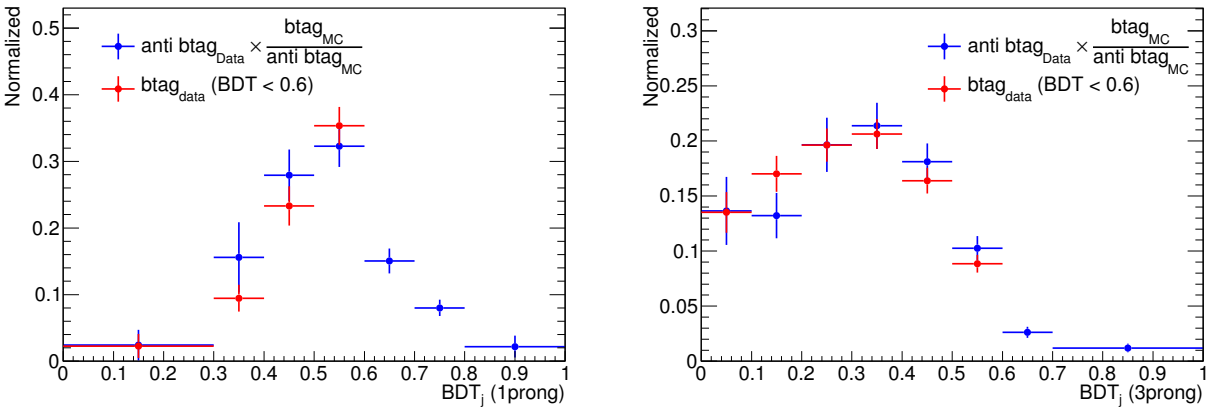

Figure 5.27: Comparison of the background BDT$_j$ distribution between the signal region (red) and the one derived from 0 b-tag control region (blue) in (left) τ_1 and (right) τ_3 candidates. The comparison is performed using BDT$_j < 0.6$ to keep blind for the signal events.

- to check the linearity for the cross-section measurement

For this purpose, five thousand sets of pseudo experiments are performed by fluctuating BDT$_j$ distributions for the signal template and the background template derived in the previous section within the possible uncertainty. The uncertainty of the background template includes the statistical, the one related to the subtraction of the real τ and electron contributions, and the one related to the MC weighting factor.

Figure 5.28 shows the result of the ensemble test and Table 5.8 summarizes the result. The average of the reduced χ^2 distribution is one, as expected, ensuring the validity of the ensemble test. The RMS of the pull distribution is almost close to 1, demonstrating that the given uncertainty is reasonable. The error distribution has a tail component, which is caused by the negative entries by the OS−SS operation in 0 $b-$tag control region. This can be, however, avoided before the template fitting by selecting the proper binning when the background template is constructed. The relative uncertainty for the signal extraction is found to be 11% for the τ_1 candidate events and 26% for the τ_3 candidate events. The combined cross-section is thus dominated by the result from the τ_1 candidate events.

	reduced χ^2	output mean	error (%)	pull RMS	MC expectation
τ_1 candidate	1.0	826.1	10.7%	0.98	829
τ_3 candidate	1.0	242.5	26.4%	0.97	243

Table 5.8: Summary of the ensemble test result. The error represents the relative uncertainty for the signal extraction.

Since the observed cross-section is unknown before the template fit is performed, the linearity and the bias of the fitting were checked by varying the amount of signals in the simulated sample, from zero to twice the SM value with 0.2 steps. For each point, the ensemble test is

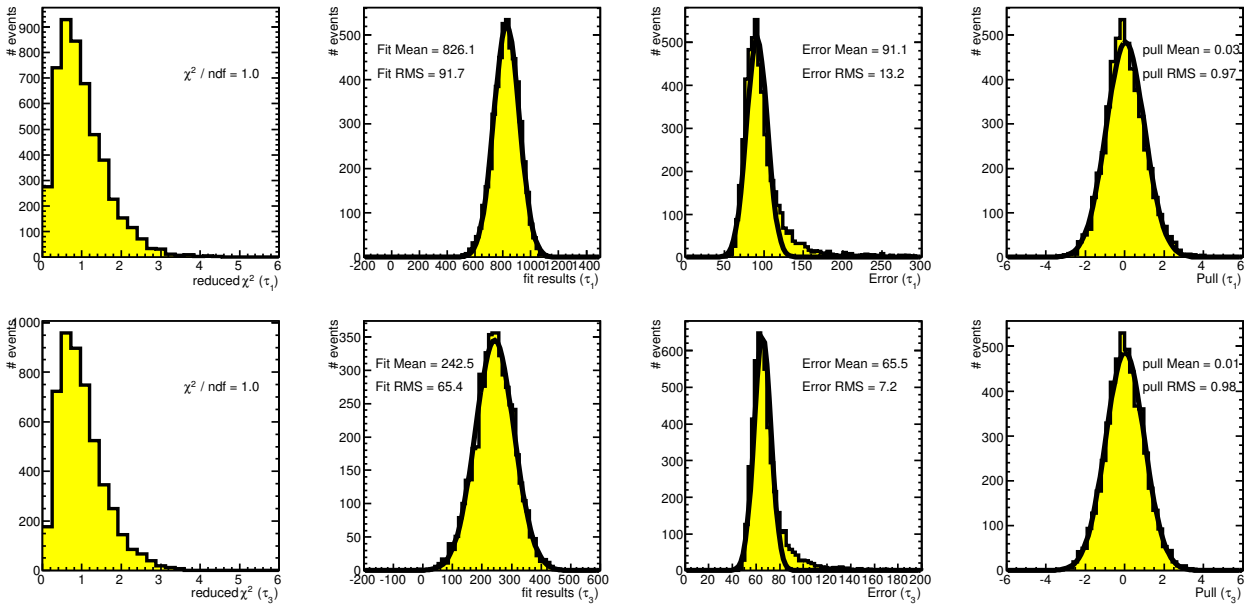

Figure 5.28: The ensemble test results for (top) τ_1 and (bottom) τ_3 candidate events. (From left to right) reduced χ^2, mean of the fitting result (muon and electron channel combined), error distribution and the pull distribution.

performed to see the extracted number of signal events. Figure 5.29 shows the linearity curve, where the good linearity is observed with its slope close to unity. The intercept of the fitting line (blue line) is almost zero, indicating almost no bias of the method.

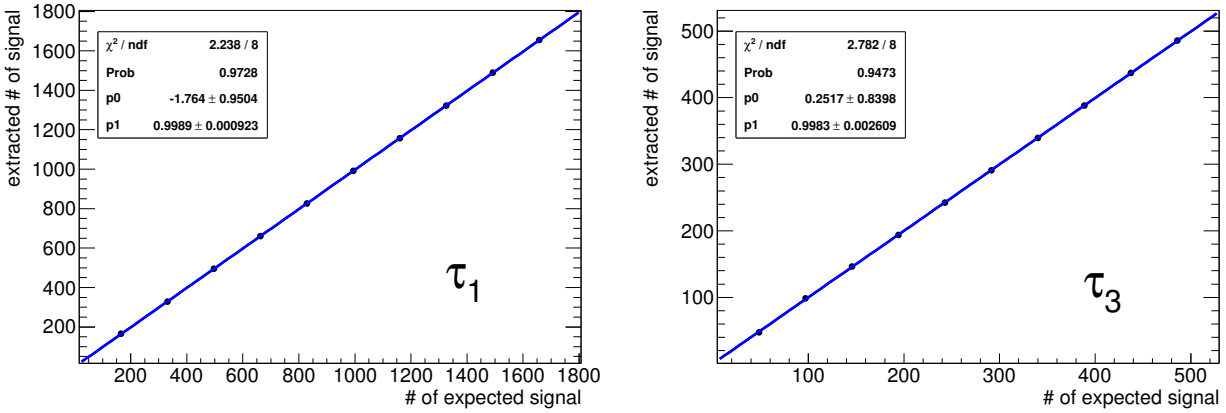

Figure 5.29: Linearity curve of the extracted number of signal events in (left) τ_1 and (right) τ_3 candidates. Both the electron and the muon channel are combined. The black points show the result, and the blue line shows the fitting result for the black points.

As the another test, the template fit method was tested using two statistically independent MC samples. One sample was used to construct the expected data, including the signal events, in the ≥ 1 b-tag signal region (50% of MC). The second sample (50% of MC) was used to create the background template. The template fit was performed to see if the method could extract the known number of signal events in the sample. The fitting results are summarized in Table 5.9. Although the uncertainties are big due to the limited statistics of the 50% MC simulation, the extracted number of events and the MC expectation shows a decent agreement.

	$\tau_1 + e$	$\tau_3 + e$	$\tau_1 + \mu$	$\tau_3 + \mu$
Fitting result	403 $\pm$ 63	187 $\pm$ 100	462 $\pm$ 129	143 $\pm$ 65
MC expectation	388	114	432	126

Table 5.9: Fitting results and the MC expectation using statistically independent MC samples as the data and for the templates.

5.7 Systematic uncertainty on the cross-section

Before applying the template fit to the signal region, all the systematic uncertainties are evaluated. In this analysis, the sources of the systematic uncertainty arise from followings:

- MC expectation on the signal acceptance ($\mathcal{A}$)
- Shape distortion of the background template due to the subtraction of the real τ and electron contributions in the 0 b-tag control region.
- Shape distortion of the signal template

All of the above sources can be accounted for by varying the signal and the background template at once within the uncertainties of each known systematics. The uncertainties on the cross-sections were derived using $\pm 1\sigma$ variation samples and performing the fitting, comparing the extracted cross-sections to the nominal samples. Note that the variations of the signal acceptance directly affect to the variation on the cross-section, while only the shape (not the absolute value) of the signal and the background template affect to the variation on the cross-section.

Table 5.10 shows the summary of the obtained systematic uncertainties on the cross-section ($\mathrm{d}\sigma/\sigma$). The systematic uncertainty on the signal acceptance ($\mathrm{d}\mathcal{A}/\mathcal{A}$) is also shown as a cross-check purpose. In the following sections, each systematic sources are described, followed by the discussion.

5.7.1 Uncertainties related to the detector performance

Uncertainties related to the lepton Uncertainties related to the lepton trigger, reconstruction and the selection efficiencies are estimated using the tag and probe method in $Z \to \ell\ell$ control region in data. $Z \to \ell\ell$ process is selected by requiring two opposite signed leptons with its invariant mass inside the Z mass window (91 GeV $< m_{\ell\ell} <$ 101 GeV). In order to

	$\tau + \mu$ $d\mathcal{A}/\mathcal{A}$ (%)	$\tau + e$ $d\mathcal{A}/\mathcal{A}$ (%)	$\tau + \mu$ $d\sigma/\sigma$ (%)	$\tau + e$ $d\sigma/\sigma$ (%)
muon p_T smearing	0.0 / +0.1	±0.0	±0.3	0.0 / +0.1
muon trigger SF	±1.6	±0.0	−1.1 / +1.5	±0.1
muon identification SF	±0.0	±0.0	−0.1 / 0.0	±0.0
electron p_T smearing	±0.0	0.0 / +0.2	±0.2	−0.2 / 0.0
electron energy scale	±0.0	±0.5	−0.3 / +0.1	−0.2 / +0.4
electron trigger SF	±0.0	±0.8	−0.1 / +0.2	−0.7 / +1.0
electron identification SF	±0.0	±2.9	−0.5 / +0.6	−2.8 / +2.7
jet energy scale	−2.8 / +2.3	−3.4 / +3.0	−2.0 / +2.2	−1.9 / +2.8
jet energy resolution	±0.5	±0.4	±1.0	±1.2
jet identification efficiency	±0.0	±0.0	±0.2	±0.0
b-tag SF	−5.7 / +5.3	−5.3 / +4.6	−7.7 / +9.0	−7.5 / +8.9
ISR/FSR	±4.5	±5.7	±4.8	±3.5
parton distribution function	±2.0	±2.1	±2.0	±2.1
parton shower	0.0 / +0.3	0.0 / +0.3	−0.3 / 0.0	−0.3 / 0.0
MC generator	±0.7	±0.7	±0.7	±0.7
τ identification (τ_1)	±5.0	±5.0	−3.0 / +3.2	−2.7 / +3.0
τ identification (τ_3)	±7.1	±7.1	−3.1 / +3.4	−2.9 / +3.2
total (τ_1)	−9.6 / +9.3	−10.6 / +10.1	−10.1 / +11.3	−9.7 / +11.1
total (τ_3)	−10.9 / +10.6	−11.7 / +11.3	−10.2 / +11.3	−9.8 / +11.2

Table 5.10: The list of systematic uncertainty. $d\mathcal{A}/\mathcal{A}$ is the uncertainty on the signal acceptance and the $d\sigma/\sigma$ on the cross-section.

avoid the trigger bias, a tag lepton is required to fire the corresponding single lepton trigger. The purity of the lepton in this control region is estimated to be more than 99%, based on the MC simulation. Scale factors are then evaluated by comparing the efficiencies between the simulated Z events in the MC simulation and the one in data. The central value is applied to the MC simulation to absorb the difference with respect to the data and its error is considered as the systematic uncertainty. The lepton momentum scale and the resolution as well as its uncertainties are evaluated by comparing the invariant mass distribution of the di-lepton ($m_{\ell\ell}$) between data and MC simulation.

Uncertainties related to the jet Uncertainties related to the jet reconstruction is dominated by the jet energy scale. The jet energy scale calibrates the measured calorimeter-level jet energy to the particle-level (Section 3), taking into account the effect from neutrons, dead materials, other detector effects, and algorithm specific biases. The knowledge of the jet energy scale becomes the uncertainty, where it is estimated by combining information from test beam data, LHC collision data and the simulation [39]. The uncertainty ranges from 4 - 8%, depending on the jet p_T and η, as is shown in Figure 5.30.

The other jet-related uncertainties are the jet reconstruction efficiency and the jet energy resolution. The jet reconstruction efficiency is estimated using a tag and probe method using di-jet events in data. The probe jet is selected by requiring a cluster of the charged tracks, so-called track-jets, in the inner tracker. The measured efficiency was found to be consistent

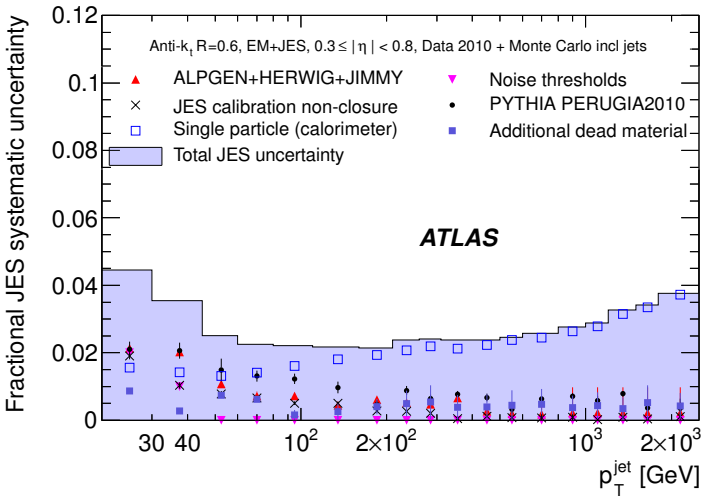

Figure 5.30: Jet energy scale uncertainty as a function of the jet p_T in $0.3 \leq |\eta| < 0.8$, as an example. The total uncertainty is shown in blue.

with unity, and its uncertainty (2%) becomes the source of systematic uncertainty. The jet energy resolution is also measured using di-jet events, as is described in section 3.4.4). The data and the MC simulation agree within the statistical uncertainty of 10%, which is used to assess the systematic uncertainty.

Uncertainty related to the b-tagging The uncertainty related to the b-tag efficiency is evaluated using b-jet enriched sample [32][40], which was selected by requiring a muon that is spatially matched to a calorimeter jet. The one of the typical efficiency measurement uses templates of the muon momentum transverse to the jet axis to fit the fraction of b-jets before and after the b-tagging to extract the b-tagging efficiency.

Since this analysis requires at least 1 b-tagged jet with 70% efficiency point (denote as $\varepsilon = 0.7$), rough calculation of the acceptance uncertainty becomes $2\Delta\varepsilon(1-\varepsilon) = 6\%$, where $\Delta\varepsilon$ is the b-tag efficiency uncertainty, which is typically $\Delta\varepsilon \sim 10\%$.

Uncertainties related to the τ identification efficiency This is already described in Section 5.6.2. The uncertainty related to the τ identification efficiency is evaluated using $Z \to \tau_\mu \tau_{\rm had}$ control region in data by performing the template fitting. The uncertainty of 5.0% in τ_1 and 7.0% in τ_3 candidate are used to estimate the systematic uncertainty.

5.7.2 Uncertainties related to the MC simulation

Uncertainty related to the event generator The uncertainty related to the choice of the event generator was estimated by comparing the MC@NLO predictions to that of the POWHEG [41][42][43]. The POWHEG also adopts the NLO approximation.

Uncertainty related to the ISR/FSR The uncertainty related to the ISR/FSR effect was evaluated using AcerMC [44] generator interfaced to the Pythia shower model, by varying the parameters controlling ISR/FSR effect such as the hadronization scale ($\Lambda_{\rm QCD}$) and the p_T cut-off for the final state radiation, in a range consistent with the past experimental data[6] [45].

Uncertainty related to the PDF The PDF uncertainty is evaluated by comparing the results derived from the standard CTEQ PDF set and the one derived from alternative PDF set [11][46], called MSTW[7] [47] and NNPDF[8] [48]. For each PDF set, there are 41 and 101 parameter variations by fluctuating possible setting parameters within $\pm 1\sigma$. The effect of the parameter variations to the PDF is shown in Figure 5.31 as the ratio of the standard CTEQ over the one under evaluation. The uncertainty is taken to be the RMS for each variations. The RMS for CTEQ, MSTW and NNPDF are added in quadrature to give an overall PDF uncertainty.

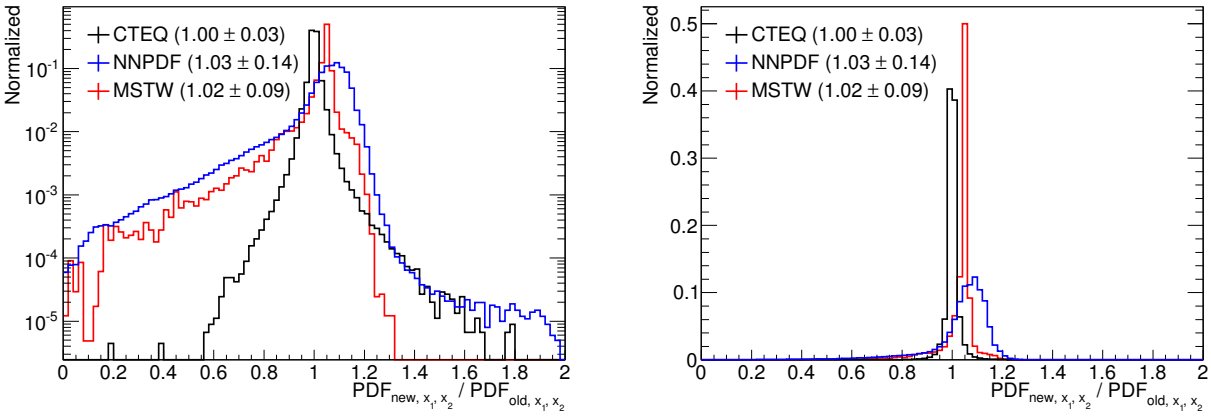

Figure 5.31: Variations of the PDF with respect to the standard CTEQ PDF. Each entry corresponds to each $t\bar{t}$ event with various parton x. (Left) log-scale, (right) linear-scale.

Uncertainty related to the parton shower simulation The uncertainty of the parton shower simulation was estimated by comparing different parton shower simulators: the Herwig and the Pythia. The uncertainty is taken as half of the variation between two samples.

Statistical uncertainty The statistical uncertainty of the simulation samples is considered as the Poisson errors

[6]The hadronic decay of the Z boson in e^+e^- collision, minimum bias collisions at $p\bar{p}$ collisions, and Drell-Yan production in $p\bar{p}$ collisions.

[7]Martin-Stirling-Thorne-Watt PDF

[8]Neural Network PDF

5.7.3 Uncertainties related to the luminosity

The uncertainty related to the luminosity determination is 3.7% (Section 5.2.1). The effect of the luminosity variation directly affects to the signal acceptance, as well as the subtraction of the real τ and electron contributions in the 0 b-tag control region.

5.7.4 Discussions on the systematic uncertainty

There are several discussions about the systematic uncertainties.

- The total uncertainty is an order of 11%, where the dominant uncertainty comes from the b-tag efficiency uncertainty (8-9%).
- The systematic sources related to the electron (muon) can affect to the uncertainty on the muon (electron) channel as the background template is constructed by combining both channels (Section 5.6.3).
- The uncertainty on the cross-section is typically almost equivalent to the uncertainty on the signal acceptance ($\mathrm{d}\sigma/\sigma \sim \mathrm{d}\mathcal{A}/\mathcal{A}$). However, this is not the case for the systematic sources related to the τ identification efficiency, ($\mathrm{d}\sigma/\sigma < \mathrm{d}\mathcal{A}/\mathcal{A}$), jet energy scale ($\mathrm{d}\sigma/\sigma < \mathrm{d}\mathcal{A}/\mathcal{A}$) and the b-tagging efficiency ($\mathrm{d}\sigma/\sigma > \mathrm{d}\mathcal{A}/\mathcal{A}$) due to the distortion of the background template.

Concerning to the last item, assume that the τ identification efficiency increases by $+1\sigma$. Then, the signal acceptance purely increases by $+1\sigma$, while its template shape is kept as it is. On the other hand, the subtraction of the real τ contributions in 0 b-tag control region will increase. As a consequence, the background template is distorted so that the higher BDT_j region becomes lower than nominal, which leads to the increase of the extracted number of signal events. Since the acceptance and the extracted number of signals move to the same direction (positive correlation), the uncertainty on the cross-section is partially cancelled out, which results in $\mathrm{d}\sigma/\sigma < \mathrm{d}\mathcal{A}/\mathcal{A}$. Figure 5.32 shows the ± 1 σ variation of the signal and the background template in case of the τ_1 candidate. The same thing can be said to the uncertainty related to the jet energy scale.

Contrary to the systematic uncertainty on the τ identification efficiency, uncertainty related to the b-tagging efficiency goes opposite direction. If the b-tagginf efficiency increases by $+1\sigma$, the acceptance increases by $+1\sigma$, too. However, the subtracted components in the 0 b-tag control region will decrease as they didn't pass the b-tag selection, by definition. This distorts the background template so that the higher BDT_j region becomes higher than nominal, which results in lower extracted number of signals. Since the acceptance and the number of extracted events move to the opposite direction (negative correlation), the uncertainty on the cross-section is enhanced, and becomes $\mathrm{d}\sigma/\sigma > \mathrm{d}\mathcal{A}/\mathcal{A}$.

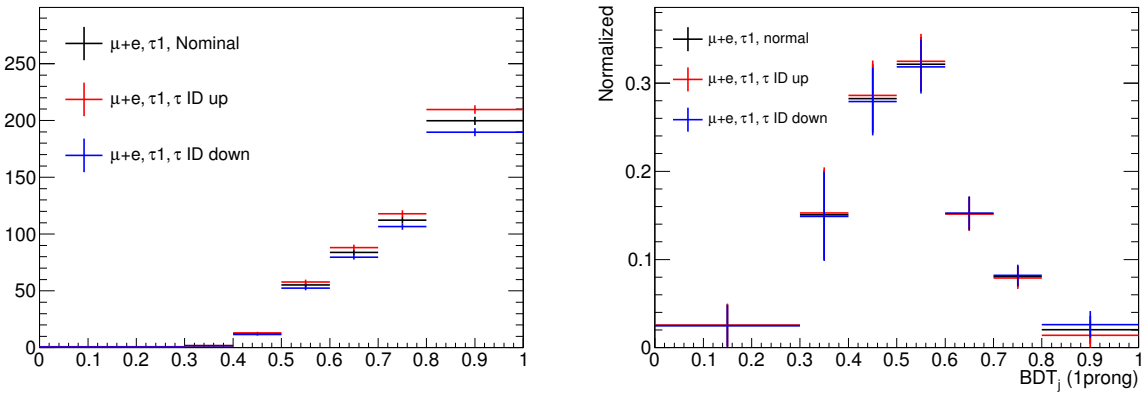

Figure 5.32: The variations of (left) the signal template and (right) the background template when varying the τ identification efficiency by $\pm 1\sigma$. Note that the signal template shape does not change.

5.8 Cross-section measurement

5.8.1 Individual cross-sections

Finally, the template fit is performed to the 2.05 fb^{-1} pp collision data accumulated by the ATLAS detector. Figure 5.33 shows the fitting results, separately for the electron and the muon channel, and for τ_1 and τ_3 candidate. Table 5.11 summarizes the results as well as the calculated cross-section.

	# of signal events	χ^2/n.d.f	MC exp.	$t\bar{t}$ cross-section
$\tau_1 + \mu$	489 ± 43	0.9	432	189 ± 17 ± 20 ± 7 pb
$\tau_3 + \mu$	135 ± 33	0.4	126	177 ± 43 ± 21 ± 6 pb
$\tau_1 + e$	443 ± 46	0.2	390	190 ± 20 ± 20 ± 7 pb
$\tau_3 + e$	116 ± 30	1.4	112	171 ± 47 ± 21 ± 6 pb

Table 5.11: (From left to right) the number of extracted signal events by the template fit, reduced χ^2, MC expectation, and the calculated cross-section. The uncertainty represents the statistical, systematic, and the luminosity uncertainty with this order.

Fitting results show a reasonable χ^2/n.d.f. around unity, showing that the method developed in this thesis works properly. When calculating the cross-section, contributions from non $t\bar{t}$ processes in the signal template are subtracted, such as τs from $Z \to \tau^+\tau^-$, diboson, and the single-top process, and electrons from $t\bar{t}$ dilepton and $Z \to e^+e^-$ process. Although the calculated cross-section tend to be slightly higher than the MC expectation, it is consistent within 1σ. The relative uncertainty on the signal extraction is an order of 9 - 10% for the τ_1 candidate and 24 - 26% for the τ_3 candidate, showing a good agreement with the ensemble test results described in section 5.6.4.

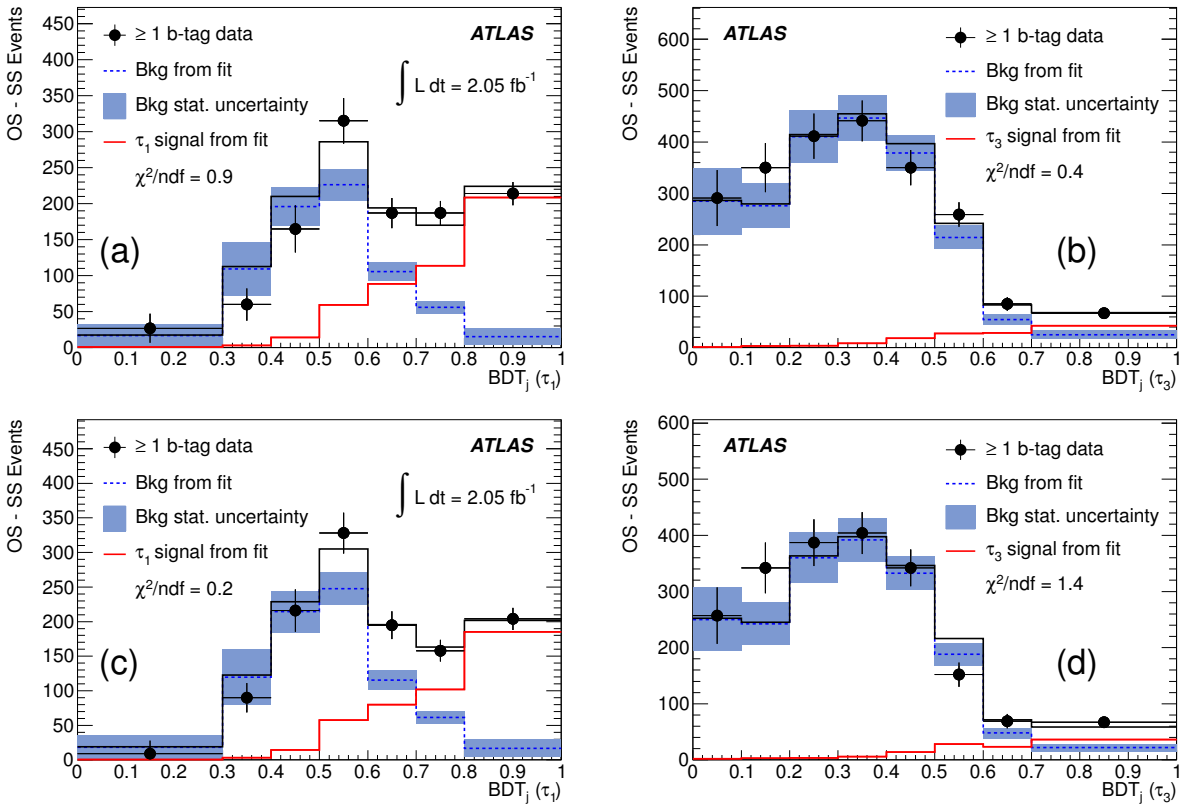

Figure 5.33: Fitting results in $\geq 1b$-tag signal region for the muon (top) and the electron (bottom) channel for the (left) τ_1 and (right) τ_3 candidate. Normalization of each template is derived from the fit to the data and are shown as the blue (signal), red (background) and the black (total) lines. The red band corresponds to the statistical uncertainty of the background template.

5.8.2 Combined cross-section

The individual cross-sections are combined using BLUE[9] [49] technique to get the final cross-section, taking into account the correlation between measurements. The statistical uncertainty is taken to be uncorrelated and the systematic uncertainties are considered to be fully correlated. In the BLUE method, the combination is taken as the weighted sum of each measurement,

$$\hat{y} = \sum \alpha_i y_i \tag{5.36}$$

where y_i denotes each cross-section, and α_i is the weight for each measurement and satisfy $\sum_i \alpha_i = 1$. Given the error matrix E, $\alpha = (\alpha_0, \alpha_1, \alpha_2, \alpha_3)$ is determined so that,

$$\chi^2 = \alpha^\dagger E \alpha \tag{5.37}$$

[9]Best Linear Unbiassed Estimator

is minimized[10]. Based on this method, the combined cross-section is calculated to be,

$$\sigma_{t\bar{t}} = 186 \pm 13 \text{ (stat.)} \pm 20 \text{ (syst.)} \pm 7 \text{ (lumi.) pb.} \tag{5.39}$$

With a total uncertainty of 13%, resulting cross-section is consistent with the perturbative QCD calculation, 164.6^{+11}_{-16} pb.

In this analysis, the background template was constructed using 0 b-tag control region in data, after subtracting real τ and electron contributions based on the MC simulation. The normalization of the subtracted $t\bar{t}$ events were based on the MC cross-section (164.6 pb). The variations of the result using the observed cross-section (186 pb), instead of the theoretical prediction has been also checked to see the stability of the measurement. The $t\bar{t}$ production cross-section was varied within the measured uncertainty, and resulted in 1.8% fluctuation. This is small enough to be covered by the current measurement uncertainty.

Figure 5.34 shows the jet multiplicity distribution, where the τ candidate is counted as a jet. The events are divided into the higher BDT_j region ($\text{BDT}_j > 0.7$) and the lower BDT_j region ($\text{BDT}_j < 0.7$). The former sample is dominated by the signal events, while the latter sample is dominated by the $t\bar{t}$ lepton plus jet background events (Figure 5.2 (a)). The data shows a clear peak at three in the higher BDT_j region, which is expected in case of the signal events: two b-jets and one τ candidate. This demonstrates that the data extracted from the analysis actually comes from the signal process. On the other hand, in lower BDT_j region, the data has a peak at four, which is also expected if the data predominantly comes from $t\bar{t}$ lepton plus jet backgrounds: two b-jets and two jets directly coming from two W bosons.

Figure 5.35 shows the invariant mass distribution between the τ candidate and the leading non b-tagged jet, denote as $m(\tau, \text{jet})$. The leading non b-tagged jet is selected if there are more than two b-tagged jets, while second leading non b-tagged jet is chosen when there is only one b-tagged jet in the event. The selected jet and the τ candidate are expected to have a mass peak around W boson in case of the $t\bar{t}$ lepton plus jet background, which is actually pronounced in the lower BDT_j region. The higher BDT_j region is expected to have a wider distribution, which is observed as well.

Figure 5.36 shows an event display of the signal candidate event including a τ_3 and a muon that passed all the event selection. The muon ($p_T = 20$ GeV) is shown in the red line, τ_3 candidate ($p_T = 53$ GeV) is shown as a jet at the lower right in the xy projection plot. The muon has a positive electric charge and the τ negative. The τ_3 candidate has $\text{BDT}_j = 0.98$, indicating that the candidate is most likely coming from real τ-lepton. The tracks inside the b-tagged jet are indicated by the light-blue tracks in the vertex region zoomed view. The b-tagged jet ($p_T = 144$ GeV) is the leading jet in the event, as expected. The missing transverse momentum observed in the event is 39 GeV. The jet multiplicity is three including a τ candidate.

[10]The error matrix E is defined in the case of two variables,

$$E = \begin{pmatrix} \sigma_1^2 & r\sigma_1\sigma_2 \\ r\sigma_1\sigma_2 & \sigma_2^2 \end{pmatrix} \tag{5.38}$$

where r is the correlation coefficient. If $r = 0$, $\hat{y} = (\sum y_i/\sigma_i^2)/(\sum 1/\sigma_i^2)$ and $1/\sigma^2 = \sum(1/\sigma_i^2)$ is derived which is the one assuming the independent measurement.

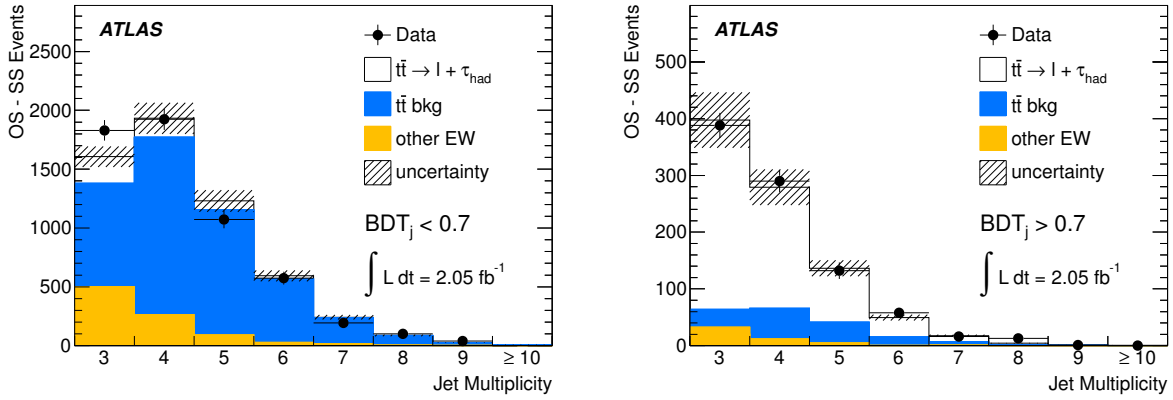

Figure 5.34: The jet multiplicity distribution for the OS−SS events in the signal region. (Left) $\mathrm{BDT}_j < 0.7$, (right) $\mathrm{BDT}_j > 0.7$. The solid circles indicate data and the histograms indicate the expected signal and background contributions from the MC simulation. The normalization of the expected signals and the backgrounds are based on the fit result.

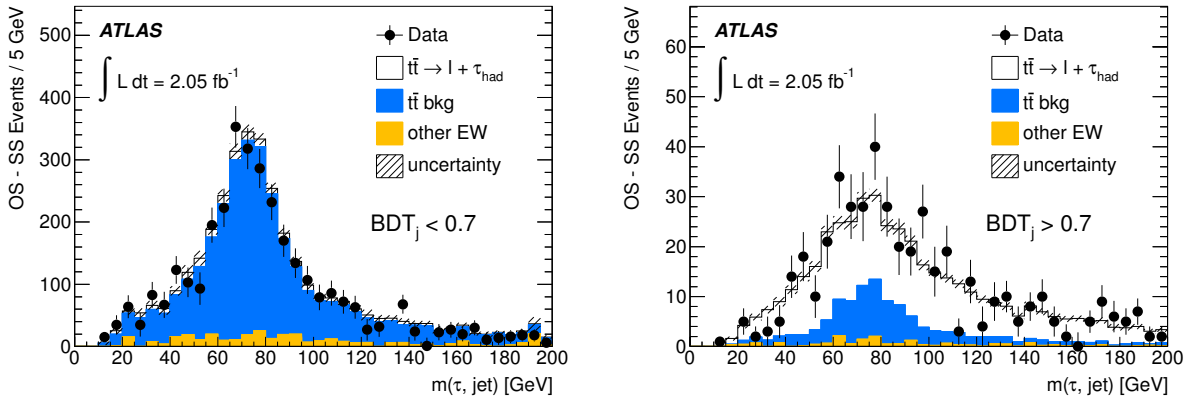

Figure 5.35: $m(\tau, \text{jet})$ distribution for the OS−SS events in the signal region. (Left) $\mathrm{BDT}_j < 0.7$, (right) $\mathrm{BDT}_j > 0.7$. Note that the W boson peak is slightly lower than actual W boson mass due to the τ energy scale.

5.8.3 Discussions on the cross-section

Interpretation of the result

This measurement is the first of the $t\bar{t}$ production cross-section in the channel with a hadronically decaying τ-lepton and an additional lepton at $\sqrt{s} = 7$ TeV with a precision of 13%. The measured cross-section, 186 ± 13 (stat.) ± 20 (syst.) ± 7 (lumi.) pb. is consistent with the perturbative QCD calculation (164^{+11}_{-16} pb), as well as the measured cross-sections using different decay channels by ATLAS [2][3][50][4] and the CMS [51][52][53][54][55] experiments performed so far. Figure 5.37 summarizes the results in both experiments.

The measured uncertainty of the ATLAS experiment in τ plus lepton channel has a better

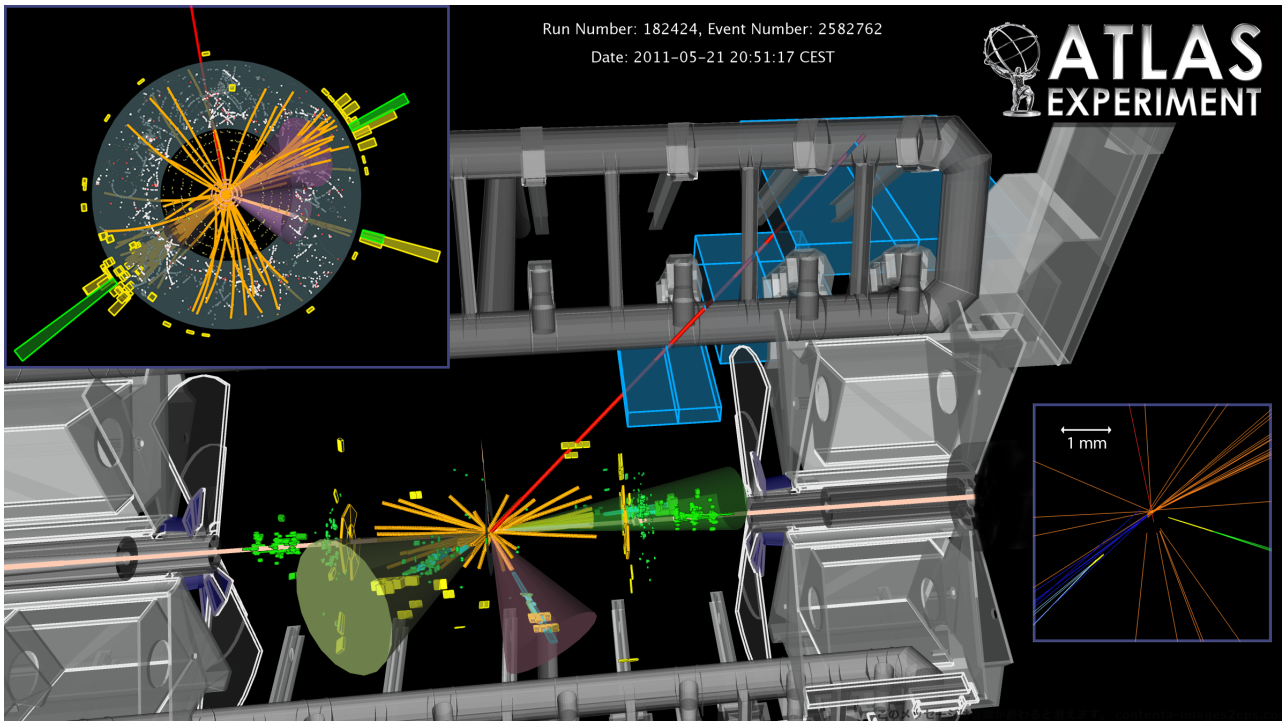

Figure 5.36: Event display of the signal candidate event ($t\bar{t} \to \tau_3^- \bar{\nu_\tau} \mu^+ \nu_\mu b\bar{b}$). The event was taken at 21$^{\text{st}}$, May, 2011.

systematic uncertainty (11%) compared to the one obtained by the CMS experiment (15%). This owe the OS−SS subtraction technique, which enable us to remove part of the backgrounds and to estimate the backgrounds in a data-driven way. This led to reduce the systematic uncertainty. In case of the CMS measurement, the number of background is estimated by assuming that the fake rate of the jet faking τ candidate is in-between the fake rate obtained in the multi-jet sample and the one in $W + 1$ fake τ candidate control sample. The fake rate is estimated from data, and the systematic uncertainty is taken as a half of the variation of the fake rate. Although the CMS experiment has a five times better S/N ratio compared to the ATLAS experiment at the expense of the signal acceptance (0.03% for CMS, 0.1% for ATLAS), the systematic uncertainty due to the background estimation overwhelm the systematic uncertainty compared to that of the ATLAS experiment.

Figure 5.38 shows the $t\bar{t}$ production cross-section as a function of the center-of-mass energy. The yellow and the blue band shows the theoretical prediction of the $p\bar{p}$ and pp collision, respectively. The dotted points show the experimental results. The data points at 1.96 TeV are measured by the former energy frontier experiment, Tevatron [56]. The measurement performed by this study corresponds to the red point.

From these results, this research has been demonstrated the validity of the SM about the t-quark decay into a τ-lepton through the $t\bar{t}$ production cross-section measurement.

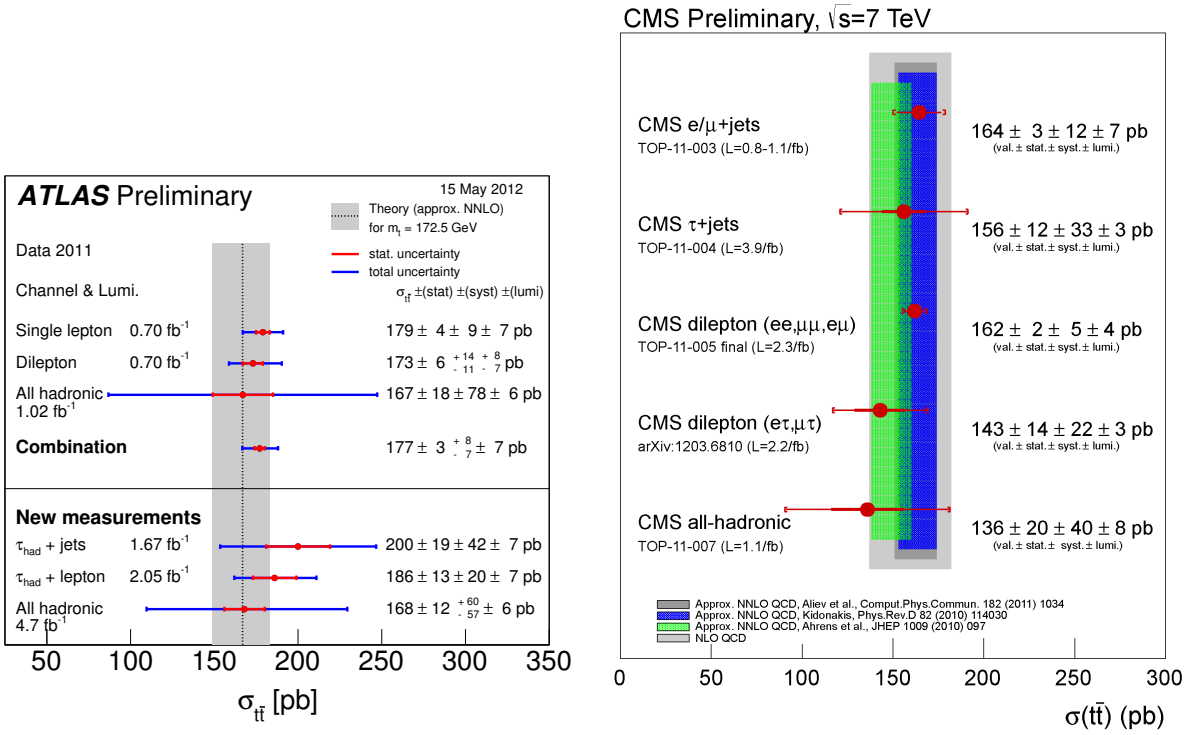

Figure 5.37: Summary of the $t\bar{t}$ production cross-section measured in ATLAS (left) and the CMS (right) experiments with corresponding theoretical expectations.

Cross-check of the result

As a cross-check purpose, the template fit is also performed with various combinations of the templates, as followings:

- The background template without the MC weighting factor
- The background template derived from $W + 1$ fake τ control region
- The signal template derived from $Z \to \tau_\mu \tau_{\mathrm{had}}$ control region, based on the MC simulation

And all of them were found to be consistent with the result within the uncertainty.

The cross-section has been also cross-checked using the another background estimation method, so-called the matrix method. The matrix method solves the simple system of equations based on the signal efficiency and the fake rate at $\mathrm{BDT}_j = 0.7$ cut, where the efficiency is estimated based on the MC simulation and the fake rate is estimated using $W + 1$ fake τ control region in data [D.4].

All the τ candidates are labeled as loose, and the τ candidates that satisfy $\mathrm{BDT}_j > 0.7$ are labeled as tight. The probability that the loose τ candidate also becomes the tight τ candidates

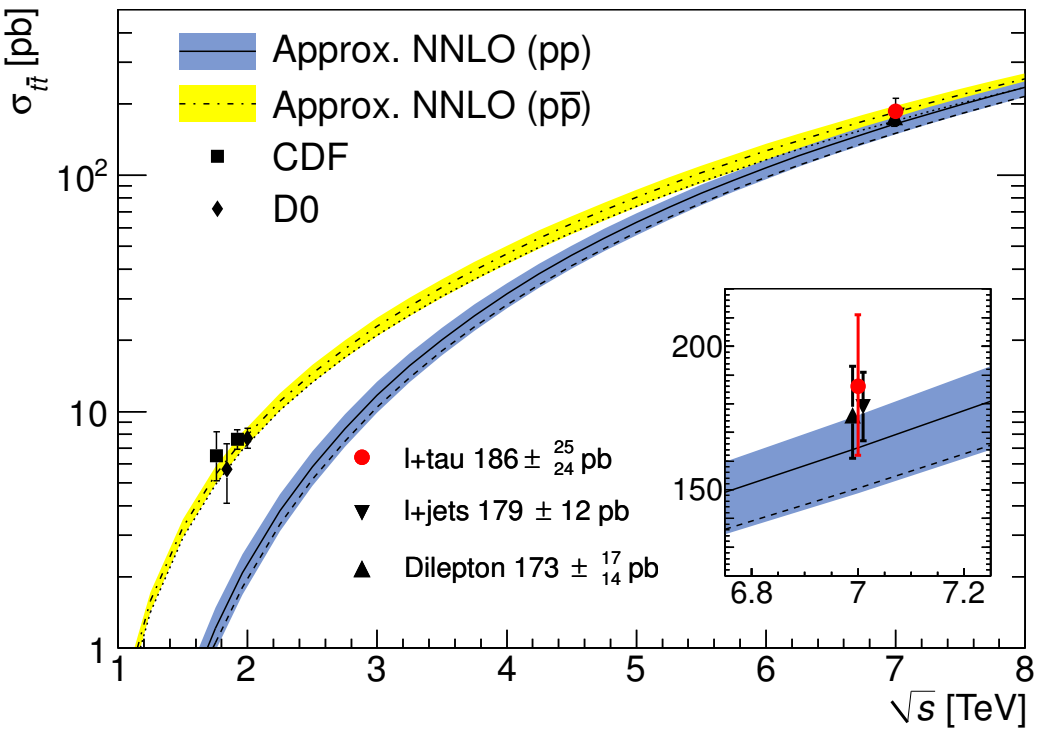

Figure 5.38: $t\bar{t}$ production cross-section as a function of the center-of-mass energy. The yellow and the blue band shows the theoretical prediction (NNLO) for $p\bar{p}$ (Tevatron) and pp (LHC) collisions, respectively.

is defined as followings, for both the τ-lepton and the fake τ-lepton:

$$\varepsilon_{\text{real}} = \frac{N_{\text{real}}^{\text{tight}}}{N_{\text{real}}^{\text{loose}}}, \qquad \varepsilon_{\text{fake}} = \frac{N_{\text{fake}}^{\text{tight}}}{N_{\text{fake}}^{\text{loose}}} \tag{5.40}$$

where the subscript "real" denotes a τ-lepton and the "fake" denotes fake τ candidate and N is the number of τ candidate. Then, the number of tight τ-lepton is given by,

$$N_{\text{real}}^{\text{tight}} = N_{\text{data}}^{\text{tight}} - \frac{\varepsilon_{\text{fake}}}{\varepsilon_{\text{real}} - \varepsilon_{\text{fake}}} \left(N_{\text{data}}^{\text{loose}} \varepsilon_{\text{real}} - N_{\text{data}}^{\text{tight}} \right) \tag{5.41}$$

Note that the OS−SS subtraction technique is also applied to the matrix method approach.

The efficiency (ϵ_{real}) and the fake rate (ϵ_{fake}) are measured separately for three f_{EM} bins, which is the ratio of the energy measured in the electromagnetic calorimeter to the total energy of the τ candidate measured in the calorimeter. This variable is an effective variable for splitting the data into regions where the shape of the OS−SS BDT$_j$ distribution in MC becomes similar between $W + 1$ fake τ control region and the background distribution in the ≥ 1 b-tag signal region [D.5]. The obtained cross-section in the matrix-method shows 165±13 (stat.)$^{+16}_{-15}$ (syst.)± 6 (lumi.) pb, which is comparable to the cross-section result obtained by the template fit.

Interpretation to the charged Higgs boson

The measured $t\bar{t}$ production cross-section in τ-lepton final state is sensitive to the charged Higgs boson, which is predicted by the supersymmetry model that in some scenarios predominantly decays into $\tau\nu_\tau$. Assuming that the difference between the observed cross-section and the predicted cross-section is attributed to the contributions from the charged Higgs boson, the upper limit has been set on the branching ratio that the t-quark decays into a charged Higgs boson ($H^\pm$) and a b-quark, where the charged Higgs boson is assumed to decay into a $\tau\nu_\tau$ with 100% probability.

In order to calculate the upper limit, $t\bar{t}$ events are simulated using PYTHIA event generator with its decay including a charged Higgs boson, assuming that the charged Higgs boson mass ($m_{H^\pm}$) to be [90, 160] GeV, with 10 GeV step. The MC samples include $t\bar{t} \to b\bar{b}H^\pm W^\mp$ and $t\bar{t} \to b\bar{b}H^\pm H^\mp$ process with the decay mode of the charged Higgs boson is fixed to be $H^\pm \to \tau^\pm\nu$. The upper limit was calculated based on the $\mathrm{CL_s}$ method [57]. Assuming the error is gaussian, $\mathrm{CL_s}$ is defined as,

$$\mathrm{CL}_b = P(N < N_{obs}; b) \tag{5.42}$$

$$\mathrm{CL}_{s+b}(\mu) = P(N < N_{obs}; \mu s + b) \tag{5.43}$$

$$\mathrm{CL}_s = \frac{\mathrm{CL}_{s+b}}{\mathrm{CL}_b} \tag{5.44}$$

where CL_b denotes the probability that the number of events (N) become smaller than the observed number of events (N_{obs}), while CL_{s+b} is the probability that the observed number of events can be explained by $s+b$ hypothesis. μ is called as the signal strength. If $\mathrm{CL}_{s+b} = 0.05$, it is said that the μ is excluded by 95% confidence level. The concept of each variables are depicted in Figure 5.39.

In case of this measurement, background only hypothesis provides the number of observed events to be

$$\mathcal{L}\sigma_{t\bar{t}}\mathcal{A} \times (1-\mathcal{B})^2 \tag{5.45}$$

where $\mathcal{A}$ is the signal acceptance and $\mathcal{B}$ is the upper limit on the branching ratio, $\mathcal{B}(t^\pm \to H^\pm b)$. On the other hand, the signal plus background hypothesis provides the number of

$$\mathcal{L}\sigma_{t\bar{t}}\mathcal{A} \times (1-\mathcal{B})^2 + \mathcal{L}\sigma_{t\bar{t}}\mathcal{A} \times 2\mathcal{B}(1-\mathcal{B}) \tag{5.46}$$

Since the above quantity is a function of $\mathcal{B}$, $\mathcal{B}$ is increased until following condition is satisfied.

$$\frac{\int_0^N P(n; s+b)dn}{\int_0^N P(n_b; b)dn_b} = 0.05 \tag{5.47}$$

This is the standard CL_s approach, giving an upper limit with 95% confidence level.

Figure 5.40 shows the resulting upper limit as a function of $m_{H^\pm}$ and the corresponding exclusion limit on $\tan\beta$ - $m_{H^\pm}$ plane. By this measurement, the upper limit is set from 4 to 8%, depending on the assumed charged Higgs boson mass. The sensitivity becomes lower as the charged Higgs boson mass becomes larger. This is due to the fact that the p_T of the b-jet

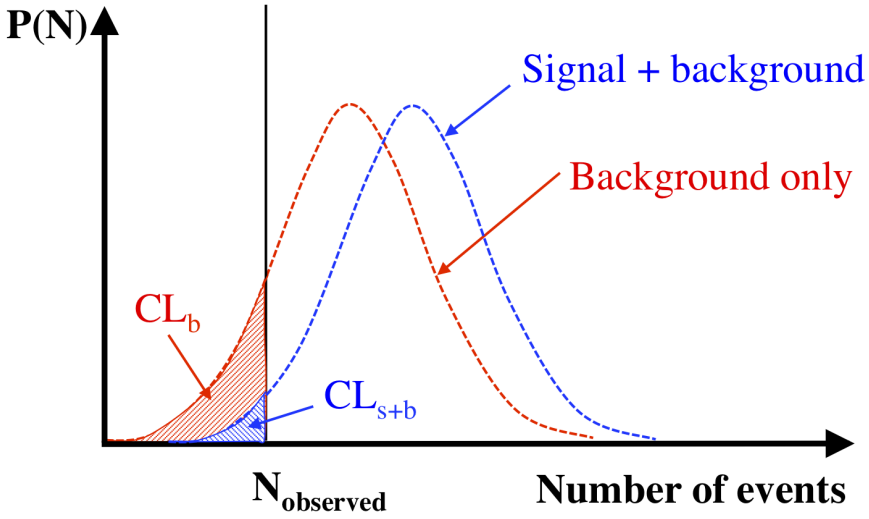

Figure 5.39: Schematic picture explaining CL_b and CL_{s+b}.

via the $t^{\pm} \to H^{\pm}b$ decay becomes softer as it is proportional to the t-quark mass minus the charged Higgs boson mass. This especially affects to the signal acceptance on the number of jet requirement, which results in lower sensitivity [D.6]. The cut efficiency for the number of jet requirement is 86% in case of $m_{H^{\pm}} = 90$ GeV, while 64% in case of $m_{H^{\pm}} = 160$ GeV.

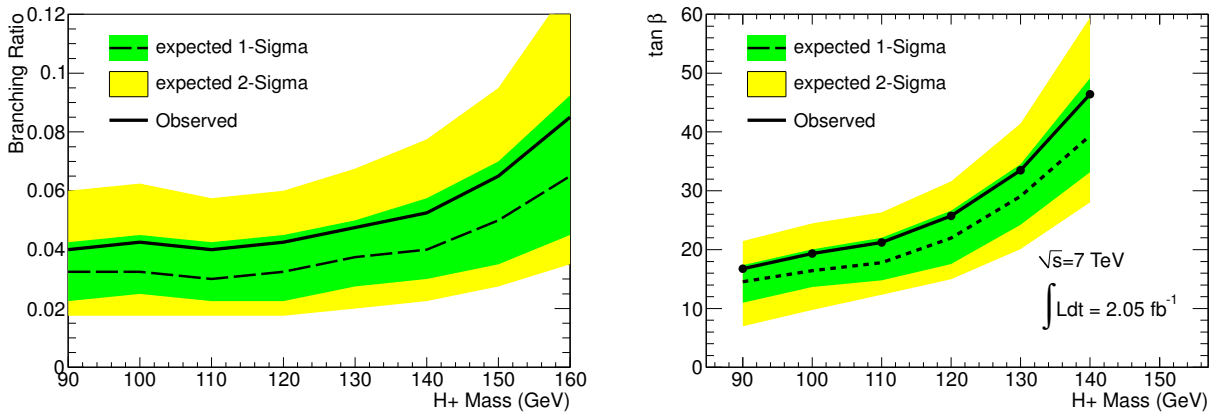

Figure 5.40: (left) observed upper limit on $\mathcal{B}(t^{\pm} \to H^{\pm}b)$ as a function of $m_{H^{\pm}}$, and (right) exclusion on $\tan\beta - m_{H^{\pm}}$ parameter plane.

The former energy frontier experiment, Tevatron set an upper limit on the branching ratio based on the 0.9 fb^{-1} $p\bar{p}$ collision data using $t\bar{t}$ events. The upper limit of 15 - 25% was obtained depending on the assumed charged Higgs boson mass between 80 GeV $< m_{H^{\pm}} <$ 155 GeV. This measurement improved the upper limit by a factor of 4.

In order to increase the sensitivity and to search for new physics in a model-independent way, the ratio of the measured $t\bar{t}$ cross-section between the di-lepton channel and the τ plus lepton channel ($\mathcal{R}_{\sigma}^{\tau\ell/\ell\ell}$) are evaluated, which is defined as

$$\mathcal{R}_{\sigma}^{\tau\ell/\ell\ell} = \frac{\sigma(t\bar{t} \to \tau + \ell)}{\sigma(t\bar{t} \to \ell + \ell)}. \tag{5.48}$$

where $\sigma(t\bar{t} \to \ell + \ell)$ and $\sigma(t\bar{t} \to \tau + \ell)$ denotes the observed cross-section in the di-lepton channel and the τ plus lepton channel. By taking a ratio, most of the systematic uncertainties which is common between two measurements are partially cancelled out, such as the luminosity uncertainty. If the charged Higgs boson exists and it predominantly decays into $\tau\nu_{\tau}$, large $\mathcal{R}_{\sigma}^{\ell\tau/\ell\ell}$ value should be observed compared to the unity. The DØ experiment at the Tevatron has been performed this measurement using 1.0 fb^{-1} $p\bar{p}$ collision data, and they obtained

$$\mathcal{R}_{\sigma}^{\ell\tau/\ell\ell} = 0.97^{+0.32}_{-0.29}\ [58]. \tag{5.49}$$

In this thesis, all the possible combinations of the ratio: $\mathcal{R}_{\sigma}^{\tau e/ee}$, $\mathcal{R}_{\sigma}^{\tau\mu/\mu\mu}$, $\mathcal{R}_{\sigma}^{\tau e/e\mu}$ and $\mathcal{R}_{\sigma}^{\tau\mu/e\mu}$ were considered. In order to avoid the real τ contributions in the di-lepton channel such as $t\bar{t} \to \tau_{\ell}\nu_{\tau}\ell\nu_{\ell}b\bar{b}$ (11% for ee, 14% for $\mu\mu$ and 12% for $e\mu$ channel) and $t\bar{t} \to \tau_{\ell}\nu_{\tau}\tau_{\ell}\nu_{\tau}b\bar{b}$ process ($0.4 - 0.5\%$) are eliminated based on the MC simulation, where τ_{ℓ} denotes the leptonic decay of the τ-lepton. Figure 5.41 shows an example of the comparison between the di-lepton ($\mu\mu$) channel and the τ plus muon channel, as well as its ratio for each systematic source. Another comparisons are shown in [D.7]. As expected, part of the systematic uncertainties are cancelled out, while the one related to the τ identification is only one-sided. The systematic uncertainty related to the $b-$tagging is not cancelled out so much due to the fact that these uncertainties distort the background template, and thus have a correlation between the signal acceptance in τ plus lepton channel (Section 5.7.4). Since the systematic uncertainty on the di-lepton channel simply comes from the uncertainty on the signal acceptance, variations of the systematic uncertainty becomes different between two channels. As a consequence, we got,

$$\mathcal{R}_{\sigma}^{\tau e/ee} = 1.02 \pm 0.13(\text{stat.})^{+0.09}_{-0.10}(\text{syst.}), \tag{5.50}$$

$$\mathcal{R}_{\sigma}^{\tau\mu/\mu\mu} = 1.06 \pm 0.10(\text{stat.})^{+0.07}_{-0.06}(\text{syst.}), \tag{5.51}$$

$$\mathcal{R}_{\sigma}^{\tau e/e\mu} = 0.97 \pm 0.10(\text{stat.}) \pm 0.06(\text{syst.}), \tag{5.52}$$

$$\mathcal{R}_{\sigma}^{\tau\mu/e\mu} = 0.97 \pm 0.09(\text{stat.}) \pm 0.08(\text{syst.}). \tag{5.53}$$

Finally, above results are combined taking into account the statistical overlap between each measurement. For this purpose, pseudo experiments are performed to evaluate possible fluctuation on the ratio by actually fluctuating observed cross-section with its statistical uncertainty. The systematic uncertainty is considered to be 100% correlated between each measurement except for electron and muon related one. The combined result is,

$$\mathcal{R}_{\sigma}^{\tau\ell/\ell\ell} = 1.00 \pm 0.07(\text{stat.}) \pm 0.06(\text{syst.}) \tag{5.54}$$

Figure 5.42 shows the summary of the ratio as well as its combined result, where all of them are found to be consistent with unity. The uncertainty of the combined result is 9%, which is the most precise measurement performed so far.

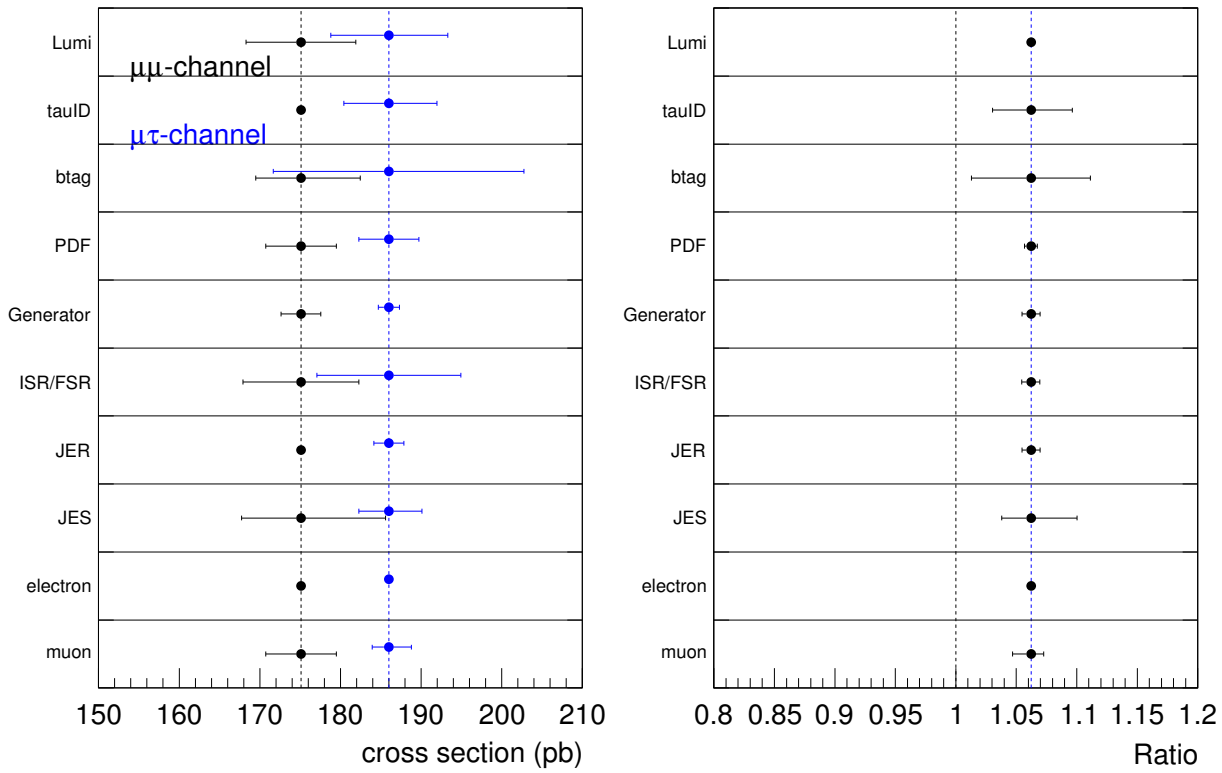

Figure 5.41: (Left) Variations of the cross-section for each systematic source between the di-muon channel (black) and the τ plus muon channel (blue). (Right) The ratio between them, $\mathcal{R}_{\sigma}^{\tau\mu/\mu\mu}$.

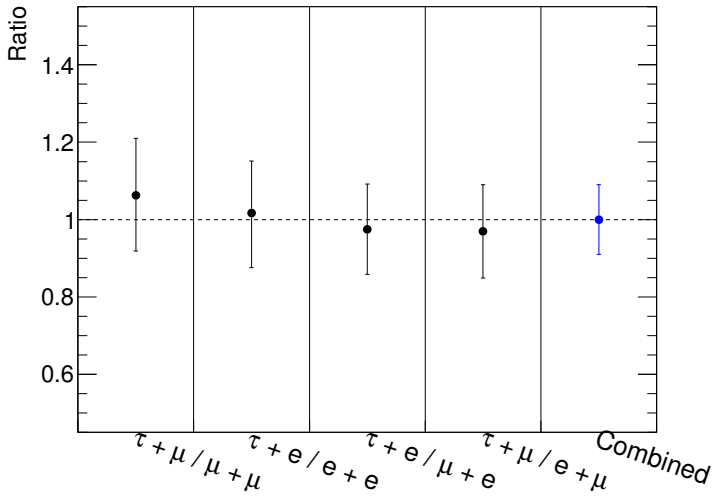

Figure 5.42: Results of the measured $\mathcal{R}_{\sigma}^{\ell\tau/\ell\ell}$ for the possible combination of the di-lepton channel and the τ plus lepton channel.

Chapter 6

Conclusion

A measurement of the t-quark pair production cross-section is presented using final states characterized by a lepton (a muon or an electron) and a hadronically decaying τ-lepton ($t\bar{t} \to \tau^+\nu_\tau\ell^-\bar{\nu}_\ell b\bar{b}$). The analysis was based on the 2.05 fb^{-1} pp collision data at $\sqrt{s} = 7$ TeV produced by the LHC and recorded by the ATLAS detector from April to August during 2011.

The candidate events are extracted based on the event topology of the final state. The selection has been optimized based on the simulation to maximize the signal significance. The analysis then exploits the multi-variate analysis based on a Boosted Decision Tree (BDT) on the reconstructed τ candidate to isolate signal events from backgrounds where one of the jets misidentified as a hadronically decaying τ-lepton. The number of background events among the candidate events has been estimated in a data-driven way to minimize the systematic uncertainty. The obtained $t\bar{t}$ production cross-section is:

$$\sigma_{t\bar{t}} = 186 \pm 13 \text{ (stat.)} \pm 20 \text{ (syst.)} \pm 7 \text{ (lumi.) pb},$$

where each uncertainty represents the statistical uncertainty, the systematic uncertainty and the uncertainty related to the luminosity determination, respectively.

A unique feature of the present analysis is the method to extract $t\bar{t}$ events with hadronically decaying τ-lepton at the LHC. This includes followings:

- The application of the multivariate analysis that has a large separation power between the signal events and backgrounds, enabling us to keep high signal acceptance.
- The usage of the same-sign events (a charge correlation between a lepton and a reconstructed τ candidate), which is composed of pure backgrounds, to model part of the backgrounds in the signal region. This makes it possible to model the backgrounds in a data-driven way, which leads to a reduction of the systematic uncertainty.

An application of the signal extraction method leads to the most precise measurement of the $t\bar{t}$ production cross-section in τ-lepton final state with $\mathrm{d}\sigma/\sigma = 13\%$. The measured cross-section is in good agreement with other measurements performed by ATLAS and the CMS experiment so far, and with the perturbative QCD calculation (164^{+11}_{-16} pb), demonstrating the validity of the Standard Model about the t-quark decay into τ-lepton. The method developed

in this thesis is being used for new physics search such as the charged Higgs boson, where the $t\bar{t}$ process in τ-lepton final state becomes the dominant background.

From the obtained cross-section, the upper limit on the branching ratio that the t-quark decays into a charged Higgs boson and a b-quark is calculated to be $\mathcal{B}(t^{\pm} \to H^{\pm}b) < 4$ - 8% with 95% confidence level, depending on the assumed charged Higgs boson mass ($m_{H^{\pm}}$) in a range of 90 GeV $< m_{H^{\pm}} <$ 160 GeV. The ratio of the observed cross-section to that of the di-lepton channel gives 1.00 ± 0.09, which also support the Standard Model expectation. Further improvement on the systematic uncertainty will lead to the better measurement that can probe new physics effect.

Appendix A

Additions for Chapter 2

A.1 Spontaneous symmetry breaking and the mass of the gauge bosons and fermions

The weak interaction is a consequence of the short-ranged force mediated by massive $W^{\pm}$ and Z bosons ($M_W = 80$ GeV, $M_Z = 91$ GeV). However, the mass of the gauge boson is originally required to be zero to keep the Lagrangian to be invariant under the gauge transformations (gauge symmetry).

To solve this problem, a spin zero field, called a Higgs field, is assumed. The Higgs field is a doublet in $SU(2)$ space and carries $U(1)$ hyper charge, but is singlet in color space. The gauge bosons and fermions can interact with this field and acquire non zero masses through the spontaneous symmetry breaking.

Suppose $SU(2)$ Higgs field, ϕ that carries hyper charge $Y = 1$ and weak isospin $T_3 = 1/2$.

$$\phi = \begin{pmatrix} \phi^+ \\ \phi^0 \end{pmatrix} \tag{A.1}$$

where ϕ^+ and ϕ^- are each complex fields,

$$\phi^+ = \frac{\phi_1 + i\phi_2}{\sqrt{2}} \tag{A.2}$$

$$\phi^0 = \frac{\phi_3 + i\phi_4}{\sqrt{2}}. \tag{A.3}$$

The charge assignment in equation (A.1) is given by the electric charge defined as

$$Q = T_3 + \frac{Y_H}{2} \tag{A.4}$$

where Y_H is the hyper charge of the Higgs field.

The Lagnrangian of the Higgs field can be written as

$$\mathcal{L}_\phi = (\partial_\mu \phi)^\dagger (\partial^\mu \phi) - \mu^2 \phi^\dagger \phi - \lambda (\phi^\dagger \phi)^2, \tag{A.5}$$

where

$$\phi^\dagger\phi = \frac{(\phi_1^2 + \phi_2^2 + \phi_3^2 + \phi_4^2)}{2}. \tag{A.6}$$

The last two term in equation (A.5) is the potential term and denote as $V(\phi) = \mu^2\phi^\dagger\phi - \lambda(\phi^\dagger\phi)^2$. Then, $V(\phi)$ is invariant under the local gauge transformation.

$$\phi(x) \rightarrow \phi^{'}(x) = e^{i\vec{\alpha}(x)\cdot\vec{\tau}/2}\phi(x) \tag{A.7}$$

where τ_1 is the Pauli matrices and α_i are the parameters.

Suppose $\mu^2 < 0$, $V(\phi)$ has a minimum at

$$\phi^\dagger\phi = \frac{-\mu^2}{2\lambda} = \frac{v^2}{2} \tag{A.8}$$

Given the definition in equation (A.6), there are many solutions that can satisfy above. Therefore, certain vacuum ϕ_0 is defined so that $\phi_3 = v$ and $\phi 1 = \phi_2 = \phi_4 = 0$. Considering the expansion around the vacuum, ϕ is chosen to be

$$\phi = \frac{1}{\sqrt{2}}\begin{pmatrix} 0 \\ v + H(x) \end{pmatrix} \tag{A.9}$$

This choice is guaranteed because one can make a gauge transformation $\phi \rightarrow \phi^{'} = e^{i\vec{\tau}\cdot\vec{\theta}/v}\phi$ for an arbitrary $\phi(x)$ and rotate $\phi(x)$ into the form of equation (A.9). By choosing a certain direction, this results in three massless goldstone boson and finally becomes the longitudinal parts of the massive W and Z boson.

Finally, in order to make the Lagrangian to be invariant under the local gauge transformation given in equation (A.7), ∂_μ is replaced by the covariant derivative D_μ, defined as

$$D_\mu = \partial_\mu - ig_1\frac{Y_H}{2}B_\mu - ig_2\frac{\vec{\tau}}{2}\cdot\vec{W} \tag{A.10}$$

where B_μ and $\vec{W_\mu}$ are the gauge fields which is introduced to keep the gauge covariance in $U(1) \oplus SU(2)_L$ transformation. $\vec{\tau} = \sigma/2$ is the $SU(2)$ generator and Y_H is the hypercharge of the Higgs field.

Once ϕ get the vacuum expectation value, the Lagrangian get the extra term,

$$\phi^\dagger\left(ig_1\frac{Y}{2}B_\mu + ig_2\frac{\vec{\tau}}{2}\cdot\vec{W_\mu}\right)^\dagger\left(ig_1\frac{Y}{2}B^\mu + ig_2\frac{\vec{\tau}}{2}\cdot\vec{W}^\mu\right)\phi \tag{A.11}$$

By substituting $Y = 1$ and $\phi = 1/\sqrt{2}(0, v)$, this becomes,

$$\left(\frac{1}{2}vg_2\right)^2 W_\mu^+ W^{-\mu} + \frac{vg^2}{2}\frac{1}{\cos^2\theta_W}Z_\mu Z^\mu \tag{A.12}$$

where $W^\pm = (W_1\mu \pm iW_2\mu)/\sqrt{2}$, $Z_\mu = \cos\theta_W W_{3\mu} - \sin\theta_W B_\mu$ and $\cos\theta_W = g_2/\sqrt{g_1^2 + g_2^2}$. Therefore, the mass term for the W and Z boson becomes,

$$m_W = \frac{gv}{2} \tag{A.13}$$

$$m_Z = \frac{gv}{2\cos\theta_W} \tag{A.14}$$

$$\tag{A.15}$$

Since there is no $A^\mu A_\mu$ term, the massless photon is expected. The vacuum expectation value is related to the Fermi's constant ($G_F = 1.16 \times 10^{-5}$ GeV^{-5}) like,

$$v = (\sqrt{2}G_F)^{-1/2} = 246 \text{ GeV}. \tag{A.16}$$

In the SM, fermion mass term $\mathcal{L} = -m(\bar{\phi_L}\phi_R + \bar{\phi_R}\phi_L)$ is required to be zero as this will break the gauge symmetry. However, using the Higgs field defined in the previous section, one can add following interaction term for the fermion. In case of the lepton,

$$\mathcal{L}_{\text{int}} = g_e \left(\bar{L}\phi \bar{e_R} + \phi^\dagger \bar{e_R} L \right). \tag{A.17}$$

where,

$$L = \begin{pmatrix} \nu_e \\ e^- \end{pmatrix} \quad \phi = \begin{pmatrix} \phi^+ \\ \phi^0 \end{pmatrix}. \tag{A.18}$$

After the spontaneous symmetry breaking, substituting equation (A.9) gives, in the case of leptons,

$$\mathcal{L}_{\text{int}} = \frac{g_e v}{2} \left(\bar{e_L} e_R + \bar{e_R} e_L \right) + \frac{g_e}{2} \left(\bar{e_L} e_R + \bar{e_R} e_L \right) H \tag{A.19}$$

The first term represents the mass term, where its mass is given by $g_e v/\sqrt{2}$. The second term represents the interaction between the Higgs field and the fermion with its coupling strength given by m_e/v.

In case of quarks, it is well known that if $\phi = \begin{pmatrix} a \\ b \end{pmatrix}$ is an $SU(2)$ doublet, then ϕ_c which is defined as

$$\phi_c = -i\tau_2 \phi^* = \begin{pmatrix} -b^* \\ a^* \end{pmatrix} \tag{A.20}$$

becomes also the $SU(2)$ doublet. Then, one can also write terms in $\mathcal{L}_{\text{int}}$ using,

$$\phi_c = \begin{pmatrix} -\phi^{0*} \\ \phi^- \end{pmatrix}. \tag{A.21}$$

One can expand ϕ_c as followings after the spontaneous symmetry breaking.

$$\phi_c \rightarrow \begin{pmatrix} -\frac{v+H}{2} \\ 0 \end{pmatrix}. \tag{A.22}$$

Then, the interaction Lagrangian of the quarks,

$$\mathcal{L}_{\text{int}} = g_d \bar{Q_L} \phi d_R + g_u \bar{Q_L} \phi_c u_R \tag{A.23}$$

$$= m_d \bar{d} d + m_u u \bar{u} + \frac{m_d}{v} \bar{d} d H + \frac{m_u}{v} \bar{u} u H \tag{A.24}$$

The first two term represents the fermion masses and the last two term represents the interaction of d and u quarks with Higgs boson. This representation is expanded to three generations of the quark and leptons. The coefficient of each term is an arbitrary parameter, and not related to each other, the masses have to be measured. The verification of the characteristics of the Higgs boson that the coupling strength is proportional to the fermion mass is an essential experimental aspect one the Higgs boson is discovered.

A.2 SuperSymmetry

The super symmetry (SUSY) is the symmetry between the fermion and the boson. It predicts the existence of the SM counterpart with spin 1/2 difference. The main motivation to introduce the SUSY is to solve the hierarchy problem, where the Higgs boson mass is fine tuned.

Theoretically, the supersymmetric operator $Q_{\alpha i}$ is introduced, where α is the spinor index and the i is the number of degree of freedom ($1 \leq i \leq N$). It operates to the bosonic state $|B\rangle$ and transform it into the fermionic state $|F\rangle$ such that,

$$Q_{\alpha i}|B\rangle \sim |F\rangle \tag{A.25}$$

This means that the $Q_{\alpha i}$ is the operator to exchange the fermion and the boson. Suppose $i = 1$, $Q_\alpha \equiv Q_{\alpha,1}$ satisfies following algebra:

$$[Q_\alpha, M^{\mu\nu}] = i(\frac{1}{2}\sigma^{\mu\nu}Q)_\alpha \tag{A.26}$$

$$[Q_\alpha, P^\mu] = 0 \tag{A.27}$$

$$\{Q_\alpha, \bar{Q}_\beta\} = -2(\gamma_\mu)_{\alpha\beta}P^\mu \tag{A.28}$$

$$\{Q_\alpha, Q_\beta\} = \{\bar{Q}_\alpha, \bar{Q}_\beta\} = 0 \tag{A.29}$$

where $\sigma^{\mu\nu} = (1/2i)[\gamma^\mu, \gamma^\nu]$, $\bar{Q} = Q^\dagger\gamma^0$. The first term means that Q_α acts as a spinor. The second term represents Q_α is the conserved quantity and that Q_α can also commute with $m^2 = P_\mu P^\mu$, thus Q_α does not change the mass. This means that the SUSY partner should have the same mass with that of the SM partners. However such SUSY particles are not yet observed and the SUSY is broken in some extent. This broken scale is acceptable up to $\mathcal{O}(1$ TeV). The third term indicates that if Q is operated twice, that becomes a momentum operator.

Though the number of particles become twice by introducing the SUSY, many possible new interactions can be considered and expect to solve several problems as followings.

Hierarchy problem of the Higgs boson mass SUSY is expected to solve the quadratical divergence of the Higgs mass. Because it can reduce the size of the quantum corrections by having automatic cancellations between fermionic and bosonic Higgs coupling. As is shown in Figure A.1, the fermionic top quark (t) loop and the scalar stop ($\tilde{t}$) squark loop can cancel out each contributions. The fermion has a infinite number of negative energy originated from the Dirac's sea, while the boson has a infinite number of positive energy originated from the zero-point oscillation of the harmonic oscillator.

Candidate of the dark matter In many SUSY models, there is a heavy stable particle with neutral charge. The existence of the supersymmetric dark matter candidate is due to the R-parity conservation, which is defined as

$$R = (-1)^{3(B-L)+2s} \tag{A.30}$$

Due to the R-parity conservation, the lightest SUSY particle (LSP) cannot decay. Therefore, LSP can be the candidate for the dark matter. In order to fit the observations, it is assumed that the mass of LSP should be around 100 GeV to 1 TeV.

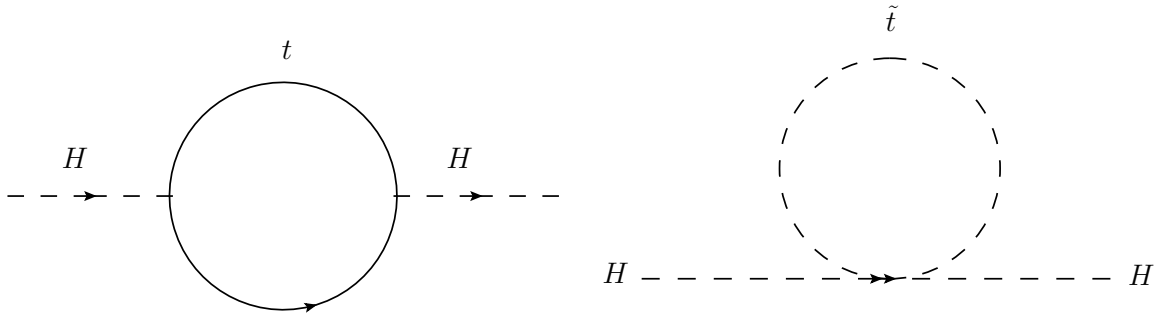

Figure A.1: By introducing the stop squark ($\tilde{t}$), i.e., the bosonic parter of the top quark, the hierarchy problem of the Higgs boson mass can be avoided.

Unification of the gauge coupling constant The renormalization group evolution of the gauge coupling constants is sensitive to the present SM particle content. Currently, these coupling constants do not meet together at the unification scale (10^{16} GeV). However if the SUSY exists, the coupling constants will be converged at approximately 10^{16} GeV [59], as is shown in Figure A.2.

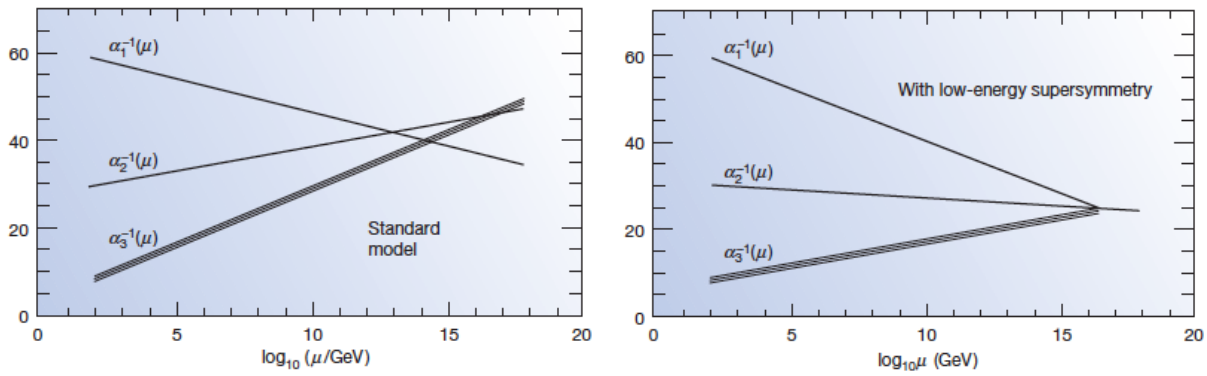

Figure A.2: By introducing SUSY particles, the coupling constant of three gauge bosons meet at the energy scale of $\mathcal{O}(10^{16}$ GeV) [60].

A.3 Measurement of the strong coupling constant

There are a wide range of methods used to measure the strong coupling constant, such as the one using deep inelastic scattering, τ lepton decay, quarkonium spectroscopy, e^+e^- annihilation, and the hadron-hadron scattering. One of the most simplest example is to use the e^+e^- annihilation process, where the absolute value of α_s is evaluated by measuring the R ratio which is given

by,

$$R(Q) = \frac{\sigma(e^+e^- \to \text{hadrons})}{\sigma(e^+e^- \to \mu^+\mu^-)} = R_{\text{EW}}(Q)(1 + \delta_{\text{QCD}}(Q)), \tag{A.31}$$

where δ_{QCD} is a function of $\alpha_s(Q^2)$.

For each measurement, the typical momentum scale Q is given together with the measured value at that scale, $\alpha_s(Q)$. It is often the case to extrapolate α_s to the Z boson mass scale, $\alpha_s(M_Z)$. Figure A.3 shows the summary of $\alpha_s(M_Z)$. The method used to evaluate α_s is also written in the plot.

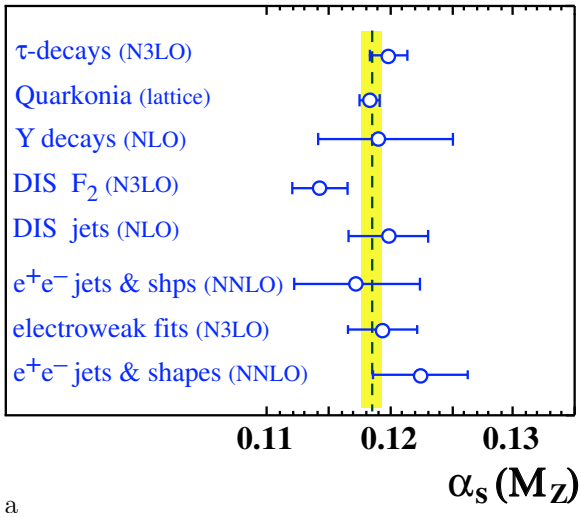

a

Figure A.3: Summary of the $\alpha_s(M_Z)$ measurement.

A.4 Evolution of the PDF

The evolution of the PDF can be derived as followings.

$$\frac{\mathrm{d}q_i(x,Q^2)}{\mathrm{d}\log(Q^2)} = \frac{\alpha_s}{2\pi}\int_x^1 \left(q_i(z,Q^2)P_{qq}\left(\frac{x}{z}\right) + g(z,Q^2)P_{qg}\left(\frac{x}{z}\right)\right)\frac{dz}{z} \tag{A.32}$$

$$\frac{\mathrm{d}g(x,Q^2)}{\mathrm{d}\log(Q^2)} = \frac{\alpha_s}{2\pi}\int_x^1 \left(\sum_i q_i(z,Q^2)P_{gq}\left(\frac{x}{z}\right) + g(z,Q^2)P_{gg}\left(\frac{x}{z}\right)\right)\frac{dz}{z} \tag{A.33}$$

where $q_i(x,Q^2)$ and $g(x,Q^2)$ represents the PDF for the quark type i and the gluon, respectively. $P_{p'p}$ is called splitting function, which is the probability that a parton type p converts into a parton type p' carrying a momentum fraction of x/z (z is the initial parton momentum). The first equation describes the change of the quark densities with Q^2 due to the gluon radiation and the gluon splitting. The second equation describes the change of the gluon density with Q^2 due to the gluon radiation off quarks and gluons. Since this equation assumes massless partons, this argument is only valid for the gluon and the light quarks (u, d, s).

Appendix B

Additions for Chapter 3

B.1 Pseudo rapidity

The center-of-mass of the parton-parton scattering is normally boosted with respect to that of two incoming hadrons. Therefore, it is useful to classify the final state in terms of variables which transform simply under longitudinal boosts. For this purpose, the rapidity y, the transverse momentum p_T and the azimuthal angle ϕ are used. The rapidity y is defined as,

$$y = \frac{1}{2}\ln\left(\frac{E+p_z}{E-p_z}\right) = \ln\left(\frac{E+p_z}{\sqrt{p_T^2+m^2}}\right) \tag{B.1}$$

where E, m and p_z is the particle mass, energy and the momentum in z direction. The rapidity y is additive under the Lorentz transformations along the z-axis. The rapidity differences are boost-invariant. Using above variables, the four momentum of the particle with mass m can be written as,

$$p^\mu = (E, p_x, p_y, p_z) \tag{B.2}$$

$$= (m_T \cosh y, p_T \sin\phi, p_T \cos\phi, m_T \sinh y) \tag{B.3}$$

where the transverse mass is defined as $m_T = \sqrt{p_T^2 + m^2}$.

If the mass of the particle is negligible or it is traveling close to the speed of light, then the pseudo rapidity η is used instead of y. Substituting $m = 0$ in equation (B.1) gives

$$\eta = \frac{1}{2}\ln\left(\frac{E+E\cos\theta}{E-E\cos\theta}\right) = \frac{1}{2}\ln\left(\frac{1}{\tan\left(\theta/2\right)^2}\right) = -\ln\left(\tan\frac{\theta}{2}\right) \tag{B.4}$$

The merit to use this variable instead of θ is that the the difference in the rapidity of two particles become independent of the Lorentz boosts along the beam axis.

B.2 Vertex Finder Algorithm

The reconstruction of primary vertices can be classified into two stages.

- Primary vertex finding : Take association of the reconstructed track to a particular vertex candidate
- Vertex fitting : Reconstruct and refit the actual vertex position every after taking the track association

Note that two stages are not distinguishable from each other. In principle, the reconstruction of primary vertices start from the preselection of the tracks compatible with the expected bunch crossing region. The selected tracks are then ordered according to the impact parameter in z direction. Then, track clusters in z projection are searched for using a sliding window approach.

The obtained clusters are regarded as independent primary vertex candidates. Each of these candidates is reconstructed using one of the vertex fitters. The χ^2 between the vertex estimate and the trajectory in test is calculated. The trajectories with $\chi^2 < 8\%$ are rejected and the candidate is refitted. The procedure is repeated until no incompatible tracks are left or the cluster size becomes too small to continue.

B.3 The Hough Transformation

The Hough transformation [61][62] is used for the track reconstruction based on the hit pattern at the Muon Spectrometer. All the lines in the xy plane that passes $(x, y) = (x_0, y_0)$ can be expressed like,

$$y_0 = ax_0 + b \tag{B.5}$$

On the other hand in the (a, b) parameter space, this can be projected like,

$$b = -ax_0 + y_0 \tag{B.6}$$

In this way, all the possible lines in xy plane that passes $(x, y) = (x_0, y_0)$ can be translated into the one line in (a, b) parameter space.

Now, if there are sets of points $(x_i, y_i), i = 1, 2, \cdots, N$ which lies in the same line, i.e., $y = a_0x + b_0$, all the corresponding lines in (a, b) parameter space has a cross points at (a_0, b_0). By using this characteristics, one can recognize the straight line in which the number of cross-points become maximum.

To avoid the mathematical difficulties (infinity or zero), it is often the case to use

$$r = x\cos(\phi) + y\sin(\phi) \tag{B.7}$$

instead of $y = ax + b$. The straight line is found so that the cross points in (r, ϕ) plane become maximum. Figure B.1 shows the example of the Hough transformation, where the each curve in (r, ϕ) plane corresponds to one point in 2-D space. The straight line can be found by searching for the parameter at which the number of cross-point become maximum.

B.4 Sagitta measurement

To measure the transverse momentum (p_T) of the muon in the barrel, sagitta measurement is performed making use of the magnetic deflection caused by the barrel toroidal magnet.

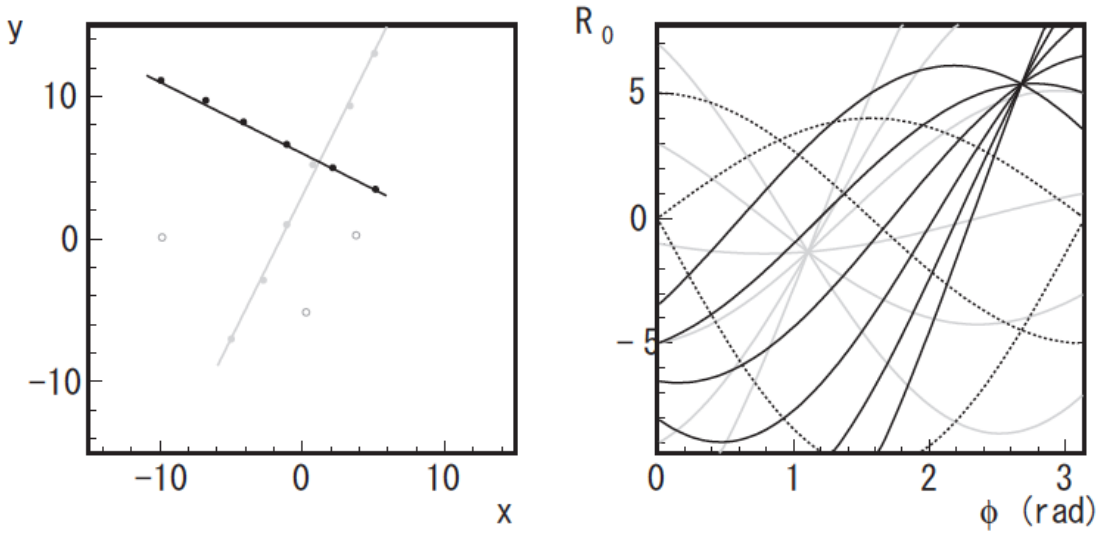

Figure B.1: A set of points (left) and their representation in the Hough Space (right).

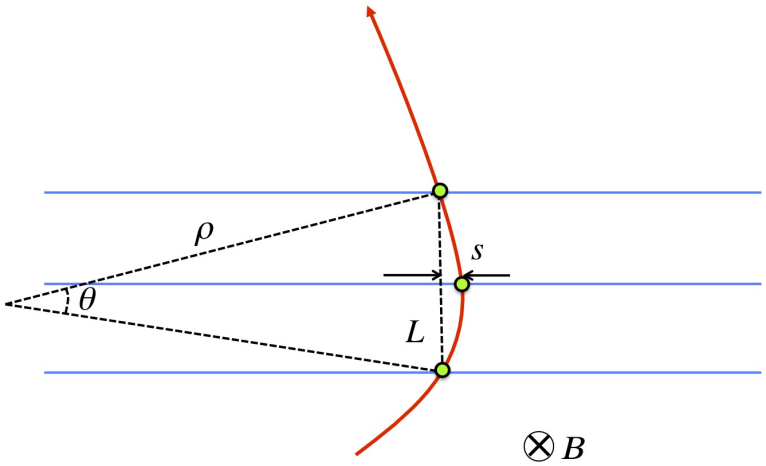

Figure B.2: Muon that traverses three layers of the barrel detector under the magnetic field with its strength B.

Suppose the muon traversing the magnetic field as shown in Figure B.2. Then since,

$$p_T(\mathrm{GeV}) = 0.3B\rho(\mathrm{T}\cdot\mathrm{m}) \tag{B.8}$$

and

$$\frac{L}{2\rho} = \frac{\sin\theta}{2} \approx \frac{\theta}{2}, \tag{B.9}$$

$\theta \approx 0.3LB/p_T$ is derived. Therefore the sagitta (s) can be calculated by

$$s = \rho(1-\cos\theta) \approx \rho\frac{\theta^2}{8} \approx \frac{0.3BL^2}{8p_T} \tag{B.10}$$

In this way, sagitta is translated into the p_T. Since the resolution is proportional to the factor of $1/(BL^2)$, ATLAS makes use of large L, while CMS makes use of large B.

It is noted that since $\Delta(1/p_T) \sim (\Delta s/s)$, $1/p_T$, (not p_T) obeys the gaussian when s obeys the gaussian. Assume the sagitta measurement is performed in xy plane with three space points with its positional resolution of $\sigma(x) \sim \sigma(y)$,

$$\frac{\sigma(p_T)}{p_T} = \frac{\sigma(s)}{s} = \frac{\frac{\sqrt{3}}{2}\sigma(x)}{s} = \frac{\frac{\sqrt{3}}{2}\sigma(x)8p_T}{0.3BL^2} \tag{B.11}$$

is derived. Generally, the p_T resolution will be followings when the number of measured space point is N ($N \geq 10$).

$$\frac{\sigma(p_T)}{p_T} = \frac{\sigma(x)p_T}{0.3BL^2}\sqrt{\frac{720}{N+4}} \tag{B.12}$$

If the $N = 10$, $\sigma(x) = 30$ μm, $B = 2$ T, $L = 1.1$ m, $p_T = 100$ GeV, 3% accuracy is feasible.

B.5 Muon p_T resolution

In Figure B.2, sagitta (s) can be calculated by

$$s = \rho\left(1 - \cos\frac{\theta}{2}\right) \tag{B.13}$$

$$\approx \frac{1}{2!}\rho\left(\frac{\alpha}{2}\right)^2 \tag{B.14}$$

$$= \frac{\rho\alpha^2}{8} \tag{B.15}$$

$$= \frac{L^2}{8\rho} \tag{B.16}$$

Therefore, $\rho = L^2/8s$. Then from equation (B.8),

$$p_T = 0.3\frac{L}{8s}\int BdL \tag{B.17}$$

The p_T resolution can be written as

$$\frac{\Delta p_T}{p_T} = \frac{\Delta s}{s} \oplus \frac{\sigma(\text{energy loss})}{p_T} \tag{B.18}$$

$$= \frac{\sigma(s)8p_T}{0.3L\int BdL} \oplus \frac{\sigma(\text{energy loss})}{p_T} \tag{B.19}$$

where $\sigma(s)$ are classified into the multiple scattering term and the intrinsic term (such as the chamber alignment etc) and can be written as $\sigma(s) = \sigma(s)_{\text{MS}} \oplus \sigma(s)_{\text{chamber}}$.

Now it is known that the multiple scattering term has a resolution which is given by the Moliere equation,

$$\sigma(s)_{\text{MS}} = \frac{L}{2}\frac{0.0136}{p_T\ (\text{GeV})}\sqrt{\frac{X}{X_0}} \tag{B.20}$$

where L is given by Figure B.2 and X_0 is the radiation length. The term $\Delta\theta \equiv \frac{0.0136}{p_T}\sqrt{\frac{X}{X_0}}$ is the angular spread due to the multiple scattering.

From above point of view, p_T resolution become,

$$\frac{\Delta p_T}{p_T} = \left[\sigma(s)_{\text{chamber}}\frac{8p_T}{0.3L\int BdL}\right] \oplus \left[\frac{0.0136}{2}\sqrt{\frac{X}{X_0}}\frac{8}{0.3\int BdL}\right] \oplus \left[\frac{\sigma(\text{energy loss})}{p_T}\right] \qquad \text{(B.21)}$$

This means that the p_T resolution can be expressed by $p_0 p_T + p_1 + p_2/p_T$, where each corresponds to intrinsic term, multiple scattering term and energy loss term. Typically, ATLAS muon spectrometer has a p_T resolution of a few % for $p_T < 100$ GeV and 10% up to $p_T = 1$ TeV. Figure B.3 shows the breakdown of the contributions for the p_T resolution.

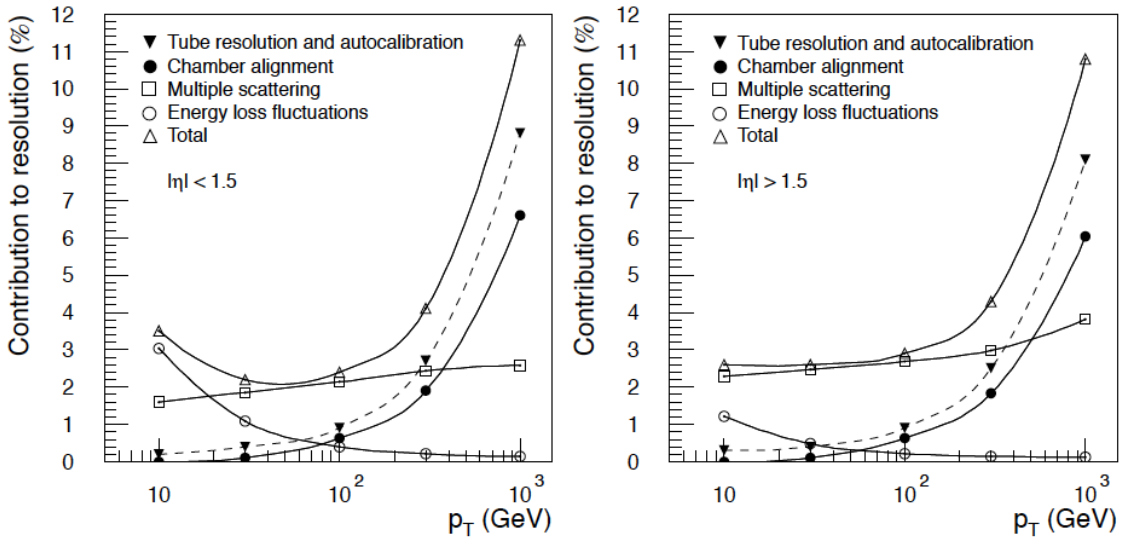

Figure B.3: A simulated muon p_T resolution. The alignment curve is for an uncertainty of 30 μm in the chamber positions. (Left) is for $|\eta| < 1.5$ and (Right) is for $|\eta| > 1.5$.

Appendix C

Additions for Chapter 4

C.1 Limited Proportional mode

TGC is operated under the so-called limited proportional mode. The limited proportional mode is one of the gas amplification process, where these process can be characterized by the applied high voltages. To see this, pulse-height as a function of the applied High voltage is shown in Figure C.1. Each operational mode has a following characteristics.

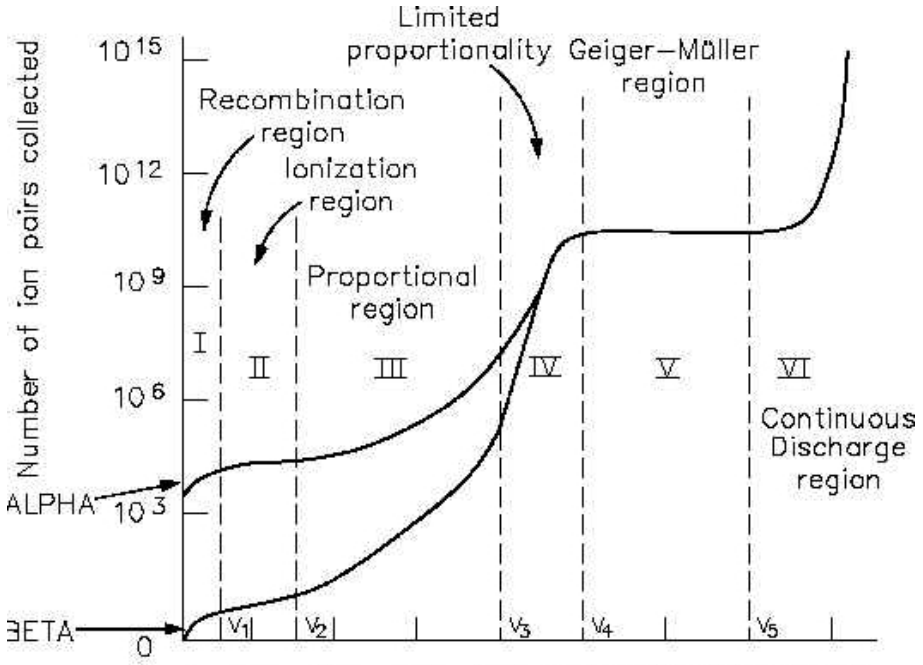

Figure C.1: Number of collected ion pairs as a function of the applied High voltage. Typically, the operational mode can be classified into six regions.

I. Recombination region The applied High voltage is too low and the recombination takes place before any charges are collected at the electrode. As a consequence, no gas amplification is taken place

II. Ionization region In this region, applied High voltage is sufficient enough to avoid the recombination. Though no gas amplification is taken place, ionized electrons can be collected by the electrode.

III. Proportional region Gas amplification is taken place with its amplitude proportional to the applied High voltage. All the electron-ion pairs are collected with its total charge proportional to the primary electron-ion pairs created by the incident particle.

IV. Limited proportional region As the applied High voltage become higher, generated positive ions by the gas amplification near the electrode create the space charge. This space charge will modify the electric field distribution around the anode (space charge effect) and the linearity is not satisfied from this region. However, this region has an advantage that the variation of the performance due to the structural distortion or the incident angle is small. Therefore, we use this region relying on this uniformity with respect to the incident particle.

V. Geiger-Muller region The applied High voltage is so high enough to allow the continuous discharge until it is limited by the own space charge effect. Therefore, the output pulse is almost constant which is independent to the number of primary electron-ion pairs created by the incident particle.

VI. Continuous discharge region Once the ionization occurs, there is a continuous discharge.

There are three merits to adopt limited proportional mode in TGC.

- Variation of the performance due to the structural distortion is small.
- Compose almost same signal shape for the muons with $\theta < 40$ deg. Since the typical incident angle is expected to be $10 < \theta < 45$ deg, this ensures the uniformity.
- No streamer is produced.

C.2 Townsend Type avalanche

As the applied High voltage becomes higher (Typically, 10^6 V/m), the kinematic energy earned during its mean free path (typically, $\mathcal{O}(1\ \mu\text{m})$) exceeds the ionization energy (Typically, $\mathcal{O}(10$ eV$)$). In this case, these electron can ionize another gas molecules and in a similar way, the 2^{nd} ionized electron can also experiences another ionization. This is so-called townsend avalanche. The production rate of the ionized electrons can be expressed by

$$\frac{\mathrm{d}n}{n} = \alpha \mathrm{d}x, \tag{C.1}$$

where α is called as the first Townsend coefficient. Since the TGC has an anode-wire and its electric field increases as it is close to it, α become increases accordingly. The solution of the equation (C.1) gives us,

$$n(x) = n(0)e^{\alpha x} \tag{C.2}$$

It is obvious that the number of derived electrons increases at an exponential rate.

Appendix D

Additions for Chapter 5

D.1 Optimization of the cut threshold

Figure D.1 shows an example of the optimization result for the p_T threshold of two jets, where x and y axis corresponds to the jet p_T for the leading and the 2$^{\text{nd}}$ leading jet, respectively. The contour shows the signal significance after all the event selection applied.

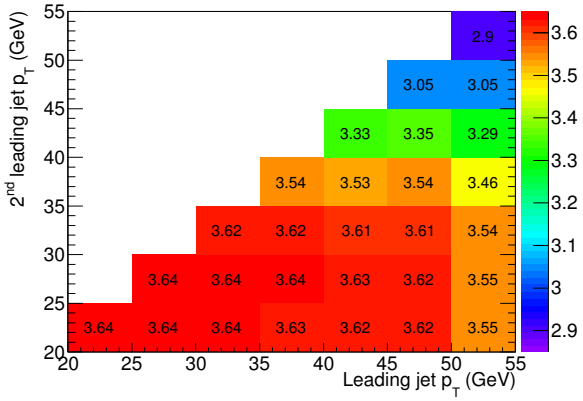

Figure D.1: Signal significance as a function of the leading (x) and 2$^{\text{nd}}$ leading jet p_T (y axis).

D.2 Distributions of the τ identification variables

Figure D.2 shows several τ identification variables used for the BDT$_j$ calculation described in section 5.5.2.

D.3 OS−SS distributions

Figure D.3 and Figure D.4 shows the transverse mass distributions after the OS−SS subtraction, for the τ_1 candidate and the τ_3 candidate, respectively.

D.4 Efficiency and the fake rate of the Matrix method

The fake rate ($\varepsilon_{\text{fake}}$) was estimated using $W + 1$ fake τ control region in data. The fake rate that the jet faking to the τ candidate shows a good agreement with the one expected from the MC simulation in the ≥ 1 b-tag region when binned by the EM-fraction (f_{EM}). On the other hand, the efficiency ($\varepsilon_{\text{fake}}$) was measured from MC simulation, including all real τ and electrons reconstructed as the τ candidate. Figure D.5 shows the efficiency and the fake rate used in the matrix method, and the Figure D.6 shows the results of the matrix method. The MC fake rate (yellow) is normalized to the matrix method prediction (red). The expected MC signal (blue) is stacked on the matrix method prediction, and shown with the data (black). Errors are statistical only. The data and the MC estimation agree within the uncertainty.

D.5 Comparison of the background BDT$_j$ distributions in $W + 1$ fake τ control region and the signal region

Figure D.7 shows the comparison of the BDT$_j$ distributions for the fake τ leptons in $W+1$ fake τ control region and the signal region, depending on the EM fraction (f_{EM}) between 0.0-0.4, 0.4-0.8, and > 0.8. Both distributions are derived from MC simulation. With this binning, both background distributions are in good agreement.

D.6 Acceptance dependence on the charged Higgs boson mass

Figure D.8 shows the absolute acceptance (left) and the relative acceptance with respect to the previous event selection (right). The variations of the color correspond to the variations of the assumed charged Higgs boson mass. The big difference arises from the number of jet requirement: the higher charged Higgs boson mass, the lower acceptance due to the available phase space becomes lower.

Figure D.9 shows several kinematic distributions: number of jets, p_T of the leading jet, E_T^{miss}, and the p_T of the τ candidate. As expected, the higher charged Higgs boson mass results in lower leading jet p_T, higher missing transverse momentum, higher tau p_T, and lower number of jets.

D.7 Ratio measurement result

Figure D.10 shows the variation of the cross section for each systematic sources, and Figure D.11 shows its ratio. From left to right, it is $e\tau$ and ee channel, $e\tau$ and $e\mu$ channel and $\mu\tau$ and $e\mu$ channel.

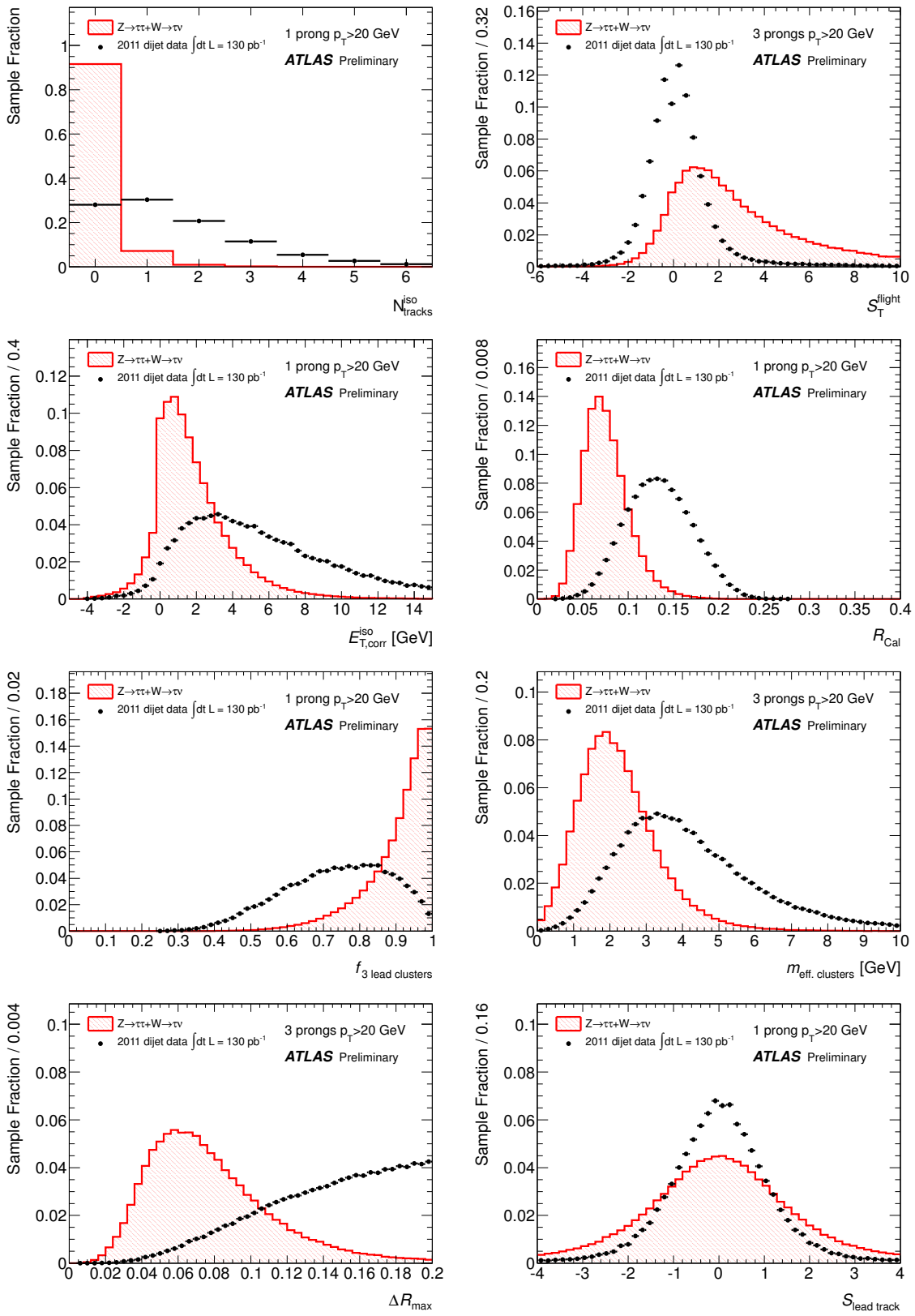

Figure D.2: Distributions of the τ identification variable used for the BDT$_j$ calculation.

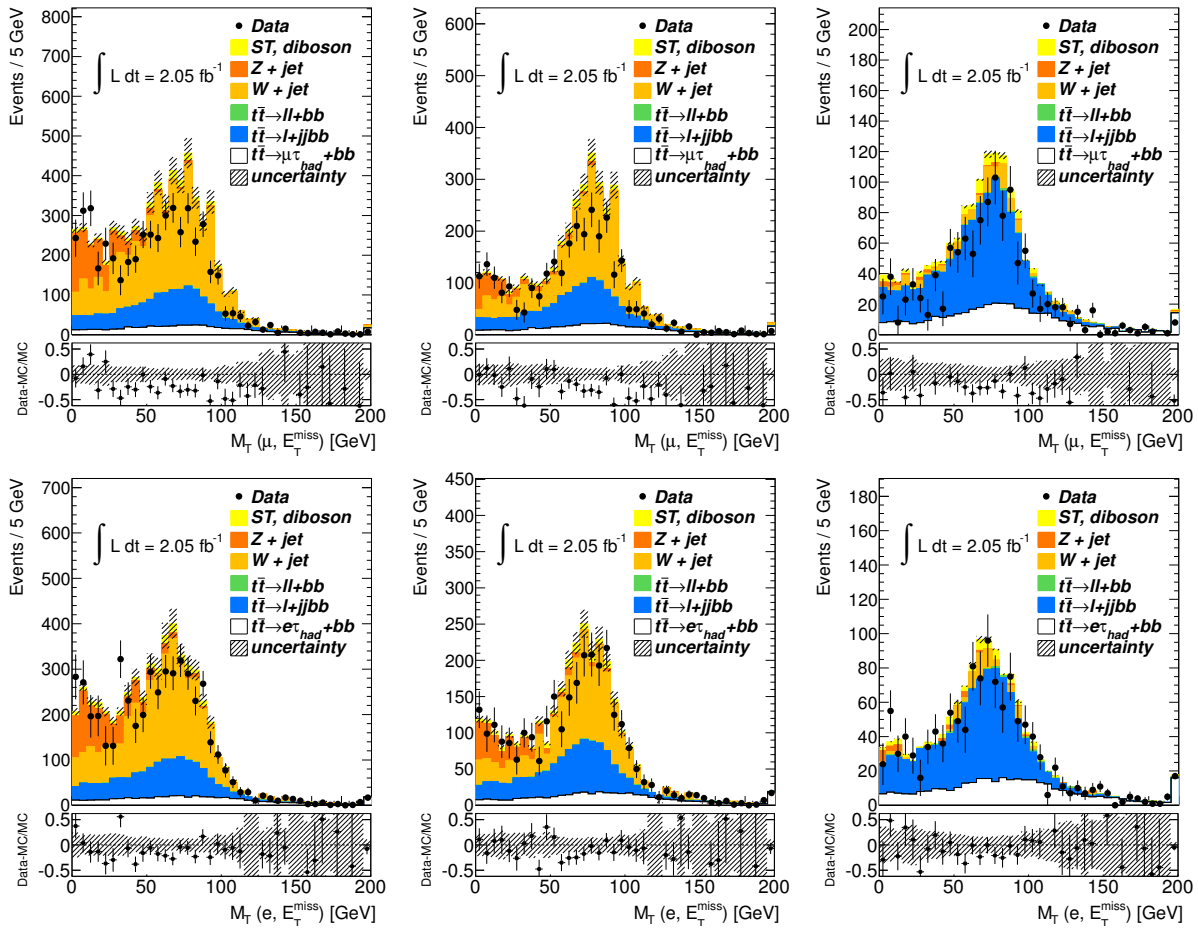

Figure D.3: Data and MC comparison for the transverse mass distribution for each stage of the event selection. (From left to right) before E_T^{miss} cut, before b-tagging, and after b-tagging. (Top) muon channel, (bottom) electron channel in τ_1 candidates.

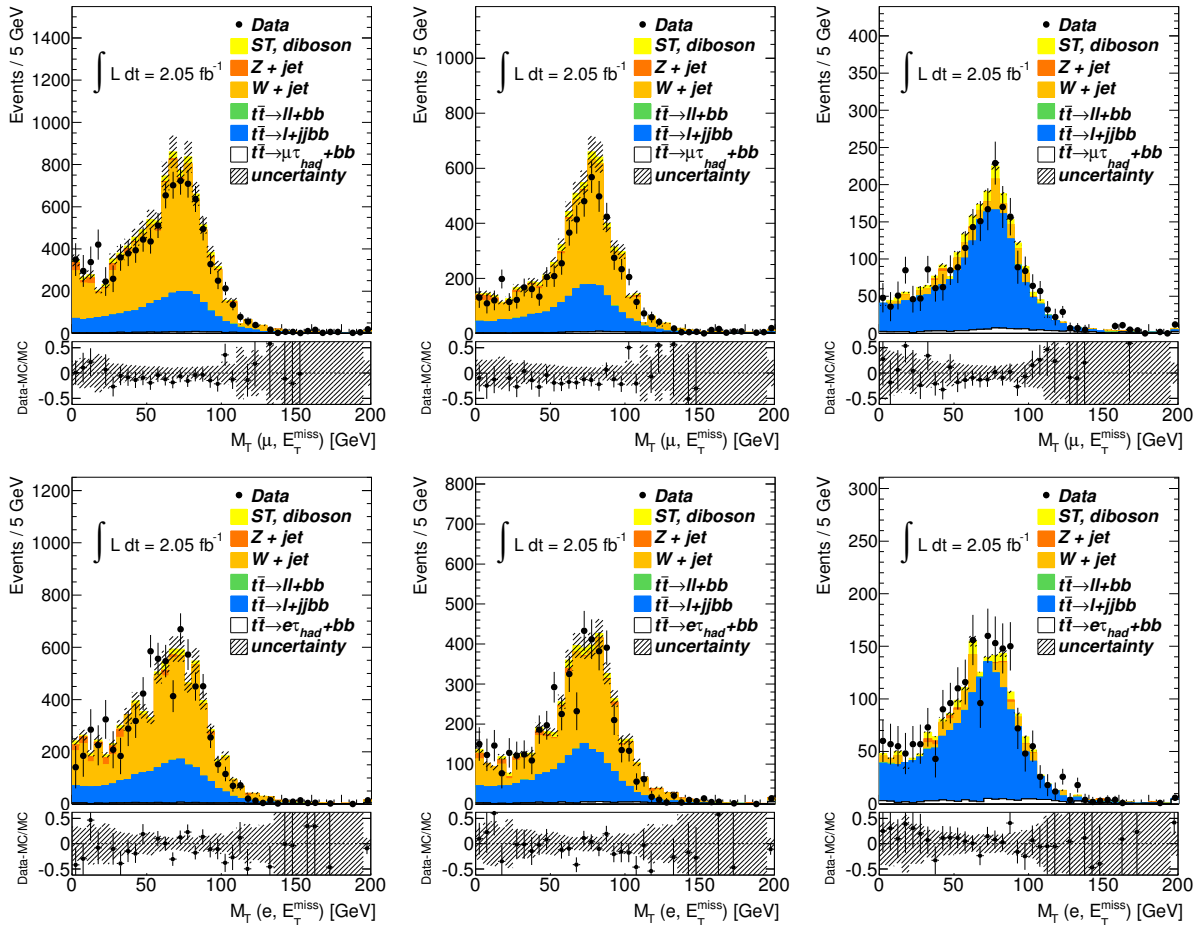

Figure D.4: Same plots with Figure D.3 in τ_3 candidates.

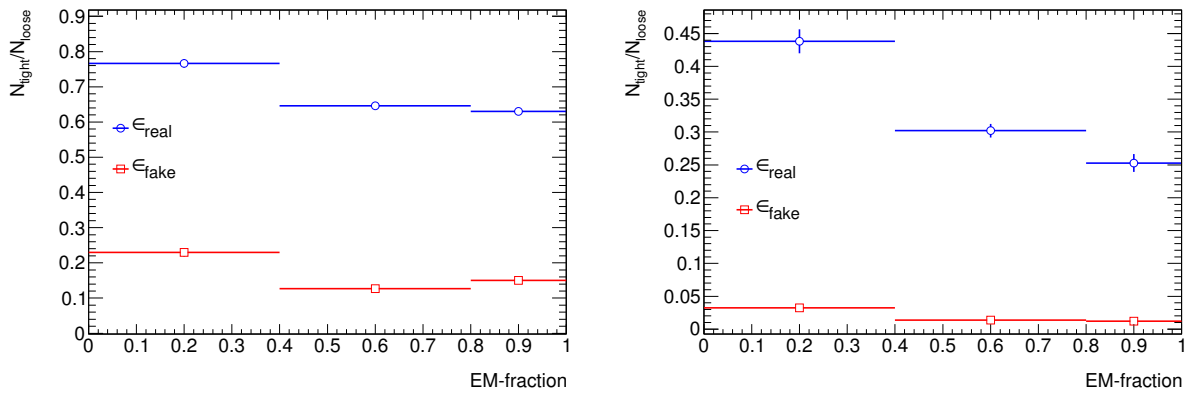

Figure D.5: The efficiency and the fake rate used in the matrix method for τ_1 (left) and for τ_3 (right).

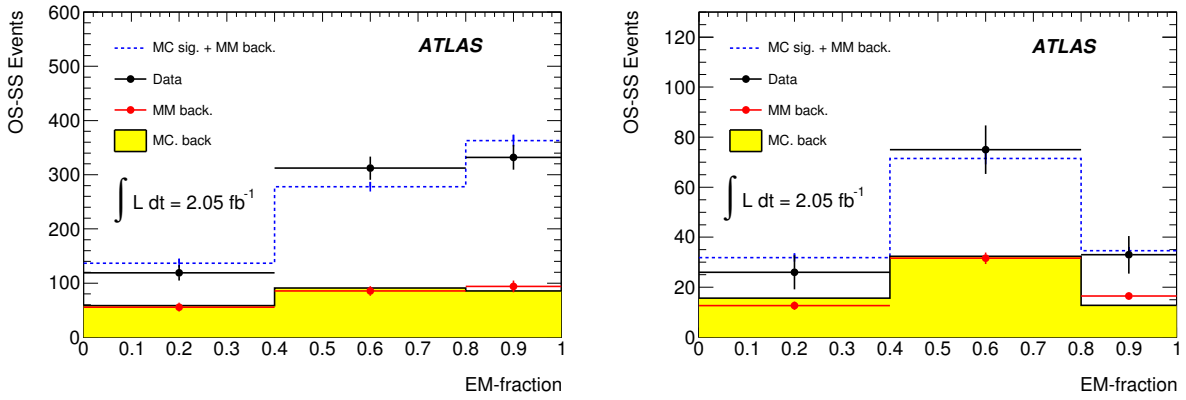

Figure D.6: Results of the matrix method for τ_1 (left) and for τ_3 (right), combining the electron and the muon channel.

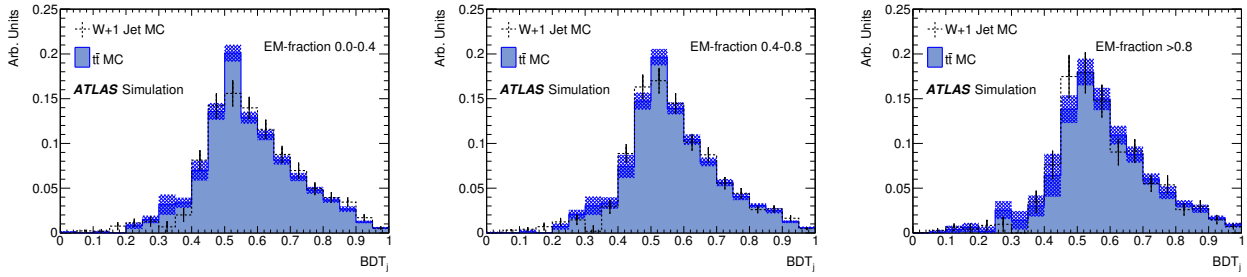

Figure D.7: Comparison of the background BDT_j distributions in $W + 1$ fake τ control region (cross point) and the signal region (blue histogram). From left to right, $0.0 < f_{\mathrm{EM}} < 0.4$, $0.4 < f_{\mathrm{EM}} < 0.8$, and $f_{\mathrm{EM}} > 0.8$.

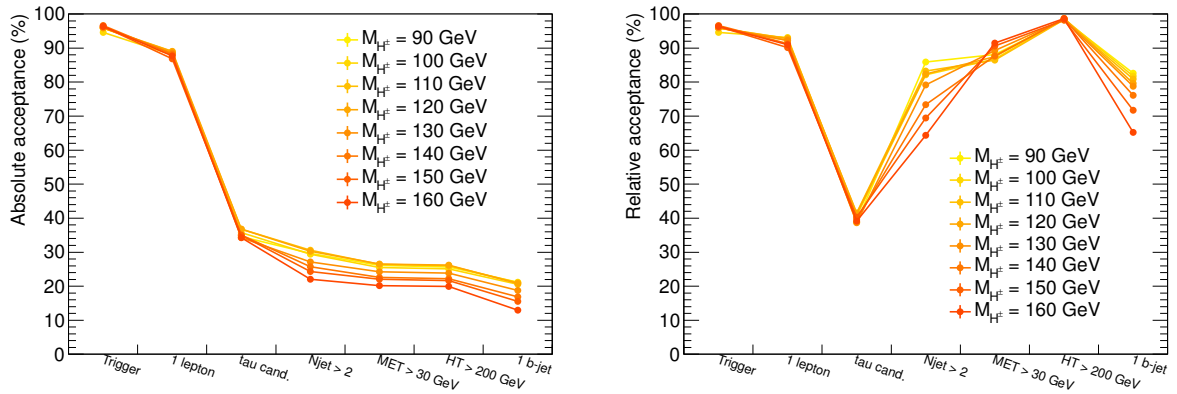

Figure D.8: The absolute (left) and the relative (right) acceptance.

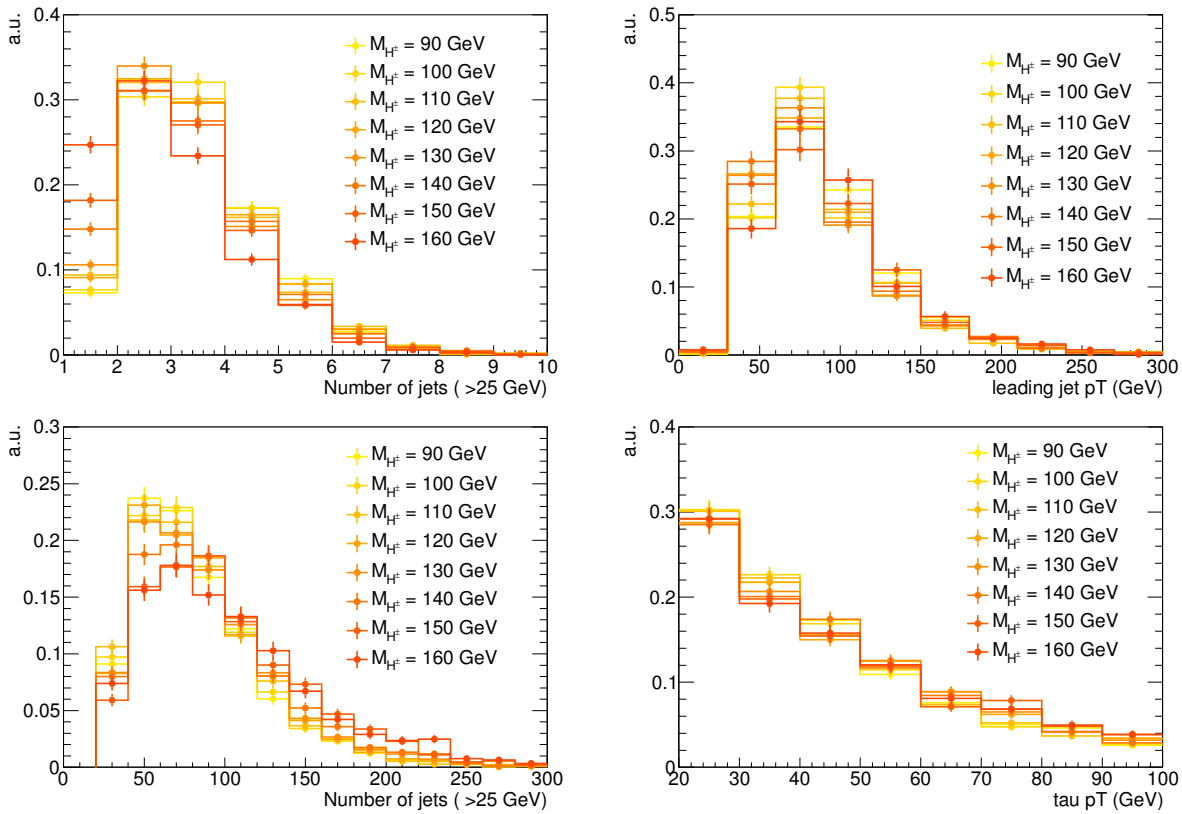

Figure D.9: (From left top to right bottom) The kinematic distributions for the number of jets, p_T of the leading jet, E_T^{miss}, and the p_T of the τ candidate.

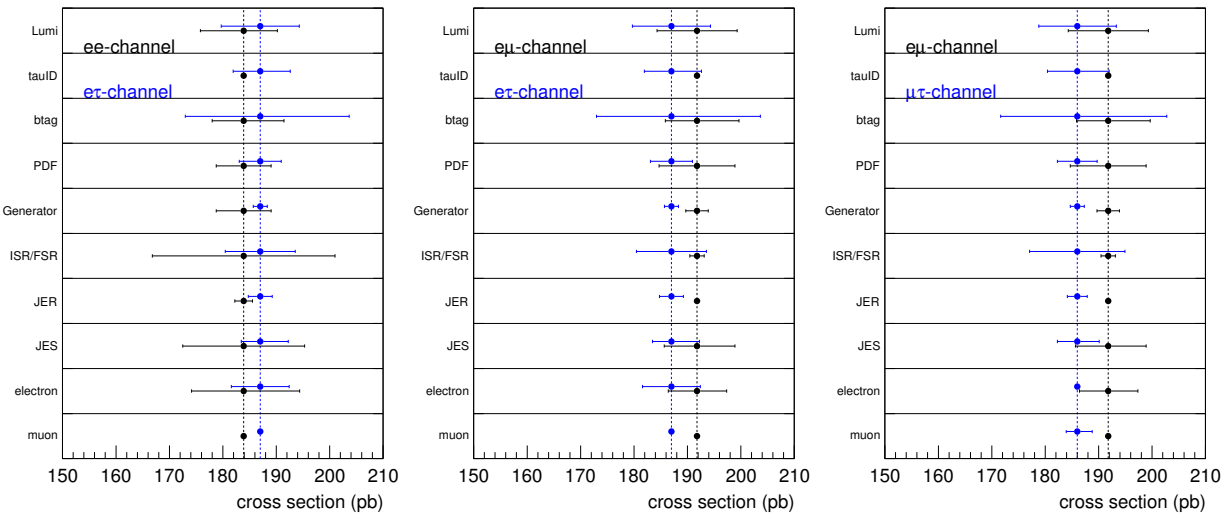

Figure D.10: The ratio of the cross section between (Left) τe and ee channel, (middle) τe and $e\mu$ channel and (right) $\tau\mu$ and $e\mu$ channel.

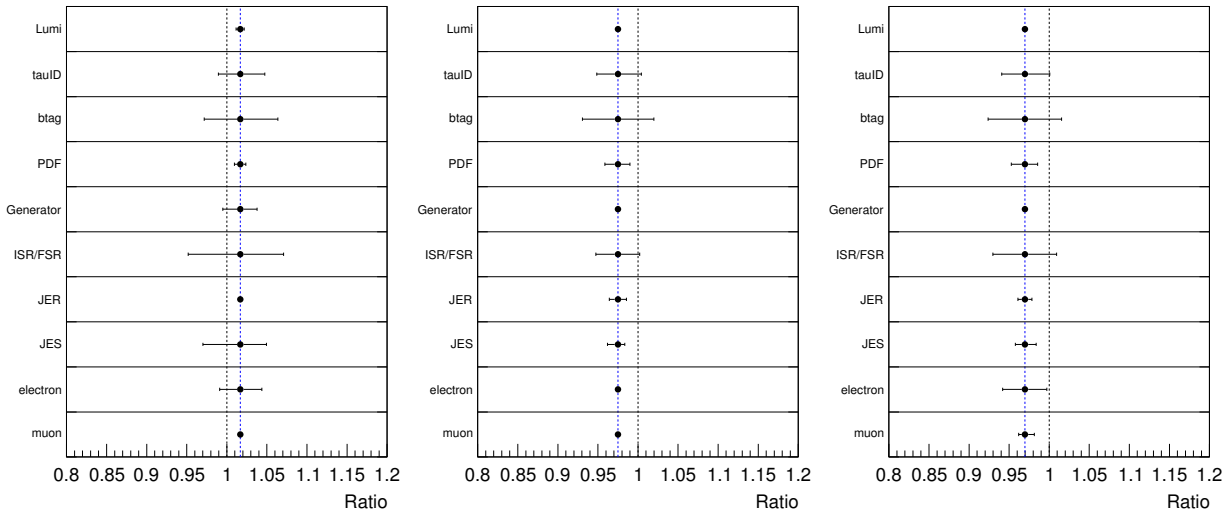

Figure D.11: The comparison of the variation of the cross section for each systematic source between (Left) τe and ee channel, (middle) τe and $e\mu$ channel and (right) $\tau\mu$ and $e\mu$ channel.

Acknowledgement

There are a number of people without whom my thesis is not completed.

First of all, I would like to express my sincere thankfulness to my supervisor, Makoto Tomoto. Without his continuous encouraging and the proper advices, this research was not completed. It was my great fortune to be the first student of him and enjoyed research together since the detector construction period. I also would like to thank his wife for her careful check of my thesis as well as her delicious dishes when they kindly invited me to the home party at Switzerland.

I deeply appreciate to my laboratory Professor, Toru Iijima and former laboratory Professor, Takayoshi Ohshima for their great support. I am pretty sure that I learned a lot from them not only about the research but also about the life as a physicist. It is my good memory that I spent a joyful time every christmas eve together with Ohshima-san's family. His family is really warm and full of humor. I dare say that it was the ohshima-san's class when I decided to jump into this research area. Nowadays, I really think this decision is correct. I am really appreciate to provide me such a great opportunity at the ATLAS experiment.

I would like to thank to the co-spokespersons of the ATLAS Japan group, Prof. Takahiko Kondo, Prof. Tomio Kobayashi and Prof. Katsuo Tokushuku for giving me this excellent opportunity to participate at the ATLAS experiment. It was really exciting that I could join from its construction period till the end of 2012, when lots of fruitful physics results emerge. I also would like to dedicate my deep thankfulness to Dr. Peter Jenni, the former ATLAS spokesperson, to be my supervisor when I was a fellow of Japan Society for the Promotion of Science (JSPS). He is really kind and gentleman enough to give me a full of smile whenever we met at the building 40.

When I have been working on the TGC commissioning, I was really helped by Prof. Osamu Sasaki and Masaya Ishino as a group leader of the TGC Japan team. Their professional skills of the electronics and the logical thinking stimulated me a lot. It is my good memory that Ishion-san invited me to his home. I also would like to thank to his wife for her delicious dishes and their daughter for her lovely characteristics enough to forget my tiredness of the research. It is my honor to express my gratitude to Hiroyuki Iwasaki, Hisaya Kurashige, Masahiro Ikeno, Shuji Tanaka, Kunihiro Nagano, Hiroshi Sakamoto, Tatsuo Kawamoto, Yoji Hasegawa, Atsuhiko Ochi, Takashi Matsushita, Susumu Oda, Chikara Fukunaga, Akimasa Ishikawa, Yoshiji Yasu, and Yorihito Sugaya for their advices of the TGC and encouraging. Mr Takashi Kubota, Takashi Kuwabara and Hiroshi Nomoto are my senior, all of them greatly helped me a lot, especially provide me a know-how about the TGC operation. Without their support, my research has not been even started.

Furthermore, I did a lot of discussions with my colleagues with Takashi Hayakawa, Yu

Suzuki, Kohei Kessoku, Yoichi Ninomiya, Mattew King, Tomoe Kishimoto, Kazutoshi Tani and Tomonori Nishiyama, which certainly helped to deepen the understanding of the TGC. I would like to thank Giora Mikenberg, Fabio Cerutti, Ludovico pontecorvo, Sotirios Vlachos, Daniel Lellouch, Lorne levinson, Shlomit tarem, Shikma bressler, Sagi ben ami, David Front, Verena martines, Alberto belloni, Laura jeanty, Joao guimaraes da costa, Frank taylor and Alon Hershenhorn for our discussions with muon detector and their help to my presentation at ICATPP international conference. They are all friendly and helpful at any times which was really vigorous for me.

When it comes to the measurement of the top-quark pair production cross section, I would like to express my great thanks to Serban Protopopescu for his powerful and brilliant leadership. His unique idea and the passion for the physics has been stimulated me a lot. I also would like to appreciate Dugan Oneil, Susana Cabrera Urban and Dick Greenwood Jr for their advices, discussions, meeting management and editing works. Jacob Searcy and Jennifer Godfrey are my sincere colleagues who cooperate together to make a set of results. Their kindness and helpfulness greatly helped the research. I also would like to thank Susie Bedikian, Catrin Bernius, Eva Valladolid Gallego, Teresa Maria Perez Garcia Estan and Allison.mccarn for their support. Noel Dawe kindly instructed me about the Boosted Decision Tree technique which is the key aspect of this analysis. He is actually the trainer of the BDT_j used in this analysis.

Throughout my research, Andrey Loginov, Markus Cristinziani, Ford Garberson, Lucio.Cerrito and Maria Jose Costa continuously encouraged and took care of the analysis progress. It is my great honor to express my gratitude to them. I also would like to thank editorial board members, Ian Brock, Frank Filthaut, Monica D'Onofrio, and Ilya Tsoukerman for their proper advices and careful check of the publication paper. Without their patience, paper publication has not been achieved.

Apart from research, I also enjoyed a lot of discussions including a small talk with Japanese colleagues at CERN. I would like to express my thankfulness to Shigeru Odaka, Junnichi Kanzaki, Soshi Tsuno, Keita Hanawa, Shoji Asai, Junichi Tanaka, Naoko Kanaya, Shinpei Yamamoto, Koji Terashi, Tatsuya Masubuchi, Koji Nakamura, Yuya Azuma, Hiroshi Yamaguchi, Takeshi Domae, Toyonobu Okuyama, Kohei Yorita, Naoki Kimura, Osamu Jinnouchi, Takayuki Kanno, Tohru Takeshita and Kiyotomo Kawagoe. I really enjoy discussions with them in a variety of theme.

Furthermore, I would like to appreciate Kazunori Hanagaki and Yuji Yamazaki for their chair of weekly ATLAS japan west meeting, where they gave me a lot of advices to push forward my analysis. It was such a priceless time for me to polish up my analysis. I would like to thank Junji Tojo, Wataru Okamura, Minoru Hirose, Jason Lee and Hidetoshi Otono for our discussions, as well.

Throughout whole my research, I cannot imagine what I am now without the presence of Nagoya ATLAS members. I would like to express my deep thanks to Takuya Sugimoto, Masato Aoki, Shima Shimizu, Yasuyuki Okumura, Satoshi Hasegawa, Ljiljana Morvaj, Jun Wakabayashi, Yuki Ito, Hideharu Shichi, Katsuya Yamauchi, and Yoshihiro Ura. Especially, I really would like to thank Yasuyuki Okumura for our discussions (even argument) and living together. We are really a close friend since Bachelor's courses. My memory with him is a

treasure for the rest of my life. I hope all of the ATLAS members will complete their research in a good shape.

Finally, I would like to thank from bottom of my heart to my family. Without their eternal love and selfless support, I am sure I could not finish my research. I would like to thank my grandfather, Yasuichi for his continuous and even long letter to me which encouraged me a lot, Eichi Goto for his warm characteristics and encouragement, my grandmother Yoshie and Chieno for their heartful word. I would like to express my deep thanks to my parent Kenji and Akiko for their unmeasurable support and to my sister Maho and my brother Shugo for their spirit of cooperation. I would like to dedicate my thesis to my late grandmother, Yoshie, who died in 8, Nov, 2011. She always cheered me up and hoped my health every time when I went back to home. I may be the bad son because I was at CERN and could not return back to my home when she died. My grandmother, thank you very much for your great supports. My memory with you will be forever.

After writing this acknowledgement, I am surprised to recognize how a large number of people supported my research. It was such a great moment for me to do the research with them. I would like to express my thankfulness again.

Yuta TAKAHASHI

Bibliography

[1] Particle Data Group K. Nakamura et al. Pdglive particle summary quarks. 2011.

[2] The ATLAS collaboration. Measurement of the $t\bar{t}$ production cross-section in pp collisions at $\sqrt{s} = 7$ tev using kinematic information of lepton+jets events. *ATLAS-CONF-2011-121.*

[3] The ATLAS collaboration. Measurement of the cross section for top-quark pair production using final states with two high-pt leptons. *arXiv:1202.4892.*

[4] The ATLAS collaboration. Measurement of $t\bar{t}$ production in the all-hadronic channel in 4.7 fb^{-1} of pp collisions at $\sqrt{s} = 7$ tev with the atlas detector. *ATLAS-CONF-2012-031.*

[5] The CDF collaboration. Observation of top quark production in $p\bar{p}$ collisions with the collider detector at fermilab. *Physical Review Letters*, Vol. 74, pp. 2626–2631, 1995.

[6] The D0 collaboration. Search for high mass top quark production in $p\bar{p}$ collisions at $\sqrt{s} = 1.8$ tev. *Physical Review Letters*, Vol. 74, pp. 2422–2426, 1995.

[7] S. Bethke. The 2009 world average of α_s. *arXiv:0908.1135.*

[8] Yuri L. Dokshitzer. Calculation of the structure functions for deep inelastic scattering and e^+e^- annihilation by perturbation theory in quantum chromodynamics. *Sov. Phys. JETP*, Vol. 46, pp. 641–653, 1977.

[9] V. N. Gribov and L. N. Lipatov. *Sov.J.Nucl.Phys*, Vol. 15, No. 438, 1972.

[10] Guido Altarelli and G. Parisi. Asymptotic freedom in parton language. *Nucl. Phys. B*, Vol. 126, No. 298, 1977.

[11] J. Huston H. Lai P. Nadolsky J. Pumpli, D. Stump and W. Tung. New generation of parton distributions with uncertainties from global qcd analysis. *JHEP*, Vol. 07, No. 012, 2002.

[12] P.M. Nadolsky et al. Implications of cteq global analysis for collider observables. *Phys. Rev. D78*, No. 013004, 2008.

[13] S. Moch and P. Uwer. Theoretical status and prospects for top-quark pair production at hadron colliders. *Phys. Rev. D*, Vol. 78, No. 034003, 2008.

[14] S. Moch U. Langenfeld and P. Uwer. New results for $t\bar{t}$ production at hadron colliders. *arXiv:hep-ph/0907.2527*, No. 034003, Workshop on Deep-Inelastic Scattering and Related Topics.

[15] M. Beneke et al. Threshold expansion of the $gg(q\bar{q}) \to \bar{q}q + x$ cross section at $\mathcal{O}(\alpha_s^4)$. *Phys. Lett. B*, Vol. 690, No. 483, 2010.

[16] Predictions in the paper are calculated with hathor with $m_{\text{top}} = 172.5$ gev.

[17] J Stirling. Mstw pdfs. `http://projects.hepforge.org/mstwpdf/plots/plots.html`.

[18] The ATLAS Collaboration. The atlas experiment at the cern large hadron collider. *JINST*, Vol. 3, No. S08003, 2008.

[19] Sov. V. E. Pafomov. The cern large hadron collider : Accelerator and experiments, lhc machine. *Phys. JETP*, Vol. 6, No. 829, 1958.

[20] G. P. Salam M. Cacciari and G. Soyez. The anti-kt clustering algorithm. *JHEP 0804*, No. 063, 2008.

[21] Sov. V. E. Pafomov. Performance of the atlas trigger system in 2010. *arXiv:1110.1530*.

[22] Y.Suzuki. *The commissioning of the ATLAS Muon Trigger System*. PhD thesis.

[23] Ellie Dobson. Performance of the atlas trigger and daq system. *ATL-DAQ-PROC-2011-032*.

[24] The ATLAS collaboration. Updated luminosity determination in pp collisions at $\sqrt{s} = 7$ tev using the atlas detector. *ATLAS-CONF-2011-011*, 2011.

[25] The ATLAS collaboration. Luminosity determination in pp collisions at $\sqrt{s} = 7$ tev using the atlas detector at the lhc. *Eur. Phys. J. C*, 2011.

[26] S. Frixione and B.R.Webber. Matching nlo qcd computations and parton shower simulations. *JHEP 06*, No. 029, 2002.

[27] N.Davidson et al. Universal interface of tauola technical and physics documentation. *arXiv:1002.0543*.

[28] H. Lai P. Nadolsky M.L. Mangano, M. Moretti and A.D. Polosa. Alpgen, a generator for hard multiparton processes in hadronic collisions. *JHEP 07*, No. 001, 2003.

[29] E. Laenen S. Frixione and P. Motylinski. Single-top production in mc@nlo. *JHEP 03*, No. 092, 2006.

[30] GEANT4 Collaboration S. Agostinelli et al. Geant4, a simulation toolkit. *Nucl. Instrum. Meth. A506*, No. 250, 2003.

[31] The ATLAS Collaboration. The atlas simulation infrastructure. *Eur. Phys. J. C70*, pp. 823–874, 2010.

[32] The ATLAS Collaboration. Commissioning of the atlas high-performance b-tagging algorithms in the 7 tev collision data. *ATL-CONF-2011-102*.

[33] The ATLAS Collaboration. Performance of the reconstruction and identification of hadronic tau decays with the atlas detector. *ATL-CONF-2011-152*.

[34] ATLAS collaboration K. Becker et al. Mis-identified lepton backgrounds in top quark pair production studies for eps 2011 analyses. *ATL-COM-PHYS-2011-768, 2011*.

[35] Y. Freund and R.E. Schapire. Proceedings of the thirteenth international conference. p. 148.

[36] J. Zhu Y. Liu I. Stancu B.P. Roe, H.-J. Yang and G. McGregor. Boosted decision trees as an alternative to artificial neural networks for particle identification. *Nucl. Instrum. Methods Phys. Res.*, p. 148, 2005.

[37] V.M. Abazov et al. Evidence for production of single top quarks. *Phys. Rev. D*, Vol. 78, No. 012005, p. 148, 2008.

[38] The ATLAS Collaboration. Measurement of the inclusive $w^{\pm}$ and z/γ cross sections in the e and μ decay channels in pp collisions at $\sqrt{s} = 7$ tev with the atlas detector. *arXiv:1109.514v3*.

[39] The ATLAS Collaboration. Jet energy measurement with the atlas detector in proton-proton collisions at $\sqrt{s} = 7$ tev. *arXiv:1112.6426*.

[40] The ATLAS collaboration. Calibrating the b-tag efficiency and misstag rate in 35 pb^{-1} of data with the atlas detector.

[41] P. Nason. A new method for combining nlo qcd with shower monte carlo algorithms. *JHEP*, Vol. 11, No. 070, 2007.

[42] P. Nason S. Frixione and C. Oleari. Matching nlo qcd computations with parton shower simulations: the powheg method. *JHEP*, Vol. 11, No. 040, 2007.

[43] C.Oleari S. Alioli, P. Nason and E. Re. A general framework for implementing nlo calculations in shower monte carlo programs: the powheg box. *JHEP*, Vol. 06, No. 043, 2010.

[44] B.P. Kersevan and E.Richter-Was. The monte carlo event generator acermc version 2.0 with interfaces to pythia 6.2 and herwig 6.5. *arXiv:hep-ph/0405247*.

[45] The ATLAS Collaboration. The atlas simulation infrastructure. *Eur. Phys. J. C*, Vol. 70, pp. 823–874, 2010.

[46] W.J. Stirling A.D Martin, R.G. Roberts and R.S. Thorne. Parton distributions: a new global anslysis. *Eur. Phys. J. C*, Vol. 4, No. 463, 1998.

[47] R.S. Thorne G. Watt A.D. Martin, W.J. Stirling. Parton distributions for the lhc. *arXiv:0901.0002v3*.

[48] NNPDF Collaboration. The pdf4lhc benchmarks on lhc observables: the nnpdf2.0 study. 2010.

[49] D. Gibaut L. Lyons and P. Clifford. How to combine correlated estimates of a single physical quantity. *Nuc. Instr. Meth. A270*, No. 110, 1988.

[50] The ATLAS collaboration. Measurement of the $t\bar{t}$ production cross section in the final state with a hadronically decaying tau lepton and jets using the atlas detector. *ATLAS-CONF-2012-032*.

[51] The CMS collaboration. Measurement of ttbar pair production cross section at $\sqrt{s} = 7$ tev using $b-$quark jet identification techniques in lepton + jet events. *CMS-PAS-TOP-11-003*.

[52] The CMS collaboration. Top pair cross section in dileptons. *CMS-PAS-TOP-11-005*.

[53] The CMS collaboration. Measurement of the top quark pair production cross section in pp collisions at $\sqrt{s} = 7$ tev in dilepton final states containing a tau. *arXiv:1203.6810*.

[54] The CMS collaboration. Measurement of the ttbar production cross section in the tau-plus-jets channel in pp collisions at sqrt(s)=7 tev. *CMS PAS TOP-11-004*.

[55] The CMS collaboration. Measurement of the ttbar production cross section in the fully hadronic decay channel in pp collisions at 7 tev. *CMS-PAS-TOP-11-007*.

[56] The CDF Collaboration. Combination of cdf top quark pair production cross-section measurements with up to 4.6 fb^{-1}. *Conf Note 9913*.

[57] G. Zech. Upper limits in experiments with background or measurement errors. *Nuc. Instr. Meth. A277*, pp. 608–610, 1989.

[58] The D0 Collaboration. Combination of $t\bar{t}$ cross section measurements and constraints on the mass of the top quark and its decays into charged higgs bosons. *Phys. Rev. D*, Vol. 80, No. 071102, 2009.

[59] Gordon L. Kane. The dawn of physics beyond the standard model. *Scientific American*, June 2003.

[60] Frank Wilczek. In search of symmetry lost. *Nature*, Vol. 433, pp. 239–247, January, 2005.

[61] P. V. C. Hough. General purpose visual input for a computer. *Annals of the New York Academy of Sciences*, Vol. 99, pp. 323–337, June, 1962.

[62] P. Hough and B. Powell. A method for faster analysis of bubble chamber photographs. *Annals of the New York Academy of Sciences*, Vol. 18, pp. 1184–1191, 1960.